LETTERS

Reduction and selective oxo group silylation of the uranyl dication

Polly L. Arnold[1], Dipti Patel[1], Claire Wilson[2] & Jason B. Love[1]

Uranium occurs in the environment predominantly as the uranyl dication $[UO_2]^{2+}$. Its solubility renders this species a problematic contaminant[1–3] which is, moreover, chemically extraordinarily robust owing to strongly covalent U–O bonds[4]. This feature manifests itself in the uranyl dication showing little propensity to partake in the many oxo group functionalizations and redox reactions typically seen with $[CrO_2]^{2+}$, $[MoO_2]^{2+}$ and other transition metal analogues[5–9]. As a result, only a few examples of $[UO_2]^{2+}$ with functionalized oxo groups are known. Similarly, it is only very recently that the isolation and characterization of the singly reduced, pentavalent uranyl cation $[UO_2]^{+}$ has been reported[10–12]. Here we show that placing the uranyl dication within a rigid and well-defined molecular framework while keeping the environment anaerobic allows simultaneous single-electron reduction and selective covalent bond formation at one of the two uranyl oxo groups. The product of this reaction is a pentavalent and monofunctionalized $[O{=}U{\cdots}OR]^{+}$ cation that can be isolated in the presence of transition metal cations. This finding demonstrates that under appropriate reaction conditions, the uranyl oxo group will readily undergo radical reactions commonly associated only with transition metal oxo groups. We expect that this work might also prove useful in probing the chemistry of the related but highly radioactive plutonyl and neptunyl analogues found in nuclear waste.

Reactions of the uranyl dication that result in the functionalization or transformation of the U=O groups are rare. Examples include atypical Lewis base behaviour of the uranyl dioxo group towards alkali metals in the solid state[13,14], and the formation of an unusual $O{=}U{=}O{\rightarrow}B(C_6F_5)_3$ adduct involving significant and asymmetric U=O bond lengthening[15]. Photolysis of uranyl phosphine oxide complexes in the presence of alcohols results in two-electron reduction and the formation of U(IV) alkoxides, via the highly oxidizing $*UO_2^{2+}$ excited state; the U(IV) complexes can be hydrolysed to regenerate the uranyl dication cleanly[16]. Usually, the $[UO_2]^{+}$ cation spontaneously disproportionates to $[UO_2]^{2+}$ and U(IV) phases in an aqueous environment. We reported recently[17] that the reaction between the mono-uranyl complex, **1** (R = H), and transition metal silylamides $[M\{N(Si(CH_3)_3)_2\}_2]$ (M = Mn, Fe, Co) forms the molecular cation–cation complexes, **2**, in which, uniquely, the transition metal bonds to the *endo*-uranyl oxygen atom (Fig. 1a), that is, the uranyl acts as a Lewis base to the transition metal[18]; in this case, no electron transfer between the metals was seen. In search of alternative synthetic routes, we have found that the one-pot reaction between **1** ($R = CH_3$), FeI_2, and the silylamide base $KN(Si(CH_3)_3)_2$ at –78 °C resulted in the formation of the new cation–cation complex $[UO(OSi(CH_3)_3)(thf)Fe_2I_2(L)]$, **3**, in 80% isolated yield, Fig. 1a (see Methods and Supplementary Information for synthetic details; thf stands for tetrahydrofuran).

The X-ray single-crystal structure of **3** (Fig. 2a, and Supplementary Information) shows that the macrocycle geometry remains wedge-shaped, even though two tetrahedral Fe cations are now incorporated in the lower cavity, and a $Si(CH_3)_3$ group is bound to the *exo*-uranyl oxygen. The uranyl cation displays a distorted pentagonal bipyramidal geometry with a linear O1–U1–O2 group (172.16(17)°). The U–O bond distances confirm that the uranyl fragment in **3** is in the pentavalent oxidation state. The *endo*-U1–O1 (1.870(4) Å) bond distance in **3** is elongated compared with those of the hexavalent $[UO_2]^{2+}$ complexes **1** (R = H: U1–O1 1.790(4) Å) and **2** (M = Mn: U1–O1 1.808(4) Å), and is similar to experimental[10–12,19] and calculated[20,21] bond distances for pentavalent $[UO_2]^{+}$ (range 1.811 to 1.934 Å). The *exo*-U1–O2 (1.993(4) Å) bond distance is appreciably longer than U1–O1 (compare with **2** (M = Mn): U1–O2 1.768(5) Å), but is significantly shorter than in tetravalent U–$OSiR_3$ complexes[22] and pentavalent U–OR compounds[23] (all greater than 2.0 Å). This implies that the *exo*-U–O bond still retains some multiple bond character, but less than that of the *endo*-U–O bond. Both Fe1 and Fe2 are four-coordinate and bound to the macrocycle by single iminopyrrolides, and to each other

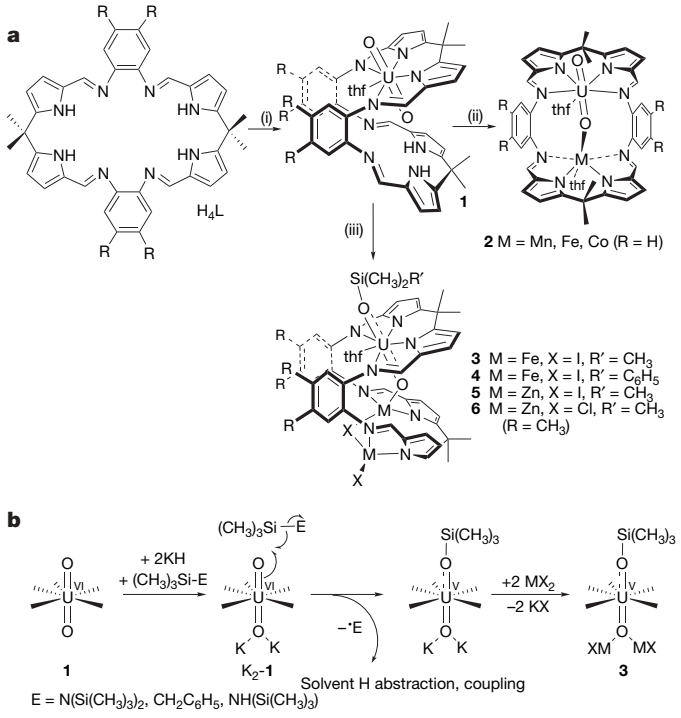

Figure 1 | Reductive silylation of the uranyl dication. a, Synthesis of the uranyl complex **1** and cation–cation complexes. **b**, Proposed mechanism. Reagents and conditions (i) $[UO_2(thf)_2\{N(Si(CH_3)_3)_2\}_2]$, thf (thf = tetrahydrofuran); (ii) $[M\{N(Si(CH_3)_3)_2\}_2]$, thf, heat (M = Mn, Fe, Co; R = H); (iii) either $KN(Si(CH_3)_2R')_2$, MX_2 (M = Fe, X = I, R′ = CH_3, C_6H_5; M = Zn, X = Cl, I, R′ = CH_3) or KH, FeI_2, $N(Si(CH_3)_3)_3$ or $C_6H_5CH_2Si(CH_3)_3$; thf, –80 °C, R = CH_3.

[1]School of Chemistry, University of Edinburgh, West Mains Road, Edinburgh EH9 3JJ, UK. [2]Rigaku Europe, Chaucer Business Park, Watery Lane, Sevenoaks, Kent TN15 6QY, UK.

by a bridging iodide (Fe1–I1 2.7317(13) Å, Fe2–I1 2.6335(13) Å, Fe1–I1–Fe2 70.30(3)°). Notably, Fe1 bonds to the *endo*-uranyl oxygen (Fe1–O1 1.946(4) Å) at a distance commensurate with a single dative bond. The Fe-bridging iodide refined to 79.7(3)% occupancy; after exploration of a number of alternative models the remaining electron density was best modelled as a bridging chloride, considering both the quality of the refinement and comparison of the resulting geometry with literature values. The chloride contaminant has accumulated in the crystal, and derives from amounts present in the original $[UO_2(thf)_2\{N(Si(CH_3)_3)_2\}_2]$ starting material.

We carried out experiments to probe the origin of the $Si(CH_3)_3$ group and to confirm the single electron transfer to form pentavalent uranyl. A mixture of **1**, FeI_2, and the phenyl-substituted $KN(Si(CH_3)_2C_6H_5)_2$ reacts to afford the phenylsilyl-functionalized $[UO(OSi(CH_3)_2C_6H_5)(thf)Fe_2I_2(L)]$ **4**, in high yield (see Supplementary Information). Thus, it is clear that the silyl group originates from either the silylamide base, $KN(Si(CH_3)_2R')_2$, or its by-product, the disilazane $HN(Si(CH_3)_2R')_2$ ($R' = CH_3$, C_6H_5). Analysis of the mass balance for the by-product KI shows that two molar equivalents are formed during the reaction, which implies that electron transfer from $KN(Si(CH_3)_2R')_2$ does not occur; that is, the silylamide acts solely as a base, and the $HN(Si(CH_3)_2R')_2$ by-product formed during the reaction provides the silyl group. In contrast, chemical analogues from the same group as uranium, the molybdenum and tungsten *cis*-dioxo complexes $[M^{VI}O_2(L')_2]^{2-}$ (M = Mo, W; L′ = 1,2-$S_2C_6H_4$), are readily silylated, even in the absence of redox reactions, to afford $[M^{VI}O(OSi(C_6H_5)_2(C_4H_9)^t)(L')_2]^-$. Furthermore, the silylated Mo compound is rapidly hydrolysed to the Mo(IV) mono-oxo compound $[Mo^{IV}O(L')_2]^{2-}$ (refs 24,25).

The isolation of the closed-shell Zn(II) compounds **5** and **6** confirms that the transition metal simply stabilizes the pentavalent $[UO(OSi(CH_3)_2R')]^+$ fragment, without participating in redox chemistry. Reaction between **1**, $KN(Si(CH_3)_3)_2$, and ZnX_2 (X = Cl, I) resulted in the formation of orange/brown $[UO(OSi(CH_3)_3)(thf)Zn_2X_2(L)]$, (X = I; **5**, Cl; **6**), in moderate yields, Fig. 1a (see online Methods and Supplementary Information). The X-ray crystal structure of **5** (Fig. 2b, and Supplementary Information) is similar to that of **3**, again with trace chloride incorporated but in this case with an occupancy of 52.7(3)%. The U⋯O bond distances in **5** (U1–O1 1.867(3) Å, U1–O2 1.975(3) Å) are similar to those in **3**, and are also consistent with pentavalent uranyl. The U = O asymmetric stretch in the infrared spectra of uranyl compounds is normally diagnostic, and should decrease by 100–180 cm^{-1} on reduction to $[UO_2]^+$ (ref. 12). However, the infrared spectra of pentavalent **3** to **6** are complex in the fingerprint region and the expected U=O absorption features between 800–700 cm^{-1} are masked by those of the macrocyclic ligand and the O–SiR_3 groups (Supplementary Fig. 1).

We have sought to generalize the reaction further, and have found that the potassium silylamide may be replaced by potassium hydride, another strong base, in combination with other sources of silyl group. Thus, the replacement of $KN(Si(CH_3)_3)_2$ by KH and either $N(Si(CH_3)_3)_3$ or $C_6H_5CH_2Si(CH_3)_3$ is equally effective in the synthesis of **3**, affording isolated yields of up to 85%, via N–Si or C–Si bond cleavage (see online Methods). In contrast, however, treatment of **1** with a reductant (rather than a base), and a source of $Si(CH_3)_3$, in these cases cobaltocene and trimethylsilyl triflate, does not result in reductive silylation.

These data suggest that this new and general reaction to reductively silylate the uranyl oxo group requires the deprotonation of the empty macrocyclic cavity by the potassium base to form potentially an oxidizing, U(VI) intermediate $\mathbf{K_2}$**-1** (Fig. 1b) in which the *endo*-U=O bond is coordinated by two K cations, and the *exo*-U=O bond is now polarized sufficiently to engage in N–Si and C–Si bond cleavage.

Transition metal oxo bonds are weakened when a strong ligand is in the *trans* position (the *trans* influence). In contrast, in uranyl compounds, covalent interactions between the oxo ligands and the metal *f* orbitals mutually strengthen the two *trans* U=O bonds, the inverse *trans* influence[26]. In high-oxidation-state porphyrin-based iron oxo chemistry, tuning the axial ligand markedly alters the reactivity of the electrophilic Fe=O group towards alkane hydroxylation and olefin epoxidation[6]. Likewise, by manipulating the uranyl oxo within the molecular cleft, we have significantly disrupted the overall UO_2 bonding to activate the *exo* oxo group towards reductive silylation. The ready formation of strong O–Si bonds in **3** to **6** parallels that seen in transition metal oxo chemistry in which hydrogen atom abstraction reactions do not require metal-based radicals, but instead depend on the strength of the bond between the oxidant and the hydrogen atom[9]. Unfortunately, attempts to isolate the proposed $\mathbf{K_2}$**-1** intermediate have been unsuccessful. Thermally stable, pentavalent, functionalized uranyl complexes are most readily isolated by substitution of the two K cations by transition metal halides in a reaction that eliminates KI and forms **3** to **6**. The reaction to afford **3** is equally successful when carried out in the dark, confirming the absence of any photochemically derived reactivity.

We recorded variable temperature magnetic measurements to compare the $f^1d^6d^6$ UFe_2 system **3** with the $f^1d^{10}d^{10}$ UZn_2 system

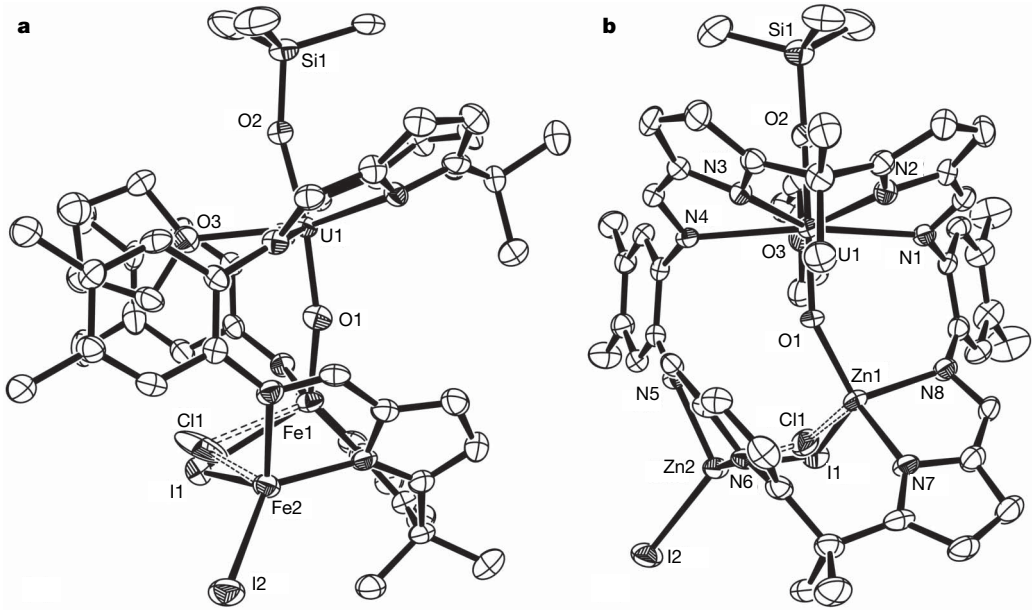

Figure 2 | X-ray crystal structures of $[UO(OSi(CH_3)_3)(thf)Fe_2I_2(L)]$ and $[UO(OSi(CH_3)_3)(thf)Zn_2I_2(L)]$. Thermal ellipsoid plot (50% probability displacement) views of (**a**) **3** and (**b**) **5**. For clarity, all hydrogen atoms and the minor thf component have been removed.

5. The room-temperature moment of 7.74 BM for **3** (BM = Bohr magnetons), and the Curie–Weiss behaviour (2 to 300 K) suggests the presence of two, high-spin, Fe(II) centres and one f^1 U(V) centre (Supplementary Fig. 2) that are magnetically independent; the thermal variation of the product of molar magnetic susceptibility and temperature, $\chi_M T$, is dominated by the magnetic contribution from the Fe ions. In contrast, the magnetic behaviour for **5** (2 to 300 K) should only contain contributions from the U centre[27]; it displays two distinct regions (Supplementary Fig. 2) associated with the depopulation of excited crystal field states of the U(V) f^1 cation and is similar to that observed for the few known organometallic pentavalent uranium complexes[28,29]. The moment at low temperature rises from 0.41 to 1.11 BM and increases to 2.38 BM at high temperature. In contrast, the moment of a U(IV) (f^2) system would be expected to be higher at room temperature (3.58 BM), and the reciprocal susceptibility would become temperature-independent below about 40 K. A preliminary electron paramagnetic resonance study of **5** in frozen methyl-thf at 5 K (Supplementary Fig. 3) displays a strong, broad resonance at $g = 2.2$ that supports the presence of a single f electron.

We have shown that the use of a macrocyclic architecture to place the uranyl ion in a rigid and asymmetric coordination environment allows the generation of a reactive and highly oxidizing uranyl complex which can selectively cleave N–Si and C–Si bonds to form singly, covalently functionalized pentavalent uranyl complexes. These reactive U oxo compounds may also provide functional chemical models for the highly radioactive f^1 plutonium and neptunium dioxo cations[30].

METHODS SUMMARY

Working under a dry, oxygen-free dinitrogen atmosphere, with reagents dissolved or suspended in aprotic solvents, and combined or isolated using cannula and glove box techniques, we first treated the free macrocycle H_4L with a bis(amido) uranyl precursor, to form the hinged macrocyclic complex $[UO_2(thf)(H_2L)]$ in which one N_4-donor compartment remains vacant. Treatment of this complex with two equivalents of potassium base and a suitable silylated reagent (or a base containing an ancillary silyl group) afforded a soluble complex in which the uranium was shown to be both singly reduced and silylated at the *exo* oxo group, as the $UO(OSiR_3)$ dication. This asymmetric pentavalent uranyl complex is then readily isolated, purified, and characterized by a final salt elimination reaction to produce two equivalents of potassium halide, and to place two transition metal cations (as Fe or Zn chloride or iodide salts, MX) into the remaining cavity of the macrocycle, affording $[UO(OSiR_3)(thf)(L)(MX)_2]$. We characterized all compounds by elemental analysis, Fourier transform infrared spectroscopy, and either variable-temperature magnetic moment measurements or nuclear magnetic resonance (NMR) spectroscopy (paramagnetic and diamagnetic compounds respectively). Additionally, we determined the solid-state structures of two of the silylated complexes by single-crystal X-ray diffraction studies.

Full Methods and any associated references are available in the online version of the paper at www.nature.com/nature.

Received 8 June; accepted 9 November 2007.

1. Amme, M., Wiss, T., Thiele, H., Boulet, P. & Lang, H. Uranium secondary phase formation during anoxic hydrothermal leaching processes of UO_2 nuclear fuel. *J. Nucl. Mater.* **341,** 209–223 (2005).
2. Lovley, D. R., Phillips, E. J. P., Gorby, Y. A. & Landa, E. R. Microbial reduction of uranium. *Nature* **350,** 413–416 (1991).
3. Suzuki, Y., Kelly, S. D., Kemner, K. M. & Banfield, J. F. Radionuclide contamination: Nanometre-size products of uranium bioreduction. *Nature* **419,** 134 (2002).
4. Denning, R. G. Electronic structure and bonding in actinyl ions and their analogs. *J. Phys. Chem. A* **111,** 4125–4143 (2007).
5. Kühn, F. E., Santos, A. M. & Abrantes, M. Mononuclear organomolybdenum(VI) dioxo complexes: Synthesis, reactivity, and catalytic applications. *Chem. Rev.* **106,** 2455–2475 (2006).
6. Nam, W. High-valent iron(IV)-oxo complexes of heme and non-heme ligands in oxygenation reactions. *Acc. Chem. Res.* **40,** 522–531 (2007).
7. Jin, N., Ibrahim, M., Spiro, T. G. & Groves, J. T. Trans-dioxo manganese(V) porphyrins. *J. Am. Chem. Soc.* **129,** 12416–12417 (2007).
8. Limberg, C. The role of radicals in metal-assisted oxygenation reactions. *Angew. Chem. Int. Edn Engl.* **42,** 5932–5954 (2003).
9. Mayer, J. M. Hydrogen atom abstraction by metal–oxo complexes: Understanding the analogy with organic radical reactions. *Acc. Chem. Res.* **31,** 441–450 (1998).
10. Burdet, F., Pecaut, J. & Mazzanti, M. Isolation of a tetrameric cation-cation complex of pentavalent uranyl. *J. Am. Chem. Soc.* **128,** 16512–16513 (2006).
11. Natrajan, L., Burdet, F., Pecaut, J. & Mazzanti, M. Synthesis and structure of a stable pentavalent-uranyl coordination polymer. *J. Am. Chem. Soc.* **128,** 7152–7153 (2006).
12. Berthet, J. C., Siffredi, G., Thuery, P. & Ephritikhine, M. Easy access to stable pentavalent uranyl complexes. *Chem.* Commun.3184–3186 (2006).
13. Burns, C. J. *et al.* A trigonal bipyramidal uranyl amido complex: Synthesis and structural characterization of $Na(thf)_2UO_2\{N(SiMe_3)_2\}_3$. *Inorg. Chem.* **39,** 5464–5468 (2000).
14. Sarsfield, M. J., Helliwell, M. & Raftery, J. Distorted equatorial coordination environments and weakening of U=O bonds in uranyl complexes containing NCN and NPN ligands. *Inorg. Chem.* **43,** 3170–3179 (2004).
15. Sarsfield, M. J. & Helliwell, M. Extending the chemistry of the uranyl ion: Lewis acid coordination to a U=O oxygen. *J. Am. Chem. Soc.* **126,** 1036–1037 (2004).
16. Kannan, S., Vaughn, A. E., Weis, E. M., Barnes, C. L. & Duval, P. B. Anhydrous photochemical uranyl(VI) reduction: Unprecedented retention of equatorial coordination accompanying reversible axial oxo/alkoxide exchange. *J. Am. Chem. Soc.* **128,** 14024–14025 (2006).
17. Arnold, P. L., Blake, A. J., Wilson, C. & Love, J. B. Uranyl complexation by a Schiff-base, polypyrrolic macrocycle. *Inorg. Chem.* **43,** 8206–8208 (2004).
18. Arnold, P. L., Patel, D., Blake, A. J., Wilson, C. & Love, J. B. Selective oxo functionalization of the uranyl ion with 3d metal cations. *J. Am. Chem. Soc.* **128,** 9610–9611 (2006).
19. Docrat, T. I. *et al.* X-ray absorption spectroscopy of tricarbonatodioxouranate(V), $[UO_2(CO_3)_3]^{5-}$, in aqueous solution. *Inorg. Chem.* **38,** 1879–1882 (1999).
20. Hay, P. J., Martin, R. L. & Schreckenbach, G. Theoretical studies of the properties and solution chemistry of AnO_2^{2+} and AnO^{2+} aquo complexes for An = U, Np, and Pu. *J. Phys. Chem. A* **104,** 6259–6270 (2000).
21. Wander, M. C. F., Kerisit, S., Rosso, K. M. & Schoonen, M. A. A. Kinetics of triscarbonato uranyl reduction by aqueous ferrous iron: A theoretical study. *J. Phys. Chem. A* **110,** 9691–9701 (2006).
22. Zi, G. *et al.* Preparation and reactions of base-free bis(1,2,4-tri-*tert*-butylcyclopentadienyl)uranium oxide, Cp'_2UO. *Organometallics* **24,** 4251–4264 (2005).
23. Cotton, F. A., Marler, D. O. & Schwotzer, W. Dinuclear uranium alkoxides: preparation and structures of $KU_2(OCMe_3)_9$, $U_2(OCMe_3)_9$, and $U_2(OCHMe_2)_{10}$, containing [U(IV),U(IV)], [U(IV),U(V)], and [U(V),U(V)], respectively. *Inorg. Chem.* **23,** 4211–4215 (1984).
24. Donahue, J. P., Goldsmith, C. R., Nadiminti, U. & Holm, R. H. Synthesis, structures, and reactivity of bis(dithiolene)molybdenum(IV,VI) complexes related to the active sites of molybdoenzymes. *J. Am. Chem. Soc.* **120,** 12869–12881 (1998).
25. Lorber, C., Donahue, J. P., Goddard, C. A., Nordlander, E. & Holm, R. H. Synthesis, structures, and oxo transfer reactivity of bis(dithiolene)tungsten(IV, VI) complexes related to the active sites of tungstoenzymes. *J. Am. Chem. Soc.* **120,** 8102–8112 (1998).
26. O'Grady, E. & Kaltsoyannis, N. On the inverse trans influence. Density functional studies of $[MOX_5]^{n-}$ (M = Pa, n= 2; M = U, n= 1; M = Np, n= 0; X = F, Cl or Br). *J. Chem. Soc., Dalton* Trans.1233–1239 (2002).
27. Costes, J. P., Dahan, F., Dupuis, A. & Laurent, J. P. Nature of the magnetic interaction in the (Cu^{2+}, Ln^{3+}) pairs: An empirical approach based on the comparison between homologous (Cu^{2+}, Ln^{3+}) and (Ni_{LS}^{2+}, Ln^{3+}) complexes. *Chem. Eur. J.* **4,** 1616–1620 (1998).
28. Castro-Rodriguez, I., Olsen, K., Gantzel, P. & Meyer, K. Uranium tris-aryloxide derivatives supported by triazacyclononane: engendering U(III) center with a single pocket for reactivity. *J. Am. Chem. Soc.* **125,** 4565–4571 (2003).
29. Rosen, R. K., Andersen, R. A. & Edelstein, N. M. A bimetallic molecule with antiferromagnetic coupling between the uranium centres. *J. Am. Chem. Soc.* **112,** 4588–4590 (1990).
30. Reilly, S. D. & Neu, M. P. Pu(VI) hydrolysis: further evidence for a dimeric plutonyl hydroxide and contrasts with U(VI) chemistry. *Inorg. Chem.* **45,** 1839–1846 (2006).

Supplementary Information is linked to the online version of the paper at www.nature.com/nature.

Acknowledgements We thank the EPSRC (UK), the Royal Society, and the Universities of Edinburgh and Nottingham for support, J. Sanchez-Benitez and P. Anderson of Edinburgh University for help with magnetic susceptibility measurements and chloride analysis respectively, R. Edge and the EPSRC EPR service at the University of Manchester, and D. Leigh for his advice.

Author Contributions D.P. synthesized and characterized the compounds, and solved the crystal structure data. C.W. mounted the crystals, collected the single-crystal X-ray crystallographic data, modelled the disorder components in the structures, and checked the final structure solutions. P.L.A. and J.B.L. generated and managed the project, helped characterize the complexes, analysed the data and wrote the manuscript.

Author Information X-ray crystallographic coordinates for **3** and **5** have been deposited at the Cambridge Crystallographic Database, numbers 649987 and 649988 respectively. Reprints and permissions information is available at www.nature.com/reprints. Correspondence and requests for materials should be addressed to P.L.A. (Polly.Arnold@ed.ac.uk) or J.B.L. (Jason.Love@ed.ac.uk).

METHODS

$[UO_2(thf)(H_2L)]$.thf, 1. To a stirred solution of $[UO_2(thf)_2\{N(Si(CH_3)_3)_2\}_2]$ (2.94 g, 4.0 mmol) in thf (20 ml, –78 °C) we added slowly a solution of H_4L (2.64 g, 4.0 mmol) in thf (20 ml, –78 °C). The resulting solution was allowed to warm to room temperature over 16 h, after which the volatiles were removed under vacuum and the residual solids redissolved in thf (15 ml). Addition of hexane (20 ml) afforded a precipitate that was isolated by filtration, washed with hexane (2 × 10 ml), and dried under vacuum to yield 3.76 g, 88% of **1** as a brown solid. Analysis. Found: C, 56.00; H, 5.55; N, 10.51. $C_{50}H_{58}N_8O_4U$ requires: C, 55.96; H, 5.46; N, 10.44%; infrared (Nujol, cm^{-1}): ν 908(s) (UO_2 asymmetric stretch).

$[UO(OSi(CH_3)_3)(thf)Fe_2I_2(L)]$, 3. To a stirred mixture of **1** (0.27 g, 0.25 mmol) and $KN(Si(CH_3)_3)_2$ (0.10 g, 0.53 mmol) we added thf (20 ml) at –78 °C, and added the resulting solution dropwise to stirred slurry of FeI_2 (0.15 g, 0.50 mmol, beads) in thf (10 ml, –78 °C). The resulting mixture was allowed to warm to room temperature over 42 h, after which we removed the solid KI by filtration and washed it with thf (2 × 5 ml). The combined filtrates were evaporated to dryness, the residual solids extracted into hot toluene (20 ml), filtered and dried under vacuum to yield 0.29 g, 80% of **3** as a dark red solid. Analysis. Found: C, 40.93; H, 4.07; N, 7.64. $C_{49}H_{57}N_8O_3Fe_2I_2SiU$ requires: C, 40.93; H, 4.00; N, 7.79%. Magnetic moment (superconducting quantum interference device (SQUID) 300 K): μ_{eff} 7.74 BM; electron impact mass spectrometry: m/z 343 (37.7%, $[UO(OSi(CH_3)_3)]^+$).

Alternative syntheses of 3. A. To a stirred mixture of **1** (0.10 g, 0.09 mmol) and KH (9 mg, 0.23 mmol) we added thf (20 ml) at –78 °C, and allowed the mixture to warm to room temperature over 45 min. We filtered the resulting mixture dropwise by cannula into a stirred slurry of FeI_2 (56 mg, 0.18 mmol) and $N(Si(CH_3)_3)_3$ (21 mg, 0.09 mmol) in thf (10 ml, –78 °C). Room-temperature work up as above yielded 0.09 g, 69% of **3** as a dark red solid. **B.** To a stirred mixture of **1** (0.10 g, 0.09 mmol) and KH (9 mg, 0.23 mmol) we added thf (20 ml) at –78 °C and allowed the mixture to warm to room temperature over 45 min. We filtered the resulting mixture dropwise on to a stirred slurry of FeI_2 (56 mg, 0.18 mmol) and $C_6H_5CH_2Si(CH_3)_3$ (15 mg, 0.09 mmol) in thf (15 ml, –78 °C). Room-temperature work up as above yielded 0.11 g, 85% of **3** as a dark red solid.

$[UO(OSi(CH_3)_3)(thf)Zn_2I_2(L)]$, 5. To a stirred mixture of **1** (0.34 g, 0.32 mmol) and $KN(Si(CH_3)_3)_2$ (0.13 g, 0.63 mmol) we added thf (20 ml) at –78 °C. After 15 min, we added the mixture dropwise to a stirred slurry of ZnI_2 (0.20 g, 0.63 mmol) in toluene (20 ml, –78 °C). Room-temperature work up as above yielded 0.21 g, 46% of **5** as a pale brown solid. Analysis. Found: C, 40.30; H, 3.91; 7.70. $C_{49}H_{57}N_8I_2O_3SiZn_2U$ requires: C, 40.40; H, 3.95; N, 7.69%. Magnetic moment (SQUID, 300 K): μ_{eff} 2.38 BM. Electron paramagnetic resonance spectroscopy (frozen glass methyl-thf solution, 5 K, 0–1.6 T, 2 mW, 9.610794 GHz): $g = 2.2$.

$[UO(OSi(CH_3)_3)(thf)Zn_2Cl_2(L)]$, 6. To a stirred mixture of **1** (0.10 g, 0.09 mmol) and $KN(Si(CH_3)_3)_2$ (0.036 g, 0.18 mmol) we added thf (15 ml) at –78 °C. After 15 min, we added the mixture dropwise to a stirred slurry of $ZnCl_2$ (0.025 g, 0.18 mmol) in toluene (20 ml, –78 °C). Room-temperature work up as above yielded 0.06 g, 56% of **6** as a pale brown solid. Analysis. Found: C, 46.30; H, 4.50; 8.72. $C_{49}H_{57}N_8Cl_2O_3SiZn_2U$ requires: C, 46.19; H, 4.52; N, 8.80%. Magnetic moment (SQUID, 300 K): μ_{eff} 3.01 BM.

Reaction between 1 and $KN(Si(CH_3)_3)_2$: attempted synthesis of $[UO(OSi(CH_3)_3)(thf)K_2L]$. To a stirred mixture of **1** (0.10 g, 0.10 mmol) and $KN(Si(CH_3)_3)_2$ (0.041 g, 0.21 mmol) we added thf (20 ml) at –78 °C. We allowed the resulting red solution to warm to room temperature over 2 h, after which we removed the volatiles from the now dark brown solution. We washed the solid residues with toluene (1 × 10 ml) and dried them to form a dark brown solid, which was redissolved in a minimal amount of thf (1–2 ml) and cooled (–30 °C) for 16 h. The resulting dark precipitate was isolated and was found to be no longer soluble in thf. Elemental analysis indicated that the compound had decomposed.

Reaction between 1 and cobaltocene and trimethylsilyl triflate: attempted synthesis of $[UO(OSi(CH_3)_3)(thf)(H_2L)]$ and cobaltocenium triflate. To a stirred mixture of **1** (0.10 g, 0.09 mmol) and $Co(C_5H_5)_2$ (0.017 g, 0.09 mmol) we added thf (20 ml) at –78 °C, and added $(CH_3)_3SiOTf$ (0.020 g, 0.09 mmol) into the mixture by syringe. We allowed the mixture to warm to room temperature over 16 h. We removed the volatiles from the now dark red solution to afford a viscous red oil. Elemental analysis indicated that the compounds had decomposed.

Reaction between 1 and excess KH for the identification of by-products. We added cold thf (0.5 ml, –35 °C) and a few drops of C_6D_6 to cold (–35 °C) **1** (10 mg, 0.009 mmol) and KH (2 mg, 0.05 mmol) in a Teflon-tapped NMR tube. Upon warming, we observed gas evolution, which we identified as dissolved dihydrogen at $\delta = 4.4$ p.p.m. in the ^1H NMR spectrum.

Reaction between 1 and 2 $KN(Si(CH_3)_3)_2$ for the identification of by-products. We added cold thf (0.5 ml, –35 °C) and a few drops of C_6D_6 to cold (–35 °C) **1** (5 mg, 0.005 mmol), and $KN(Si(CH_3)_3)_2$ (1.8 mg, 0.009 mmol) in a Teflon-tapped NMR tube. By integration, one molar equivalent of $HN(Si(CH_3)_3)_2$ was observed in the ^1H NMR spectrum.

Crystallography. Dark red single crystals of **3** (needle-shaped) and **5** (parallelepiped) were grown from saturated C_6D_6 solutions at room temperature.

Reduction and Selective Oxo Group Silylation of the Uranyl Dication

A review of the inorganic chemistry behind the original work completed by Polly L. Arnold, Dipti Patel, Claire Wilson, & Jason B. Love

Samantha J. Brannick*

Department of Biochemistry and Chemistry, University of Delaware, Newark, Delaware 19713

RECEIVED DATE: November 23, 2010; E-mail: sbrannic@udel.edu

Uranium is a radioactive actinide metal that is typically found at low concentrations in soil and rock. There is a greater amount of uranium present on earth than some other metals; in fact uranium is nearly forty times more abundant than silver.[1] Uranium occurs in the environment predominantly as the uranyl dication $[UO_2]^{2+}$.[2] It is characteristically unreactive due to the stability of its uranium-oxygen double bond.[3] Recently, however, Arnold et al. has discovered a method of reducing and selectively functionalizing the uranyl dication to a product that is a pentavalent and monofunctionalized cation. The research show the pentavalent uranyl cation can be isolated and characterized when first row cations are simultaneously present. The chemistry involved in this reduction may provide further insight into other reactions involving various highly radioactive elements found in nuclear waste, such as plutonyl.[2]

Uranium contamination is a large environmental concern. It can be found deposited throughout both surface and ground water. This contamination is caused by uranium mining, irrigation of agricultural lands, and disposal of nuclear waste. Uranium is most commonly found in its oxidized form U^{VI}, $[UO_2]^{2+}$. Reducing the soluble uranyl dication to an insoluble U^{IV} form, $[UO_2]$, is an important mechanism for the immobilization of uranium in aquatic sediments and for the formation of some uranium ores.[3] This would allow for an easier way to harvest uranium which would be beneficial due to its ability to be a radioactive energy source. The reduction of the uranyl dication sets precedent for chemistry that may characterize other radioactive actinide metals that have multiple redox states and are insoluble in their reduced form.[3]

The fact that the uranyl dication is very soluble is caused by the linear and strongly covalent U=O bonds. This strong covalent bond makes functionalization of the oxo groups difficult and therefore the pentavalent uranyl complex uncommon. Essentially, Arnold et al. attempted to do what nature does, only better. This seems to be an ongoing theme in most inorganic and organic chemistry. Though uranium reduction is most often thought of as a non-biological process, it has been shown by Lovley et al. that its precedence lies within dissimilatory Fe(III)-reducing microorganisms, or organisms that can produce an inorganic element from an organic element.[3]

The important feature of these microorganisms is that they can obtain energy for growth by electron transport to U^{VI}.[3] Microorganisms, such as geobacter metallireducens strain GS-15, thrive in anaerobic environments by performing, essentially, a redox reaction with Fe(III) acting as the oxidizing agent and acetate as the reducing agent (Equation 1).

$$CH_3COO^- + 8Fe(III) + 4H_2O \rightarrow 8Fe(II) + 2HCO_3^- + 9H^+ \quad (1)$$

Lovley et al. reported thermodynamic calculations that show, per electron transferred, acetate oxidation coupled to U^{VI} reduction has the potential to yield more than twice the energy that is available from Fe^{III} reduction.[3] If more energy is produced, a more efficient process for removal of uranium contamination, and possibly other nuclear waste, can be achieved. Lovley et al. also show that when GS-15 is placed into an anaerobic environment with acetate as the only reducing agent and U^{VI} as the only possible reductant, U^{VI} was reduced to U^{IV} over time as shown in Figure 1a.[3]

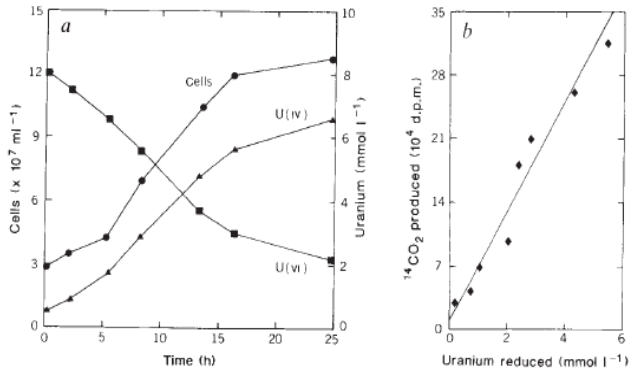

Figure 1. (a) Relationship between GS-15 placed in an anaerobic environment with acetate as the only available reducing agent and U(VI) as the only possible reductant. (b) Addition of [2-^{14}C]-acetate into the media caused the production of $^{14}CO_2$ to be directly proportional to the reduction of U^{VI}. Both figures support the idea that the reduction of U^{VI} to U^{IV} and the oxidation of acetate to carbon dioxide provided energy to probe the growth of GS-15.

One of the key features of this redox reaction is the pentavalent uranyl cation, UO_2^+. This intermediate, however, is very unstable due to its strong covalent U=O bonds. Although microorganisms are naturally able to readily reduce U^{VI} to U^{IV}, it has been quite a struggle for chemists to do the same.[2] If functionalization of the uranyl oxygens is achieved, the covalent bond between the uranium and its oxygens will weaken and therefore make the reduction of $[UO_2]^{2+}$ more feasible.

Functionalization of the oxo groups on the uranyl dication will create a pentavalent uranyl complex. If the formation of a stable UO_2^+ complex is found, this will afford scientists the opportunity to better understand its structure and other chemical properties

and therefore possibly provide a better understanding of the natural reduction of uranium by microorganisms, such as GS-15.

Unlike other similar elements that form stable and isolatable AnO^+ species, the UO_2^+ is very unstable because it readily disproportionates, or acts as both a reductant and an oxidant, into U(IV) and $[UO_2]^{2+}$.[4] This characteristic causes the formation of pentavalent uranyl species to be limited. In order to probe formation of a stable pentavalent uranyl complex, the utilization of cation-cation interactions must be employed.[5,6] In order to comprehend the impact cation-cation interactions have on the stability of a pentavalent uranyl complex, the uranyl dication must first be understood.

As previously stated, uranium is found in its most common, soluble form $[UO_2]^{2+}$. This uranyl dication contains a uranium atom double-bonded to two oxygen atoms with linear geometry (O=U=O). Because this portion of the molecule is linear, ligands can only attach perpendicular to the O=U=O. However, it is clear from the work of Arnold et al. and others that there is a way to allow the oxygen atoms to react.[2] While in an anaerobic media, if the $[UO_2]^{2+}$ is placed in a rigid asymmetric molecular framework, it will allow for both selective covalent bond formation at one of the oxo groups as well as single-electron transfer.[2] Boncella suggests that the uranyl complexes adapt a Pac-Man-like structure in which the *endo*-uranyl oxygen atom interacts with the two potassium atoms ultimately perturbing the U=O bond and therefore allowing the *exo*-uranyl oxygen to be selectively functionalized.[7] This is demonstrated by Arnold and Love's recent finding that binding the linear O=U=O molecule within a Schiff base pyrrole macrocycle with a hinged geometry.[8] Ultimately, this structural adaptation produces an isolable pentavalent and monofunctionalized $[O=U\text{-}OR]^+$ cation.

Burdet et al. believe that the production of these pentavalent and monofunctionalized uranyl species will favor metal cation interactions and therefore lead to the formation of cation-cation complexes. This phenomenon is due to the fact that the U=O oxygens have a lower Lewis basicity, making them more prone to accept electrons. The *endo*-oxygen is able to coordinate to the cations, leaving the *exo*-oxygen open for functionalization.

The preparation of stable pentavalent uranium compounds $[UO_2]^+$ is a tedious process that involves careful consideration of both ligands and the media.[4] Burdet et al. reported the synthesis and characterization of the first isolated stable pentavalent uranyl iodide, $\{[UO_2Py_5][KI_2Py_2]\}_n$, (**1**).[4] This crystalline polymer is a result of cation-cation interactions between pentavalent uranyl complexes, $[UO_2]^+$, and potassium. When **1** reacts with two equivalents of Kdbm in pyridine to produce blue crystals of $\{[UO_2(dbm)_2]_4[K_6Py_{10}]\}\cdot I_2\cdot Py_2$ (**2**). This complex contains four pentavalent uranyl complexes presented in Figure 2.[4]

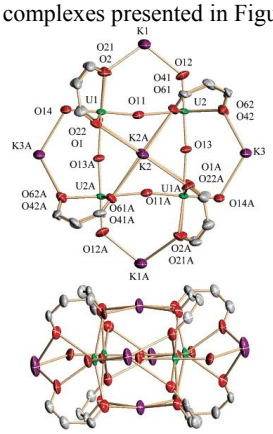

Figure 2. Top and side ORTEP representations of $\{[UO_2(dbm)_2]_4[K_6Py_{10}]\}\cdot I_2\cdot Py_2$ (**2**).

Another noteworthy synthesis of a pentavalent uranyl complex was that of Natrajan et al. who have recently formed the first pentavalent uranium silicate.[9] Their synthesis of **1** is the first known reproducible synthetic route to a UO_2^+ coordination complex (Figure 3).[9] They also report the first structurally characterized dioxouranium(V). Their product was synthesized via the reduction of $UI_3\cdot thf$ by water and a pyridine solution (PyNO). This reaction is done through a two-electron oxidation of U^{III}. The reaction of $[UO_2Py_x]I$ and 2PyHI in the presence of potassium iodide led to the reproducible isolation of **1**, suggesting the pyridine stabilizes the UO_2^+ species against disproportionation.[9]

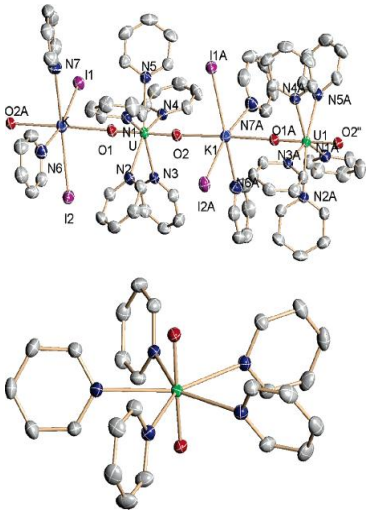

Figure 3. ORTEP representations, both top and bottom, of the uranyl complex $\{[UO_2Py_5][KI_2Py_2]\}_n$ (**1**).

Both Burdet et al. and Natrajan et al. provide some precedence for the reduction and selective oxo silylation of the uranyl dication performed by Arnold et al. The creation of **1** allows chemists to comprehend the electronic structure of the pentavalent uranyl species.[9] Uranium, in this complex, is a seven-coordinate species affording pentagonal bipyramidal coordination geometry. It is coordinated by two trans oxo ligands and five coplanar pyridine nitrogen as shown in Figure 3.[9] It can be noted that the large negative charge from the U=O oxygens allows the molecule to form the cation-cation complexes and the fact that the iodide ion is not coordinated to the metal ion in **1** allows easier dissociation of the U-I bond due to the higher electron density of U^V.[9]

Though $[UO_2]^+$ is usually prone to disproportionation, Arnold et al. has been able to form a cation-cation complex through the reaction of a mono-uranyl complex (**3**), FeI_2, and $KN(Si(CH_3)_3)_2$ to afford a phenylsilyl-functionalized $[UO(OSi(CH_3)_3)(thf)FeI_2(L)]$, (**4**) as seen in Figure 4.[2] In this reaction, the silylation occurs at the *exo*-uranyl oxygen atom via single electron transfer. It was concluded that the silyl group comes from the silylated base or from the by-product, disilazane.[2] Like previously stated, bond distance between the uranium and oxygen atoms provide verification that a pentavalent complex was formed.

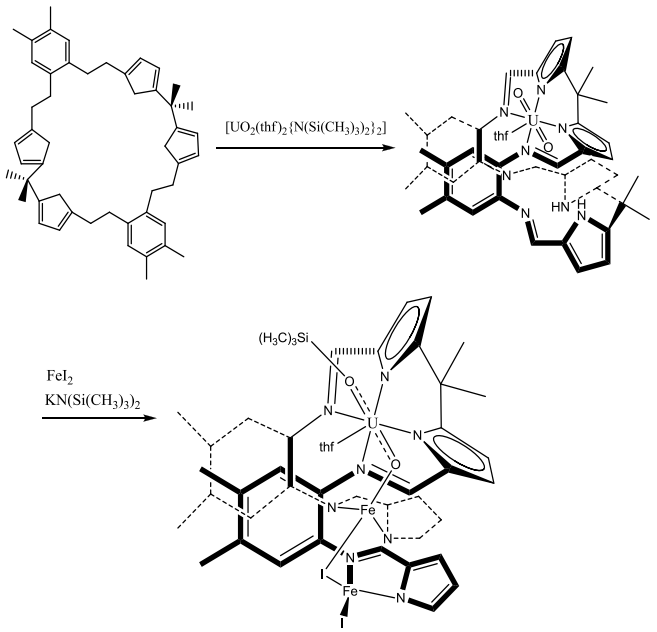

Figure 4. The formation of a cation-cation complex through a mono-uranyl species (**3**), FeI_2, and $KN(Si(CH_3)_3)_2$ affords a phenylsilyl-functionalized $[UO(OSi(CH_3)_3)(thf)FeI_2(L)]$, (**4**).

The ability of this uranyl ion to undergo selective silylation stems from the use of a flexible ligand that allows the pentavalent complex to adapt a rigid scaffold-type geometry.[7] The deprotonation of this macrocyclic ligand by the potassium base allows the endo-uranyl oxygen to coordinate to the two potassium cations.[2] This ultimately weakens the U=O bond and allows the *exo*-uranyl oxygen atom to become reactive. The structure for the observed uranyl complexes are defined because of the existence of non-valence, core electrons.[7] According to Boncella, the energies of electrons in uranium are distorted, due to its high atomic number (z = 92), causing non-valence 6p core electrons to be pushed into a high-energy orbital with a large radius.[7] Because the non-valence electrons are pushed to a higher-energy orbital, they are able to interact with 5f electrons resulting in a set of hybrid orbitals. The weak interaction of these uranium f hybrid orbitals and the oxo ligands causes the two *trans* U=O bonds to strengthen.[2] This is what is known as the inverse *trans* influence.[10] When the bonding interaction that stabilizes the U=O bonds is perturbed, the uranyl ion allows for reduction and selective oxo group silylation.[7]

Silylation of the *exo*-uranyl oxygen probes a new relationship between actinide and transition metal oxo chemistry.[2] The formation of the oxygen-silicon bond seen in the pentavalent uranyl complex is similar to hydrogen atom abstraction reactions in which the strength of the oxidant-hydrogen atom bond is the main driving force.[2]

As shown by the aforementioned authors, the formation of a stable pentavalent and monofunctionalized uranyl species is a difficult task due to the readily occurring disproportionation of the UO_2^+. Placing the O=U=O species into a Pac-man-like ligand structure can allow for reduction of the uranyl dication to U^V with stability lying within the cation-cation interaction. The coordination of the *endo*-uranyl oxygen to the cations causes an inverse *trans* influence and therefore makes the *exo*-uranyl oxygen a more reactive species that is easily functionalized through selective silylation.

The ability to create a stable pentavalent and selectively silylated uranyl species will allow chemists to further investigate its structure and various chemical properties in hopes of finding a way to efficiently reduce the soluble uranyl dication to an insoluble reduced form. This investigation will be expanded to other radioactive actinides possessing similar properties, such as neptunyl(V) and plutonyl(V).[5,6] Further research will hopefully lead to an effective way to remove nuclear waste from the environment.

Acknowledgement. This work was made possible in part by the teaching of Advanced Inorganic Chemistry by Dr. Joel Rosenthal, University of Delaware, Newark, DE 19713 and Inorganic Chemistry by Dr. Joseph Keane, Muhlenberg College, Allentown, PA 18104.

References

(1) U.S. Department of Energy Office of Environmental Management, http://web.ead.anl.gov/uranium/pdf/UraniumCharacteristicsFS.PDF
(2) Arnold, P. L.; Patel, D.; Wilson, C.; Love, J. B. *Nature* **2008**, *451*, 315.
(3) Lovley, D. R.; Phillips, E. J. P.; Gorby, Y. A.; Landa, E. R. *Nature* **1991**, *350*, 413.
(4) Burdet, F.; Pécaut, J.; Mazzanti, M. *J. Am. Chem. Soc.* **2006**, *128*, 16512.
(5) Mougel, V.; Horeglad, P.; Nocton, G.; Pécaut, J.; Mazzanti, M. *Angew. Chem. Int. Ed.* **2009**, *48*, 8477.
(6) Nocton, G. g.; Horeglad, P.; Vetere, V.; Pécaut, J.; Dubois, L.; Maldivi, P.; Edelstein, N. M.; Mazzanti, M. *J. Am. Chem. Soc.* **2009**, *132*, 495.
(7) Boncella, J. M. *Nature* **2008**, *451*, 250.
(8) Yahia, A.; Arnold, P. L.; Love, J. B.; Maron, L. *Chem. Eur. J.* **2010**, *16*, 4881.
(9) Natrajan, L.; Burdet, F.; Pécaut, J.; Mazzanti, M. *J. Am. Chem. Soc.* **2006**, *128*, 7152.
(10) O'Grady, E.; Kaltsoyannis, N. *J. Chem. Soc. Dalt. Trans.* **2002**, 1233.

Direct Observation and Quantification of CO_2 Binding Within an Amine-Functionalized Nanoporous Solid

Ramanathan Vaidhyanathan,[1]* Simon S. Iremonger,[1] George K. H. Shimizu,[1]* Peter G. Boyd,[2] Saman Alavi,[2] Tom K. Woo[2]*

Understanding the molecular details of CO_2-sorbent interactions is critical for the design of better carbon-capture systems. Here we report crystallographic resolution of CO_2 molecules and their binding domains in a metal-organic framework functionalized with amine groups. Accompanying computational studies that modeled the gas sorption isotherms, high heat of adsorption, and CO_2 lattice positions showed high agreement on all three fronts. The modeling apportioned specific binding interactions for each CO_2 molecule, including substantial cooperative binding effects among the guest molecules. The validation of the capacity of such simulations to accurately model molecular-scale binding bodes well for the theory-aided development of amine-based CO_2 sorbents. The analysis shows that the combination of appropriate pore size, strongly interacting amine functional groups, and the cooperative binding of CO_2 guest molecules is responsible for the low-pressure binding and large uptake of CO_2 in this sorbent material.

The capture and storage of CO_2 emitted from industrial processes are global challenges. In many industrial processes, CO_2 is present at low partial pressures among other gases that ideally should be recycled. The currently employed capture method involves alkanolamine-based solvents that act as CO_2 scrubbers (*1*, *2*) by chemisorptive formation of N-C bonded carbamate species (bonding energies are typically 100 kJ mol^{-1}). Regeneration of the amine requires cleavage of this covalent bond by heating (at 100° to 150°C) to release CO_2. Major drawbacks of this process include the corrosive nature and volatility of the amines, their occasional decomposition, and most prominently, the high energy cost of their regeneration (*1*, *2*). The challenge is thus to couple efficient CO_2 capture with facile release in a sorbent material.

Porous systems, including zeolitic/zeotypic materials (*3*, *4*), mesoporous silica (*5*–*8*), porous carbon (*9*), and, more recently, metal-organic frameworks (MOFs) (*10*–*19*), have been investigated for CO_2 storage. Merging the inherent sorptive behavior of porous solids with less-basic amines offers a route to the sort of easy-on/easy-off materials described above. Less-basic amines would favor physisorption over chemisorption of CO_2, thus greatly reducing the energy of regeneration. This prospect has prompted research on many amine-functionalized solid materials that on the whole demonstrates that amines can enhance CO_2 uptake (*5*–*8*, *17*–*19*). Despite this conclusion, experimental insights at a molecular level on the nature of the $NH_2 \cdots CO_2$ interaction are lacking (*20*). For materials such as silica and carbon, a combination of factors (lack of order, large voids, flexible amine groups, and random adsorption sites) makes the study of individual sorptive interactions virtually unfeasible. In contrast, the crystallinity of MOFs enables diffraction experiments to study structure at a molecular level. Beyond characterization of the framework, in exceptional cases, x-ray or neutron diffraction can allow direct visualization of gases within pores (*21*–*27*) to elucidate specific binding interactions and enable better sorbent design. Locating gas molecules in a MOF is challenging, but the systems typically display strong confinement effects on the guest molecules and/or specific sites of strong interaction (such as bare metal sites) that can serve as excellent models for understanding the interactions of gases in all porous systems.

We previously noted (*28*) that the MOF $Zn_2(Atz)_2(ox)$ (**1**) (Atz, 3-amino-1,2,4-triazole; ox, oxalate) showed CO_2 uptake at low pressures with an initial heat of adsorption (ΔH_{ads}) of ~40 kJ mol^{-1} (Fig. 1 and fig. S4). After manifesting the expected trend of decreased ΔH_{ads} with increased coverage, the material showed a subsequent increase in ΔH_{ads}, which remained over 35 kJ mol^{-1} during continuous gas exposure, suggesting a cooperativity effect in the binding mechanism. Here we describe a detailed study, via a combination of crystallographic and computational methods, of the nature of CO_2 binding in **1**. In a crystal structure of **1** loaded with CO_2 mol-

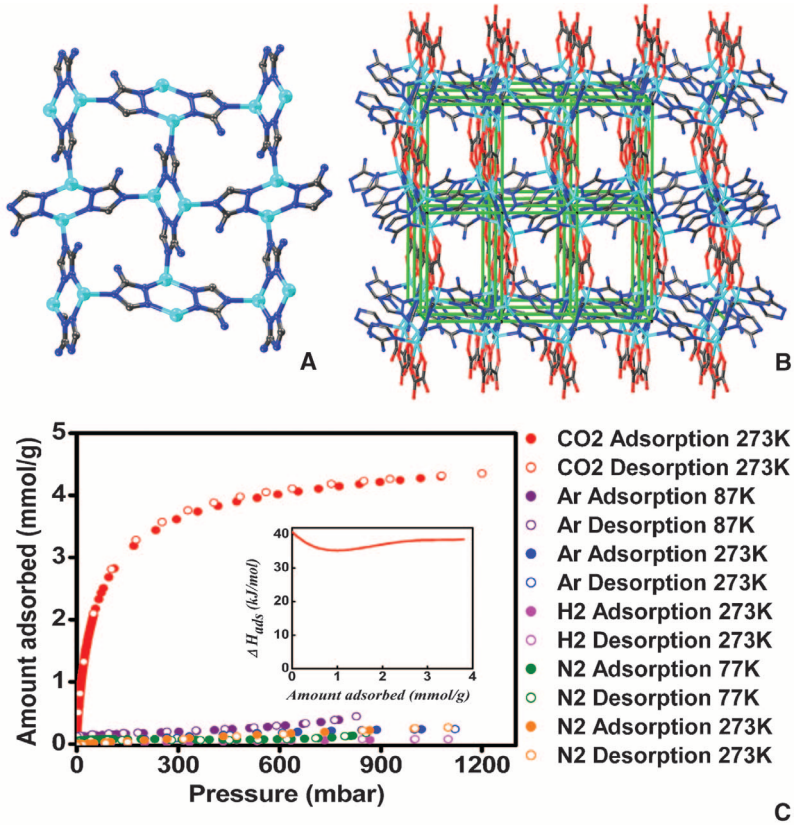

Fig. 1. (**A**) Structure of the Zn-Atz layer in **1** (Zn, cyan; C, black; N, blue; H, not shown). (**B**) Three-dimensional structure of **1**, wherein the Zn-Atz layers are pillared by oxalate moieties (O, red) to form a six-connected cubic network shown as green struts. (**C**) Adsorption isotherms for different gases carried out using **1**. The inset shows heat-of-adsorption data calculated with the CO_2 isotherms measured at 273 and 293 K (fig. S5). The zero-loading heat of adsorption was calculated, using a model based on the virial equation (figs. S6 and S7 and table S2), to be 40.8 ± 0.8 kJ mol^{-1}.

[1]Department of Chemistry, University of Calgary, Calgary T2N 1N4, Canada. [2]Department of Chemistry, Centre for Catalysis Research and Innovation, University of Ottawa, Ottawa, K1N 6N5, Canada.

*To whom correspondence should be addressed. E-mail: vvramana@ucalgary.ca (R.V.); gshimizu@ucalgary.ca (G.K.H.S.); twoo@uottawa.ca (T.K.W.)

ecules, the CO_2 binding sites are readily identified, even from room temperature diffraction data. The characteristics of CO_2 uptake in **1**, including isotherm, heat of adsorption, and location of CO_2 molecules, are modeled with high accuracy via a combination of classical grand canonical Monte Carlo (GCMC) simulations, molecular dynamics (MD) simulations, and periodic density functional theory (DFT) calculations. Thus, **1**·$(CO_2)_{1.3}$ serves to calibrate these methods for modeling gas sorption in MOFs. The modeling enables the partitioning of CO_2 binding in **1** into components based both on neighboring groups and the nature of interaction (electrostatics/dispersion).

Single crystals of **1** were prepared via a procedure modified from that previously reported (*28*), for the phases with hydrated and evacuated pores (*29*). X-ray crystallography of evacuated **1** showed no electron density in the voids, thus confirming the effectiveness of the activation procedure and the stability of the crystal. CO_2 was then loaded into evacuated crystals of **1,** and x-ray diffraction experiments conducted at 123, 173, 195, and 293 K all yielded refinable data. The CO_2 molecules could be located within the pores in all cases and were ordered except at 293 K, where the disorder could be modeled. The 173-K data set yielded the best refinement parameters [refinement factor (R) = 2.7%, weighted R (R_w) = 6.5%] and will be used for structural discussions.

The 173-K structure refinement gave a formula of **1**·$(CO_2)_{1.30}$, which agrees well with the calculated loading of 1.35 CO_2 from the adsorption isotherms at 840 mbar and 293 K (which are comparable conditions to those of single-crystal experiments). In the lattice Zn, aminotriazolate layers are pillared by oxalate ions, with free amine groups lining the pores (Fig. 1).

Within each pore, two independent CO_2 binding sites were located: CO_2-I [O(100)-C(100)-O(101)] and CO_2-II [O(200)-C(200)-O(201)] (Fig. 2 and fig. S1). CO_2-I, near the free amine group, was 80% occupied, and CO_2-II, closer to the oxalates, was 50% occupied; in filled pores, neither CO_2 molecule showed positional disorder. CO_2 could interact with an amine via N-H···O hydrogen bonding or via an interaction between the N lone pair and the C atom of CO_2. The H atoms of the amine groups were readily located in the x-ray structure of **1**·$(CO_2)_{1.30}$, enabling direct visualization of the H-bonding. CO_2-I was adjacent to the amine, with its electropositive C atom oriented toward the electronegative N atom [C(δ+)···N(δ–) = 3.151(8) Å; the C-N of monoethanolamine carbamate was modeled as 1.45 Å (*30*) and factoring C and N van der Waal radii = 3.25 Å]. The bowing of the protons on the N atoms (~21° from the mean triazole plane) confirms that the lone pair is not delocalized into the triazole ring (Fig. 2). Both O atoms of CO_2-I are within the range of longer H-bonds to the amine [N4-H···O100 = 3.039(4), O101 = 3.226(9) Å], with angles also corroborating very weak interactions [∠ N-H···O: O100 = 97.486(1)°; O101 = 95.822(1)°]. The C atom of CO_2-I also interacts with an oxalate O atom lining the pore [C(δ+)…O(δ–) = 3.155(8) Å]. The amine undergoes stronger H-bonding with oxalate O atoms [N4-H···O2 = 2.888(7), O4 = 2.122(2) Å, ∠ N-H···O = 154.718(1)° and 137.843(1)°, respectively].

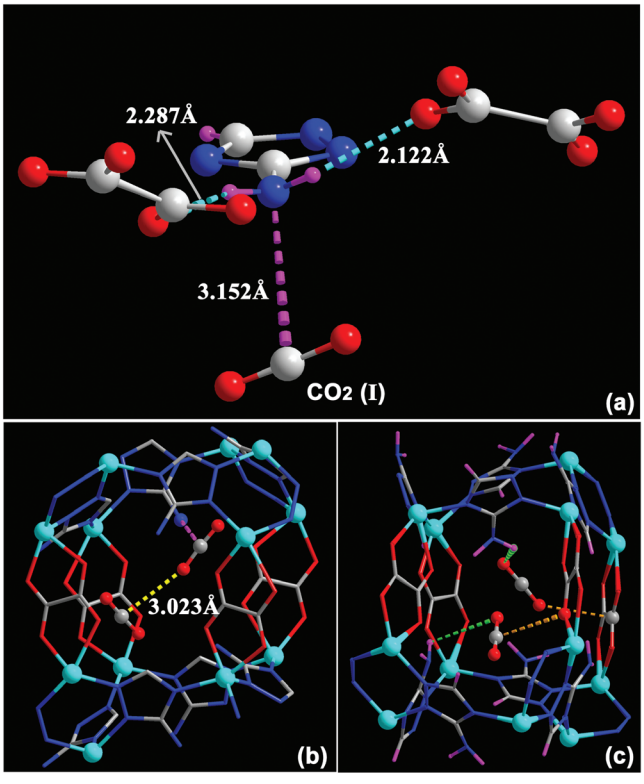

Fig. 2. X-ray structure of CO_2 binding in **1**·$(CO_2)_{1.3}$ at 173 K. (**A**) The role of the amine group of Atz in binding CO_2-I is depicted. The H atoms of the amine group (located crystallographically) H-bond to oxalate O atoms, directing the N lone pair toward the C(δ+) atom of the CO_2 molecule. H-bond distances shown are for H-acceptor interactions. (**B**) Both crystallographically independent CO_2 molecules are shown trapped in a pore, showing the cooperative interaction between CO_2-I and CO_2-II molecules. The CO_2…NH_2 interaction is represented as a dotted purple bond, and the CO_2…CO_2 interaction is indicated as a dotted yellow bond. (**C**) This panel shows the other interactions present. The CO_2-I…Ox interactions are shown in orange, and the CO_2…NH_2 hydrogen bond interactions are shown in green. For clarity, H atoms are shown in purple.

CO_2-II was located between oxalate groups along the *b* axis. The O(δ–) of CO_2-II interacts with the C(δ+) of the oxalate [$O(\delta-)_{(CO2)}$…$C(\delta+)_{(Ox)}$ = 2.961(5) Å]. In contrast to CO_2-I, CO_2-II interacts with a proximal amine via only a single H-bond [(N8-H···O200 = 2.783(8), ∠ N-H···O = 101.953(1)°]. There is an interaction between CO_2 molecules as one O atom of CO_2-I forms a contact with the C of CO_2-II [(C(δ+)…O(δ–) = 3.023(7) Å, C200···O100]. This CO_2-CO_2 interaction is highly relevant because it is most likely the origin of the observed increasing ΔH_{ads} with loading.

Regarding the geometries of the CO_2 molecules, both appear, with sizeable uncertainties, slightly bent [∠O-C-O: CO_2-I, 175.72(1.01)°; CO_2-II, 177.15(1.66)°]. Given that a 3σ range of angles approaches or includes linearity and the fact that neither chemical intuition nor the modeling studies support a nonlinear structure, the apparent bend of the CO_2 molecules probably arises from their positional distributions rather than any true distortion in bonding. The C-O bond lengths [CO_2-I: 1.137(8), 1.079(9) Å; CO_2-II: 1.141(13), 1.125(13) Å] were slightly shorter than reported [1.155(1) Å] in a 150-K/ambient pressure structure of pure CO_2 (*31*). Variable-temperature x-ray crystallography showed that although the CO_2 bond lengths and angles varied slightly with temperature, their occupancies and orientations did not appreciably change (table S1). A decrease in total gas uptake would be expected with increasing temperature; however, for **1**, this did not change between 195 and 273 K. This observation, coupled with the order of the gas molecules, reinforces the fact that the collective interactions are highly favorable for CO_2 binding. Insight regarding the specific interactions was gained through computational modeling.

To investigate the nature of the CO_2 interactions with **1** and the cooperative guest-guest binding effects, we used a combination of dispersion-corrected (*32*) periodic DFT calculations and classical GCMC simulations and MD simulations (*33*), in which the partial charge parameters were derived from the periodic DFT calculations by means of the REPEAT method (*34*). Figure 3A displays the excellent agreement between the experimental and GCMC-simulated CO_2 adsorption isotherms of **1** at 273 K. The parameters associated with the CO_2-**1** intermolecular potential were not adjusted to obtain this quality of fit. Figure 3B shows a center-of-mass probability density plot from a GCMC simulation of **1** (at 850 mbar and 273 K), where darker regions reveal a greater probability of finding CO_2. Even at 273 K, binding sites are well localized, and the symmetry of the probability clouds suggests two distinct binding sites, corroborating the crystallography. To compare the CO_2 binding sites determined computationally and crystallographically, the experimental CO_2 positions are superimposed on three-dimensional isosurfaces of the probabilities for C and O in Fig. 3C. The remarkable agreement between the simulated and experimental CO_2 positions suggests that GCMC simulations that are often used to study gas adsorption in MOFs (*33*, *35*)

not only reproduce adsorption isotherms but can also accurately reproduce specific binding sites.

The nature of the CO_2 binding was further studied with dispersion-corrected periodic DFT calculations. With all 16 binding sites in the unit cell occupied, the resulting fully optimized geometry is in excellent agreement with the x-ray structure, including the relevant CO_2-amine and CO_2-oxalate distances (fig. S8). The exception to this was the geometries of both CO_2 molecules, which, unlike their geometry in the x-ray analysis, were optimized to linear configurations, revealing that there is minimal geometric distortion from interaction with the framework. Radial distribution plots extracted from the GCMC simulations are also in agreement with the geometric parameters determined by crystallography (fig. S10). Although specific binding sites were located experimentally, the CO_2 binding is expected to be dynamic in nature. This prospect has been investigated via classical MD simulations, which show that, in a 1.4-ns time span, the CO_2 molecule can hop between several of the binding sites I and II (Fig. 3D).

The CO_2 binding energies were calculated at various occupancies at the DFT level (*29*). When **1** is empty, CO_2-I has a binding energy of 39.6 kJ mol^{-1}, which is in good agreement with the experimental zero-loading ΔH_{ads} (40.8 ± 0.8 kJ mol^{-1}). We see a strong cooperative enhancement of CO_2 binding that increases with loading. Specifically, the binding energy of CO_2-II increases by 4.6 kJ mol^{-1} to 37.0 kJ mol^{-1} when an adjacent site I is occupied. When **1** is fully occupied less one binding site, the binding energy for CO_2-II increases to 38.1 kJ mol^{-1}, whereas that of CO_2-I is 44.2 kJ mol^{-1}. Further insight into the nature of the CO_2 binding can be gained by partitioning the total binding energy. This analysis reveals that 82% of the binding energy of site I is due to dispersion, whereas 18% results from electrostatics (*29*). This contrasts with site II, where the binding energy is almost entirely (99%) due to dispersion interactions.

The cooperative binding in **1** can be attributed to a combination of dispersion and electrostatic interactions between CO_2 molecules, which can be quantified by using DFT to evaluate the interaction energy between two CO_2 molecules at sites I and II in a vacuum (*29*). This calculation gives a CO_2-CO_2 interaction energy of 3.9 kJ mol^{-1}, which accounts for most of the observed 4.6–kJ mol^{-1} binding enhancement. Of the 3.9–kJ mol^{-1} interaction between CO_2 molecules, 66% can be attributed to dispersion and 34% can be assigned to electrostatics. The same analysis, with the MOF fully loaded, attributes 61% of the interaction to dispersion and 39% to electrostatics, suggesting similar cooperativity at higher loadings.

Several key insights obtained from the detailed analysis of the binding interactions in **1** have implications for the design of future materials used for the physisorption of CO_2. The relatively high binding energies observed in the material are dominated by dispersion interactions. Because CO_2 has a substantial quadrupole moment, there is opportunity to further increase the binding energies through appropriately designed binding sites that maximize the electrostatic interactions with CO_2. The importance of the cooperative guest binding to the uptake of CO_2 in **1** is another key insight. In particular, the proper mutual orientation and high density of binding sites can be used as a strategy to increase CO_2 binding energies. Further, we believe that these strategies can be incorporated into materials with larger pores, in order to increase the overall CO_2 uptake capacity and binding energies, thereby improving the uptake properties in the important low–partial-pressure regime. In the broadest sense, via detailed modeling, this study lays the groundwork for the design of easy-on/easy-off physisorptive materials for CO_2 capture, designed from the characteristics of the guest molecules outward rather than from the host framework inward.

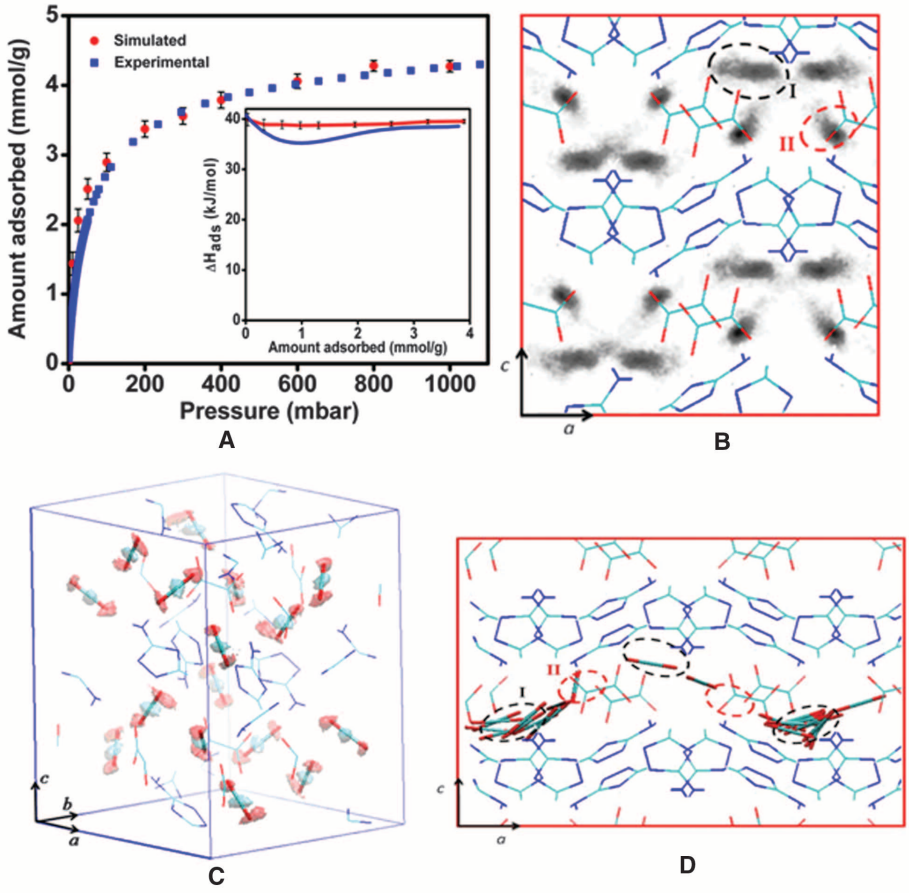

Fig. 3. (**A**) Comparison of the simulated (red) and experimental (blue) CO_2 gas adsorption isotherm of **1** at 273 K. The inset shows a comparison of experimental and simulated heats of adsorption as a function of guest loading. (**B**) Center-of-mass probability density plots of CO_2 molecules in **1** from a GCMC simulation at 850 mbar and 273 K. Probabilities along the *b* axis are summed and projected onto the *ac* plane. (**C**) Comparison of the location of the CO_2 binding sites in **1** obtained from x-ray analysis and those predicted by simulation. Probability isosurface plots of the CO_2 O atoms are shown as transparent red surfaces and those of the C atoms as transparent cyan surfaces. The 16 experimentally determined CO_2 molecule positions are shown as tubes. An isosurface value of 0.15 $Bohr^{-3}$ is used. (**D**) Trace of a single CO_2 molecule during a MD simulation of **1** with five CO_2 molecules per unit cell or a loading of 1.6 mmol g^{-1}. Shown are 23 successive snapshots, separated by 62.5 ps. Other CO_2 molecules present in the simulation are not shown. In (B) and (D), the approximate locations of binding sites I and II in a single channel are shown with dotted ellipses (site I, black; site II, red). In (B) and (C), a single unit cell of MOF **1** is shown, whereas in (D) a 2 × 1 × 1 cell is depicted. In (B) to (D), the MOF framework is shown as lines and the CO_2 molecules are shown as tubes (C, light blue; O, red; N, dark blue; Zn, not shown).

References and Notes

1. G. T. Rochelle, *Science* **325**, 1652 (2009).
2. B. Arstad, R. Blom, O. Swang, *J. Phys. Chem. A* **111**, 1222 (2007).
3. A. Zukal, I. Dominguez, J. Mayerová, J. Cejka, *Langmuir* **25**, 10314 (2009).
4. R. V. Siriwardane, M. S. Shen, E. P. Fisher, J. Losch, *Energy Fuels* **19**, 1153 (2005).
5. Y. Belmabkhout, A. Sayari, *Adsorption* **15**, 318 (2009).
6. S. Kim, J. Ida, V. V. Guliants, J. Y. S. Lin, *J. Phys. Chem. B* **109**, 6287 (2005).
7. S. N. Kim, W. J. Son, J. S. Choi, W. S. Ahn, *Microporous Mesoporous Mater.* **115**, 497 (2008).
8. J. Wei *et al.*, *Microporous Mesoporous Mater.* **116**, 394 (2008).
9. B. J. Kim, K. S. Cho, S. J. Park, *J. Colloid Interface Sci.* **342**, 575 (2010).

10. B. Wang, A. P. Côté, H. Furukawa, M. O'Keeffe, O. M. Yaghi, *Nature* **453**, 207 (2008).
11. P. K. Thallapally *et al.*, *J. Am. Chem. Soc.* **130**, 16842 (2008).
12. A. R. Millward, O. M. Yaghi, *J. Am. Chem. Soc.* **127**, 17998 (2005).
13. N. A. Ramsahye *et al.*, *J. Phys. Chem. C* **112**, 514 (2008).
14. S. R. Caskey, A. G. Wong-Foy, A. J. Matzger, *J. Am. Chem. Soc.* **130**, 10870 (2008).
15. A. Phan *et al.*, *Acc. Chem. Res.* **43**, 58 (2010).
16. K. S. Walton *et al.*, *J. Am. Chem. Soc.* **130**, 406 (2008).
17. A. Demessence, D. M. D'Alessandro, M. L. Foo, J. R. Long, *J. Am. Chem. Soc.* **131**, 8784 (2009).
18. J. An, S. J. Geib, N. L. Rosi, *J. Am. Chem. Soc.* **132**, 38 (2010).
19. B. Arstad, H. Fjellvåg, K. O. Kongshaug, O. Swang, R. Blom, *Adsorption* **14**, 755 (2008).
20. C. Villiers, J. P. Dognon, R. Pollet, P. Thuéry, M. Ephritikhine, *Angew. Chem. Int. Ed.* **49**, 3465 (2010).
21. R. Kitaura *et al.*, *Science* **298**, 2358 (2002).
22. R. Matsuda *et al.*, *Nature* **436**, 238 (2005).
23. S. Takamizawa *et al.*, *J. Am. Chem. Soc.* **132**, 3783 (2010).
24. J. P. Zhang, X. M. Chen, *J. Am. Chem. Soc.* **131**, 5516 (2009).
25. P. D. C. Dietzel *et al.*, *Chem. Commun. (Camb.)* **41**, 5125 (2008).
26. H. Wu, J. M. Simmons, G. S. Srinivas, W. Zhou, T. Yildirim, *J. Phys. Chem. Lett* **1**, 1946 (2010).
27. V. K. Peterson, Y. Liu, C. M. Brown, C. J. Kepert, *J. Am. Chem. Soc.* **128**, 15578 (2006).
28. R. Vaidhyanathan, S. S. Iremonger, K. W. Dawson, G. K. H. Shimizu, *Chem. Commun. (Camb.)* **35**, 5230 (2009).
29. Supporting material on *Science* Online includes complete details of the crystallography (crystallographic information files for all temperatures), gas sorption experiments, and computational modeling (including a movie showing the correlation of experimental and modeled CO_2 positions in **1**).
30. H. Deguchi *et al.*, *Ind. Eng. Chem. Res.* **49**, 6 (2010).
31. A. Simon, K. Peters, *Acta Crystallogr. B* **36**, 2750 (1980).
32. S. Grimme, *J. Comput. Chem.* **27**, 1787 (2006).
33. T. Düren, Y. S. Bae, R. Q. Snurr, *Chem. Soc. Rev.* **38**, 1237 (2009).
34. C. Campañá, B. Mussard, T. K. Woo, *J. Chem. Theory Comput.* **5**, 2866 (2009).
35. M. Tafipolsky, S. Amirjalayer, R. Schmid, *Microporous Mesoporous Mater.* **129**, 304 (2010).

36. T.K.W. and G.K.H.S. thank the Natural Sciences and Engineering Research Council of Canada. G.K.H.S. thanks the Institute for Sustainable Energy, Environment and Economy at the University of Calgary and the Alberta Energy Research Institute for partial financial support of this work. T.K.W. and P.G.B. thank the Canada Research Chairs Program and the High Performance Computing Virtual Laboratory for financial support. Crystallographic data for the structures reported in this paper have been deposited with the Cambridge Crystallographic Data Centre (CCDC) under reference numbers CCDC 782638 to 782642. These data can be obtained free of charge via www.ccdc.cam.ac.uk/conts/retrieving.html (or from the CCDC, 12 Union Road, Cambridge CB2 1EZ, UK).

Supporting Online Material

www.sciencemag.org/cgi/content/full/330/6004/650/DC1
Materials and Methods
SOM Text
Figs. S1 to S12
Tables S1 to S5
References
Movie S1

25 June 2010; accepted 30 September 2010
10.1126/science.1194237

The Occurrence and Mass Distribution of Close-in Super-Earths, Neptunes, and Jupiters

Andrew W. Howard,[1,2]* Geoffrey W. Marcy,[1] John Asher Johnson,[3] Debra A. Fischer,[4] Jason T. Wright,[5] Howard Isaacson,[1] Jeff A. Valenti,[6] Jay Anderson,[6] Doug N. C. Lin,[7,8] Shigeru Ida[9]

The questions of how planets form and how common Earth-like planets are can be addressed by measuring the distribution of exoplanet masses and orbital periods. We report the occurrence rate of close-in planets (with orbital periods less than 50 days), based on precise Doppler measurements of 166 Sun-like stars. We measured increasing planet occurrence with decreasing planet mass (M). Extrapolation of a power-law mass distribution fitted to our measurements, $df/d\log M = 0.39\ M^{-0.48}$, predicts that 23% of stars harbor a close-in Earth-mass planet (ranging from 0.5 to 2.0 Earth masses). Theoretical models of planet formation predict a deficit of planets in the domain from 5 to 30 Earth masses and with orbital periods less than 50 days. This region of parameter space is in fact well populated, implying that such models need substantial revision.

The architecture of our solar system, with small rocky planets orbiting close to the Sun and gas-liquid giant planets farther out, provides key properties that inform theories of planet formation and evolution. As more planetary systems are discovered, the planet occurrence fractions and distributions of mass and orbital distance similarly shape our understanding of how planets form, interact, and evolve. Such properties can be measured using precise Doppler measurements of the host stars that interact gravitationally with their planets. These measurements reveal the planetary orbits and minimum masses ($M \sin i$, due to unknown orbital inclinations i).

In the core-accretion theory of planet formation, planets are built from the collisions and sticking together of rock-ice planetesimals, growing to Earth size and beyond, followed by the gravitational accretion of hydrogen and helium gas. This process has been simulated numerically (*1*–*4*), predicting the occurrence of planets in a two-parameter space defined by their masses and orbital periods (P). These simulations predict that there should be a paucity of planets, a "planet desert" (*3*), in the mass range from ~1 to 30 Earth masses ($M_{\rm Earth}$) orbiting inside of ~1 astronomical unit (AU), depending on the exact treatment of inward planet migration.

We used precise Doppler measurements of a well-defined sample of nearby stars to detect planets having masses of 3 to 1000 $M_{\rm Earth}$ orbiting within the inner 0.25 AU. The 235 main-sequence G-, K-, and M-type dwarf stars in our NASA–University of California Eta-Earth Survey were selected from the Hipparcos catalog on the basis of brightness ($V < 11$), distance (<25 pc), luminosity ($M_V > 3.0$), low chromospheric activity ($\log R'_{\rm HK} < -4.7$), lack of stellar companions, and observability from Keck Observatory. The resulting set of stars is nearly free of selection bias; in particular, stars were neither included nor excluded based on their likelihood to harbor a planet. [The stars and planets are listed in the supporting online material (SOM).] Here we focus on the 166 G- and K-type stars, with masses of 0.54 to 1.28 solar masses and $B - V < 1.4$. We analyzed previously announced planets, new candidate planets, and nondetections on a star-by-star basis to measure close-in planet occurrence as a function of planet mass.

We measured at least 20 radial velocities (RVs) for each star, achieving 1 m s^{-1} precision (*5*) with the HIRES echelle spectrometer (*6*) at Keck Observatory. To achieve sensitivity on time scales ranging from years to days, the observations of each star were spread over 5 years, with at least one cluster of 6 to 12 observations in a 12-night span. Stars with candidate planets were observed intensively, leading to several discoveries (*5*, *7*, *8*). In total, 33 planets (Fig. 1) have been detected around 22 stars in our sample (*5, 7, 9–22*), some of which were discovered by other groups. Sixteen of these planets have $P <$ 50 days. Our analysis also includes five candidate low-mass planets from the Eta-Earth Survey with $P < 50$ days and false alarm probabilities (*5*) of <5%.

[1]Department of Astronomy, University of California, Berkeley, CA 94720, USA. [2]Space Sciences Laboratory, University of California, Berkeley, CA 94720, USA. [3]Department of Astrophysics, California Institute of Technology, Pasadena, CA 91125, USA. [4]Department of Astronomy, Yale University, New Haven, CT 06511, USA. [5]Department of Astronomy and Astrophysics, The Pennsylvania State University, University Park, PA 16802, USA. [6]Space Telescope Science Institute, 3700 San Martin Drive, Baltimore, MD 21218, USA. [7]University of California Observatories/Lick Observatory, University of California, Santa Cruz, CA 95064, USA. [8]Kavli Institute for Astronomy and Astrophysics, Peking University, Beijing, China. [9]Tokyo Institute of Technology, Ookayama, Meguro-ku, Tokyo 152-8551, Japan.

*To whom correspondence should be addressed. E-mail: howard@astro.berkeley.edu

Introduction to metal-organic frameworks and the application on adsorption of CO_2

Di Cui*

Department of Chemistry and Biochemistry, University of Delaware, Newark, Delaware, 19711

RECEIVED DATE (automatically inserted by publisher); Email: dicui@udel.edu

ABSTRACT Different methods of adsorption of CO_2 are reviewed. By comparison, functionalized metal-organic frameworks merge the inherent physisorption of porous solids with the chemical sorption of weak bases, showing advantages of less energy cost and higher uptake of CO_2. Detailed discussion focuses on the choices of metal ions and organic ligands for synthesis of metal-organic frameworks. Also, incorporating experimental work with computational analysis reveal the specific binding interaction between guest molecules and the amine groups of the metal-organic frameworks, which can provide useful direction for the design of more efficient and selective functional metal-organic frameworks.

Carbon dioxide is a kind of gas that is often produced during the industrial processes. However, direct emissions of CO_2 into the atmosphere may cause green house effect that is responsible for change to warmth of the global climate. Therefore, separation of low partial pressures CO_2 from other gases would be highly attractive for the purpose of ameliorating anthropogenic climate change.

Several methods have been developed to capture CO_2 among other gases and regenerate it later. Acids can react with bases, based on this simple principle, technology for gas desulfurization by using lime or limestone slurry has been developed. [1] Similarly, aqueous amine solutions can be used for CO_2 absorption. [2] There are several mechanisms about this reaction; one general accepted mechanism shows as in the Scheme 1.

Scheme 1. Mechnism of CO_2 absorption by aqueous amine solution

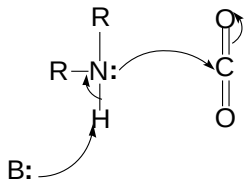

This is a termolecular concerted mechanism. The lone pair electrons on the nitrogen atom, serving as nucleophilic reagent, attack the electrophilic CO_2. Simultaneously, proton transfers from the amino nitrogen atom to a nearby base molecule. The base can be water or another amine. The reasonableness of this mechanism has been proved by quantum chemical calculations. Calculations show that direct reaction of monoethanolamine and CO_2 without addition base has a quite high barrier for changing from ground state to transition state with the activation energy about 170kJ/mol. [3] On the other hand, if termolecular reaction is considered, which regards a water molecule will serve as additional base, the activation energy will lower to 108kJ/mol. The decrease in activation energy shows that it is reasonable to think that carbamate acid molecule is formed from one CO_2 molecule and one amine molecule with one water molecule or another amine molecule acting as catalyst.

Although widely used, this method has a major drawback. Releasing of CO_2 from the carbamate acid requires the cleavage of C-N bond that has bonding energy about 100kJ/mol, [4] which means that regeneration of CO_2 by this method is a high energy cost process. Besides, in the gas-liquid systems, a low concentration of amines present in the aqueous solution, causing corrosion problem.

An alternative method to separate CO_2 is the use of solid sorbents. Adsorption and separation of CO_2 over a range of porous solid adsorbents have been well studied. Common physical absorbents, including activated carbons [5-6] and zeolites, [7-9] process relatively high CO_2 adsorption capacities; however, they decline rapidly with increasing temperature. Solid chemical adsorbents, including hydrotalcite [10] and various basic metal oxides [11] can adsorb CO_2 at high temperatures; however, they suffered from either low CO_2 capacities or severe energy cost due to the high desorption temperatures.

Another kind of promising solid sorbent is metal-organic frameworks, which is a new development on the interface between molecular coordination chemistry and materials science. They are composed of two major components: metal ions and organic molecules called linkers. The organic units are typically mono-, di-, tri-, or tetravalent ligands. Different combinations of metal ions and organic molecules can have different effects on the structure and properties of the metal-organic frameworks. Dictating how many ligands can bind to the metal ions and in which orientation can give some information of the metal's coordination preference, which affects the size and shape of pores a lot.

In order to make metal-organic frameworks, in principle, it is only necessary to react a potentially bridging ligand with a metal ion which has more than one vacant site. [12] However, for the purpose of characterization, it is only applicable to investigate several specific kinds of metal-ligand combination. Crystal structure of metal-organic frameworks is quite important to interpret their observed properties. Two kinds of structure can arise, either infinite extended polymetric or discrete closed oligometrc structures. The most detailed structural information will be gained from single crystal X-ray crystallography. Therefore, it is quite difficult to investigate structure of amorphous solid phases. To avoid an amorphous product, complexes that are used should be labile. From inorganic lecture, we know that complexes that can react very rapidly are called labile. One criterion for lability is that a reaction has half-life of one minute or less. Complexes that are labile usually have low

activation energy, which means that bond formation is rapidly reversible, so the initial formed kinetic products, which may be mixtures, have the opportunity to rearrange and give a single thermodynamically favored product. Usually, labile metal ions include Cu^{+}, Cu^{2+}, Ag^{+}, Cd^{2+}, Zn^{2+}, Co^{2+} and Ni^{2+}. Although there are exceptions, general rules can be given for the labile electronic structures. Labile complexes are generally those with low ligand field stabilization energies, including d^1, d^2, high-spin d^4, high-spin d^5, high-spin d^6, d^7, d^9, d^{10}.

Ligand types also need to be considered for the formation of ordered crystal structures. If a ligand has a number of possible conformations, the geometry of the frameworks will be hard to predict. A good way is to use rigid ligands that can reduce the orientation freedom of the ligand lone pairs, such as the following ligands.

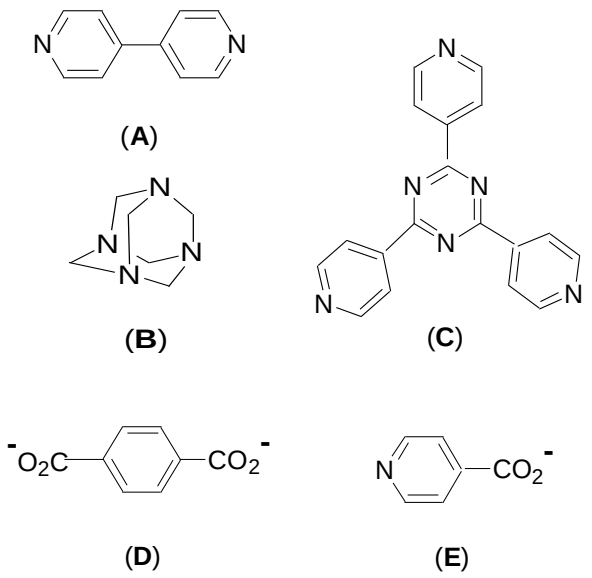

Figure 1 Examples of rigid ligands used in the synthesis of metal-organic frameworks

Large pore metal-organic frameworks are quite effective for storing high capacities of the gas, usually at higher pressures. When the pressure is low, the effectiveness of the adsorption goes down. Also, the selection of adsorption is poor based on pore size only. One method to improve this is to chemically functionate the pores of the metal-organic frameworks with groups capable of interacting strongly with the guest molecules. Since amine groups can react easily with CO_2 gas molecules, using amine-derivative metal-organic frameworks to adsorb CO_2 gas molecules have been investigated. [13] However, details on the interaction between functional amine groups and CO_2 are still lacking both on experimental level. In this article, [4] porous Zn-aminotriazolato-oxalate compound, with a formula $Zn_2(C_2O_4)(C_2N_4H_3)_2$ is used as the adsorbent. Diffraction experiments have been conducted to study the specific binding interactions between guest molecules and the metal-organic frameworks. Direct visualization of gases molecules within pores by the diffraction experiments, combining with computational modeling, makes the molecular details of CO_2-sorbent interactions understandable. Cooperative binding of CO_2 guest molecules has been proved by both experimental method and computational method. This is a key factor to influence the uptake of CO_2. The meaning of this work is that with the foundational understanding of the binding between guest molecules and adsorbent, the theory-aided design of future metal-organic frameworks that have low-pressure binding and large uptake of CO_2 is possible.

Details study of the nature of CO_2 binding in Zn-aminotriazolato-oxalate compound can be obtained via a combination of experimental and computational methods.

X-ray crystallography of evacuated metal-organic frameworks shows no electron density in the voids, confirming the stability of the crystal. After loading into CO_2, X-ray diffraction experiments shows that the CO_2 molecules could be located within the pores. More detailed information about the location of CO_2 within the pores can also be obtained. Typically, the metal-organic frameworks display strong confinement effects on the CO_2, so it is possible to localize these gases molecules in the pores. Calculations based on this method shows a formula of $Zn_2(C_2O_4)(C_2N_4H_3)_2.(CO_2)_{1.30}$.

Via thermodynamics experiments, adsorption isotherms for different gases by $Zn_2(C_2O_4)(C_2N_4H_3)_2$ are obtained, which shows the fact that $Zn_2(C_2O_4)(C_2N_4H_3)_2$ can capture CO_2 selectively by comparison with other kinds of gases. Calculations based on these thermodynamic data show the formula of $Zn_2(C_2O_4)(C_2N_4H_3)_2.(CO_2)_{1.35}$, which agrees well with the one obtains from the crystallography.

One important phenomena that is observed within $Zn_2(C_2O_4)(C_2N_4H_3)_2$ is the cooperativity effect in the binding of CO_2. $Zn_2(C_2O_4)(C_2N_4H_3)_2$ showed CO_2 uptake at low pressures with an initial heat of adsorption of 40kJ/mol. With the increasement of pressure of the CO_2, the heat of adsorption of the material decreased. However, continuity of the exposure showed an increasement of the heat of adsorption. Another example of cooperativity effect of CO_2 binding is that with increasing temperature, there would be expected to observe a decrease of the uptake of the gas. However, experiments conducting at temperature between 195 and 273K show that there is little change of the amount of uptake. To illustrate these facts, a combination of crystallographic and computational methods has been used. Study shows that within each pore, there are two independent CO_2 binding sites. One can show as CO_2-I, which locates near the free amine group; another can show as CO_2-II, which locates closer to the oxalates. There are two ways of interaction between CO_2 and amine. One is that CO_2 interacts with an amine via N-H...O hydrogen bonding; another one is the interaction between the N lone pair and the C atom of CO_2. Besides these, there is an interaction between two neighboring CO_2 molecules. One O atom of CO2-I can form a contact with the C atom of CO_2-II, which accounts for the cooperative effect.

Details investigation of cooperative binding in $Zn_2(C_2O_4)(C_2N_4H_3)_2$ by DFT shows that the nature of interaction between two neighboring CO_2 molecules should include two kinds of interaction: dispersion and electrostatic interactions. Calculation shows that the interaction energy of CO_2-CO_2 is 3.9kJ/mol, which is in accordance with the observed 4.6kJ/mol. Among the interaction energy, 66% is derived from dispersion and 34% is derived from the electrostatics.

These carefully and complicatedly calculations provide a key insight to fully understand the binding interactions between CO_2 and the metal organic framework, which can give a guidance for the future design of the materials for CO_2 adsorption. Studies show that three main factors, including appropriate pore size,

interaction between amine functional groups and guest molecules , and the cooperative binding of CO_2 guest molecules, are responsible for the low-pressure binding and large uptake of CO_2 within the $Zn_2(C_2O_4)(C_2N_4H_3)_2$ frameworks. One aspect of the future research on this topic should focus on the enhancement of the cooperativity of guest molecules. To enhance the cooperative effect, either dispersion interactions or electrostatic interactions should be strengthened. Since CO_2 has a substantial quadrupole moment, it is possible to increase the electrostatic interactions between two neighboring CO_2 molecules by improve the binding sites. Also, metal-organic frameworks with larger pores should be investigated more in order to discover materials with higher CO_2 uptake capacity and more selective on CO_2 during low partial pressure.

Acknowledgment

Supporting Information Available:

REFERENCES

1. Nonhebel, G.; *Trans. Faraday Soc*; 1936, 32, 1291
2.Rochelle, G. T.; *Science*; 2009, 325, 1652.
3.Arstad, B.; Blom, R.; Swang, O.; *J. Phys. Chem. A*; 2007, 111, 1222.
4.Vaidhyanathan, R.; Iremonger, S. S.; Shimizu, G.K.H.; Boyd, P. G. ; Alavi, S. Woo, T. K.; *Science*, 2010, 330, 650
5. Yong, Z.; Mata, V.; Rodrigues, A. E; *Adsorption*; 2001, 7, 41.
6.Ottiger, S.; Pini, R.; Storti, G.; Mazzotti, M.; *Langmuir*, 2008, 24, 9531.
7.Siporin, S. E.; McClaine, B. C.; Davis, R. J.; *Langmuir*, 2003, 19, 4707.
8. Plant, D. F.; Maurin, G.; Deroche, I.; Gaberova, L.; Llewwllyn, P. L.; *Chem. Phys. Lett.*; 2006, 426, 387.
9.Pawlesa, J.; Zukal, A.; Cejka, J.; *Adsorption*; 2007, 13, 2413.
10. Reijers, H. Th. J.; Valster-Schiermeier, S. E. A.; Cobden, P. D.; *Ind. Eng. Chem. Res.*; 2006, 45, 2522.
11. Gaffney, T. R.; Golden, T. C.; Mayorga, S. G.; Brozozowski, J. R.; Talyer, F. W. U. S. Patent 5, 917, 136, 1999.
12. James, Stuart L.; *Chem. Soc. Rev.*; 2003, 32, 276.
13. Vaidhyanathan. R.; Iremonger, S. S.; Dawson, K. W.; Shimizu, G. K. H.; *Chem. Commun*.; 2009, 35, 5230.

18. M. Saito, M. Sakaguchi, T. Tajima, K. Ishimura, S. Nagase, *Phosphorus Sulfur Silicon Relat. Elem.* 10.1080/10426501003773399 (2010).
19. Methods are detailed in supporting material available on *Science* Online.
20. U. Edlund, T. Lejon, P. Pyykkö, T. K. Venkatachalam, E. Buncel, *J. Am. Chem. Soc.* **109**, 5982 (1987).
21. J.-H. Hong, P. Boudjouk, S. Castellino, *Organometallics* **13**, 3387 (1994).
22. All calculations were performed with Gaussian 03 revision D.02 (*36*).
23. A. D. Becke, *J. Chem. Phys.* **98**, 5648 (1993).
24. C. Lee, W. Yang, R. G. Parr, *Phys. Rev. B* **37**, 785 (1988).
25. M. Douglas, N. M. Kroll, *Ann. Phys.* **82**, 89 (1974).
26. B. A. Hess, *Phys. Rev. A* **32**, 756 (1985).
27. B. A. Hess, *Phys. Rev. A* **33**, 3742 (1986).
28. B. O. Roos, R. Lindh, P.-Å. Malmqvist, V. Veryazov, P.-O. Widmark, *J. Phys. Chem. A* **108**, 2851 (2004).
29. R. Krishnan, J. S. Binkley, R. Seeger, J. A. Pople, *J. Chem. Phys.* **72**, 650 (1980).
30. W. J. Hehre, R. Ditchfield, J. A. Pople, *J. Chem. Phys.* **56**, 2257 (1972).
31. W. R. Wadt, P. J. Hay, *J. Chem. Phys.* **82**, 284 (1985).
32. T. H. Dunning Jr., P. J. Hay, *Methods of Electronic Structure Theory*, Vol. 2, H. F. Schaefer III, Ed. (Plenum, New York, 1977).
33. The NICS, which is an abbreviation of nucleus-independent chemical shifts, was first proposed as a probe of aromaticity on the basis of magnetic criteria (*37*) and is now generally used to characterize the aromaticity of compounds (*38*).
34. V. Y. Lee, R. Kato, M. Ichinohe, A. Sekiguchi, *J. Am. Chem. Soc.* **127**, 13142 (2005).
35. A. J. Ashe III, T. R. Diephouse, M. Y. El-Sheikh, *J. Am. Chem. Soc.* **104**, 5693 (1982).
36. M. J. Frisch *et al.*, Gaussian 03 revision D.02 (Gaussian, Wallingford, CT, 2004).
37. P. R. Schleyer, C. Maerker, A. Dransfeld, H. Jiao, N. J. R. E. Hommes, *J. Am. Chem. Soc.* **118**, 6317 (1996).
38. Z. Chen, C. S. Wannere, C. Corminboeuf, R. Puchta, P. v. R. Schleyer, *Chem. Rev.* **105**, 3842 (2005).

39. This work was partially supported by Grants-in-Aid for Scientific Research (no. 20038010 to M.S., no. 18066017 to S.N., and no. 19029037 to M.H.) in Priority Areas "Molecular Theory for Real Systems" and by the Nanotechnology Support Project from the Ministry of Education, Culture, Sports, Science, and Technology of Japan. M.S. acknowledges a research grant from Toray Science Foundation. Deposition nos. CCDC-750458 and 750459 contain the supplementary crystallographic data for compounds **1** and **4**, respectively. These data can be obtained free of charge at www.ccdc.cam.ac.uk/conts/retrieving.html (or from the Cambridge Crystallographic Data Centre, 12 Union Road, Cambridge CB2 1EZ, UK; fax, 44-1223-336-033; e-mail, deposit@ccdc.cam.ac.uk).

Supporting Online Material

www.sciencemag.org/cgi/content/full/328/5976/339/DC1
Methods
Reference

21 October 2009; accepted 11 December 2009
10.1126/science.1183648

A Fast Soluble Carbon-Free Molecular Water Oxidation Catalyst Based on Abundant Metals

Qiushi Yin,[1] Jeffrey Miles Tan,[1] Claire Besson,[1,2] Yurii V. Geletii,[1] Djamaladdin G. Musaev,[1] Aleksey E. Kuznetsov,[1] Zhen Luo,[1] Ken I. Hardcastle,[1] Craig L. Hill[1]*

Traditional homogeneous water oxidation catalysts are plagued by instability under the reaction conditions. We report that the complex $[Co_4(H_2O)_2(PW_9O_{34})_2]^{10-}$, comprising a Co_4O_4 core stabilized by oxidatively resistant polytungstate ligands, is a hydrolytically and oxidatively stable homogeneous water oxidation catalyst that self-assembles in water from salts of earth-abundant elements (Co, W, and P). With $[Ru(bpy)_3]^{3+}$ (bpy is 2,2′-bipyridine) as the oxidant, we observe catalytic turnover frequencies for O_2 production $\geq 5\ s^{-1}$ at pH = 8. The rate's pH sensitivity reflects the pH dependence of the four-electron O_2-H_2O couple. Extensive spectroscopic, electrochemical, and inhibition studies firmly indicate that $[Co_4(H_2O)_2(PW_9O_{34})_2]^{10-}$ is stable under catalytic turnover conditions: Neither hydrated cobalt ions nor cobalt hydroxide/oxide particles form in situ.

Producing renewable clean energy has become one of the most profound challenges of the 21st century (*1*). Most of the world's current energy supplies come from sunlight converted to chemical energy by plant photosynthesis. A central thrust of the current energy research focuses on artificial photosynthesis (*2*, *3*). Despite the intense global efforts to develop viable abiological water splitting systems, breakthroughs are needed in selectivity, speed, and stability of all three operational units: the sensitizer for light absorption and catalysts for water reduction and oxidation. Developing a viable water oxidation catalyst (WOC) has proven particularly challenging (*4*). An effective WOC must be fast; capable of water oxidation at a potential minimally above the thermodynamic value ($H_2O \rightarrow O_2 + 4H^+ + 4e^-$; $1.229 - 0.059 \times$ pH at 25°C); and, critically, stable to air, water, and heat (oxidative, hydrolytic, and thermal stability). There are many research groups working on heterogeneous and homogeneous WOCs. Heterogeneous WOCs generally have the advantages of low cost, ease of interface with electrode systems, and, critically, oxidative stability; but they are harder to study and thus optimize than homogeneous catalysts, and they tend to deactivate by surface poisoning or aggregation (*5*–*9*). Recently, Kanan and Nocera reported a robust heterogeneous WOC based on earth-abundant cobalt and phosphate (*8*), after earlier work by Creutz and Sutin (*10*), and demonstrated self-assembly under turnover conditions, a key to self-repair (*11*). More recently, the groups of Mallouk (*9*) and Frei (*12*) reported high catalytic water oxidation rates by using colloidal $IrO_2 \cdot nH_2O$ particles and Co_3O_4 (spinel) particles, respectively. In contrast, homogeneous WOCs are more amenable to spectroscopic, crystallographic, physicochemical, and computational investigation and thus more readily optimized. In addition, each individual molecule of a homogeneous catalyst is, in principle, capable of doing chemistry (a cost issue when precious metals such as Ru are involved). However, nearly all homogeneous catalysts contain organic ligands that are thermodynamically unstable with respect to oxidative degradation. As a result, all homogenous WOCs with organic ligands reported to date are oxidatively deactivated (*13*–*23*). A

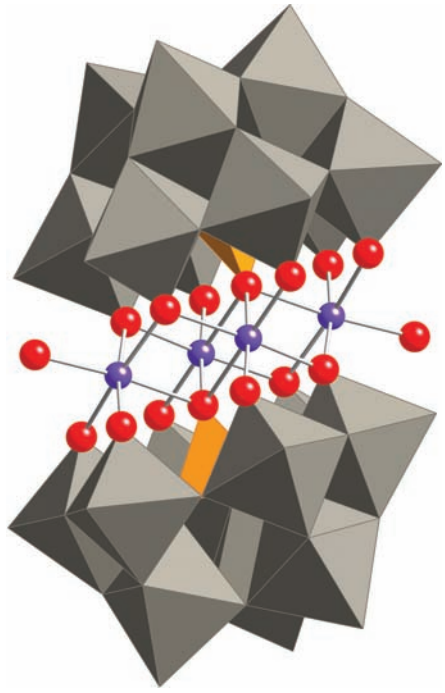

Fig. 1. X-ray structure of $\mathbf{Na_{10}}$-**1** in combined polyhedral ($[PW_9O_{34}]$ ligands) and ball-and-stick (Co_4O_{16} core) notation. Co atoms are purple; O/OH_2(terminal), red; PO_4, orange tetrahedra; and WO_6, gray octahedra. Hydrogen atoms, water molecules, and sodium cations are omitted for clarity.

[1]Department of Chemistry, Emory University, Atlanta, GA 30322, USA. [2]Institut Parisien de Chimie Moléculaire, UMR CNRS 7201, Université Pierre et Marie Curie Univ. Paris 06, Case 42, 4 place Jussieu, 75005 Paris, France.

*To whom correspondence should be addressed. E-mail: chill@emory.edu

general goal is to realize WOCs that have the stability, durability, and accessibility of heterogeneous metal oxide catalysts with the activity, selectivity, and tunability of homogeneous catalysts. To this end, a homogeneous polyoxometalate (POM) WOC with oxidatively resistant polytungstate units multiply ligating a Ru_4O_4 core was recently reported (*24*–*26*). This WOC is as fast as reported homogeneous catalysts containing organic ligands, but Ru is neither abundant nor inexpensive and thus very likely prohibitive for use on a realistic scale. Therefore, discovery of a stable and fast homogenous WOC, without organic ligands, based on earth-abundant elements would be highly useful.

We report here a homogeneous catalyst, B-type $[Co_4(H_2O)_2(\alpha\text{-}PW_9O_{34})_2]^{10-}$ (**1**), that is free of carbon-based ligands (Fig. 1). It is easily prepared from readily available salts and oxides of earth-abundant elements (Co, W, and P). To explore POM-stabilized multi–Co-oxide clusters as WOCs, we used the relatively strong and stable stoichiometric oxidant, tris(2,2′-bipyridyl)triperchlororuthenium(III), (henceforth $[Ru(bpy)_3]^{3+}$; Eq. 1). The oxygen yield was monitored with gas chromatography by withdrawing gas samples from the reaction vessel headspace (*24*, *27*).

$$4[Ru(bpy)_3]^{3+} + 2\ H_2O \xrightarrow{WOC} 4\ [Ru(bpy)_3]^{2+} + 4\ H^+ + O_2 \quad (1)$$

We examined eight cobalt-containing POMs as WOCs (Table 1). Only $[Co_4(H_2O)_2(\alpha\text{-}PW_9O_{34})_2]^{10-}$ (**1**) was active. Cyclic voltammetry of 1 mM **1** shows a large catalytic current with a low overpotential for the water oxidation (Fig. 2A). This characteristic feature is not observed for complexes **2** through **8**. Close examination of the studied complexes reveals that all cobalt-containing POMs have different cobalt-core structures than **1**, with the exception of $[Co_4(H_2O)_2(P_2W_{15}O_{56})_2]^{16-}$ (**2**) (fig. S11). However, **2** was synthesized and crystallized at a much lower pH than **1** and is also known to be unstable under our catalytic conditions (pH = 7.5 to 8.0) (*28*). The total yield of oxygen is always less than 100% based on oxidant because of competing bipyridyl ligand oxidation (*10*). A first-order hyperbolic fit of the O_2 yield to the concentration of **1** is consistent with this description (fig. S1).

The turnover frequency (TOF) for **1** (Eq. 1) at pH = 8 was >5 s^{-1}, which compares well to the 0.9 s^{-1} observed for the [Cp*(Cl)Ir(ppy)] (where Cp* is 1,2,3,4,5-pentamethylcyclopentadiene and ppy is 2-phenylpyridine) WOC recently reported by Brudvig, Crabtree, and coworkers (*22*). The rate of water oxidation catalyzed by **1** is highly sensitive to pH. Increasing pH from the initial value of 7.5 to 8.0 (sodium phosphate buffer, NaPi) decreased the reaction time from 270 s to 90 s (respective final pH values after reaction are 7.3 and 7.5). The reaction was faster still in a solution with a higher buffer capacity at pH = 8.0 (a mixture of 30 mM NaPi and 30 mM sodium borate buffer; final pH > 7.9). With 1.2×10^{-4} mM **1** and 2.4 mM $[Ru(bpy)_3]^{3+}$, we obtained a turnover number (TON, $n_{O2}/n_{catalyst}$) ~ 10^3 in under 3 min. Accordingly, the apparent TON also increases sharply at higher pH because of the faster rate of water oxidation. TON is limited by the concentration of the $[Ru(bpy)_3]^{3+}$, which, in turn, is limited by the formation of an insoluble adduct between **1** and $[Ru(bpy)_3]^{3+/2+}$.

As noted above, the cobalt-containing POM, **1**, is undemanding to synthesize. We prepared it in over 35% yield in a one-pot equilibration synthesis, as first reported by Weakley *et al.*, that entailed simply heating Co^{2+}, phosphate, and tungstate in a 2:1:9 ratio in water at reflux (*29*). This synthesis of **1** defines a mechanism for self-repair, a strategy used in our previous work (*11*) and in the recent work by Kanan and Nocera on their heterogeneous cobalt phosphate catalyst (*8*). Homogeneous catalysts like **1** use discrete molecules in solution for turnover as opposed to only select sites on the surface of most heterogeneous catalysts. This is a likely

Table 1. Catalytic water oxidation by soluble POM systems. Reactions were run in 30 mM NaPi buffer, initial pH = 8.0, 1.5 mM $[Ru(bpy)_3](ClO_4)_3$, and ambient temperature. bpy is 2,2′-bipyridine, and O_2 yield = $\frac{4n_{O_2}}{n_{Ru(bpy)_3}} \cdot 100$.

Complex	Complex concentration (mM)	bpy (mM)	TON	O_2 yield (%)
$[Co_4(H_2O)_2(PW_9O_{34})_2]^{10-}$ (**1**)	0.0032	0.06	75	64
$[Co_4(H_2O)_2(P_2W_{15}O_{56})_2]^{10-}$ (**2**)	0.0064	0.06	0	0
$[Co(H_2O)PW_{11}O_{39}]^{5-}$ (**3**)	0.0064	0.06	0	0
$[Co(H_2O)SiW_{11}O_{39}]^{6-}$ (**4**)	0.0064	0.06	0	0
$[Co_3(H_2O)_3(PW_9O_{34})_2]^{12-}$ (**5**)	0.0064	0.06	0	0
$[Co_3(H_2O)_3SiW_9O_{37}]^{10-}$ (**6**)	0.0064	0.06	0	0
$[WCo_3(H_2O)_2(CoW_9O_{34})_2]^{12-}$ (**7**)	0.0064	0.06	0	0
$[Co_7(H_2O)_2(OH)_2P_2W_{25}O_{94}]^{16-}$ (**8**)	0.0064	0.06	0	0

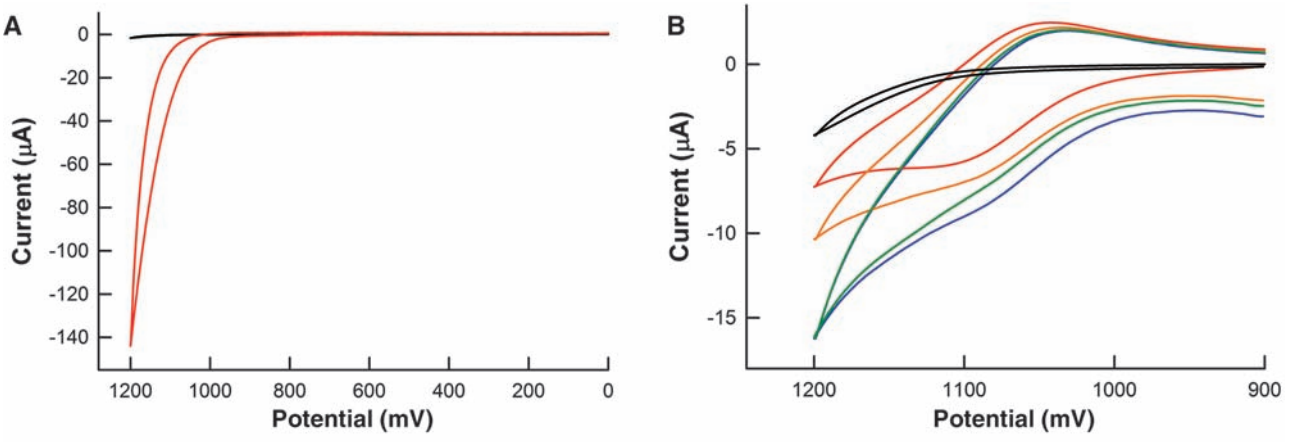

Fig. 2. (**A**) Cyclic voltammogram (CV) of 50 mM sodium phosphate solution at pH = 8 without **1** (black) and with 1 mM **1** (red). (**B**) CV of aqueous 0.857 mM $[Ru(bpy)_3]^{2+}$ alone (red), 3.2 μM **1** alone (black), 0.857 mM $[Ru(bpy)_3]^{2+}$ combined with 3.2 μM **1** (green) or 1.6 μM **1** (yellow), and a postreaction solution in which initially dissolved 0.857 mM $[Ru(bpy)_3]^{3+}$ was reduced through water oxidation catalyzed by 3.2 μM **1** (blue). The series of CVs for 0 μM **1** (red), 1.6 μM **1** (yellow), and 3.2 μM **1** (green) added to 0.857 mM $[Ru(bpy)_3]^{2+}$ shows increasing anodic current and decreasing cathodic current, demonstrating the correlation between increasing catalytic current and the concentration of **1**. Conditions are as follows: 60 mM NaPi, pH = 8, scan rate 25 mV s^{-1}; potentials measured and reported versus an Ag/AgCl reference electrode.

factor in a far higher observed efficiency of catalytic water oxidation per cobalt atom in the case of **1** relative to the heterogeneous cobalt phosphate catalyst.

Aqueous cobalt ions and cobalt hydroxide/oxides that form in situ from the former are both known to be WOCs (*6*, *8*, *10*). Thus, we now describe seven lines of experimental evidence that **1** is a stable molecular WOC under turnover conditions and does not form either aqueous cobalt ions or cobalt hydroxide/oxide. The first two arguments are that no changes are observed in either the ultraviolet and visible absorption (UV-Vis) or the ^{31}P nuclear magnetic resonance (NMR) spectra of a solution of **1** at pH = 8 (the pH in the catalytic experiments) over a 1-month period (figs. S3 and S4C). UV-Vis and ^{31}P NMR spectra also both establish that **1** is stable for at least 1 day within the pH range of 3.5 to 9 (fig. S4).

The third experimental probe of the stability of **1** involved selective catalyst poisoning experiments using 2,2′-bipyridine (bpy) as an inhibitor (fig. S2). Bpy reacts with $Co(aq)^{2+}$ to form $[Co(bpy)_3]^{2+}$ (*30*), inhibiting all water oxidation activity. In contrast, the addition of the same molar excess of bpy to solutions of **1** has a relatively minor effect on the apparent water oxidation activity (Table 2). The observed slight decrease in activity can be attributed to bpy competitively coordinating to the cobalt core of **1** or the irreversible oxidative degradation of bpy, which is proportional to the bpy concentration. Similarly, aging **1** under reaction conditions for 3 days had no effect on its catalytic water oxidation activity (Table 2), whereas aging $Co(NO_3)_2$ under the same conditions for 3 days substantially decreased its catalytic activity. This observation tracks with well-known cobalt hydroxide/oxide formation above neutral pH (*31*), decreasing the effective surface area and catalytic activity. In addition, at pH = 6.2, no water oxidation was observed for reactions catalyzed by **1**, whereas $Co(NO_3)_2$ was still capable of catalyzing a small extent of water oxidation (Table 2). These results are consistent with **1** being the catalytically active species and its polydentate polytungstate ligands preventing formation of cobalt hydroxide/oxide particles.

For our fourth probe of the stability of **1**, we characterized the postreaction solution containing **1** by using ^{31}P NMR despite the low solubility of **1** in the presence of excess $[Ru(bpy)_3]^{2+}$. When [**1**] = 0.015 mM, as few as 40 equivalents of $[Ru(bpy)_3]^{3+/2+}$ (corresponding to a TON of eight to nine) made the postreaction solution supersaturated, as indicated by the formation of a light yellow precipitate that forms in minutes to hours. To prevent precipitation, we removed $[Ru(bpy)_3]^{2+}$ from the postreaction solution by adding $NaBPh_4$ and removing solid $[Ru(bpy)_3][BPh_4]_2$ by filtration. In the ^{31}P NMR spectrum of this solution, **1** [1850 parts per million, full width at half maximum ($\Delta\nu_{1/2}$) = 600 Hz] was the only species detected besides the free phosphate originating from the buffer solution, indicating that **1** remains intact under catalytic water oxidation conditions (fig. S5).

The fifth and sixth experimental probes of the stability of **1** involved IR characterization and reuse of the WOC after an initial catalytic run, which we carried out under conditions scaled up by a factor of 19 relative to run 1 in Table 2. After the reaction was complete, we saturated the solution with $[Ru(bpy)_3]^{2+}$, which acts as a counterion for complex **1**, resulting in its precipitation. The infrared spectrum of the precipitate showed the characteristic peaks of **1**, a B-type sandwich polytungstate, $[Co_4(H_2O)_2(PW_9O_{34})_2]^{10-}$, at 1037, 939, 882, and 767 cm^{-1} (fig. S6), indicating that the POM framework remains intact after catalysis. For simplicity, we assumed a 1:1 ratio of the $[Ru(bpy)_3]^{2+}$ and **1** in the precipitate and assigned the molecular formula of the precipitate to be **$Na_8Ru(bpy)_3$-1**. Applying the corresponding molecular weight, we used ~0.0032 mM **$Na_8Ru(bpy)_3$-1** as catalyst in the reaction of $[Ru(bpy)_3]^{3+}$ with water in pH = 8 NaPi buffer in the presence of bpy. This reaction gave an O_2 yield of 49.3% and a TON of 58 per **1**, exactly reproducing the activity of pure crystalline **Na_{10}-1** (run 2, Table 2).

The seventh argument for the stability of **1** during catalysis is voltammetric behavior demonstrating that catalytic activity of the active species is retained after turnover. Specifically, we document an electrochemical-chemical mechanism involving **1**: in absence of **1**, a conventional voltammogram was observed for the $[Ru(bpy)_3]^{3+}$/$[Ru(bpy)_3]^{2+}$ couple; however, upon addition of **1**, an increased anodic current peak and a decreased cathodic current peak were observed for this couple (Fig. 2B). This indicates the rapid reduction of $[Ru(bpy)_3]^{3+}$ by **1** followed by reduction of the oxidized **1** by water. The observed catalytic current increased with catalyst concentration (*24*). In addition, Fig. 2B compares the current for a freshly prepared solution of $[Ru(bpy)_3]^{2+}$ and **1** (green line) with that for a solution that has already undergone catalytic chemical reduction of an equivalent amount of $[Ru(bpy)_3]^{3+}$ by **1** (blue line). These two catalytic currents match, implying that there is no evident catalyst deactivation and that the concentration of **1** remains constant after catalysis. In contrast, the same cyclic voltammetric experiment using $Co(NO_3)_2$ in place of **1** showed a marked decrease in the catalytic water oxidation current for the solution after chemical water oxidation when compared with that of an analogous solution containing unreacted $[Ru(bpy)_3]^{2+}$ and $Co(NO_3)_2$ (fig. S7). Once again, this finding is consistent with aqueous cobalt hydrolyzing and condensing to hydroxide/oxide particles under oxidative conditions, decreasing the effective catalyst concentration.

Computational studies of the electronic structure of **1** provide additional support for the oxidative stability of the polytungstate ligands. The four highest occupied molecular orbitals (HOMOs) of a high-spin ground state **1** are mostly cobalt core orbitals, and there is almost no involvement of tungstate orbitals (fig. S8). These findings indicate that the polytungstate ligands are unlikely to participate in the water oxidation reaction and should be effectively inert under catalytic conditions.

Our reporting of this catalyst establishes d-electron–transition metal oxide clusters stabilized by robust polydentate POM ligands as a compelling class of self-assembling inorganic complexes capable of catalyzing fast water oxidation in a homogeneous medium. This prompts the examination of other POM-stabilized multi–

Table 2. The effect of bpy on the catalytic water oxidation activity of **1** and $Co(aq)^{2+}$. Dashed entry indicates not applicable.

Run	Complex	Complex concentration (mM)	bpy (mM)	Buffer	TON	O_2 yield (%)
1	**1**	0.0032	0	pH = 8 NaPi	78.1	66.7
2	**1**	0.0032	0.3012	pH = 8 NaPi	56	48
3	$Co(NO_3)_2$	0.013*	0.3012	pH = 8 NaPi	0	0
4	$Co(NO_3)_2$	0.060†	0.3012	pH = 8 NaPi	0.2	<4
5	$Co(NO_3)_2$	0.013	0	pH = 8 NaPi	23.4	80
6	No catalyst	–	0	pH = 8 NaPi	0	0
7	**1**	0.0032	0	pH = 6.2 NaPi/phthalic acid‡	0	0
8	$Co(NO_3)_2$	0.013	0	pH = 6.2 NaPi/phthalic acid	10	35
9	**1**	0.0032	0.135	pH = 8 NaPi	70.3	60
10	**1** (aged)§	0.0032	0.135	pH = 8 NaPi	71.2	60.8
11	$Co(NO_3)_2$ (aged)§	0.013	0	pH = 8 NaPi	9.8	33.6
12	CoO‖	0.0032	0	pH = 8 NaPi	0	0

*Same theoretical cobalt concentration as 0.0032 mM **1**. †Same solid mass as 0.0032 mM **1**. ‡A mixed buffer of 30 mM NaPi and 30 mM phthalic acid at pH = 6.2 was used. §A 1 mM stock solution in 30 mM pH = 8 NaPi was left for 72 hours before use. ‖Not soluble, suspension obtained after 10 min of sonication.

transition-metal oxide cluster molecules involving both other metals (e.g., Fe and Mn) and new POM ligands as candidate WOCs. Moreover, the identification of a molecular Co-based WOC may allow further investigation of its mechanism of action, providing a basis for the understanding of Co-based water oxidation catalysis in general. In addition, **1** may serve as a template for future optimizations of all-inorganic WOCs as well as their incorporation into water splitting systems. No photosensitizers were used in this report. Although $[Ru(bpy)_3]^{3+}$ was used as a stoichiometric oxidant in this study in order to demonstrate the water oxidation activity of **1**, it is ultimately desirable to use solar power to accomplish water oxidation. The apparently straightforward use of $[Ru(bpy)_3]^{2+}$ as a photosensitizer, however, might not be optimal given the oxidative instability of this complex.

References and Notes

1. J. Chow, R. J. Kopp, P. R. Portney, *Science* **302**, 1528 (2003).
2. N. S. Lewis, D. G. Nocera, *Proc. Natl. Acad. Sci. U.S.A.* **103**, 15729 (2006).
3. V. Balzani, A. Credi, M. Venturi, *ChemSusChem* **1**, 26 (2008).
4. R. Eisenberg, H. B. Gray, *Inorg. Chem.* **47**, 1697 (2008).
5. V. Y. Shafirovich, N. K. Khannanov, V. V. Strelets, *Nouv. J. Chim.* **4**, 81 (1980).
6. A. Harriman, I. J. Pickering, J. M. Thomas, P. A. Christensen, *J. Chem. Soc., Faraday Trans. I* **84**, 2795 (1988).
7. G. L. Elizarova, G. M. Zhidomirov, V. N. Parmon, *Catal. Today* **58**, 71 (2000).
8. M. W. Kanan, D. G. Nocera, *Science* **321**, 1072 (2008); published online 31 July 2008 (10.1126/science.1162018).
9. W. J. Youngblood *et al.*, *J. Am. Chem. Soc.* **131**, 926 (2009).
10. P. K. Ghosh, B. S. Brunschwig, M. Chou, C. Creutz, N. Sutin, *J. Am. Chem. Soc.* **106**, 4772 (1984).
11. I. A. Weinstock *et al.*, *Nature* **414**, 191 (2001).
12. F. Jiao, H. Frei, *Angew. Chem. Int. Ed.* **48**, 1841 (2009).
13. S. W. Gersten, G. J. Samuels, T. J. Meyer, *J. Am. Chem. Soc.* **104**, 4029 (1982).
14. T. Wada, K. Tsuge, K. Tanaka, *Angew. Chem. Int. Ed.* **39**, 1479 (2000).
15. J. Limburg *et al.*, *J. Am. Chem. Soc.* **123**, 423 (2001).
16. J. K. Hurst, *Coord. Chem. Rev.* **249**, 313 (2005).
17. R. Zong, R. P. Thummel, *J. Am. Chem. Soc.* **127**, 12802 (2005).
18. J. T. Muckerman, D. E. Polyansky, T. Wada, K. Tanaka, E. Fujita, *Inorg. Chem.* **47**, 1787 (2008).
19. R. Brimblecombe, G. F. Swiegers, G. C. Dismukes, L. Spiccia, *Angew. Chem. Int. Ed.* **47**, 7335 (2008).
20. S. Romain, F. Bozoglian, X. Sala, A. Llobet, *J. Am. Chem. Soc.* **131**, 2768 (2009).
21. S. W. Kohl *et al.*, *Science* **324**, 74 (2009).
22. J. F. Hull *et al.*, *J. Am. Chem. Soc.* **131**, 8730 (2009).
23. H. Kunkely, A. Vogler, *Angew. Chem. Int. Ed.* **48**, 1685 (2009).
24. Y. V. Geletii *et al.*, *Angew. Chem. Int. Ed.* **47**, 3896 (2008).
25. A. Sartorel *et al.*, *J. Am. Chem. Soc.* **130**, 5006 (2008).
26. Y. V. Geletii *et al.*, *J. Am. Chem. Soc.* **131**, 7522 (2009).
27. Materials and methods are available as supporting material on *Science* Online.
28. L. Ruhlmann, L. Nadjo, J. Canny, R. Contant, R. Thouvenot, *Eur. J. Inorg. Chem.* **2002**, 975 (2002).
29. T. J. R. Weakley, H. T. Evans Jr., J. S. Showell, G. F. Tourné, C. M. Tourné, *J. Chem. Soc. Chem. Commun.* **4**, 139 (1973).
30. F. H. Burstall, R. S. Nyholm, *J. Chem. Soc.* **1952**, 3570 (1952).
31. J. Baes, F. Charles, R. E. Mesmer, *The Hydrolysis of Cations* (Wiley, New York, 1976).

32. We thank the U.S. Department of Energy through grant DE-FG02-03ER-15461 for support of this work. C.B. thanks the French Ministère de l'Éducation Nationale, de la Recherche, et de la Technologie for a research fellowship. Additional details on the crystal structure investigations may be obtained from the Fachinformationszent Wrum Karlsruhe, 76344 Eggenstein-Leopoldshafen, Germany, on quoting registry number CSD-421465.

Supporting Online Material

www.sciencemag.org/cgi/content/full/science.1185372/DC1
Materials and Methods
Figs. S1 to S11
References

1 December 2009; accepted 25 February 2010
Published online 11 March 2010;
10.1126/science.1185372
Include this information when citing this paper.

Oxoboryl Complexes: Boron–Oxygen Triple Bonds Stabilized in the Coordination Sphere of Platinum

Holger Braunschweig,* Krzysztof Radacki, Achim Schneider

Monomeric oxoboranes have hitherto been detected only as short-lived species in gas-phase or low-temperature matrix experiments. Here, we report formation of the oxoboryl complex *trans*-$[(Cy_3P)_2BrPt(B{\equiv}O)]$ (Cy being cyclohexyl) by means of reversible liberation of trimethylsilylbromide from the boron–bromine oxidative addition product of dibromo (trimethylsiloxy)borane and $[Pt(PCy_3)_2]$ in room-temperature toluene solution. The platinum complex is inert toward oligomerization, even under photolytic conditions and at elevated temperatures. The bromide was substituted by thiophenolate, and spectral parameters of both products as well as results of computational and x-ray diffraction studies are in agreement with the formulation of a triple bond between boron and oxygen. The boron–oxygen distance of 120.5(7) picometers shows a bond shortening of 7.2% as compared with a double bond, which is similar to the shortening observed in carbon–carbon analogs.

The element boron is popularly known for its unique propensity to participate in multicenter bonds to compensate its intrinsic electron-deficiency. Thus, various structural motifs have been described that exhibit boron with coordination numbers higher than its actual valency (*1*). However, not least because of the importance of boranes in organic syntheses (*2*) the chemistry of boron-containing compounds featuring exclusively classical, electron-precise bonds has been established during the last century, and therefore examples with tricoordinate boron likewise are plentiful. Though species with dicoordinate boron are considerably more unusual, different strategies to prepare and stabilize those compounds have been applied successfully (*3*–*8*).

Since boroxine ($H_3B_3O_3$) could be identified as the product of highly energetic reactions of different ternary systems (*9*), numerous attempts have been undertaken to synthesize its monomeric counterparts, namely oxoboranes (XBOs). However, those species could be detected only in either gas-phase (*10*–*13*) or low-temperature matrix isolation studies (*14*–*19*). Further evidence for the existence of those compounds was obtained through different trapping experiments (*20*–*22*) or nuclear magnetic resonance (NMR) spectroscopic observation of the corresponding Lewis base adduct (*22*). Microwave (*11*) and infrared (IR) data (*14*–*19*) suggest a very strong linkage of boron and oxygen; because of the similarity of the photoelectron spectrum of H_3CBO with the isoelectronic H_3CCN molecule (*12*, *13*), the B–O linkage was described by a triple bond. Nevertheless, probably because of the polar nature of this bond, the highly reactive monomers readily undergo cyclooligomerization even at temperatures of approximately 50 K (*19*, *23*) and an x-ray structural elucidation could not be performed.

Commonly, kinetic lability of low-valent species can be compensated by use of bulky substituents that inhibit bimolecular attack, as was successfully demonstrated by the preparation of a stable disilyne (*24*). In contrast, XBOs contain-

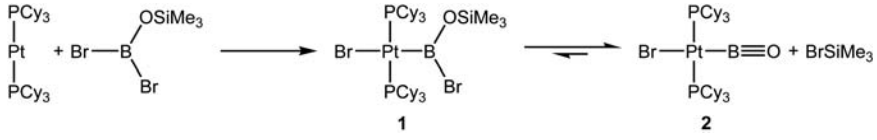

Scheme 1. Preparation of *trans*-$[(Cy_3P)_2BrPt(BO)]$ (**2**).

Institut für Anorganische Chemie, Julius-Maximilians-Universität Würzburg, Am Hubland, 97074 Würzburg, Germany.

*To whom correspondence should be addressed. E-mail: h.braunschweig@mail.uni-wuerzburg.de

A Novel Brand of Water Oxidation Catalysts: the Groundwork for a New Generation

John DiMeglio

Department of Chemistry and Biochemistry, University of Delaware, Newark DE, 19716

Inspired by the global shift to renewable energy sources, there has been much effort to design viable water oxidation catalysts (WOCs). Previous WOCs have been plagued with instabilities or based on rare and expensive metals. Herein an analysis of a novel WOC based on earth abundant metals is described. This WOC was characterized via CV, ^{31}P NMR, UV-Vis and IR spectroscopy. Further studies are suggested for the design and use of this new brand of WOC.

Renewable energy has been a scientific and politic hot-topic for the past several decades. Inspired by the ever rising CO_2 levels in the atmosphere and our dependence on foreign oil , science has made strides toward alternative energy sources. Many of these advances have been in the area of solar energy. Nevertheless, we still lack a reliable way to store energy captured by the sun.[1] Plants have perfected this, however by storing this energy in the form of chemical bonds via photosynthesis.[2] Inspired by this process, chemists have develop a series of water oxidation catalysts (WOCs). These WOCs are intended to use solar radiation to oxidize water to H_2 and O_2(Scheme 1). Recently a novel type of WOC, composed of abundant metals has been reported by Yin and co workers.[3] To demonstrate the significance of this discovery, a brief history of WOC research is discussed.

$$H_2O \rightleftharpoons O_2 + 4H^+ + 4e^-$$

$$4H^+ + 4e^- \rightleftharpoons H_2$$

Scheme 1. The two half reactions for the oxidation of water to oxygen and hydrogen.

Fujishima and Honda were the first to report conditions for the photo-electrochemical oxidation of water. Using a TiO_2 electrode and a potential of nearly -0.5 V, they observed the evolution of $O_{2(g)}$ signifying water oxidation.[4] However, since then more efficient pathways for water oxidation have been uncovered, included a series of homogeneous and heterogeneous catalysts. The former has the advantage of being easier to study and more efficient, while the ladder is typically cheaper and more stable.[3]

Some examples of homogeneneous WOCs include the $[(bpy)_2(H_2O)Ru\text{-}O\text{-}Ru(H_2O)(bpy)_2]$ system that oxidized water via the pathway shown (Scheme 2). However, this dimer is unstable and after a few cycles a loss of catalytic activity as well as its distinctive blue color is observed.[5] Newer homogeneous systems include the $[Ru^{III}_2(O)_2(3,6\text{-}^tBu_2qui)_2(btpyan)]^{4+}$ system (where 3,6-^{t}Bu$_2$qui =3,6-di-*tert*-butyl-1,2-semiquinone and btpyan = 1,8-bis(2,2‘:6‘,2‘‘-terpyridyl)anthracene) which have been shown to have promote the catalytic oxidation of water.[6] However, this complex and several other similar are limited by the use of organic ligands, which are thermodynamically unstable in the presence of O_2.[3]

$$4CE(IV) + 2H_2O \xrightarrow{\text{cat.}} 4Ce(III) + O_2 + 4H^+$$

Scheme 2. Oxidation of water proposed by Grensten, Samuels, and Myer, where cat. = $[(bpy)_2(H_2O)Ru\text{-}O\text{-}Ru(H_2O)(bpy)_2]$.[5]

Heterogeneous catalysts, however, are much more stable under these conditions. Examples include the self-assembling Co, P, and K based catalyst reported by Kanan and Nocera, as well as $IrO_2\bullet nH_2O$ based nanoparticles reported by Youngblood and coworkers.[7,8] Drawbacks to these systems include the inherit inefficiency of heterogeneous catalysis as well as the tendency for catalysts of these types to deactivate by surface poisoning and aggregation.[3]

It is clear that the most efficient WOC must have the activity and selectivity of a homogeneous catalyst with the efficiency and durability of a heterogeneous catalyst. With this in mind a homogeneous polyoxometalate (POM) WOC with oxidatively stable polytungstate ligands around a Ru_4O_4 core has been reported.[9] Although this POM WOC has demonstrated the viability of homogeneous catalysts, it was limited by the rarity and expense of ruthenium.

An effort was therefore put forth to investigate potential POM WOC based on abundant metals. Yin and coworkers were the first to publish the use of $[Co_4(H_2O)_2(PW_9O_{34})_2]^{10-}$ (**1**, Figure 1) as a WOC.[3] The synthesis of this complex is trivial and involves a one-pot reaction of Co^{2+}, phosphate, and tungstate salts as previously reported by Weakley *et al.*[10] Other POM based Co complexes were made(**2-8**), however none of them showed reactivity toward water under oxidizing conditions (Table 1). Modeling studies have shown that **1** has a unique Co core structure that **3-8** lacked. Unfortunately, **2** which shares this core structure is unstable at the desired pH range of 7.5-8.0.

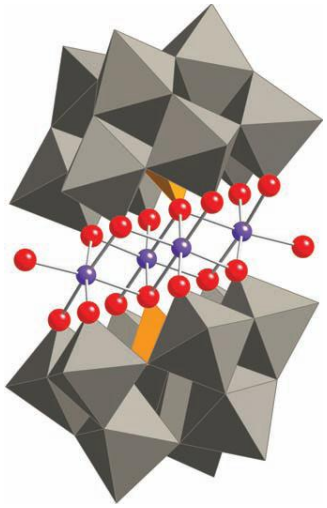

Figure 1. X ray structure of **1**, highlighting the Cu_4O_{16} core with a ball and stick representation and the POM ligands as polyhedrons.[3]

Table 1. List of all POM based complexes investigated by Yin and co-workers. these reactions were run in a 30 mM NaPi buffer, initial pH = 8.0, 1.5 mM $[Ru(bpy)_3](ClO_4)_3$, **1** was run at a complex concentration of 0.032 mM, while **2**-**8** were run at 0.0064 mM complex concentration.[3]

Complex	TON	O_2 yield (%)
$[Co_4(H_2O)_2(PW_9O_{34})_2]^{10-}$ (**1**)	75	64
$[Co_4(H_2O)_2(P_2W_{15}O_{56})_2]^{10-}$ (**2**)	0	0
$[Co(H_2O)PW_{11}O_{39}]^{5-}$ (**3**)	0	0
$[Co(H_2O)SiW_{11}O_{39}]^{6-}$ (**4**)	0	0
$[Co_3(H_2O)_3(PW_9O_{34})_2]^{12-}$ (**5**)	0	0
$[Co_3(H_2O)_3SiW_9O_{37}]^{10-}$ (**6**)	0	0
$[WCo_3(H_2O)_2(CoW_9O_3)_2]^{12-}$ (**7**)	0	0
$[Co_7(H_2O)_2(OH)_2P_2W_{25}O_{94}]^{16-}$ (**8**)	0	0

These POM systems were evaluated by mixing the catalyst with the strong stoichiometric oxidant tris(2,2'-bipyridyl)triperchlororuthenium(III) ($[Ru(bpy)_3]^{3+}$) (Scheme 3). Aliquots were taken from the head space of this reaction and analyzed using GC. It was found that only **1** showed propensity to oxidize water to give an O_2 yield (4n O_2/n $Ru(bpy)_3$) of 64 % and a turnover number (TON, n O_2/n catalyst) of 75. The O_2 yield is limited by the $Ru(bpy)_3$ because of a competing reaction where the bipyridyl ligand gets oxidized. Likewise, the TON is limited by the amount of $Ru(bpy)_3$, since this reagent is stoichiometric. Once it was determined that **1** was a potential WOC, further analytical information was obtained via CV, ^{31}P NMR, UV-Vis and IR spectroscopy.[3]

$$4[Ru(bpy)_3]^{3+} + 2H_2O \xrightarrow{\text{cat.}} 4[Ru(bpy)_3]^{2+} + 4H^+ + O_2$$

Scheme 3. Oxidation scheme proposed by Yin and co workers, where cat. = $[Co_4(H_2O)_2(PW_9O_{34})_2]^{10-}$.

Cyclic voltamitry (CV) is a common electrochemical experiment where the oxidation and reduction potentials of a complex are evaluated by varying the potential across a working and reference electrode, while the current of the solution is measured. A third electrode, a reference is required to standardize these results to NHE.[11] With this electrochemical technique in hand it was determined that **1** operates at a low-over potential for the water oxidation by examining the reductive wave corresponding to the catalytic current. (Figure 2) It was further shown that upon addition of **1** to a solution of $[Ru(bpy)_3]^{3+}$, there is an increase in anodic current and a decrease in cathoic current. Further, as the concentration of **1** increases, the greater the change in anodic and cathodic currents. (Figure 3) These observations support that upon reduction of $[Ru(bpy)_3]^{3+}$ by **1**, there is a reduction of the oxidized form of **1** by water.

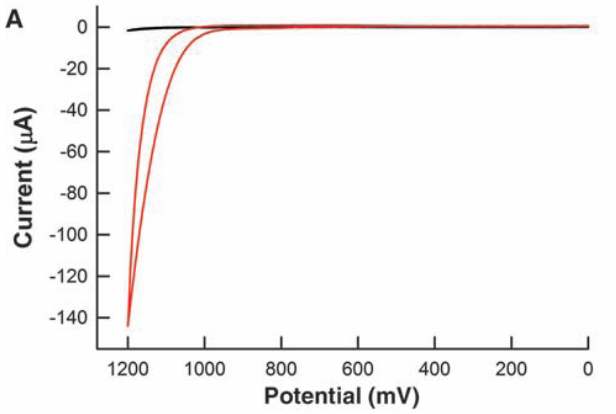

Figure 2. CV of a 50 mM sodium phosphate solution without **1** (black) and with 1 mM **1** (red).[3]

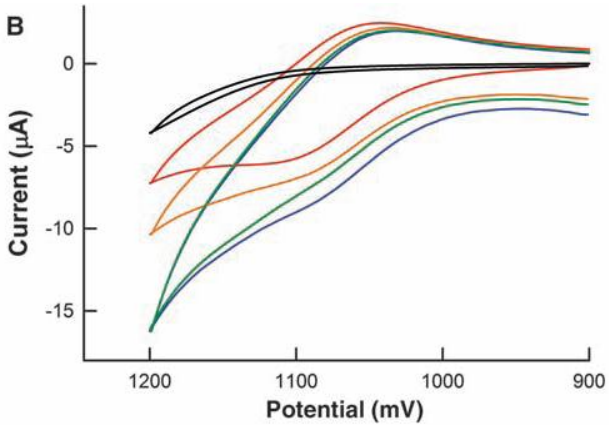

Figure 3. CV of 0.857 mM $[Ru(bpy)_3]^{2+}$ alone (red), 3.2 μM **1** alone (black), 0.857 mM $[Ru(bpy)_3]^{2+}$ with 1.6 μM **1** (yellow) or 3.2 μM **1** (green), and a postreaction solution of 0.857 mM $[Ru(bpy)_3]^{3+}$ and 3.2 μM **1** (blue).[3]

Since stability was a major issue for past WOCs an extensive effort was put forth to evaluate the longevity of **1** under various conditions. It was shown that over one month there was no change in the ^{31}P NMR or UV-Vis spectra of **1** at a pH = 8. In another experiment, a molar excess of 2,2'-bupridine (bpy), a known inhibitor that reacts with free Co^{2+} ions was added to a solution of **1**. After little change to its catalytic activity it is believed that there was minimal $Co^{2+}_{(aq)}$ ions in solution. Third, a ^{13}P NMR spectrum of a post reaction solution displayed no unexpected resonances. Further, **1** was precipitated out of a post reaction solution and characterized with IR spectroscopy. This solid was shown to retain its catalytic ability and via the presence

of characteristic peaks, have its POM framework intact. Further CV experiments demonstrate that over time there is little change in the oxidation/reduction potentials for **1**. (Figure 3) Lastly a computational analysis determined that four highest occupied molecular orbitals (HOMOs) for the high-spin ground state of **1** have very little contribution from the POM orbitals. (Figure 4). Therefore, they are likely to be inert under catalytic conditions.

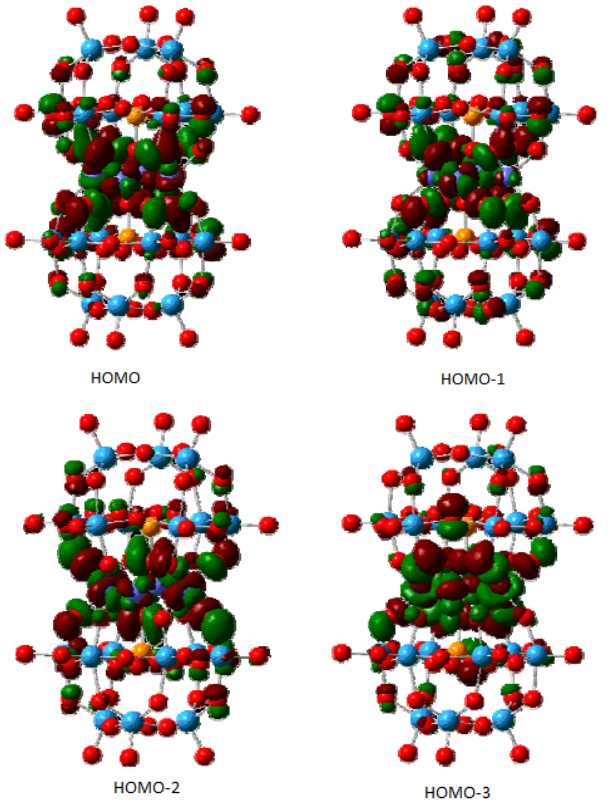

Figure 4. RI-PBE/PCM calculations for the four HOMO orbitals of **1**, demonstrating the small contribution of the POM orbitals.

In conclusion Yin and coworkers have characterized a POM WOC that is stable under a variety of conditions and composed of abundant earth metals. However, further research is still needed for the practical use of such catalysts. In addition it would also be useful to study the efficiency of this catalysts under electrical potential (i.e. from a PV cell) rather than the chemical potential supplied by $Ru(bpy)_3$. Further studies are also needed to fully under the mechanism of this reaction and perhaps allow the design of future POM WOC.

Refrences

(1) Chow, J.; Kopp, J. R.; Portney, P. R. *Science* **2003**, *302*, 1528.
(2) Hall, D. O.; Rao, K. K. Importance and Role of Photosynthesis. In *Photosynthesis*, 6, Press Syndicate of the University of Cambridge: Cambridge, United Kingdom, 2001; 2.
(3) Yin, Q *et al*., *Science* **2010**, *328*, 342.
(4) Fujishima, A.; Honda, K. *Nature* **1972**, *238*, 37.
(5) Shafirovich, V.Y.; Khannanov, N. K.; Strelets, V. V. *Nouv. J. chim*. **1980**, *4*, 81.
(6) Wada, T.; Tsuge, K.; Tanaka, K. *Inorg. chem.* **2001**, *40*, 329.
(7) Kanan, M. W.; Nocera, D. G. *Science* **2008**, *321*, 1072.
(8) Jiao, F.; Frei, H. *Angew. Chem. Int. Ed.* **2000**, *39*, 1479.
(9) Geletii, Y. V. *et al*. *JACS* **2009**, *131*, 7522
(10) Weal;ey, T. J. R.; Evans Jr., H. T.; Showell, J. S.; Tourné, C. M. *J. Chem. Soc. Chem. Commun.* **1973**, *4*, 139.
(11) Compton, R. G.; Banks, C.E. Cyclic Voltammetry at Macroelectrodes. In Understanding Voltammetry, World Sci. Publishing co. Hackensack, NJ, 2001; 107.

Stable Magnesium(I) Compounds with Mg-Mg Bonds

Shaun P. Green,[1,2] Cameron Jones,[1]* Andreas Stasch[1]*

The chemistry of the group 2 metals (beryllium, magnesium, calcium, strontium, and barium) is dominated by the +2 oxidation state. Here, we report the reductions of two magnesium(II) iodide complexes with potassium metal in toluene, leading to thermally stable magnesium(I) compounds, (L)MgMg(L) (where L is $[(Ar)NC(NPr^i_2)N(Ar)]^-$ or $\{[(Ar)NC(Me)]_2CH\}^-$, Ar is 2,6-diisopropylphenyl, Me is methyl, and Pr^i is isopropyl) in moderate yields. The results of x-ray crystallographic and theoretical studies are consistent with central Mg_2^{2+} units that have single, covalent magnesium-magnesium bonding interactions with 2.8508 ± 0.0012 (standard deviation) and 2.8457 ± 0.0008 angstrom bond lengths, respectively, and predominantly ionic interactions with the anionic ligands (L).

Magnesium is ubiquitous in living organisms, Earth's crust, and seawater (*1*). Like the other alkaline earth metals (group 2 metals), magnesium is present in all its known stable compounds in the +2 oxidation state. It plays a major role in nature as the central ion in chlorophyll because its redox-inert character is important for the charge separation in photosynthesis (*1*). The reduction of other metal ions has involved the formation of direct metal-metal bonds. For example, homonuclear compounds, RM^IM^IR (where R represents an organic or similar substituent and M is a metal), of *p*- or *d*-block metals have been prepared with the metal centers formally in the +1 oxidation state. Two recent landmark advances in this field are the synthesis of a chromium(I) dimer [L'CrCrL', where L' is $C_6H_3(C_6H_3Pr^i_2\text{-}2,6)_2$-2,6 and Pr^i is isopropyl] containing a metal-metal quintuple bonding interaction (*2*) and the synthesis of a zinc(I) compound, $(\eta^5\text{-}C_5Me_5)ZnZn(\eta^5\text{-}C_5Me_5)$ (where Me is methyl) (*3*). Since the report on the latter, the chemical similarities between zinc and the lighter group 2 metals have prompted theoreticians to examine the possibility of preparing complexes of the type RMMR (where M is Be, Mg, or Ca), with the conclusion that such reduced *s*-block compounds should be stable given the correct choice of ligand (*4*–*6*). A number of magnesium(I) compounds, for example, HMgMgH, have previously been studied under, for example, matrix isolation conditions (*7*), and mononuclear compounds, for example, $Mg^I(NC)$, have been detected in circumstellar clouds (*8*). Moreover, the formation of synthetically important Grignard reagents, RMgX (where X is a halide), has been proposed to proceed via magnesium(I) compounds of the type RMgMgX (*9*). In addition, related cluster compounds, RMg_4X, of undetermined structure have been investigated by using mass spectrometry experiments (*10*). However, no examples of stable molecular group 2 metal(I) compounds have been isolated.

In the past 2 years, we have developed and used the bulky guanidinate ligands, $[(Ar)NC(NR'_2)N(Ar)]^-$ [where Ar is 2,6-diisopropylphenyl and R' is isopropyl (Priso) or cyclohexyl (Giso)] to access complexes of *p*-block elements in the +1 oxidation state, for example, Ga^I(Giso) (*11*) and $[Ge^I(Priso)]_2$ (*12*). The ability of these sterically hindered, N,N'-chelating ligands to stabilize low oxidation state complexes is strikingly similar to that of bulky examples from the well-studied β-diketiminate class of ligand, for example, $\{[(Ar)NC(Me)]_2CH\}^-$ (Nacnac) (*13*). Here, we report the use of both Priso and Nacnac ligands to prepare molecular magnesium(I) compounds that contain structurally characterized magnesium-magnesium bonds. We examined the nature of the bonding in these compounds by theoretical studies and also carried out preliminary reactivity studies.

The new magnesium(II) complex, $(Priso)Mg(\mu\text{-}I)_2Mg(OEt_2)(Priso)$ (OEt_2 is diethyl ether), was prepared as a precursor to one of the target magnesium(I) compounds (*14*). This was spectroscopically characterized, and its x-ray crystal structure was determined (fig. S2). Reduction of $(Priso)Mg(\mu\text{-}I)_2Mg(OEt_2)(Priso)$ and the known compound, $MgI(OEt_2)(Nacnac)$ (*15*), with an excess of potassium metal in toluene over 24 hours led to the crystalline magnesium(I) compounds $[Mg(Priso)]_2$ **1** (colorless, yield of 28.5%) and $[Mg(Nacnac)]_2$ **2** (yellow, yield of 56.5%), respectively, after workup (Fig. 1) (*14*). Although both compounds are air- and moisture-sensitive, they are thermally stable and fully decompose only at temperatures in excess of 170°C and 300°C, respectively, the former with deposition of elemental magnesium. The x-ray crystal structure of each compound was obtained (Figs. 2 and 3) (*16*). Both possess distorted trigonal planar coordination geometries with delocalized ligand backbones. Although their Mg-N distances [2.0736(10) (or ±0.0010) Å for **1** and a mean value of 2.060 Å for **2**; the number in parentheses indicates the standard deviation] are in the known range for Mg-N bonds (*17*), they are longer than all such bonds in complexes in which β-diketiminates ligate three-coordinate magnesium(II) centers. Despite the paucity of Mg-Mg bonds for comparison, the lengths of those interactions in **1** and **2** are similar [2.8508(12) Å and 2.8457(8) Å, respectively]. Although these distances are considerably shorter than those in diatomic or elemental magnesium (3.890 Å and 3.20 Å, respectively) (*18*, *19*), they are longer than the sum of two magnesium covalent radii (2.72 Å) (*19*). The distances are, however, in the range of previously

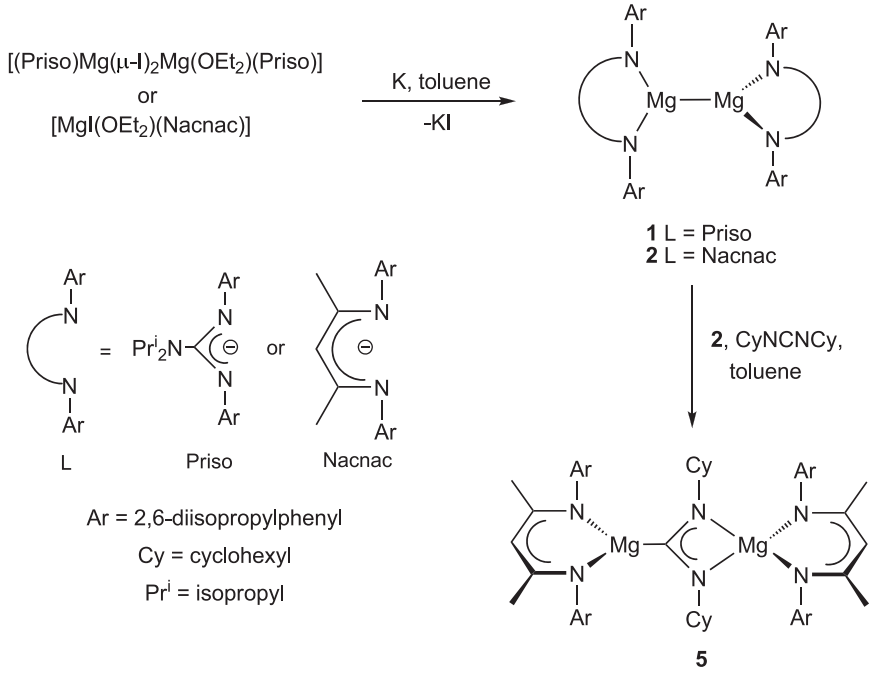

Fig. 1. Formation of compounds **1**, **2**, and **5**.

[1]School of Chemistry, Monash University, Post Office Box 23, Victoria 3800, Australia. [2]School of Chemistry, Main Building, Cardiff University, Cardiff CF10 3AT, UK.

*To whom correspondence should be addressed. E-mail: cameron.jones@sci.monash.edu.au (C.J.); andreas.stasch@sci.monash.edu.au (A.S.)

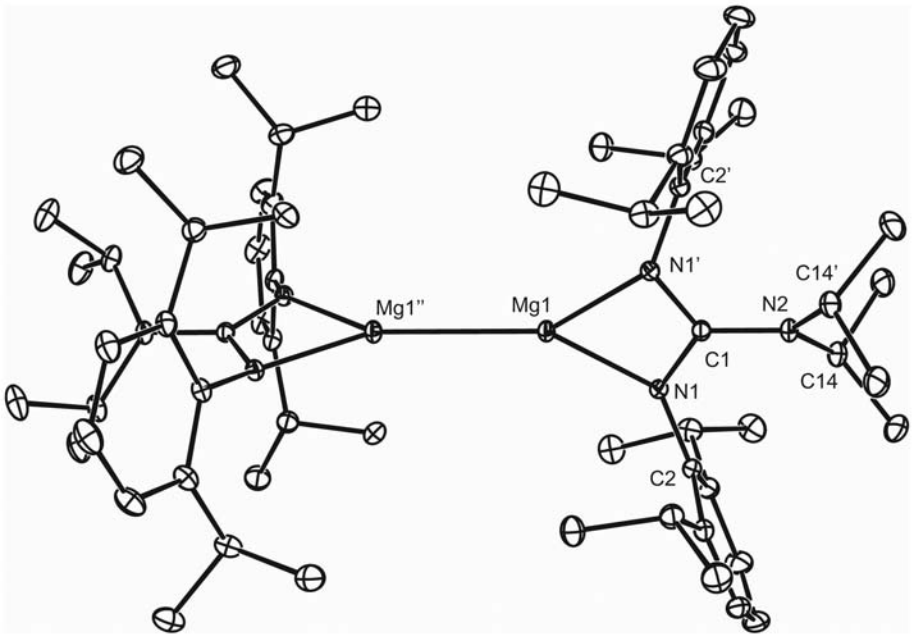

Fig. 2. Molecular structure of **1** (hydrogen atoms omitted, ellipsoids shown at the 20% probability level). Selected bond lengths and angles: Mg(1)-Mg(1)" 2.8508(12) Å, Mg(1)-N(1) 2.0736(10) Å, N(1)-C(1) 1.3497(12) Å, N(2)-C(1) 1.389(2) Å; N(1)-Mg(1)-N(1)' 65.54(5)°, N(1)-C(1)-N(1)' 112.53(13)°, N(1)-Mg(1)-Mg(1)" 147.23(3)°.

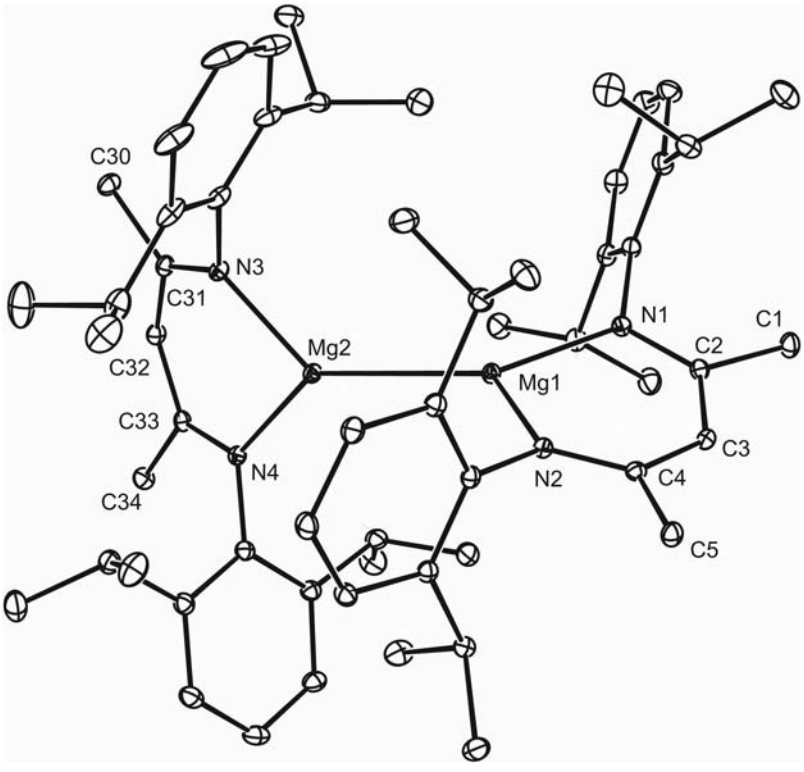

Fig. 3. Molecular structure of **2** (hydrogen atoms omitted, ellipsoids shown at the 20% probability level). Selected bond lengths and angles: Mg(1)-Mg(2) 2.8457(8) Å, Mg(1)-N(2) 2.0547(13) Å, Mg(1)-N(1) 2.0643(13) Å, N(1)-C(2) 1.3354(18) Å, C(1)-C(2) 1.5135(19) Å, Mg(2)-N(3) 2.0571(13) Å, Mg(2)-N(4) 2.0656(12) Å, N(2)-C(4) 1.3251(17) Å, C(2)-C(3) 1.4041(19) Å, N(3)-C(31) 1.3269(18) Å, C(3)-C(4) 1.4041(19) Å, N(4)-C(33) 1.3368(17) Å, C(4)-C(5) 1.5116(19) Å, C(30)-C(31) 1.514(2) Å, C(31)-C(32) 1.409(2) Å, C(32)-C(33) 1.398(2) Å, C(33)-C(34) 1.5157(19) Å; N(2)-Mg(1)-N(1) 91.78(5)°, N(2)-Mg(1)-Mg(2) 128.50(4)°, N(1)-Mg(1)-Mg(2) 139.35(4)°, N(3)-Mg(2)-N(4) 91.80(5)°, N(3)-Mg(2)-Mg(1) 129.65(4)°, N(4)-Mg(2)-Mg(1) 138.24(4)°.

calculated Mg-Mg separations in theoretical molecular compounds, for example, the cyclopentadienyl magnesium(I) dimer, $(C_5H_5)MgMg(C_5H_5)$ [2.776 Å (B3LYP calculations) (*4*) and 2.809 Å (BP86) (*5*)], the 2,6-diphenylphenyl magnesium(I) dimer, $\{[C_6H_3(C_6H_5)_2\text{-}2,6]MgMg[C_6H_3(C_6H_5)_2\text{-}2,6]\}$ [2.838 Å (BP86) (*6*)], and HMgMgH [2.862 Å (B3LYP) (*4*) and 2.884 Å (BP86) (*5*)]. It should also be noted that two nonbonded Mg···Mg interactions in one cluster compound, $[Mg(THF)(\mu\text{-}C_6H_4)]_4$ (THF is tetrahydrofuran) (*20*), are shorter [2.804(2) Å and 2.841(2) Å] than the separations in **1** and **2**.

Considering the relatively long Mg-Mg bonds in **1** and **2**, the possibility that these compounds actually exist as hydride-bridged magnesium(II) dimers, $[Mg(L)(\mu\text{-}H)]_2$ (L is Priso or Nacnac), cannot be overlooked. However, the combined weight of the crystallographic, spectroscopic, theoretical, and chemical evidence discounts this possibility (*vide infra*). First, the heterocycle least squares planes in **1** are orthogonal, whereas compound **2** has close to orthogonal heterocycle planes (dihedral angle is 80.2°) and is isostructural with the related metal(I) dimers, $[M^I(Nacnac)]_2$ [M is Zn (*21*) or Mn (*22*)]. If **1** and **2** were hydride-bridged dimers, their heterocycles would, instead, be expected to be close to coplanar. In addition, in the final difference maps of the structural refinements of both compounds, there were no regions of residual electron density of greater than 0.15 electrons per cubic angstrom close to the Mg-Mg vectors, again suggesting the absence of hydride ligands.

The nuclear magnetic resonance (NMR) spectroscopic data for diamagnetic **1** and **2** are consistent with their proposed formulations. No bridging hydride resonances were observed in the expected chemical shift range in the ^{1}H NMR spectra of the complexes (*23*). In addition, their electron ionization high-resolution accurate mass spectra exhibit molecular ion envelopes with isotopic mass distributions that match well those calculated for the hydride-free complexes (fig. S1). In this respect, the stability of **2** in the gas phase is demonstrated by the fact that it can be sublimed intact at 230°C (circa 10^{-6} mm Hg). The Raman spectra of the compounds display a number of low-frequency absorptions, although none of these can be confidently assigned as arising from Mg-Mg stretching modes. Similarly, little information regarding the structures of the complexes can be obtained from their infrared spectra. Mg-H-Mg stretching absorptions originating from the alternatively formulated complexes, $[Mg(L)(\mu\text{-}H)]_2$, would certainly lie in the fingerprint region (*24*) and would, thus, be difficult to assign due to overlap with low-frequency ligand modes. Because we have not yet been able to prepare authentic samples of $[Mg(L)(\mu\text{-}H)]_2$ by rational routes (*14*), we cannot compare their infrared spectra {and the infrared spectra of their deuterated analogs, $[Mg(L)(\mu\text{-}D)]_2$} with those of **1** and **2**.

In order to examine the nature of the bonding in **1**, density functional theory (DFT) calcula-

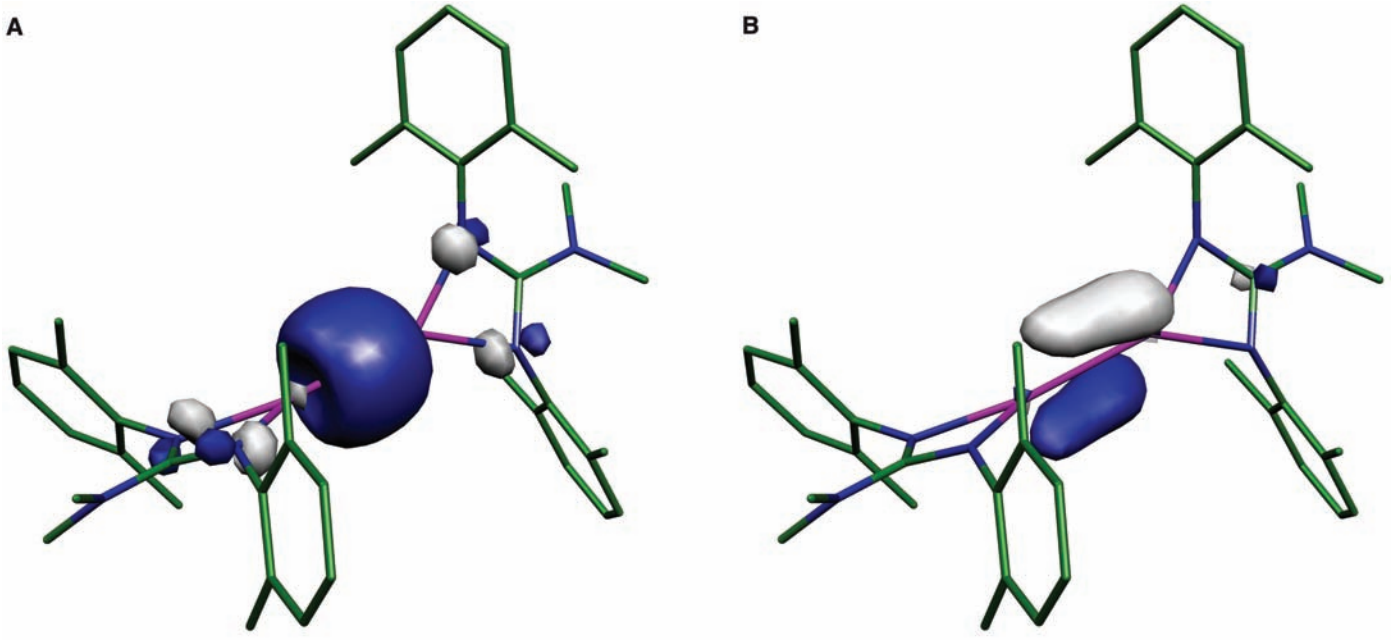

Fig. 4. Representations of (**A**) the HOMO (–4.75 eV) and (**B**) the LUMO (–0.722 eV) of the model system $\{Mg[(Ar'N)_2C(NMe_2)]\}_2$ **3** (Ar' is $C_6H_3Me_2$-2,6).

tions (B3LYP and BP86) (*25*) were carried out on the model complex, $\{Mg[(Ar'N)_2C(NMe_2)]\}_2$ **3** (Ar' is $C_6H_3Me_2$-2,6). The geometry of the optimized structure was found to be in close agreement with that in the crystal structure of **1** (i.e., with effectively orthogonal heterocycle planes) but with slightly underestimated Mg-Mg bond lengths (with B3LYP, 2.828 Å; with BP86, 2.839 Å) and slightly overestimated Mg-N distances (with B3LYP, mean = 2.102 Å; with BP86, mean = 2.114 Å). Figure 4A depicts the highest occupied molecular orbital (HOMO) of the complex, which largely comprises the metal-metal σ-bonding interaction. The two lowest unoccupied orbitals, LUMO (Fig. 4B) and LUMO+1 (fig. S4), are almost degenerate (energy difference of 0.11 eV, 2.6 kcal mol^{-1}) and predominantly encompass metal-metal π-bonding orbitals derived from metal p_x- and p_y-orbital overlaps respectively. A similar arrangement of frontier orbitals has been calculated for $[C_6H_3(C_6H_5)_2$-2,6]ZnZn$[C_6H_3(C_6H_5)_2$-2,6] (*26*). The HOMO-LUMO gap in **3** (4.02 eV, 93.0 kcal mol^{-1}) is comparable with those calculated for both $(C_5H_5)MgMg(C_5H_5)$ (3.87 eV, 89.5 kcal mol^{-1}) (*5*) and $[C_6H_3(C_6H_5)_2$-2,6]ZnZn$[C_6H_3(C_6H_5)_2$-2,6] (4.25 eV, 97.6 kcal mol^{-1}) (*26*). In addition, the results of a natural bonding orbital (NBO) analysis (B3LYP) of the Mg-Mg interaction in **3** indicate a high s-character, single covalent bond (93.2% s-, 6.0% p-, and 0.8% d-character; Wiberg bond index = 0.914), whereas the metal-ligand interactions are predominantly ionic (natural charge for Mg, +0.82 mean, and for N, –0.97 mean). Accordingly, the molecule can be viewed as an anion-stabilized Mg_2^{2+} unit, as has been discussed for other model RMgMgR systems (*4*–*6*).

We were prompted to analyze the theoretical hydride complex, $\{Mg[(Ar'N)_2C(NMe_2)](\mu\text{-}H)\}_2$ **4**, using DFT calculations (B3LYP) for purposes of comparison with **1** and **3**. In contrast to those complexes, the optimized geometry of **4** exhibits coplanar heterocycles, oriented nearly orthogonal to the bridging, symmetrical Mg_2H_2 unit. Scans of the potential energy hypersurface of the less bulky model, $\{Mg[(HN)_2C(NH_2)](\mu\text{-}H)\}_2$, at density functional (B3LYP) and ab initio (MP2) levels of theory, show this conformation to be the global minimum (*14*). Moreover, there are no local minima associated with any conformation of the molecule in which the planes of the magnesium heterocycles are orthogonal or close to orthogonal with each other. Surprisingly, the Mg···Mg separation in **4** at 2.770 Å (Mg-H mean distance = 1.890 Å) is substantially shorter than in **3**, despite a less pronounced metal-metal interaction (Wiberg bond index = 0.307). In this respect, previous theoretical studies have concluded that metal-metal distances in hydride bridged complexes can be shorter than in corresponding hydride-free, metal-metal bonded complexes (*27*). The results of all calculations undertaken are fully consistent with **1** (and by implication **2**) being a magnesium(I) dimer, not a hydride bridged magnesium(II) dimer.

Although **1** and **2** would be expected to be highly reducing, we have found that they do not react with dihydrogen or dinitrogen in toluene, even at elevated temperatures (80°C) or when irradiated with ultraviolet light (λ = 254 nm). The lack of reactivity of the complexes toward dihydrogen is not surprising when it is considered that the closely related addition of H_2 to $[(C_5H_5)MgMg(C_5H_5)]$ [to generate two molecules of $(C_5H_5)MgH$] has been calculated to be an endothermic process (*4*). Surprisingly, exposure of the three-coordinate magnesium centers in **1** and **2** to THF in C_6D_6 solutions does not lead to evidence of THF coordination as judged by ^1H or $^{13}C\{^1H\}$ NMR spectroscopy. However, a weak, transient coordination of THF cannot be ruled out in these experiments on the basis of the results of the reaction of **2** with the carbodiimide CyNCNCy (Cy is cyclohexyl) in toluene at –70°C (Fig. 1). This led to immediate loss of the yellow color of **2** and the isolation of the magnesium magnesioamidinate complex, **5**, after warming the reaction mixture to 20°C (*14*). Presumably, this reaction occurs via an initial coordination of one N-center of the carbodiimide at a magnesium center, followed by a double reduction of the carbodiimide and its concomitant insertion into the Mg-Mg bond of **2** (*28*, *29*). The spectroscopic data for **5** are consistent with the solid-state structure determined by an x-ray crystallographic study (fig. S4). In contrast to the nearly orthogonal Mg(Nacnac) least squares planes in **2**, these planes in **5** are mutually parallel and orthogonal to the CyNCNCy unit. Reaction of the carbodiimide with the alternative hydride-bridged magnesium(II) complex, $[Mg(Nacnac)(\mu\text{-}H)]_2$, would not be expected to give compound **5** but instead C=N bond hydromagnesiation.

References and Notes

1. W. Kaim, B. Schwederski, *Bioinorganic Chemistry: Inorganic Elements in the Chemistry of Life - An Introduction and Guide* (Wiley, Chichester, 1994), chapters 2 and 4.
2. T. Nguyen *et al.*, *Science* **310**, 844 (2005); published online 22 September 2005 (10.1126/science.1116789).
3. I. Resa, E. Carmona, E. Gutierrez-Puebla, A. Monge, *Science* **305**, 1136 (2004).
4. Y. Xie, H. F. Schaefer III, E. D. Jemmis, *Chem. Phys. Lett.* **402**, 414 (2005).
5. A. Velazquez, I. Fernandez, G. Frenking, G. Merino, *Organometallics* **26**, 4731 (2007).
6. M. Westerhausen *et al.*, *Chem. Eur. J.* **13**, 6292 (2007).
7. X. Wang, L. Andrews, *J. Chem. Phys. A* **108**, 11511 (2004).
8. S. Petrie, *Aust. J. Chem.* **56**, 259 (2003).

9. P. G. Jasien, C. E. Dykstra, *J. Am. Chem. Soc.* **105**, 2089 (1983).
10. L. A. Tjurina *et al.*, *Organometallics* **23**, 1349 (2004).
11. C. Jones, P. C. Junk, J. A. Platts, A. Stasch, *J. Am. Chem. Soc.* **128**, 2206 (2006).
12. S. P. Green, C. Jones, P. C. Junk, K.-A. Lippert, A. Stasch, *Chem. Commun.* 3978 (2006).
13. L. Bourget-Merle, M. F. Lappert, J. R. Severn, *Chem. Rev.* **102**, 3031 (2002).
14. Materials and methods are available on *Science* Online.
15. J. Prust *et al.*, *Z. Anorg. Allg. Chem.* **627**, 2032 (2001).
16. Crystal data for **1** and **2** were obtained at 123(2) K with use of an Enraf-Nonius Kappa charge-coupled device diffractometer and MoK_α radiation (λ = 0.71073 Å). The crystal data are as follows. For **1**: $a = b$ = 18.409(3) Å, c = 17.640(4) Å, tetragonal, $I4_1/a$, Z = 4, R_1 for 3176 [data intensity $I > 2\sigma(I)$] unique data = 0.0448, and wR_2 (all 4353 unique data) = 0.1256. For **2**: a = 14.444(3) Å, b = 14.203(3) Å, c = 26.742(5) Å, β = 94.87(3)°, monoclinic, $P2_1/c$, Z = 4, R_1 for 9054 [data intensity $I > 2\sigma(I)$] unique data = 0.0428, and wR_2 (all 11,843 unique data) = 0.1145.
17. As determined from a survey of the Cambridge Crystallographic Database, September 2007.
18. K. P. Huber, G. Herzberg, *Constants of Diatomic Molecules* (Van Nostrand, New York, 1979), pp. 116 and 394.
19. J. Emsley, *The Elements* (Clarendon, Oxford, ed. 2, 1995).
20. M. A. G. M. Tinga *et al.*, *J. Am. Chem. Soc.* **115**, 2808 (1993).
21. Y. Wang *et al.*, *J. Am. Chem. Soc.* **127**, 11944 (2005).
22. J. Chai *et al.*, *J. Am. Chem. Soc.* **127**, 9201 (2005).
23. R. E. Mulvey *et al.*, *Chem. Commun.* 376 (2002).
24. E. C. Ashby, A. B. Goel, *Inorg. Chem.* **18**, 1306 (1979).
25. M. J. Frisch *et al.*, Gaussian 98, Revision A.10, Gaussian, Incorporated, Pittsburgh, PA (2001).
26. Z. Zhu *et al.*, *Angew. Chem. Int. Ed.* **45**, 5807 (2006).
27. M.-H. Baik, R. A. Friesner, G. Parkin, *Polyhedron* **23**, 2879 (2004).
28. A recent precedent for these reactions exists with the insertions of the carbodiimide, CyN=C=NCy, into the Fe-B bonds of terminal iron borylene complexes, e.g., $(C_5H_5)Fe(CO)_2(BNCy_2)$, to give ferro-amidinate complexes of boron, e.g., $[(C_5H_5)Fe(CO)_2C(NCy)_2]BNCy_2$. These reactions are thought to proceed via initial N-coordination of the carbodiimide at the borylene center (*29*).
29. G. A. Pierce *et al.*, *Angew. Chem. Int. Ed.* **46**, 2043 (2007).

30. We are grateful to the Australian Research Council for providing fellowships to C.J. and A.S. We also thank the Engineering and Physical Sciences Research Council of the UK for a partly funded studentship (S.P.G.). Metrical data for (Priso)Mg(μ-I)$_2$Mg(OEt$_2$)(Priso)·(hexane)$_{0.5}$, **1**, **2**, and **5**·(toluene)$_2$ are freely available from the Cambridge Crystallographic Database Center (CCDC codes 661565 to 661568).

Supporting Online Material

www.sciencemag.org/cgi/content/full/1150856/DC1
Materials and Methods
Figs. S1 to S4
Tables S1 to S3
References

24 September 2007; accepted 26 October 2007
Published online 8 November 2007;
10.1126/science.1150856
Include this information when citing this paper.

Activity of CeO_x and TiO_x Nanoparticles Grown on Au(111) in the Water-Gas Shift Reaction

J. A. Rodriguez,[1]* S. Ma,[1] P. Liu,[2] J. Hrbek,[1] J. Evans,[3] M. Pérez[3]

The high performance of Au-CeO_2 and Au-TiO_2 catalysts in the water-gas shift (WGS) reaction ($H_2O + CO \rightarrow H_2 + CO_2$) relies heavily on the direct participation of the oxide in the catalytic process. Although clean Au(111) is not catalytically active for the WGS, gold surfaces that are 20 to 30% covered by ceria or titania nanoparticles have activities comparable to those of good WGS catalysts such as Cu(111) or Cu(100). In TiO_{2-x}/Au(111) and CeO_{2-x}/Au(111), water dissociates on O vacancies of the oxide nanoparticles, CO adsorbs on Au sites located nearby, and subsequent reaction steps take place at the metal-oxide interface. In these inverse catalysts, the moderate chemical activity of bulk gold is coupled to that of a more reactive oxide.

Nearly 95% of the hydrogen supply is produced from the reforming of crude oil, coal, natural gas, wood, organic wastes, and biomass (*1*), but this reformed fuel contains 1 to 10% CO, the presence of which degrades the performance of the Pt electrode in fuel cell systems (*2*). To get clean hydrogen for fuel cells and other industrial applications, the water-gas shift (WGS) reaction ($CO + H_2O \rightarrow CO_2 + H_2$) is critical. Current industrial catalysts for the WGS (mixtures of Fe-Cr or Zn-Al-Cu oxides) are pyrophoric and normally require lengthy and complex activation steps before usage (*3*). Au-CeO_2 and Au-TiO_2 nanomaterials have recently been reported to be very efficient catalysts for the WGS (*3*–*5*). This is remarkable because neither bulk Au (*6*) nor bulk ceria and titania are known as WGS catalysts (*3*, *4*).

The nature of the active phase(s) in these metal/oxide nanocatalysts and the WGS reaction mechanism are still unclear. For example, the as-prepared Au-CeO_2 catalysts contain nanoparticles of pure gold and gold oxides (AuO_x) dispersed on a nanoceria support. Each of these gold species could be in the active phase (*3*–*5*), and the ceria support may not be a simple spectator in these systems (*7*). Although pure ceria is a very poor WGS catalyst, the properties of this oxide were found to be crucial for the observed activity of the Au-CeO_2 nanocatalysts (*4*, *6*, *8*). Several studies dealing with metal/oxide powder catalysts and the WGS reaction indicate that the oxide plays a direct role in the reaction (*3*, *4*, *9*, *10*), but because of the complex nature of these systems, there is no agreement on its role. Thus, we performed a series of experiments to test the chemical and catalytic properties of CeO_2 and TiO_2 nanoparticles (NPs) dispersed on a Au(111) template, as inverse model catalysts. Results of density-functional calculations point to a very high barrier for the dissociation of H_2O on Au(111) or Au(100) (*11*), which leads to negligible activity for the WGS process. Even gold NPs cannot dissociate water and catalyze the WGS reaction (*11*).

Part of the experiments described below were carried out in ultrahigh-vacuum (UHV) chambers that have attached a batch reactor (*12*) or have capabilities for scanning tunneling microscopy (STM) (*13*). High-resolution x-ray photoelectron spectroscopy (XPS) spectra, probing only the near-surface region in the oxide/gold systems (*5*, *14*), were acquired at the U7A beamline of the National Synchrotron Light Source. To prepare the TiO_2/Au(111) surfaces, Ti atoms were vapor deposited on a gold substrate covered with NO_2 at 100 K (*15*). The temperature was then raised to 700 K and the $TiNO_x$ particles were transformed into TiO_2. STM images indicated that this methodology produces flat NPs of TiO_2 exhibiting a combination of rutile and anatase phases (*15*). The NPs of ceria were prepared according to two different procedures. In the first one, labeled CeO_2-I here, alloys of $CeAu_x$/Au(111) were exposed to O_2 ($\sim 5 \times 10^{-7}$ torr) at 500 to 700 K for 5 to 10 min (*13*, *14*). The CeO_2 NPs grew dispersed on the herringbone structure of Au(111) (Fig. 1A) and had a rough three-dimensional structure that did not exhibit any particular face of ceria (Fig. 1B). In the second procedure, labeled CeO_2-II here, Ce was vapor deposited onto Au(111) under an atmosphere of O_2 ($\sim 5 \times 10^{-7}$ torr) at 550 K and then heated to 700 K. In these cases, the CeO_2 NPs grew preferentially at the steps between the terraces in the Au(111) substrate (Fig. 1C) and displayed regions with a CeO_2(111) orientation. When there was a deficiency of oxygen, groups or clusters of O vacancies were seen in STM images (Fig. 1D). This result is similar to that found for bulk CeO_{2-x}(111) (*16*). High-resolution XPS showed that Au atoms do not incorporate into the ceria lattice (*14*). Gold 4f spectra taken at photon energies of 240 to 380 eV, probing only two to three layers near the surface, showed the absence of the features expected for Au cations incorporated into ceria (*5*).

In Fig. 2, the WGS activity of a series of TiO_2/Au(111), CeO_2-I/Au(111), and CeO_2-II/Au(111) surfaces is shown. The fraction of the Au(111) substrate covered by the TiO_2 or CeO_2 particles was determined by means of ion-scattering spectroscopy (*5*, *7*). In the kinetics measurements, the sample was transferred from the

[1]Chemistry Department, Brookhaven National Laboratory, Upton, NY 11973, USA. [2]Center for Functional Nanomaterials, Brookhaven National Laboratory, Upton, NY 11973, USA. [3]Facultad de Ciencias, Universidad Central de Venezuela, Caracas, 1020-A Venezuela.

*To whom correspondence should be addressed. E-mail: rodrigez@bnl.gov

Stable Magnesium(I) Compounds with Mg-Mg Bonds: A Summary and Expansion of Research Done By Andreas Stasch [1]

Amber A. S. Gietter

Department of Chemistry and Biochemistry, University of Delaware, Newark, DE 19716

RECEIVED: November 23, 2010

Our knowledge of chemistry is in a constant state of flux, as one discovery can single-handedly change our understanding of science and discoveries made in the future. Advances in the ever-evolving field that is chemistry allow seemingly once impossible and implausible ideas to become real molecules and reactions. One area where this is exceptionally true is metal chemistry. Transition metals are constantly investigated and, as this research details, advances in transitional metal chemistry has led to the creation, isolation, and application of Mg_2^{2+} complexes.

One of the most interesting properties of metals is their ability to have multiple oxidation states. Not only does this affect physical properties such as color and boiling point, but also ligand coordination and chemical reactivity. The multiple oxidation states of transition metal complexes have been thoroughly investigated, but those of the main group elements are less explored. Typically, when dealing with alkali earth metals, a +2 oxidation state is expected, with the electronic configuration $1s^2 2s^2 2p^6$. However, as this research has shown, it is possible to obtain a stable +1 oxidation state (electronic configuration $1s^2 2s^2 2p^6 3s^1$) on Mg when using an $L_xM\text{-}ML_x$ framework. One of the first groundbreaking examples of M-M bonds was by Cotton and came in the form of $[Re_2Cl_8]^{2-}$.[2] This discovery proved that it was possible to form stable M-M bonds without the assistance of a bridging hydride. A landmark discovery, and an inspiration to the research presented here occurred in 2004 by the Carmona group.[3] The Carmona group successfully synthesized and characterized Zn_2^{2+} complexes. Although this had already been accomplished with the heavier (and thus larger atomic radii) metals of group 12, (Cd and Hg),[4] the isolation of a Zn^I complex, with many physical and chemical similarities to group 2 metals, fostered hope that isolating an $Mg^I\text{-}Mg^I$ bond was achievable.

Although prior to this research, there were no examples of isolated $Mg^I\text{-}Mg^I$ bonds, there are several examples of uncharacterized $L_xMg\text{-}MgL_x$ complexes.[5-7] Andrews and co-workers successfully synthesized an HMgMgH complex.[5] Through IR and DFT calculations, they determined the $Mg^I\text{-}Mg^I$ bond length to be 2.867 Å. Another investigation probed RMgMgX complexes for use as Grignard reagents.[6] Here, $Mg^I\text{-}Mg^I$ bond lengths ranged from 2.880 Å to 2.916 Å depending on the ligands used. A general trend showed (he more electron withdrawing the ligand, the shorter the Mg-Mg bond length. Finally, Mg^I had been isolated in a $Mg^I(CN)$ complex,[7] although there was no investigation into the possibility of the formation of a M-M bond. Spectroscopic data on these complexes is limited however because most are highly unstable and readily decompose.

A previous investigation by Stasch and co-workers led to the isolation of the M^{1+} form of *p*-block elements Ge **1** and Ga **2** using the $L_xM\text{-}ML_x$ framework.[8,9] In both instances, a bidentate nitrogen ligand with the general formula $[(Ar)NC(NR'_2)N(Ar)]^-$ was employed (Figure 1). Using this success as a guide, N-heterocyclic carbene (NHC) ligand frameworks were again investigated. The priso $[(Ar)NC(N^iPr_2)N(Ar)]^-$ **3** and nacnac $[(Ar)NC(Me)]_2CH^-$ **4** derivatives were isolated and used for further characterization (Figure 1). These ligands were ideal for two reasons. First, NHC ligands are notoriously good σ donors, and therefore able to aid to the stability of the Mg-Mg bond. Also, it was later found the steric bulk of the ligands prevented disproportionation of the Mg-Mg bond,[10] likely due to the strong secondary stabilizing interactions of the ligands.[11]

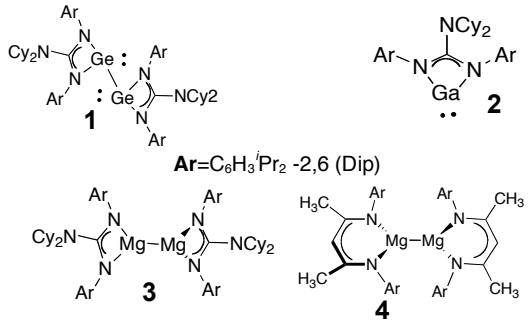

Figure 1. Investigated M-L Frameworks of Ge^I, Ga^I, and Mg^I

The synthesis of **3** and **4** is described in Scheme 1. The iodine derivative of both complexes was reacted at room temperature in the presence of a potassium mirror for 24 hours. After work up, **3** (colorless) and **4** (yellow) were obtained in moderate yield (28.5% and 56.5% respectively). Surprisingly, the complexes exhibited good thermal stability. Compound **3** decomposed at 170°C while **4** was stable up to 300°C. Compound **4** is also stable in the gas phase, subliming at 230°C (10^{-6} mm Hg). Compound **3** decomposed to Mg solid.[12]

Scheme 1. Formation of compounds **3** and **4**

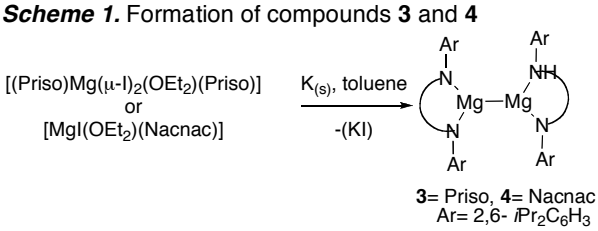

Once the complexes where successfully made, it was important to properly characterize the compounds to assure there was no bridging ligands causing an Mg^{II} complex.

Several techniques were used to accomplish this. First, x-ray analysis was obtained for **3** and **4** (Figure 2) and the bond lengths analyzed. It was determined the bond lengths were 2.8508 Å (**3**) and 2.8457 Å (**4**). Initially, these results were worrisome as the bond lengths were close to those reported for other Mg^{I}-Mg^{I} (see above), but not indicative of failure. These numbers were also drastically different from diatomic (3.890 Å), elemental (3.20 Å), and nonbonded interactions between (Mg•••Mg, 2.804 Å) magnesium.

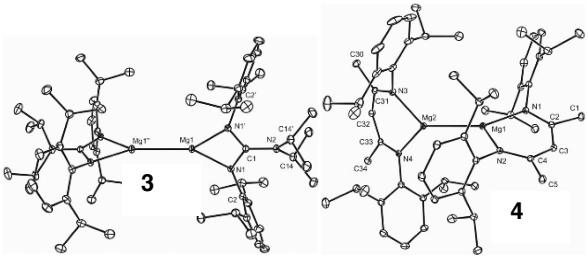

Figure 2: X-ray spectra of complexes **3** and **4**

Even though the results coincided with other Mg^{I} species, it was important to further confirm the structure. Several factors contributed to the dismissal of the presence of a bridging hydrogen. First, inspection of the x-ray structures showed the NHC ligands to be nearly orthogonal, which is inconsistent with the coplanar ligand geometry normally observed in bridging complexes. Further conformation came when creation of electron-density difference maps showed no regions with a $\rho > 0.15$ $e^{-}/Å^{3}$ near the M-M bond. Raman and IR spectroscopy were performed, but the results were unable to confirm or deny the existence of a bridge. The final proof arose from NMR analysis. Analysis of the NMR spectra did not show a hydride resonance near 3.70 ppm (obtained in $C_6D_5CD_3$), the shift expected from bridged complexes.[13]

Investigation into the nature of the Mg^{I}-Mg^{I} bond of **3** was also conducted. DFT calculations (B3LYP/BP86) showed the HOMO corresponding to a M-M bond with high σ-character. Additional investigation into the M-M bond was done via a natural bonding orbital (NBO) analysis (B3LYP). The results indicated one, covalent bond of almost entirely σ character (93.2% s, 6.0% p, 0.8% d).

The reactivity of **3** and **4** was also investigated. Contrary to expectations, neither compound was highly reducing as shown by their inertness to H_2 and N_2.[1] Neither increased temperature nor UV light irritation facilitated reactivity. Reactivity (Scheme 2) was observed between **4** and CyNCNCy. When the reaction warmed to room temperature, a color loss of compound **4** was observed, and the unique magnesium magnesioamidinate, compound **5**, was isolated. X-ray data showed the NHC ligands had shifted and were parallel to each other and orthogonal to CyNCNCy, consistent to insertion of the ligand into the M-M bond. Encouraged by the reactivity with CyNCNCy, the investigation into the ability of the complex to act as a two-electron/ two-center reductant was continued.[10] It was discovered that **4** showed promise as a selective reducing agent toward both organic and inorganic molecules (**6-9**, Scheme 2).[10] Some examples, such as the use of Mg complexes to reduce cot^{2-} were known, but were not able to be efficiently crystallized.[14] The isolation and characterization of **6** shed light onto the Mg-cot interactions. X-ray data showed η^2 coordination between metal and ligand. As with formation of **6**, reduction of isocyanates **7** was known,[15] but a compound where the ligands bridge two magnesium complexes has never been reported. It is hypothesized this is caused by the sterics of the nacnac ligands. The reaction of **4** with the azide species, AdN_3 is the most interesting. The product **8** contains six contiguous nitrogen atoms, yet was thermally and shock stable unlike similar compounds (and azides themselves for that matter).[16] Finally, azobenzene, a molecule previously only reducible by La^{II} complexes,[17] was reduced to yield **9**. This is also one of the first examples of an azobenzene acting as a dianionic bis(κ^{2}-azaallyl) ligand. The structure of all complexes was confirmed crystallographically. It was found the tetrahedral geometry of the metal center was distorted (although to varying degrees) by the bridging ligands.

Scheme 2.. Compounds formed from two-center/ two-electron reductions by Mg^{I}-Mg^{I} bonds

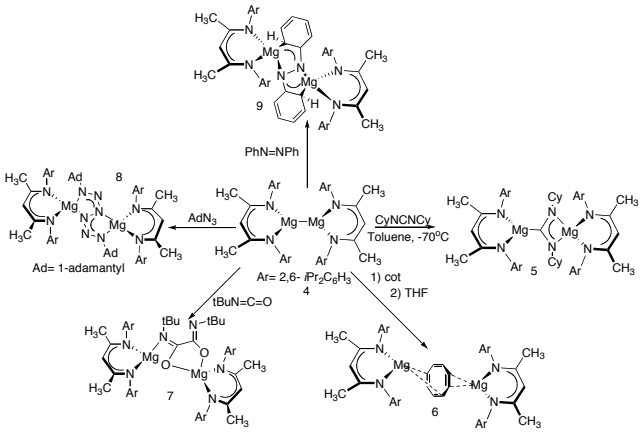

In a separate study by Stasch and coworkers, the bridged magnesium (II) hydride Nacnac complex, **10**, was isolated.[18] This presented the opportunity to study the reactivity of the bridged complex as a comparison. Although bridged hydride structures similar to **10** were known, the results of reactivity were inconsistent and uninformative.[19] Scheme 3 shows the results of a sister experiment. There was no reactivity observed with *t*BuNCO or cot. The other reagents, PhN=NPh, AdN_3, and CyN=C=NCy all cleaved (rather than inserted into) the Mg-Mg bond affording compounds **11-13** in good yields. These results were analogous to previous studies done with calcium hydride and iron hydride complexes: [20,21] fostering hope more applications were obtainable.

Scheme 3. Ability of [(nacnac)Mg-(μ-H)$_2$Mg(nacnac)] to act as a reducing agent.

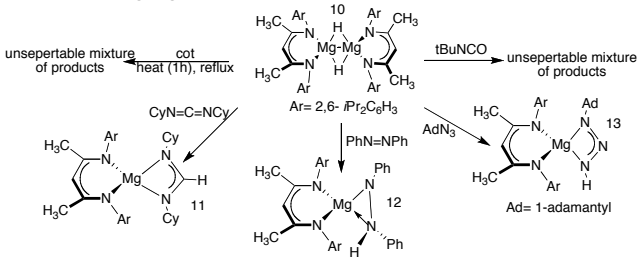

Compound **4** was also investigated for its reactivity towards Lewis bases and ethers.[18] As shown in Scheme 4, **4** reacted with several ethers and Lewis bases to afford crystalline products **14-17**. THF (**14**) and dioxane (**15**) proved to be only weakly coordinating as shown by the regeneration of **4** when placed under a vacuum or high temperatures. NMR studies conducted showed the equilibrium heavily favored **4**. DMAP (**16**) and 4-*t*BuPy (**17**) however showed exceptional stability under both thermal (decomposing at 159-160°C and 248-250°C respectively) and vacuum conditions. NMR spectra showed no evidence of free Lewis base in solution. All the complexes proved to be very stable towards disproportionation into $Mg_{(s)}$ and $Mg^{2+}{}_{(aq)}$.

Scheme 4, Ether or Lewis Base Coordination to **4**.

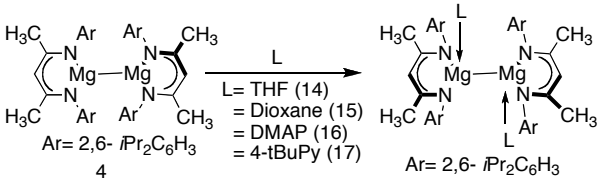

An x-ray analysis of all structures was also conducted. As seen when **4** was used as a reducing agent, the Nacnac ligands rotated from orthogonal to essentially parallel and a distorted tetrahedral geometry was observed. The most intriguing data collected however related to the exceptionally long Mg-Mg bond lengths. As stated previously, the Mg-Mg bond length in **4** is 2.8457 Å. The observed bond lengths showed surprising variability (**14**= 3.0560 Å, **15**= 3.1499 Å, **16**= 3.1962 Å, **17**= 3.1260 Å). More interesting still is the ligand donation strength does not correlate with the bond length. The weakly donating dioxane (**15**) has the second longest bond length and the strongly coordinating 4-*t*BuPy (**17**) has the second shortest. These observations force one to conclude electronic factors do not play a major role in determination of bond length for these complexes. DFT investigation (B3LYP) of a similar complex ($[(Mg[(HNCH)_2CH]]_2$) and the THF adduct ($[(Mg[(HNCH)_2CH](THF)]_2$) yielded a bond length difference of 0.08 Å (2.865 Å and 2.945 Å respectively) which is almost three times lower than observed (ΔÅ= 0.21). Although sterics likely play some role in the discrepancy, a partial potential energy diagram was constructed to investigate the energy required to elongate the Mg-Mg bond (Figure 3). As shown, the equilibrium is shallow so a 0.20 Å difference only increases the entire energy of the system by 1.2 kcal/mol. This means a sizeable bond elongation can occur with relatively small thermodynamic implications.

Using these findings as a stepping-stone, Stasch and coworkers began even further expanding on the reductive ability of **4**. One path inspired by the above findings was the possibility of isolating a derivative of the Gomberg-Bachmann magnesium ketyl ($[IMg(OCPh_2•)]$).[22] The reaction was successfully accomplished to afford **18** (Scheme 5) in good yield. Characterization and conformation of the product was obtained via x-ray analysis. A sister experiment was conducted focusing on the reduction of a tricyclic aromatic compound, anthracene. Scheme 5 details these reactions. The original ligand was unreactive towards anthracene, so a modified aromatic group, $C_6H_2Me_3$-2,4,6 (Mes **4a**) was introduced. This alteration proved effective, giving the reduced product **19** in good yield. X-ray and NMR analysis

Figure 3. Potential Energy Curve of ($[(Mg[(HNCH)_2CH]]_2$) As a Function of Distance

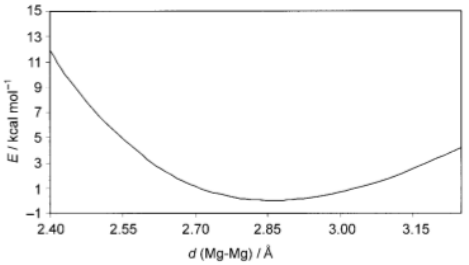

confirmed the supposed structure. These were the first examples of compounds of these types being successfully characterized.

Scheme 5. Preperation of Gomberg- Bachmann Magnesium Ketyl and Reduction of Anthracene

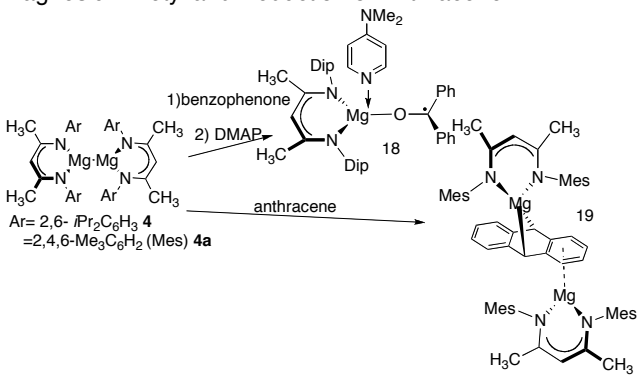

A final unique example is the ability of **4** and **4a** to act as a reducing agent for organometallic complexes.[23] As shown in Scheme 6 below, the successful reduction of **20** to **21** was observed, but the yields (5% for **4** and 20% for **4a**) were poor. This successful reduction however was encouraging. There is precedence to believe the yield of these complexes and the scope of organometallic complexes reduced by magnesium will be expanded in the not so distant future (Stasch published the successful synthesis of dimeric alumninum complexes in October 2010).[24]

Scheme 6. Utilizing **4** and **4a** as Reductive Agents Towards Organometallic Reagents

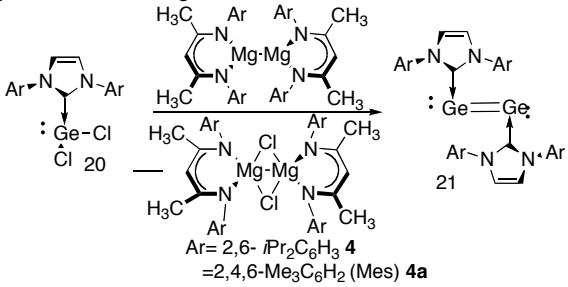

Stasch and coworkers have shattered the previous view of alkaline metals as only existing as M^{II} compounds. They have forever changed the chemistry of magnesium and have opened the doors to exciting and intriguing new possibilities. Research relating to the expansion in practical application and improvement of Mg complexes is still expanding, although the current focus is mainly on its Lewis acid/base properties. Also, obtaining clean reactions with dihydrogen to yield magnesium

hydride are being pursed.[25] The investigation into new Priso, Giso, and Nacnac type ligands and the reactivity differences caused by both stereo and electronic altercations is ongoing.[26] It is also important to note, most of the above examples are the first with the small, lightweight, inexpensive, non-toxic magnesium metal. Magnesium has shown ability to chemically replace highly toxic samarium among other undesirable metals. Also, the development of other group II metals, such as calcium and strontium, can be examined. The already developed chemistry can be applied to Mg complexes and the developing chemistry of Mg complexes can shed insight onto the new reactivity of the other group II metals.[27,28] These facts make the investigation and development of synthetically useful methodology even more alluring.

References

(1) Green, S. P.; Jones, C.; Stasch, A. *Science* **2007**, *318*, 1754.

(2) Cotton, F. A.; Curtis, N. F.; Harris, C. B.; Johnson, B. F. G.; Lippard, S. J.; Mague, J. T.; Robinson, W. R.; Wood, J. S. *Science* **1964**, *145*, 1305.

(3) Resa, I.; Carmona, E.; Gutierrez-Puebla, E.; Monge, A. *Science* **2004**, *305*, 1136.

(4) F.A. Cotton, G. W., C.A. Murillo, M. Bochmann *Advanced Inorganic Chemistry*; 6 ed.; Wiley: New York, 1999.

(5) Wang, X.; Andrews, L. *J. Phys. Chem. A* **2004**, *108*, 11511.

(6) Jasien, P. G.; Dykstra, C. E. *J. Amer. Chem. Soc.* **1983**, *105*, 2089.

(7) Petrie, S. *Australian Journal of Chemistry* **2003**, *56*, 259.

(8) Green, S. P.; Jones, C.; Junk, P. C.; Lippert, K.-A.; Stasch, A. *Chem. Comm.* **2006**, 3978.

(9) Jones, C.; Junk, P. C.; Platts, J. A.; Stasch, A. *J. Amer. Chem. Soc.* **2006**, *128*, 2206.

(10) Bonyhady, S. J.; Green, S. P.; Jones, C.; Nembenna, S.; Stasch, A. *Angew. Chem. Int. Ed.* **2009**, *48*, 2973.

(11) Buchanan, W. D.; Allis, D. G.; Ruhlandt-Senge, K. *Chem. Comm.* **2010**, *46*, 4449.

(12) Westerhausen, M. *Angew. Chem. Int. Ed.* **2008**, *47*, 2185.

(13) Gallagher, D. J.; Henderson, K. W.; Kennedy, A. R.; O'Hara, C. T.; Mulvey, R. E.; Rowlings, R. B. *Chem. Comm.* **2002**, 376.

(14) Alonso, T.; Harvey, S.; Junk, P. C.; Raston, C. L.; Skelton, B.; White, A. H. *Organomet.* **1987**, *6*, 2110.

(15) Yuan, F.; Shena, Q.; Sun, J. *Polyhedron* **1998**, *17*, 2009.

(16) Mackay, D.; McIntyre, D. D.; Taylor, N. J. *J. Org. Chem.* **1982**, *47*, 532.

(17) Evans, W. J.; Drummond, D. K.; Chamberlain, L. R.; Doedens, R. J.; Bott, S. G.; Zhang, H.; Atwood, J. L. *J. Amer. Chem. Soc.* **1988**, *110*, 4983.

(18) Green, S. P.; Jones, C.; Stasch, A. *Angew. Chem. Int. Ed.* **2008**, *47*, 9079.

(19) Ashby, E. C.; Lin, J. J.; Goel, A. B. *J. Org. Chem.* **1978**, *43*, 1557.

(20) Spielmann, J.; Harder, S. *Chem. – Euro. J.* **2007**, *13*, 8928.

(21) Yu, Y.; Sadique, A. R.; Smith, J. M.; Dugan, T. R.; Cowley, R. E.; Brennessel, W. W.; Flaschenriem, C. J.; Bill, E.; Cundari, T. R.; Holland, P. L. *J. Amer. Chem. Soc.* **2008**, *130*, 6624.

(22) Jones, C.; McDyre, L.; Murphy, D. M.; Stasch, A. *Chem. Comm.* **2010**, *46*, 1511.

(23) Sidiropoulos, A.; Jones, C.; Stasch, A.; Klein, S.; Frenking, G. *Angew. Chem. Int. Ed.* **2009**, *48*, 9701.

(24) Bonyhady, S. J.; Collis, D.; Frenking, G.; Holzmann, N.; Jones, C.; Stasch, A. *Nat Chem* **2010**, *2*, 865.

(25) Schulz, S. *Chem – Euro. J.* **2010**, *16*, 6416.

(26) Jin, G.; Jones, C.; Junk, P. C.; Lippert, K.-A.; Rose, R. P.; Stasch, A. *New Journal of Chemistry* **2009**, *33*, 64.

(27) Barrett, A. G. M.; Crimmin, M. R.; Hill, M. S.; Procopiou, P. A. *Proceedings of the Royal Society A: Mathematical, Physical and Engineering Science* **2010**, *466*, 927.

(28) Bonyhady, S. J.; Jones, C.; Nembenna, S.; Stasch, A.; Edwards, A. J.; McIntyre, G. J. *Chem. – Euro. J.* **2010**, *16*, 938.

LETTERS

Cleaving carbon–carbon bonds by inserting tungsten into unstrained aromatic rings

Aaron Sattler[1] & Gerard Parkin[1]

The cleavage of C–H and C–C bonds by transition metal centres is of fundamental interest and plays an important role in the synthesis of complex organic molecules from petroleum feedstocks[1–6]. But while there are many examples for the oxidative addition of C–H bonds to a metal centre, transformations that feature oxidative addition of C–C bonds are rare. The paucity of transformations that involve the cleavage of C–C rather than C–H bonds is usually attributed to kinetic factors arising from the greater steric hindrance and the directional nature of the sp″ hybrids that form the C–C bond, and to thermodynamic factors arising from the fact that M–C bonds are weaker than M–H bonds[2–5]. Not surprisingly, therefore, most examples of C–C bond cleavage either avoid the kinetic limitations by using metal compounds in which the C–C bond is held in close proximity to the metal centre, or avoid the thermodynamic limitations by using organic substrates in which the cleavage is accompanied by either a relief of strain energy or the formation of an aromatic system[2–5]. Here, we show that a tungsten centre can be used to cleave a strong C–C bond that is a component of an unstrained 6-membered aromatic ring. The cleavage is enabled by the formation of an unusual chelating di(isocyanide) ligand, which suggests that other metal centres with suitable ancillary ligands could also accomplish the cleavage of strong C–C bonds of aromatic substrates and thereby provide new ways of functionalizing such molecules.

We are currently developing the coordination chemistry of molybdenum with respect to heterocyclic aromatic nitrogen compounds to acquire a more detailed understanding of the reactions involved in hydrodenitrogenation, the important process by which nitrogen is removed from compounds in fossil fuels[7,8]. As part of these investigations, we reported that quinoxaline (QoxH) reacts with electron-rich $Mo(PMe_3)_6$ to give $(\eta^2\text{-}N,C\text{-Qox})Mo(PMe_3)_4H$ via oxidative addition of a C−H bond, and further demonstrated that this complex converts sequentially to $(\eta^6\text{-}C_4N_2\text{-QoxH})Mo(PMe_3)_3$ and $(\eta^6\text{-}C_6\text{-QoxH})Mo(PMe_3)_3$ in which the quinoxaline ligand coordinates in an η^6 manner through the heterocyclic and carbocyclic rings, respectively (Fig. 1)[8]. (Here italics indicate the coordinating atoms.) Seeking to discover a system that would achieve cleavage of a C–N bond of the aromatic ring, we explored tungsten compounds because this metal shows a greater ability to accomplish bond cleavage via oxidative addition than does molybdenum[9].

As illustrated in Fig. 1, the reaction of $W(PMe_3)_4(\eta^2\text{-}CH_2PMe_2)H$ with QoxH indeed proceeds very differently to that for the molybdenum system (see Supplementary Information for experimental details regarding synthesis and compound characterization). Thus, instead of tungsten simply coordinating QoxH in an η^6 manner, $W(PMe_3)_4(\eta^2\text{-}CH_2PMe_2)H$ reacts with QoxH either (1) to induce C–C bond cleavage and dehydrogenation to give $[\kappa^2\text{-}C_2\text{-}C_6H_4(NC)_2]W(PMe_3)_4$, or (2) to form the dihydride complex $(\eta^4\text{-}C_2N_2\text{-QoxH})W(PMe_3)_3H_2$ (15% and 24% yields, respectively, after 18 h at 90 °C). The dihydride complex does not convert to $[\kappa^2\text{-}C_2\text{-}C_6H_4(NC)_2]W(PMe_3)_4$ under the reaction conditions. The transformations observed for QoxH are also observed for 6-methylquinoxaline ($Qox^{Me}H$) and 6,7-dimethylquinoxaline ($Qox^{Me_2}H$), thereby demonstrating the generality of the reactions (see Supplementary Information).

In addition to the dihydride $(\eta^4\text{-}C_2N_2\text{-QoxH})W(PMe_3)_3H_2$, the tetrahydride $W(PMe_3)_4H_4$ is also formed in low yield (<5%) during the course of the reaction. Although an obvious source for the hydride ligands of these complexes is the H_2 that is liberated during the formation of $[\kappa^2\text{-}C_2\text{-}C_6H_4(NC)_2]W(PMe_3)_4$, we note that the conversion of QoxH to 2,2′-biquinoxaline, $(2,2'\text{-Qox})_2$ (identified by X-ray diffraction, see Supplementary Fig. 3) may also serve as a source of H_2. Not unexpectedly, the yield of $(\eta^4\text{-}C_2N_2\text{-QoxH})W(PMe_3)_3H_2$ (86%),

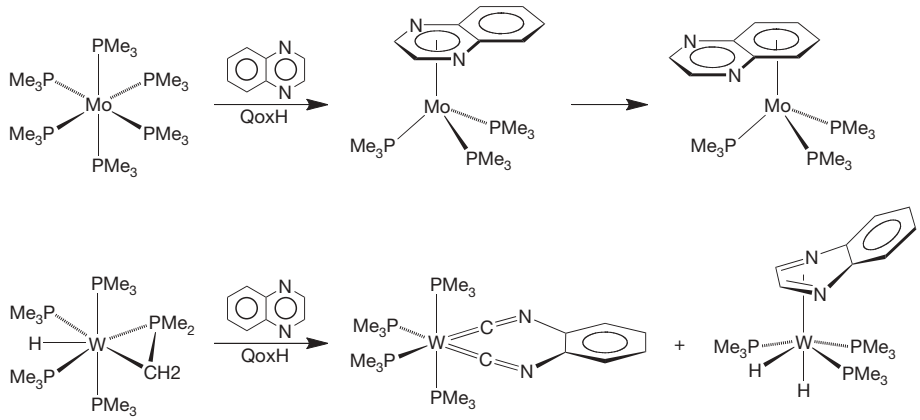

Figure 1 | Different reactivity of quinoxaline towards $Mo(PMe_3)_6$ and $W(PMe_3)_4(\eta^2\text{-}CH_2PMe_2)H$.

[1]Department of Chemistry, Columbia University, New York, New York 10027, USA.

relative to that of $[\kappa^2\text{-}C_2\text{-}C_6H_4(NC)_2]W(PMe_3)_4$, increases considerably if the reaction between $W(PMe_3)_4(\eta^2\text{-}CH_2PMe_2)H$ and QoxH is performed under an atmosphere of H_2 (see Supplementary Information).

The dihydride complexes $(\eta^4\text{-}C_2N_2\text{-}Qox^{R_2}H)W(PMe_3)_3H_2$ (where R_2 = H, H; Me, H; or Me, Me) represent unprecedented examples of η^4-coordination of this dinuclear aromatic compound via the heterocyclic ring, as clearly seen from the structure of $(\eta^4\text{-}C_2N_2\text{-}Qox^{Me_2}H)W(PMe_3)_3H_2$ shown in Fig. 2. As such, $(\eta^4\text{-}C_2N_2\text{-}Qox^{R_2}H)W(PMe_3)_3H_2$ provide important new structural motifs for the means by which heterocyclic nitrogen compounds may bind to the surface of hydrodenitrogenation catalysts.

The most significant aspect of the reactions between $W(PMe_3)_4(\eta^2\text{-}CH_2PMe_2)H$ and $Qox^{R_2}H$, however, pertains to the formation of $[\kappa^2\text{-}C_2\text{-}C_6H_2R_2(NC)_2]W(PMe_3)_4$: as is evident from the structure of $[\kappa^2\text{-}C_2\text{-}C_6H_2Me_2(NC)_2]W(PMe_3)_4$ in Fig. 3, the formation of these compounds requires the breaking of an aromatic C–C bond that is substantially stronger than a typical C–C single bond[10]. Remarkably, this unprecedented cleavage of the aromatic C–C bond takes place in preference to that of the C–N bond. The latter bond might have been expected to be more reactive because the cleavage of the C-N bond in pyridine[11] and its derivatives[12–15] has been achieved by various metal centres, thereby making the cleavage of the C–C bond in the present system all the more remarkable.

The cleaved quinoxaline fragments within $[\kappa^2\text{-}C_2\text{-}C_6H_2R_2(NC)_2]W(PMe_3)_4$, namely $C_6H_2R_2(NC)_2$, correspond to known di(isocyanide) compounds[16]. As such, $[\kappa^2\text{-}C_2\text{-}C_6H_2R_2(NC)_2]W(PMe_3)_4$ may be viewed as simple transition-metal isocyanide complexes of the type $ML_4(CNR)_2$ for which there is precedent. However, the $[\kappa^2\text{-}C_2\text{-}C_6H_2R_2(NC)_2]W(PMe_3)_4$ complexes exhibit several interesting structural features. For example, whereas the majority of transition-metal isocyanide compounds have almost linear C–N–C bond angles (the mean C–N–C bond angle for isocyanide compounds listed in the Cambridge Structural Database (Version 5.30) is 172°), the geometries at nitrogen in each of the $[\kappa^2\text{-}C_2\text{-}C_6H_2R_2(NC)_2]W(PMe_3)_4$ complexes are severely bent (125–128°). Such bending, which has also been observed for some monodentate isocyanide complexes[17], is consistent with considerable metal-to-ligand π-backbonding so that W=C=N–R is a better description of the interaction than is $W{\leftarrow}C^-{\equiv}N^+$–R (ref. 18). Further evidence for the multiply bonded nature of the W–C interactions in $[\kappa^2\text{-}C_2\text{-}C_6H_2R_2(NC)_2]W(PMe_3)_4$ is the observed average W–C bond length

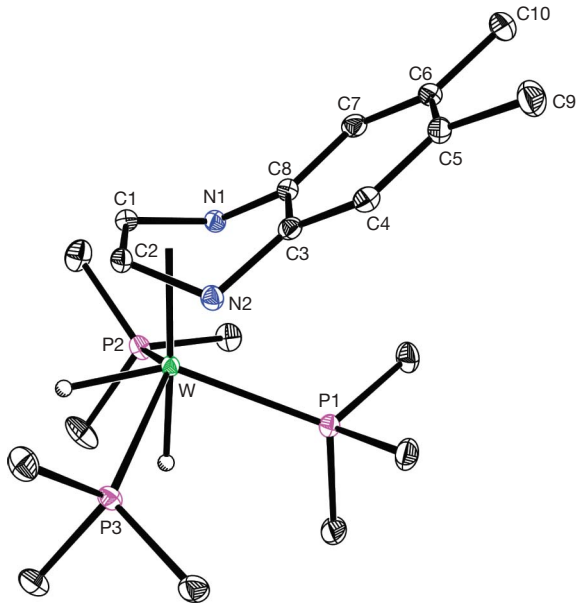

Figure 2 | Molecular structure of $(\eta^4\text{-}C_2N_2\text{-}Qox^{Me_2}H)W(PMe_3)_3H_2$.

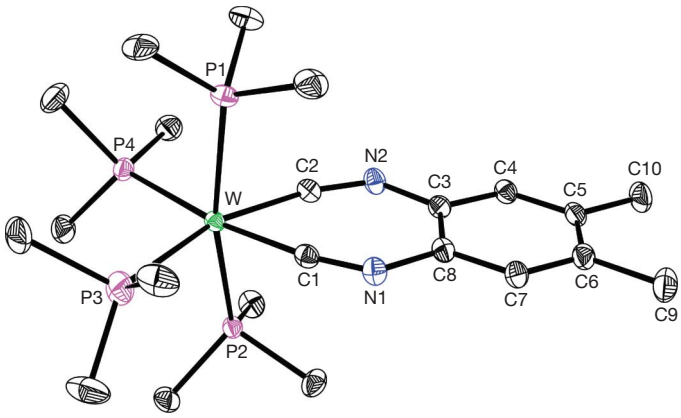

Figure 3 | Molecular structure of $[\kappa^2\text{-}C_2\text{-}C_6H_2Me_2(NC)_2]W(PMe_3)_4$.

of 1.93 Å, which compares favourably with the mean value of 1.98 Å for structurally characterized compounds with $W{=}CR_2$ double bonds listed in the Cambridge Structural Database (Version 5.30), but is much shorter than the mean W–C single bond length of 2.23 Å.

A high degree of backbonding is also suggested by the ν(CN) stretching frequencies of $[\kappa^2\text{-}C_2\text{-}C_6H_2R_2(NC)_2]W(PMe_3)_4$ ranging from 1,698–1,709 cm^{-1} (see Supplementary Information), which is at the low end for transition-metal isocyanide complexes; for comparison, ν(CN) for isocyanide complexes span a range of at least 2,310 cm^{-1} to 1,670 cm^{-1} (refs 19, 20). Similarly, the ^{13}C nuclear magnetic resonance (NMR) spectroscopic signals of transition-metal isocyanide compounds span at least 151.8–238.7 parts per million (p.p.m.) (refs 20, 21), with the compound having the most downfield chemical shift, namely $[Fe(CNXyl)_4]^{2-}$, having the lowest ν(CN) stretching frequency and a highly bent C–N–C bond angle of 144(3)° (e.s.d. in parentheses; ref. 20). The ^{13}C NMR chemical shift of 211.4 p.p.m. for $[\kappa^2\text{-}C_2\text{-}C_6H_3Me(NC)_2]W(PMe_3)_4$ (see Supplementary Information) is thus also consistent with considerable backbonding in this molecule.

An interesting point to note is that chelating isocyanide ligands are not common because M–C–N–R moieties prefer to adopt linear coordination at both nitrogen and carbon[21]. For this reason, although $o\text{-}(CN)_2C_6H_4$ has been employed as a ligand, it does not chelate but instead serves as a bridging ligand[22]. In accord with such behaviour, the smallest ring size previously reported for a complex of a bidentate di(isocyanide) ligand is 12, as illustrated by $[\kappa^2\text{-}C_2\text{-}CH_2\{OC_6H_4(NC)\}_2]Cr(CO)_4$ (ref. 23). The 7-membered ring of $[\kappa^2\text{-}C_2\text{-}C_6H_4(NC)_2]W(PMe_3)_4$, featuring two W–C–N bond angles that are close to linear (165°–169°), is thus exceptionally small for a transition-metal complex of a bidentate di(isocyanide) ligand. The ability to isolate such an unusual compound may result from the fact that its mechanism of formation involves insertion of the tungsten centre into the aromatic ring; indeed, treatment of $W(PMe_3)_4(\eta^2\text{-}CH_2PMe_2)H$ with $o\text{-}(CN)_2C_6H_4$ at room temperature results in the immediate formation of an unidentified precipitate, with no evidence for formation of $[\kappa^2\text{-}C_2\text{-}C_6H_4(NC)_2]W(PMe_3)_4$ by ^1H NMR spectroscopy.

Several different mechanisms could explain the observed formation of $[\kappa^2\text{-}C_2\text{-}C_6H_4(NC)_2]W(PMe_3)_4$, of which one involves the direct insertion of tungsten into the C–C bond followed by two α-hydrogen elimination steps. Such a process is in line with the observation that electron-donating substituents on olefins promote C–C bond cleavage, as exemplified by the use of enetetramines to generate *N*-heterocyclic carbene compounds[24,25]. However, we favour the alternative mechanism outlined in Fig. 4 that comprises a series of C–H bond cleavage reactions to access a benzyne-type intermediate $[\eta^2\text{-}C_2\text{-}C_6H_4(NCCN)]W(PMe_3)_4H_2$, from which $[\kappa^2\text{-}C_2\text{-}C_6H_4(NC)_2]W(PMe_3)_4$ is then obtained via a sequence that involves reductive elimination of H_2 and C–C bond cleavage. The feasibility of this mechanism is supported by the report of the ruthenium benzyne

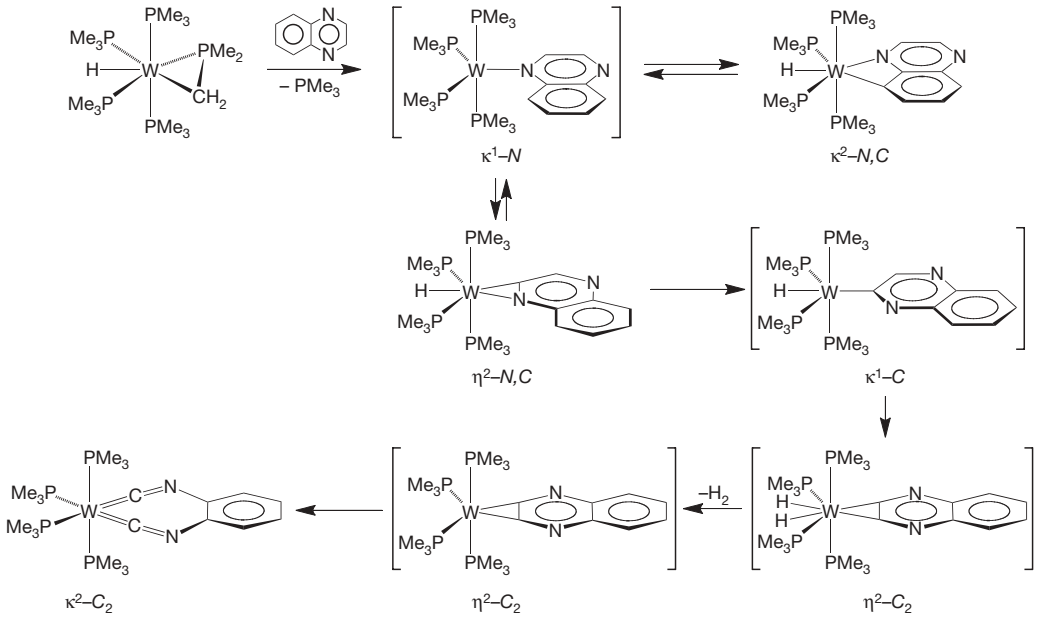

Figure 4 | Possible mechanism for formation of $[\kappa^2\text{-}C_2\text{-}C_6H_4(NC)_2]W(PMe_3)_4$.

complex $(\eta^2\text{-}C_6H_4)Ru(PMe_3)_4$ (ref. 26), a structural analogue of the proposed intermediate $[\eta^2\text{-}C_2\text{-}C_6H_4(NCCN)_2]W(PMe_3)_4$. Furthermore, the observation of several other compounds such as mononuclear $(\eta^2\text{-}N,C\text{-Qox})W(PMe_3)_4H$ and $(\kappa^2\text{-}N,C\text{-Qox})W(PMe_3)_4H$ (Fig. 4), and dinuclear $(\mu\text{–}\eta^2\text{-}N,C\text{-}\kappa^2\text{-}N,C\text{-Qox}')[W(PMe_3)_4H]_2$ (Supplementary Fig. 2), during the course of the reaction provides evidence that C–H bond cleavage is facile in this system. Note, however, that C–H bond cleavage is reversible and that the mere observation of $(\eta^2\text{-}N,C\text{-Qox})W(PMe_3)_4H$ is thus not proof that this species is directly involved in the C–C bond cleavage process. A computational analysis of the reaction is, therefore, needed to establish which of the different mechanisms is the most reasonable for the observed transformations.

Finally, we note that the overall cleavage of the C–C bond of the benzyne-type species proposed in this system resembles the formation of *bis*(isocyanide) compounds by base-induced cleavage of diaminoacetylene species[27], a process that is the reverse of the well-known coupling reactions of isocyanides[25,28,29]. It is also worth noting that acetylenic C–C bonds have been successfully cleaved using metal-cluster complexes[30].

In conclusion, we note that the cleavage of an aromatic C–C bond by insertion of tungsten into an aromatic ring enables a quinoxaline compound to be converted to an *o*-diisocyanobenzene derivative, a transformation that may potentially be extended to other systems and thereby provide a new means of functionalizing aromatic molecules.

Received 29 May; accepted 9 November 2009.

1. Jones, W. D. in *Comprehensive Organometallic Chemistry III*, Vol. 1, Ch. 1.25 (eds Crabtree, R. H. & Mingos, D. M. P.) (Elsevier, 2006).
2. Jones, W. D. The fall of the C–C bond. *Nature* **364,** 676–677 (1993).
3. Jun, C. H. Transition metal-catalyzed carbon-carbon bond activation. *Chem. Soc. Rev.* **33,** 610–618 (2004).
4. van der Boom, M. E., &. Milstein, D. Cyclometalated phosphine-based pincer complexes: Mechanistic insight in catalysis, coordination, and bond activation. *Chem. Rev.* **103,** 1759–1792 (2003).
5. Crabtree, R. H. The organometallic chemistry of alkanes. *Chem. Rev.* **85,** 245–269 (1985).
6. Rybtchinski, B., &. Milstein, D. Metal insertion into C–C bonds in solution. *Angew. Chem. Int. Edn Engl.* **38,** 870–883 (1999).
7. Zhu, G. Tanski, J. M., Churchill, D. G., Janak, K. E. & Parkin, G. The reactivity of $Mo(PMe_3)_6$ towards heterocyclic nitrogen compounds: transformations relevant to hydrodenitrogenation. *J. Am. Chem. Soc.* **124,** 13658–13659 (2002).
8. Zhu, G. Pang, K. & Parkin, G. New modes for coordination of aromatic heterocyclic nitrogen compounds to molybdenum: catalytic hydrogenation of quinoline, isoquinoline, and quinoxaline by $Mo(PMe_3)_4H_4$. *J. Am. Chem. Soc.* **130,** 1564–1565 (2008).
9. Buccella, D., &. Parkin, G. p-tert-butylcalix[4] arene complexes of molybdenum and tungsten: reactivity of the calixarene methylene C-H bond and the facile migration of the metal around the phenolic rim of the calixarene. *J. Am. Chem. Soc.* **128,** 16358–16364 (2006).
10. Cyranski, M. K. Energetic aspects of cyclic pi-electron delocalization: evaluation of the methods of estimating aromatic stabilization energies. *Chem. Rev.* **105,** 3773–3811 (2005).
11. Kleckley, T. S. Bennett, J. L., Wolczanski, P. T. & Lobkovsky, E. B. Pyridine C=N bond cleavage mediated by $(silox)_3Nb(silox = {}^tBu_3SiO)$. *J. Am. Chem. Soc.* **119,** 247–248 (1997).
12. Bonanno, J. B. Veige, A. S., Wolczanski, P. T. & Lobkovsky, E. B. Amide derivatives of tantalum and a niobium-promoted ring opening of 3,5-lutidine. *Inorg. Chim. Acta* **345,** 173–184 (2003).
13. Gray, S. D. Weller, K. J., Bruck, M. A., Briggs, P. M. & Wigley, D. E. Carbon-nitrogen bond-cleavage in an η^2(N, C)-pyridine complex-induced by intramolecular metal-to-ligand alkyl migration - models for hydrodenitrogenation catalysis. *J. Am. Chem. Soc.* **117,** 10678–10693 (1995).
14. Weller, K. J. Filippov, I. Briggs, P. M. & Wigley, D. E. Pyridine degradation intermediates as models for hydrodenitrogenation catalysis: preparation and properties of a metallapyridine complex. *Organometallics* **17,** 322–329 (1998).
15. Bailey, B. C. Fan, H. Huffman, J. C., Baik, M. H. & Mindiola, D. J. Room temperature ring-opening metathesis of pyridines by a transient Ti≡C linkage. *J. Am. Chem. Soc.* **128,** 6798–6799 (2006).
16. Ito, Y. Ohnishi, A. Ohsaki, H. & Murakami, M. A preparative method for ortho-diisocyanoarenes. *Synthesis* 714–715 (1988).
17. Wagner, N. L. Laib, F. E. & Bennett, D. W. Conformational isomerism in $(p\text{-}RC_6H_4NC)_2W(dppe)_2$: substantial structural changes resulting from subtle differences in the pi-acidity of $p\text{-}RC_6H_4NC$. *J. Am. Chem. Soc.* **122,** 10856–10867 (2000).
18. Kuznetsov, M. L. Theoretical studies of transition metal complexes with nitriles and isocyanides. *Russ. Chem. Rev.* **71,** 265–282 (2002).
19. Strauch, H. C. *et al.* Reactions of (butadiene)tantalocene cation with alkyl isocyanides. *Organometallics* **18,** 3802–3812 (1999).
20. Brennessel, W. W., &. Ellis, J. E. $[Fe(CNXyl)_4]^{2-}$: an isolable and structurally characterized homoleptic isocyanidemetalate dianion. *Angew. Chem. Int. Edn Engl.* **46,** 598–600 (2007).
21. Hahn, F. E. The coordination chemistry of multidentate isocyanide ligands. *Angew. Chem. Int. Edn Engl.* **32,** 650–665 (1993).
22. Espinet, P. Soulantica, K. Charmant, J. P. H. & Orpen, A. G. 1,2-Phenylene diisocyanide for metallotriangles. *Chem. Commun.* 915–916 (2000).
23. Hahn, F. E. Tamm, M. Imhof, L. & Lugger, T. Preparation and crystal structures of a bidentate isocyanide and its tetracarbonylchromium complex. *J. Organomet. Chem.* **526,** 149–155 (1996).
24. Lappert, M. F. Contributions to the chemistry of carbene metal chemistry. *J. Organomet. Chem.* **690,** 5467–5473 (2005).
25. Wilker, C. N. ;. Hoffmann, R. & Eisenstein, O. Coupling methylenes, methynes and other π-systems on one or two metal centers. *Nouv. J. Chim.* **7,** 535–544 (1983).
26. Hartwig, J. F. Bergman, R. G. & Andersen, R. A. Structure, synthesis, and chemistry of $(PMe_3)_4Ru(\eta^2\text{-benzyne})$. Reactions with arenes, alkenes, and heteroatom-containing organic-compounds. Synthesis and structure of a monomeric hydroxide complex. *J. Am. Chem. Soc.* **113,** 3404–3418 (1991).

27. Pombeiro, A. J. L. da Silva, M. & Michelin, R. A. Aminocarbyne complexes derived from isocyanides activated towards electrophilic addition. *Coord. Chem. Rev.* **218,** 43–74 (2001).
28. Carnahan, E. M. Protasiewicz, J. D. & Lippard, S. J. 15 years of reductive coupling: what have we learned? *Acc. Chem. Res.* **26,** 90–97 (1993).
29. Ito, Y. *et al.* Aromatizing oligomerization of 1,2-di-isocyanoarene to quinoxaline oligomers. *J. Chem. Soc. Chem. Commun.* 403–405 (1990).
30. Clauss, A. D. ;. Shapley, J. R.; Wilker, C. N. & Hoffmann, R. Alkyne scission on a trimetallic framework: experimental evidence and theoretical analysis. *Organometallics* **3,** 619 (1984).

Supplementary Information is linked to the online version of the paper at www.nature.com/nature.

Acknowledgements We thank the US Department of Energy, Office of Basic Energy Sciences (DE-FG02-93ER14339) for supporting this research. We thank The National Science Foundation (CHE-0619638) for the acquisition of an X-ray diffractometer. We thank W. Sattler for discussions.

Author Contributions G.P. supervised the project. A.S. synthesized and characterized the compounds. G.P. and A.S. analysed the data and wrote the manuscript.

Author Information Reprints and permissions information is available at www.nature.com/reprints. The authors declare no competing financial interests. X-ray crystallographic coordinates have been deposited at the Cambridge Crystallographic Database (CCDC #734113–734121). Correspondence and requests for materials should be addressed to G.P. (parkin@columbia.edu).

A review of the process of carbon-carbon bond cleavage by insertion of tungsten into unstrained aromatic rings.

Parikshit V. Gokhale.

Department of Chemistry, University of Delaware.

RECEIVED DATE (automatically inserted by publisher); pgokhale@udel.edu

In the present paper, the authors disclose a method which uses a tungsten metal center and it can be used to cleave a strong C-C bond of an unstrained 6-membered aromatic ring. The reaction proceeds through an unusual chelating di(isocyanide) ligand. Thus, this method provides a new way of functionalizing strong C-C bonds.

As we all know, the cleavage of C-H and C-C bonds and funtionalizing them plays an important role in organic synthesis of complex molecules. This is mostly accomplished by using transition metal centers. The review[2] deals with a number of recent advancements dealing with methodologies directed towards the activation of C-C bonds in strained and unstrained molecules catalyzed by transition metal complexes. The review[3] in Angew Chem International Edition deals with the transition metal insertion into strong C-C bonds in solution, the reaction mechanisms involved, reactivity patterns, factors controlling the competition between C-C and C-H bond cleavage, use of different metals, thermodynamics and kinetics of C-C bond cleavage etc. There are many examples of oxidative addition of C-H bonds to a metal center in literature, but the same involving C-C bonds is quite rare. This is mainly because of the kinetic factors arising from the greater steric hindrance and the directional nature of the sp^n hybrid orbitals that form the C-C bond. It can also be attributed to the thermodynamic factors due to the fact that M-C bonds are weaker than M-H bonds. So C-H bond cleavage is more prevalent.
In current literature, examples of C-C bond cleavage find some loopholes. For examples, they avoid the kinetic limitations by using metal compounds in which the C-C bond is held in close proximity to the metal center. So the C-C bond effectively gets cleaved. Other examples which avoid the thermodynamic limitations make use of organic substrates in which C-C bond cleavage is accompanied by either a relief of strain energy or formation of a more stable aromatic system. Again the C-C bond effectively gets cleaved.

In the present paper, the authors disclose a method which uses a tungsten metal center and it can be used to cleave a strong C-C bond of an unstrained 6-membered aromatic ring. The reaction proceeds through an unusual chelating di(isocyanide) ligand. Thus, this method provides a new way of functionalizing strong C-C bonds.
A paper by Parkin[4] studies the reactivity of $Mo(PMe_3)_6$ towards heterocyclic nitrogen compounds in transformations relevant to hydrodenitrogenation (HDN). HDN is a process by which nitrogen is removed from fossil fuels for minimizing NO_x emissions. Again, a paper by Parkin[5] discloses a method which uses a molybdenum catalyst, namely, $Mo(PMe_3)_4H_4$ to effect hydrogenation of quinolone, isoquinoline and quinoxaline which is a necessary step in HDN. While studying the hydrodenitrogenation reaction of compounds by using molybdenum, the authors of the present paper found out that molybdenum reacts with quinoxaline via oxidative addition of C-H bond. In order to find a system which can cleave C-N bond of an aromatic ring, the metal tungsten was explored as it shows a greater ability to accomplish bond cleavage via oxidative addition than molybdenum[6].

Scheme 1. Reaction of quinoxaline with the molybdenum and tungsten complexes.

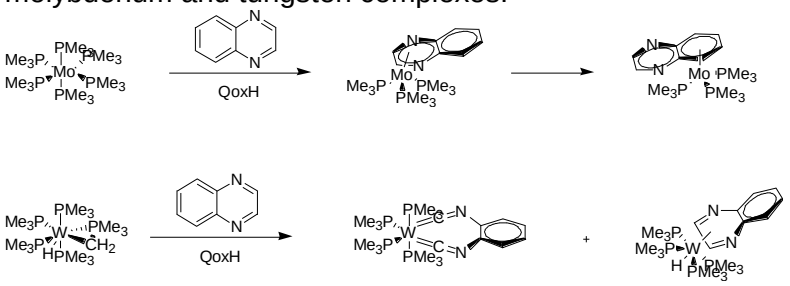

The reaction with tungsten proceeded differently as compared to molybdenum. $W(PMe_3)_4(\eta^2\text{-}CH_2PMe_2)H$ reacts with QoxH to form: 1) $[\kappa^2\text{-}C_2\text{-}C_6H_4(NC)_2]W(PMe_3)_4$ by inducing C-C bond

cleavage and further dehydrogenation and 2) (η^4-C_2N_2-QoxH)$W(PMe_3)_3H_2$ which is the dihydride complex. The dihydride complex does not convert to the C-C bond cleavage product under the reaction conditions. The same transformations were observed for 6-methylquinoxaline and 6,7-dimethylquinoxaline. Hence, the reaction can be applicable to a number of similar substrates. The tetrahydride $W(PMe_3)_4H_4$ is also formed in a very small quantity (<5 %). The source of hydride ligands for the reaction is the hydrogen that is liberated during the formation of the C-C bond cleavage complex, namely, [κ^2-C_2-$C_6H_4(NC)_2$]$W(PMe_3)_4$.

The yield of the dihydride complex (η^4-C_2N_2-QoxH)$W(PMe_3)_3H_2$ increases considerably if the reaction between the tungsten complex and QoxH is carried out in an atmosphere of H_2 which is expected. The same η^4 coordination is observed for the methylated QoxH: (η^4-C_2N_2-Qox^{R2}H)$W(PMe_3)_3H_2$. Where, R_2= H,H ; Me,H ; Me, Me. These complexes provide new important structural motifs for hydrodenitrogenation reaction.

The most significant aspect of this reaction however is the formation of the complex: [κ^2-C_2-$C_6H_2R_2(NC)_2$]$W(PMe_3)_4$ where R= H,H or Me,H or Me,Me. The formation of these complexes involves an aromatic C-C bond cleavage. Aromatic C-C bonds are substantially stronger than the already strong aliphatic C-C bond. A paper by Wigley[7] deals with the C-N bond cleavage in an η^2-(N,C)-Pyridine complex induced by intramolecular metal to ligand alkyl migration as a model for HDN catalysis. IN the present paper, this aforementioned C-C bond cleavage takes place in presence of the more reactive C-N bond which is surprising. These κ^2 complexes can be compared to simple transition metal isocyanide complexes of the type $ML_4(CNR)_2$. The cleaved QoxH fragments, namely, $C_6H_2R_2(NC)_2$ correspond to known di(isocyanide) compounds. These κ^2 complexes exhibit some interesting features:

1) The C-N-C bond angles are around 125-128^o as compared to the almost linear (mean is 172^o) C-N-C bond angles for other transition metal isocyanide complexes. Such bending is consistent with considerable metal to ligand π-backbonding (it has been observed for some monodentate isocyanide compounds). This π-backbonding can be shown as: W=C=N-R rather than the compound being shown as $W-\overset{-}{C}\equiv\overset{+}{N}-R$. A paper by Kuznetsov[8] deals with the study of transition metal complexes with nitriles and isocyanides and π-backbonding has been discussed extensively.

2) The observed average W-C bond length is 1.93Å which is comparable to structurally characterized compounds with $W=CR_2$ double bonds whereas the average bond length for a W-C single bond is much larger at 2.23 Å. This is another evidence for π-backbonding.

3) The stretching frequency of the [κ^2-C_2-$C_6H_2R_2(NC)_2$]$W(PMe_3)_4$ compounds for the CN bond are in the range of 1698 to 1709 cm^{-1}. These values are at the low end for transition metal isocyanide complexes. The normal range is 2310 to 1670 cm^{-1}. This is further evidence of multiple bond character of the W-C bond.

4) The ^{13}C NMR chemical shift of 211.4ppm is also consistent with the backbonding in the κ^2 complexes.

Usually M-C-N-R groups prefer to adopt a linear coordination geometry at nitrogen and carbon and hence, chelating isocyanide ligands are not common[9]. The ligand in this paper o-$(NC)_2C_6H_4$ also serves as a bridging ligand instead of a chelating ligand. A paper by Espinct[10] gives us the example of 1,2-Phenylene diisocyanide as a bridging ligand for metallotriangles. In accordance with this observation, the smallest ring size reported for a complex of a bidentate di(isocyanide) ligand is 12. The ring of the [κ^2-C_2-$C_6H_4(NC)_2$]$W(PMe_3)_4$ consists of 7 members with two W-C-N bonds that are close to linear (165^o to 169^o). this ring is thus exceptionally small for a transition metal complex of a bidentate di(isocyanide) ligand.

Scheme 2. Plausible mechanism for the reaction.

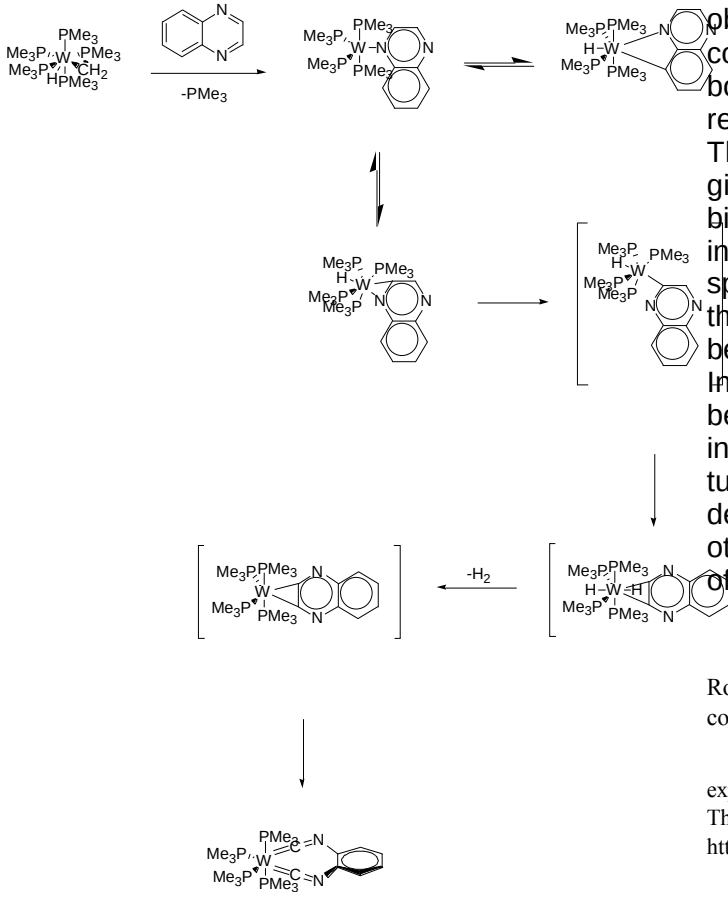

There are several mechanisms proposed for the formation of the [κ^2-C_2-$C_6H_4(NC)_2$]$W(PMe_3)_4$ complex. One mechanism outlined involves the direct insertion of tungsten into the C-C bond which is then followed by two α-hydrogen eliminations. This mechanism has been said to be in accordance with the fact that electron donating substituents on olefins promote C-C bond cleavage. The authors however, present another mechanism which they think is more favorable. In this mechanism, initially there is a series of C-H bond cleavage reactions which gives access to a benzyne type intermediate [η^2-C_2-C_6H_4(NCCN)]$W(PMe_3)_4H_2$. This intermediate is further converted to [κ^2-C_2-$C_6H_4(NC)_2$]$W(PMe_3)_4$ through reductive elimination of H_2 and C-C bond cleavage. The authors cite that this mechanism is supported by a report of ruthenium benzyne complex [η^2-C_6H_4]$Ru(PMe_3)_4$ [11]. This complex can be considered as a structural analogue of the intermediate [η^2-C_2-$C_6H_4(NCCN)_2$]$W(PMe_3)_4H_2$. Some other intermediates that are observed in this reaction are: (η^2-N,C-Qox)$W(PMe_3)_4H$, (κ^2-N,C-Qox)$W(PMe_3)_4H$, (μ-η^2-N,C- **κ^2-**N,C-Qox')$[W(PMe_3)_4H]_2$. The presence of these intermediates confirm that the reaction proceeds through the second mechanism and that C-H bond cleavage is facile in this system. Still the observation of (η^2-N,C-Qox)$W(PMe_3)_4H$ cannot confirm that this species is involved in the C-C bond cleavage as C-H bond cleavage is reversible.

The overall cleavage of the C-C bond in the given system resembles the process by which bis(isocyanide) compounds are formed by base-induced cleavage of diaminoacetylene species[12,13]. Another points the authors note is that the cleaving of acetylenic C-C bonds have been cleaved using metal cluster complexes.

In summary, the authors have provided a beautiful method in which an aromatic C-C bond in quinoxaline can be cleaved by insertion of tungsten to yield a o-diisocyanobenzene derivative. This methodology can be extended to other systems as well thus providing new ways of functionalizing organic molecules.

Acknowledgement. The author is grateful to Professor Joel Rosenthal and the University of Delaware and to the scientific community.

SUPPORTING INFORMATION AVAILABLE: Detailed experimental procedures including spectroscopic and analytical data. This material is available free of charge via the internet at http://pubs.acs.org.

References

(1) Jones, W. D. The fall of the C–C bond. Nature 364, 676–677 (1993).

(2) Jun, C. H. Transition metal-catalyzed carbon-carbon bond activation. Chem. Soc. Rev. 33, 610–618 (2004).

(3) Rybtchinski, B., &. Milstein, D. Metal insertion into C–C bonds in solution. Angew. Chem. Int. Edn Engl. 38, 870–883 (1999).

(4) Zhu, G. Tanski, J. M., Churchill, D. G., Janak, K. E. & Parkin, G. The reactivity of Mo(PMe3)6 towards heterocyclic nitrogen compounds: transformations relevant to hydrodenitrogenation. J. Am. Chem. Soc. 124, 13658–13659 (2002).

(5) Zhu, G. Pang, K. & Parkin, G. New modes for coordination of aromatic heterocyclic nitrogen compounds to molybdenum: catalytic hydrogenation of quinoline, isoquinoline, and quinoxaline byMo(PMe3)4H4. J. Am. Chem. Soc. 130, 1564–1565 (2008).

(6) Buccella, D., &. Parkin, G. p-tert-butylcalix[4] arene complexes of molybdenum and tungsten: reactivity of the calixarene methylene C-H bond and the facile migration of the metal around the phenolic rim of the calixarene. J. Am. Chem. Soc. 128, 16358–16364 (2006).
(7) Gray, S. D. Weller, K. J., Bruck, M. A., Briggs, P. M. & Wigley, D. E. Carbon-nitrogen bond-cleavage in an g2(N, C)-pyridine complex-induced by intramolecular metal-to-ligand alkyl migration - models for hydrodenitrogenation catalysis. J. Am. Chem. Soc. 117, 10678–10693 (1995).
(8) Kuznetsov, M. L. Theoretical studies of transition metal complexes with nitriles and isocyanides. Russ. Chem. Rev. 71, 265–282 (2002).
(9) Hahn, F. E. The coordination chemistry of multidentate isocyanide ligands. Angew. Chem. Int. Edn Engl. 32, 650–665 (1993).
(10) Espinet, P. Soulantica, K. Charmant, J. P. H. & Orpen, A. G. 1,2-Phenylene diisocyanide for metallotriangles. Chem. Commun. 915–916 (2000).
(11) Hartwig, J. F. Bergman, R. G. & Andersen, R. A. Structure, synthesis, and chemistry of (PMe3)4Ru(g2-benzyne). Reactions with arenes, alkenes, and heteroatomcontaining organic-compounds. Synthesis and structure of a monomeric hydroxide complex. J. Am. Chem. Soc. 113, 3404–3418 (1991).
(12) Pombeiro, A. J. L. da Silva, M. & Michelin, R. A. Aminocarbyne complexes derived from isocyanides activated towards electrophilic addition. Coord. Chem. Rev. 218, 43–74 (2001).
(13) Ito, Y. et al. Aromatizing oligomerization of 1,2-di-isocyanoarene to quinoxaline oligomers. J. Chem. Soc. Chem. Commun. 403–405 (1990).

In Situ Formation of an Oxygen-Evolving Catalyst in Neutral Water Containing Phosphate and Co^{2+}

Matthew W. Kanan and Daniel G. Nocera*

The utilization of solar energy on a large scale requires its storage. In natural photosynthesis, energy from sunlight is used to rearrange the bonds of water to oxygen and hydrogen equivalents. The realization of artificial systems that perform "water splitting" requires catalysts that produce oxygen from water without the need for excessive driving potentials.
Here we report such a catalyst that forms upon the oxidative polarization of an inert indium tin oxide electrode in phosphate-buffered water containing cobalt (II) ions. A variety of analytical techniques indicates the presence of phosphate in an approximate 1:2 ratio with cobalt in this material. The pH dependence of the catalytic activity also implicates the hydrogen phosphate ion as the proton acceptor in the oxygen-producing reaction. This catalyst not only forms in situ from earth-abundant materials but also operates in neutral water under ambient conditions.

Sunlight is the only renewable and carbon-neutral energy source of sufficient scale to replace fossil fuels and meet rising global energy demand (*1*). The diurnal variation in local insolation, however, demands a cost-effective storage of solar energy for its large-scale utilization. Of the possible storage methods, nature provides the blueprint for storing sunlight in the form of chemical fuels (*1*, *2*). The primary steps of natural photosynthesis involve the absorption of sunlight and its conversion into spatially separated electron/hole pairs. The holes of this wireless current are then captured by the oxygen-evolving complex (OEC) to oxidize water to oxygen and the electrons are captured by photosystem I to reduce $NADP^+$ (nicotinamide adenine dinucleotide phosphate) to NADPH (the reduced form of $NADP^+$), nature's form of hydrogen (*3*). Thus, the overall primary events of photosynthesis store solar energy in a fuel by rearranging the chemical bonds of water to form H_2 (i.e., NADPH) and O_2.

An approach to duplicating photosynthesis outside of a photosynthetic membrane is to convert sunlight into spatially separated electron/hole pairs within a photovoltaic cell and then capture the charges with catalysts that mediate "water splitting" (*1*, *4*). The four holes are captured by a catalyst at the anode to produce oxygen, and the four electrons are captured by a separate catalyst at the cathode to produce hydrogen. The net result is the storage of solar energy in the chemical bonds of H_2 and O_2.

A key determinant of energy storage in artificial photosynthesis is the efficiency of the water-splitting catalysts. Electrocatalysts that are efficient for solar-to-fuels conversion must operate close to the Nernstian potentials (E) for the H_2O/O_2 and H_2O/H_2 half-cell reactions shown in Scheme 1 (half-cell potentials given in the convention of reduction potentials).

The voltage in addition to E that is required to attain a given catalytic activity—referred to as overpotential—limits the efficiency of converting light into catalytic current. Of the two reactions, the H_2O/O_2 reaction is considerably more complex (*5*). This reaction requires a four-electron oxidation of two water molecules coupled to the removal of four protons to form a relatively weak oxygen-oxygen bond. In addition to controlling this proton-coupled electron transfer (PCET) (*6*, *7*), a catalyst must tolerate prolonged exposure to oxidizing conditions. Even at the thermodynamic limit, water oxidation requires an oxidizing power that causes most chemical functional groups to degrade. Accordingly, the generation of oxygen from water presents a substantial challenge toward realizing artificial photosynthesis (*8*).

The fine-tuned molecular machinery of the OEC oxidizes water at a low overpotential using a Mn_4O_4Ca cluster (*9*–*12*). Outside the OEC, examples of water oxidation catalysts include first-row spinel and perovskite metal oxides, which require concentrated basic solutions (pH > 13) and moderate overpotentials (<400 mV), and precious metals and precious metal oxides, which operate with similar efficiencies under acidic conditions (pH < 1) (*13*–*15*). However, few catalysts operate in neutral water under ambient conditions. Neutral water is oxidized at Pt electrodes, and some precious metal oxides have been reported to operate electrocatalytically in neutral or weakly acidic solutions (*16*). The development of an earth-abundant, first-row catalyst that operates at pH 7 at low overpotential remains a fundamental chemical challenge. Here, we report an oxygen-evolving catalyst that forms in situ upon anodic polarization of an inert electrode in neutral aqueous phosphate solutions containing Co^{2+}. Oxygen generation occurs under benign conditions: pH = 7, 1 atm, and room temperature.

Cobalt ions in the presence of chemical oxidants such as $Ru(bpy)_3^{3+}$ (bpy, bipyridine; E^o = 1.26, where E^o is the standard potential) catalyze the oxidation of water to O_2 in neutral phosphate solutions (*17*, *18*). Oxygen yields drop in these reactions when oxidized Co species precipitate from solution because the catalytically active species is removed from the solution-phase reaction. However, an oxidation-induced precipita-

$$O_2 + 4H^+ + 4e^- \rightleftharpoons 2H_2O \qquad E_{anodic} = 1.23\,V - 0.059\,(pH)\,V \text{ vs NHE}$$

$$4H^+ + 4e^- \rightleftharpoons 2H_2 \qquad E_{cathodic} = 0\,V - 0.059\,(pH)\,V \text{ vs NHE}$$

$$2H_2O \longrightarrow 2H_2 + O_2 \qquad E_{rxn} = -1.23\,V$$

Scheme 1.

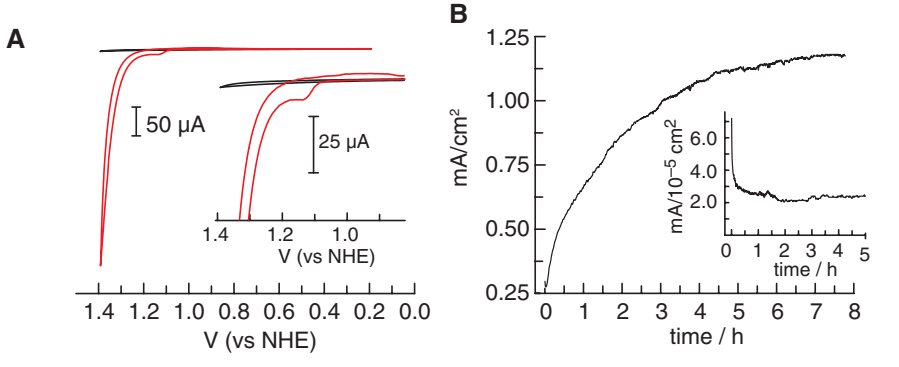

Fig. 1. (**A**) Cyclic voltammagram in 0.1 M KPi electrolyte at pH 7.0 with no Co^{2+} ion present (black line) and with 0.5 mM Co^{2+} present (red line). The potential was measured against a Ag/AgCl reference and converted to NHE potentials by using E(NHE) = E(Ag/AgCl) + 0.197 V. (**B**) Current density profile for bulk electrolysis at 1.29 V (versus NHE) in 0.1 M KPi electrolyte at pH 7.0 containing 0.5 mM Co^{2+}. (Inset) Profile in the absence of Co^{2+}.

Department of Chemistry, 6-335, Massachusetts Institute of Technology, Cambridge, MA 02139–4307, USA.

*To whom correspondence should be addressed. E-mail: nocera@mit.edu

tion may be exploited to prepare electrocatalysts in situ if the precipitated material remains catalytically active and can be oxidized at an electrode surface. To explore this possibility for Co-catalyzed water oxidation, we examined electrochemical oxidations of aqueous solutions containing phosphate and Co^{2+}. Cyclic voltammetry of a 0.5 mM solution of $Co(NO_3)_2$ in 0.1 M potassium phosphate pH 7.0 (KPi electrolyte) exhibits an oxidation wave at $E_p = 1.13$ V (where E_p is the peak potential) versus the normal hydrogen electrode (NHE), followed by the onset of a strong catalytic wave at 1.23 V (Fig. 1A). A broad, relatively weak reduction wave is observed on the cathodic scan. The presence of a catalytic wave prompted us to examine the electrode activity during controlled-potential electrolysis.

Indium tin oxide (ITO) was used as the electrode for bulk electrolysis to ensure a minimal background activity for O_2 production. An electrolysis at 1.29 V without stirring in neutral KPi electrolyte containing 0.5 mM Co^{2+} exhibits a rising current density that reaches a peak value >1 mA/cm^2 after 7 to 8 hours (Fig. 1B). During this time, a dark coating forms on the ITO surface, and effervescence from this coating becomes increasingly vigorous (*19*).The same results are observed with either $CoSO_4$, $Co(NO_3)_2$, or $Co(OTf)_2$ (where OTf = triflate) as the Co^{2+} source, which indicates that the original Co^{2+} counterion is unimportant and that this activity does not depend on an impurity found in a specific source. The amount of charge passed during the course of an 8-hour electrolysis far exceeds what could be accounted for by stoichiometric oxidation of the Co^{2+} in solution (*20*). These observations are indicative of the in situ formation of an oxygen-evolving catalyst. Catalyst formation also proceeds on a fluorine tin oxide electrode and if KPi is replaced by NaPi electrolyte. In a control experiment, the current density during bulk electrolysis under identical conditions in the absence of Co^{2+} rapidly drops to a baseline level of ~25 nA/cm^2 (inset in Fig. 1B).

The morphology of the electrode coating formed during electrolysis in the presence of Co^{2+} was examined by scanning electron microscopy (SEM). The electrodeposited material consists of particles that have coalesced into a thin film and individual micrometer-sized particles on top of the film (Fig. 2A). The ITO substrate can be seen through cracks in the film that form upon drying, as evidenced by particles that are split into complementary pieces. The film thickness gradually increases over the course of the electrodeposition (see fig. S4 for additional images). At maximum activity under these electrolysis conditions, the film is >2 μm thick. The x-ray powder diffraction pattern of an electrodeposited catalyst shows broad amorphous features and no peaks indicative of crystalline phases other than the peaks associated with the ITO layer (fig. S1).

In the absence of detectable crystallites, the composition of the electrodeposited material was analyzed by three complementary techniques. Energy-dispersive x-ray analysis (EDX) spectra were obtained from multiple 100-to-300–m^2 regions of several independently prepared samples. These spectra identify Co, P, K, and O as the principal elemental components of the material (Fig. 2B). Although the material's morphology is not ideally suited for quantitative EDX, the analyses consistently indicate a Co:P:K ratio between ~2:1:1 and 3:1:1. To obtain an independent determination of elemental composition, electrolysis was performed with several larger ITO electrodes; the deposited material was scraped off and combined for a total yield of ~3 mg. Microanalytical elemental analysis of the combined material indicates 31.1% Co, 7.70% P, and 7.71% K, corresponding to a 2.1:1.0:0.8 Co:P:K ratio. Finally, the surface of an electrodeposited catalyst on the ITO substrate was analyzed by x-ray photoelectron spectroscopy (XPS). All peaks in the XPS spectra are accounted for by the elements detected above, in addition to In and Sn from the ITO substrate. The high-resolution P 2p peak at 133.1 eV is consistent with phosphate. The Co 2p peaks at 780.7 and 795.7 eV are in a range typical of Co^{2+} or Co^{3+} bound to oxygen (fig. S2) (*21*). Together, the x-ray diffraction and analytical results indicate that electrolysis of a Co^{2+} solution in neutral KPi electrolyte results in the electrodeposition of an amorphous Co oxide or hydroxide incorporating a substantial amount of phosphate anion at a stoichiometric ratio of roughly 2:1:1 for Co:P:K.

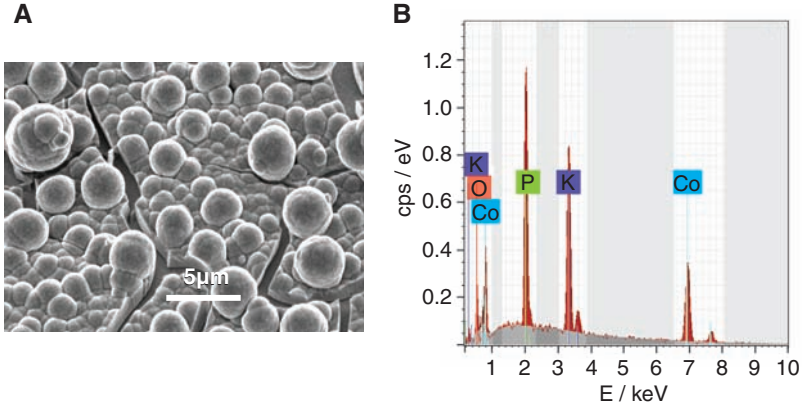

Fig. 2. (**A**) SEM image (30° tilt) of the electrodeposited catalyst after 30 C/cm^2 were passed in 0.1 M KPi electrolyte at pH 7.0, containing 0.5 mM Co^{2+}. The ITO substrate can be seen through cracks in the dried film. (**B**) Typical EDX histogram acquired at 12 kV. cps, counts per second.

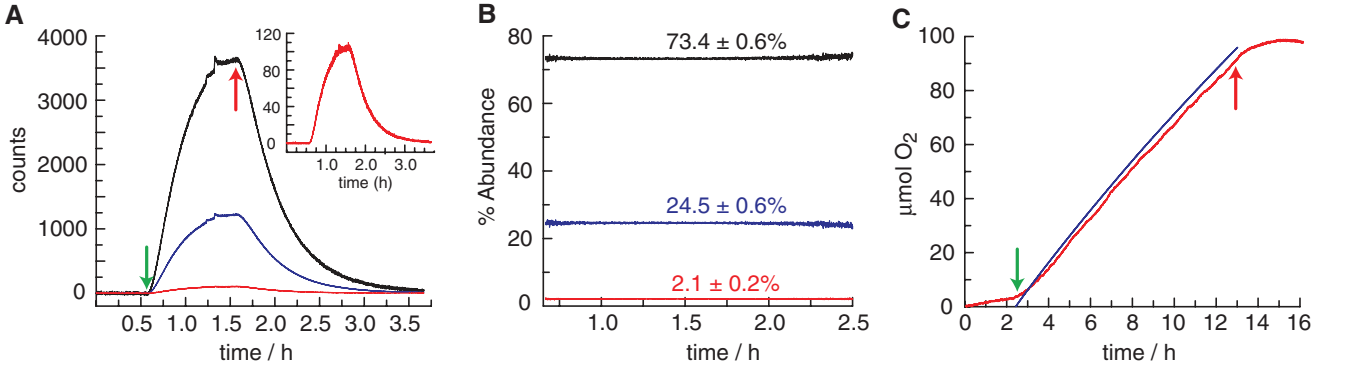

Fig. 3. (**A**) Mass spectrometric detection of isotopically labeled $^{16,16}O_2$ (black line), $^{16,18}O_2$ (blue line), and $^{18,18}O_2$ (red line) during electrolysis of a catalyst film on ITO in a KPi electrolyte containing 14.6% $^{18}OH_2$. The green arrow indicates the initiation of electrolysis at 1.29 V (NHE), and the red arrow indicates the termination of electrolysis. (Inset) Expansion of the $^{18,18}O_2$ signal. (**B**) Percent abundance of each isotope over the course of the experiment. Average observed abundance of ±2σ is indicated above each line. Statistical abundances are 72.9, 24.9, and 2.1%. (**C**) O_2 production measured by fluorescent sensor (red line) and theoretical amount of O_2 produced (blue line), assuming a Faradic efficiency of 100%. The green arrow indicates the initiation of electrolysis at 1.29 V, and the red arrow indicates the termination of electrolysis.

Three experiments were performed to establish that the catalytic activity observed with this material corresponds to authentic water oxidation. Each of these experiments was performed in neutral KPi electrolyte in the absence of Co^{2+}. Catalyst coatings (~1.3 cm^2) were prepared in a preliminary step as described above and stored under ambient laboratory conditions until they were used.

To confirm that water is the source of the O_2 produced, electrolysis was performed in helium-saturated electrolyte containing 14.6% $^{18}OH_2$ in a gas-tight electrochemical cell in line with a mass spectrometer. The helium carrier gas was continuously flowed through the headspace of the anodic compartment into the mass spectrometer, and the relative abundances of $^{32}O_2$, $^{34}O_2$, and $^{36}O_2$ were monitored at 2-s intervals. Within minutes of initiating electrolysis at 1.29 V, the signals for the three isotopes began to rise above their background levels as the O_2 produced by the catalyst escaped into the headspace. Upon terminating the electrolysis 1 hour later, these signals slowly returned to their background levels (Fig. 3A). The $^{32}O_2$, $^{34}O_2$, and $^{36}O_2$ isotopes were detected in the statistical ratio (72.9, 24.9, and 2.1% relative abundances, respectively) (Fig. 3B).

The Faradaic efficiency of the catalyst was measured with a fluorescence-based O_2 sensor. Electrolysis was performed in KPi electrolyte in a gas-tight electrochemical cell under an N_2 atmosphere with the sensor placed in the headspace. After initiating electrolysis at 1.29 V, the percentage of O_2 detected in the headspace rose in accord with what was predicted by assuming that all of the current was caused by $4e^-$ oxidation of water to produce O_2 (Fig. 3C). The amount of O_2 produced (95 μmol, 3.0 mg) greatly exceeds the amount of catalyst (~0.2 mg), which shows no perceptible decomposition during the course of the experiment.

The stability of phosphate under catalytic conditions was assayed by ^{31}P nuclear magnetic resonance (NMR). Electrolysis in a two-compartment cell with 10 mL of KPi electrolyte (1 mmol phosphate) on each side was allowed to proceed until 45 C had been passed through the cell (0.46 mmol electrons). Electrolysis solutions from both chambers show single, clean ^{31}P resonances, which indicate that the electrolyte is robust under these conditions (fig. S3). Together, the mass spectrometry, Faradaic efficiency, and ^{31}P NMR results demonstrate that the electrodeposited catalyst cleanly oxidizes H_2O to O_2 in neutral KPi solutions.

The current density of a catalyst on ITO was measured as a function of the overpotential (η) in KPi electrolyte without Co^{2+} (black circles in Fig. 4A). At pH 7.0, appreciable catalytic current is observed beginning at η = 0.28 V, and a current density of 1 mA/cm^2 (corresponding to 9 μmol O_2 cm^{-2} h^{-1}) requires η = 0.41 V. The Tafel plot deviates slightly from linearity, possibly reflecting an uncompensated iR drop caused by the surface resistivity of the ITO (8 to 12 ohms per square). Substantial improvements in the activity profile may be attainable without changing the catalyst composition by depositing on alternative substrates or improving ohmic contact to the ITO.

The catalyst used to obtain the Tafel plot at pH 7 was subsequently transferred to KPi electrolyte at pH 4.6, and the current density was measured at a constant applied potential (1.24 V) while the pH was increased incrementally to 9.4 by adding aliquots of concentrated KOH. A plot of the log of current density versus pH exhibits a steep initial rise that levels off in the high-pH range such that increasing the pH from 8 to 9.4 at this applied potential has little effect (Fig. 4B). These data can be converted to a Tafel plot by using Eq. 1 (Scheme 1) and accounting for iR drop (see Fig. 4 legend). A comparison to the Tafel plot obtained at pH 7 indicates that the catalyst exhibits approximately Nernstian behavior from pH 5 to 8: Increasing the pH by one unit at constant applied potential (1.24 V) has nearly the same effect as increasing the overpotential by 0.059 V at pH 7 (red circles in Fig. 4A). This result implicates a reversible ne^-, nH^+ removal before the rate-determining step for O_2 evolution in this pH range (here, n is the number of equivalents). Thus, an important component of the activity at pH 7 with this catalyst is the existence of one or more intermediates preceding O_2 formation that are deprotonated reversibly by HPO_4^{2-} in a PCET event (*22*). The pH-independent behavior above pH 8 at the applied potential may indicate a change in mechanism, most likely involving a deprotonated intermediate.

In addition to mediating the deprotonation required for catalysis, the KPi electrolyte provides a medium for in situ catalyst formation. Given that phosphate is a structural element and that the catalyst forms under oxidizing conditions, it is plausible that deposition is driven by the interaction of phosphate and Co^{3+}. By judicious choice of other metal-anion pairs or combinations of multiple metals and anions, it may be possible to access other oxygen-evolving catalysts that form in situ and operate in neutral solutions. In situ formation is advantageous because, in principle, it enables catalyst deposition on a variety of substrates, including those that are too delicate to tolerate traditional catalyst preparation techniques. This attribute is important for interfacing a catalyst with a variety of electrochemical or photoelectrochemical cell designs.

In situ formation also implies a self-repair mechanism. Proposed molecular mechanisms involving O_2/H_2O cycles at Co centers suggest that catalytic reactions cycle among Co^{2+}-, Co^{3+}-, and Co^{4+}-oxo oxidation states (*18*, *23*). The propensity of metal ion dissolution has been shown to correlate with ligand substitution (*24*). Given that Co^{3+} is substitutionally inert relative to Co^{2+}, a dynamic equilibrium between Co^{2+}-HPO_4^{2-} in solution and Co^{3+}-HPO_4^{2-} on the anodically poised electrode may be established. More generally, if a catalytic cycle involves an oxidation state that is prone to dissolution, this process can be countered by continual catalyst formation by establishing an equilibrium with the judicious choice of an anion.

The results reported herein highlight a new area of exploration for the development of easily prepared, earth-abundant catalysts that oxidize water. If artificial photosynthesis is to enable the storage of solar energy commensurate with global demand, water-splitting chemistry will need to be performed at a daunting scale. Storing the equivalent of the current energy demand would require splitting more than 10^{15} mol/year of water, which is roughly 100 times the scale of nitrogen fixation by the Haber-Bosch process. The conditions under which water splitting is performed will determine how solar energy is deployed. The catalyst reported here has many elements of natural photosynthesis, including (i) its formation from earth-abundant metal ions in aqueous solution, (ii) a plausible pathway for self-repair, (iii) a carrier for protons in neutral water, and (iv) the generation of O_2 at low overpotential, neutral pH, 1 atm, and room temperature.

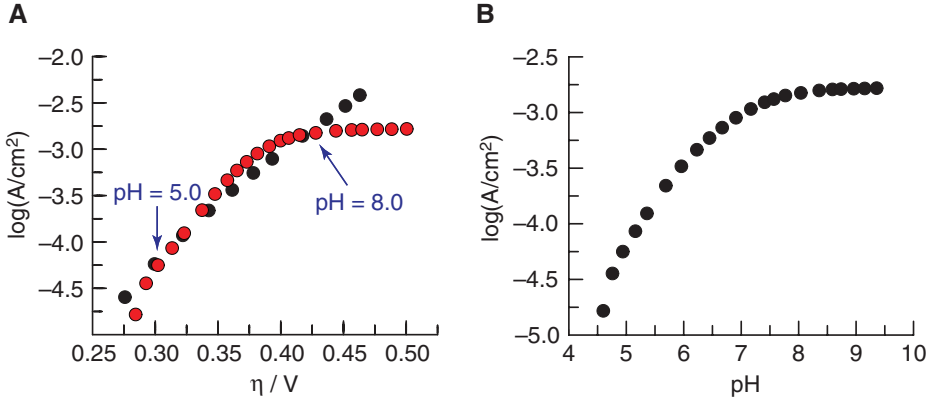

Fig. 4. (**A**) Tafel plot (black circles), $\eta = (V_{appl} - iR) - E(pH\ 7)$ (where V_{appl} is the applied potential), of a catalyst film on ITO in 0.1 M KPi electrolyte pH 7.0, corrected for the iR drop of the solution. pH data were converted into a Tafel plot (red circles), $\eta = (V_{appl} + 0.059\Delta pH - iR) - E(pH\ 7)$, assuming Nernstian behavior and correcting for the iR drop of the solution. The pH = 5 and pH = 8 data points are indicated by arrows. (**B**) Current density dependence on pH in 0.1 M KPi electrolyte. The potential was set at 1.24 V (versus NHE) with no iR compensation.

References and Notes

1. N. S. Lewis, D. G. Nocera, *Proc. Natl. Acad. Sci. U.S.A.* **103**, 15729 (2006).
2. N. Nelson, A. Ben-Shem, *Nat. Rev. Mol. Cell Biol.* **5**, 971 (2004).
3. J. Barber, *Philos. Trans. R. Soc. London Ser. A* **365**, 1007 (2007).
4. A. J. Bard, M. A. Fox, *Acc. Chem. Res.* **28**, 141 (1995).
5. T. A. Betley, Q. Wu, T. Van Voorhis, D. G. Nocera, *Inorg. Chem.* **47**, 1849 (2008).
6. R. I. Cukier, D. G. Nocera, *Annu. Rev. Phys. Chem.* **49**, 337 (1998).
7. M. H. V. Huynh, T. J. Meyer, *Chem. Rev.* **107**, 5004 (2007).
8. R. Eisenberg, H. B. Gray, *Inorg. Chem.* **47**, 1697 (2008).
9. K. N. Ferreira, T. M. Iverson, K. Maghlaoui, J. Barber, S. Iwata, *Science* **303**, 1831 (2004), published online 5 February 2004; 10.1126/science.1093087.
10. S. Iwata, J. Barber, *Curr. Opin. Struct. Biol.* **14**, 447 (2004).
11. J. Yano *et al.*, *Science* **314**, 821 (2006).
12. B. Loll, J. Kern, W. Saenger, A. Zouni, J. Biesiadka, *Nature* **438**, 1040 (2005).
13. S. Trassati, in *Electrochemistry of Novel Materials*, J. Lipkowski, P. N. Ross, Eds. (VCH, New York, 1994), chap. 5.
14. J. O. Bockris, T. J. Otagawa, *J. Electrochem. Soc.* **131**, 290 (1984).
15. M. R. Tarasevich, B. N. Efremov, in *Electrodes of Conductive Metal Oxides*, S. Trasatti, Ed. (Elsevier, Amsterdam, 1980), chap. 5.
16. M. Yagi, E. Tomita, S. Sakita, T. Kuwabara, K. Nagai, *J. Phys. Chem. B* **109**, 21489 (2005).
17. V. Y. Shafirovich, N. K. Khannanov, V. V. Strelets, *Nouv. J. Chim.* **4**, 81 (1980).
18. B. S. Brunschwig, M. H. Chou, C. Creutz, P. Ghosh, N. Sutin, *J. Am. Chem. Soc.* **105**, 4832 (1983).
19. Materials and methods, videos of an active electrode, and figs. S1 to S4 are available as supporting material on *Science* Online.
20. In a typical experiment, >40 C are passed over 8 hours, whereas oxidation of all the Co^{2+} in solution requires 1.9 C per oxidation-state change.
21. K. D. Bomben, J. F. Moulder, P. E. Sobol, W. F. Stickel, in *Handbook of X-Ray Photoelectron Spectra: A Reference Book of Standard Spectra for Identification*, J. Chastain, Ed. (Perkin Elmer, Eden Prairie, MN, 1992).
22. T. Irebo, S. Y. Reece, M. Sjödin, D. G. Nocera, L. Hammarström, *J. Am. Chem. Soc.* **129**, 15462 (2007).
23. C. J. Chang, Z.-H. Loh, C. Shi, F. C. Anson, D. G. Nocera, *J. Am. Chem. Soc.* **126**, 10013 (2004).
24. W. H. Casey, *J. Colloid Interface Sci.* **146**, 586 (1991).

25. This work was supported by a grant from the NSF Chemical Bonding Center (CHE-0802907). M.W.K. is supported by a Ruth L. Kirchenstein National Research Service Award postdoctoral fellowship provided by NIH (F32GM07782903). We thank E. Shaw for obtaining XPS spectra, G. Henoch for providing the videos in the supporting online material, and Y. Surendranath for many productive discussions.

Supporting Online Material

www.sciencemag.org/cgi/content/full/1162018/DC1
Materials and Methods
Figs. S1 to S4
Movies S1 and S2

19 June 2008; accepted 18 July 2008
Published online 31 July 2008;
10.1126/science.1162018
Include this information when citing this paper.

The Global Atmospheric Circulation on Moist Isentropes

Olivier Pauluis,[1]* Arnaud Czaja,[2] Robert Korty[3]

The global atmospheric circulation transports energy from the equatorial regions to higher latitudes through a poleward flow of high-energy and -entropy parcels and an equatorward flow of air with lower energy and entropy content. Because of its turbulent nature, this circulation can only be described in some averaged sense. Here, we show that the total mass transport by the circulation is twice as large when averaged on moist isentropes than when averaged on dry isentropes. The additional mass transport on moist isentropes corresponds to a poleward flow of warm moist air near Earth's surface that rises into the upper troposphere within mid-latitudes and accounts for up to half of the air in the upper troposphere in polar regions.

Earth absorbs shortwave radiation from the Sun and emits back longwave radiation to space. Although the total amounts of energy received and emitted are about equal, Earth absorbs more energy than it emits in the equatorial regions and emits more energy than it absorbs at high latitudes (*1*). Such imbalance requires an energy transport by the atmosphere and the oceans, with the former responsible for the bulk of the transport in mid-latitudes (*2*). Determining the relationship between the atmospheric energy transport and the global distribution of temperature and humidity is a central question for our understanding of the Earth's climate.

Averaging the global atmospheric circulation usually implies computing a zonal and temporal mean over a sufficiently long period. One of the most common descriptions is the Eulerian mean circulation (*1*), obtained by averaging the flow at constant pressure or geopotential height. The Eulerian mean stream function Ψ_p is defined as

$$\Psi_p(p,\phi) = \frac{1}{\tau}\int_0^\tau \int_0^{2\pi} \int_p^{p_{\mathrm{surf}}} va\cos\phi \frac{dp}{g} d\lambda dt \quad (1)$$

Here, p is pressure, ϕ is latitude, τ is the time period over which the average is computed, p_{surf} is surface pressure, λ is longitude, a is Earth's radius, v is the meridional velocity, and g is the gravitational acceleration. Figure 1A shows the annual mean stream function on pressure surfaces based on the National Centers for Environmental Prediction–National Center for Atmospheric Research (NCEP-NCAR) Reanalysis monthly data (*3*) from January 1970 to December 2004. The Eulerian-mean circulation exhibits a three-cell structure in each hemisphere: the Hadley cell in the tropics, the Ferrel cell in mid-latitudes, and a polar cell at high latitudes. The Hadley and polar cells, with air parcels moving poleward at high altitude and equatorward at low altitude, are direct circulations that transport energy toward the poles. In the Ferrel cell, the flow is poleward near the surface and equatorward at high altitude. This corresponds to an energy transport toward the equator. Nonetheless, in mid-latitudes, synoptic-scale (~1000 km) eddies transport more energy toward the poles than is brought equatorward by the Ferrel cell, so that the total energy transport in the atmosphere remains poleward.

An alternative to the Eulerian mean circulation is to average the circulation on isentropic surfaces (*4*–*6*). In atmospheric sciences, it is common to use the potential temperature θ instead of entropy. The potential temperature is given by $\theta = \left(\frac{p_0}{p}\right)^{\frac{R}{C_p}} T$, with p the pressure, R the ideal gas constant, C_p the specific heat, T the temperature, and p_0 = 1000 mbar an arbitrary reference pressure. Potential temperature is conserved for reversible adiabatic transformations in the absence of a phase transition, and a surface of constant potential temperature corresponds to isentropic surfaces. The stream function $\Psi_\theta(\theta,\phi)$ on potential temperature surfaces is defined by

$$\Psi_\theta(\theta_0,\phi) = \frac{1}{\tau}\int_0^\tau \int_0^{2\pi} \int_0^{p_{\mathrm{surf}}} H(\theta_0-\theta) va\cos\phi \frac{dp}{g} d\lambda dt \quad (2)$$

Here, $H(x)$ is the Heavyside function, with $H(x) = 1$ for $x \geq 0$ and $H(x) = 0$ for $x < 0$. Figure 1B shows the annual mean stream function on potential temperature surfaces based on the NCEP-NCAR Reanalysis daily data from January 1970 to December 2004.

In contrast to the Eulerian mean circulation, the circulation in isentropic coordinates exhibits a single overturning cell in each hemisphere. Because the atmosphere is stratified in potential temperature ($\partial_z\theta > 0$), the isentropic circulation corresponds to a poleward flow at upper levels balanced by a return flow near Earth's surface—in the direction opposite to the Eulerian mean circulation (*4*). The meridional mass transport on an isentrope can be written as

$$\overline{\rho_\theta v} = \overline{\rho}_\theta \overline{v} + \overline{\rho_\theta' v'} \quad (3)$$

[1]Courant Institute of Mathematical Sciences, New York University, 251 Mercer Street, New York, NY 10012, USA. [2]Space and Atmospheric Physics Group, Department of Physics, Imperial College, Huxley Building, Room 726, London SW7 2AZ, UK. [3]Department of Atmospheric Sciences, Texas A&M University, 3150 TAMU, College Station, TX 77843–3150, USA.

*To whom correspondence should be addressed. E-mail: pauluis@cims.nyu.edu

Review of: In Situ Formation of an Oxygen-Evolving Catalyst in Neutral Water Containing Phosphate and Co^{2+}

Eric Guardino*

Department of Chemistry University of Delaware, Newark, DE 19716 USA

RECEIVED DATE 11-23-10; **eguardin@udel.edu**

The world is in an energy crisis and in need of a renewable resource for energy. Solar energy is a renewable source that could provide the energy that is needed, but for it to be an effective source of energy there needs to be a way to store the energy it can produce. Nature stores solar energy by converting water into oxygen and hydrogen through photosynthesis. Artificial systems of water splitting need catalysts that can split water without very high potentials. This paper reports a catalyst that forms on an inert indium tin oxide electrode in phosphate-buffered water containing cobalt(II) ions. Many techniques were used to determine that this catalyst splits water with very little overpotential. The catalytic activity is pH dependent and the hydrogen phosphate ion is the proton acceptor in the oxygen-producing reaction. The catalyst forms in situ from earth-abundant materials and also functions in neutral water under ambient conditions.

CO_2 levels are rising at a rapid rate and are currently greater than 380 ppm. Over the past 650,000 years and probably longer, CO_2 levels have been between 210 and 300 ppm. At the rate CO_2 levels have been increasing the concentration of CO_2 is expected to be between 550 – 650 ppm before the end of the 21st century. The exact repercussions of a CO_2 concentration this high are not for certain, but it could have potentially disastrous effects on the environment.

In order to try and contain the CO_2 level and keep it from rising indefinitely, carbon neutral energy sources are needed. There are three main sources of carbon neutral energy that could be employed to help slow the increase of CO_2 concentration. The three ways are nuclear fission, carbon capture and storage, and renewable energy. The problem with using nuclear fission is the impracticality of building enough nuclear reactors in a short enough period of time to have the desired effect. A nuclear reactor would need to be built every 1.6 days for the next 45 years to produce enough power to limit CO_2 emissions. The time scale for nuclear fission is too long to have an important effect on carbon emissions in the near future. Carbon capture and storage involves dissolving CO_2 into underground aquifers and keeping it there. Underground aquifers can leak and if this is the case the trapped CO_2 will end up back in the atmosphere. It is very difficult to determine the amount of leakage in an aquifer and even if it is determined for one aquifer, every aquifer is different. If leakage can be minimized CO_2 sequestration through this method could help limit CO_2 emissions in the short term, but is not a long term solution. The third way of slowing down the carbon emission rate is to use renewable energy. There are multiple forms of renewable energy including biomass, wind power, and solar power. Of these three sources of energy solar power provides the greatest amount. More solar energy strikes the surface of the earth in one hour than all of the energy consumed on the planet in one year.

The use of solar power requires the capture of energy from the sun and then its storage. Due to the intermittency of sunlight, storage of excess energy produced during the day is vital to making solar power a viable energy source. There are three main ways to store energy on the scale needed to power the world when the sun is not out. The first is to store the energy in batteries, but there are no batteries cheap enough to store the required amount of energy and there is not very much room for improvement in battery technology. A second way to store energy would be to store it mechanically. For example, the excess energy during the day could be used to power a turbine to pump water up hill and then at night the water would flow back down and create energy. This method is not practical due to the large volumes of water that would need to be pumped and released every day. A third way in which solar energy could be stored is by storing it chemically. This means using solar energy to break and make chemical bonds. Nature stores solar energy chemically through photosynthesis. In photosynthesis the energy from the sun is used to convert water molecules into oxygen and natures equivalent of hydrogen, NADPH (1).

One way to recreate photosynthesis outside of a cellular membrane is to convert the sunlight into spatially separated electron/hole pairs and then capture the charges with catalysts that mediate water splitting. The holes are found at the anode and a catalyst there produces oxygen whereas the electrons are found at the cathode and a catalyst turns them into hydrogen. This process stores the solar energy in the chemical bonds of H_2 and O_2 (2). Bard and Fox state that figuring out how to efficiently undergo this process is the holy grail of chemistry (3). The major problem with this is the efficiency of the catalyst. Efficient catalysts will operate close to the Nernstian potentials for the half-cell reactions and must be able to withstand oxidizing conditions. The half-cell reactions for the oxidation of water can be seen in Scheme 1 (2).

Half-cell reactions are a part of reduction-oxidation (redox) chemistry. Redox chemistry is a class of chemistry that involves the transfer of electrons among reactants. In a redox reaction there are two parts (halves) of the reaction, the oxidation half and the reduction half. The reason a redox equation can be broken into two halves is that in order for an oxidation to occur a reduction also needs to occur. This is because when a chemical species is oxidized it loses electrons and these electrons need to go into another molecule. When this second molecule gains these electrons that is called

Scheme 1. Half-Cell Reactions for the Oxidation of Water

$$O_2 + 4H^+ + 4e^- \rightleftharpoons 2H_2O \qquad E_{anodic} = 1.23\ V - 0.059\ (pH)\ V\ vs\ NHE$$

$$4H^+ + 4e^- \rightleftharpoons 2H_2 \qquad E_{cathodic} = 0\ V - 0.059\ (pH)\ V\ vs\ NHE$$

$$2H_2O \longrightarrow 2H_2 + O_2 \qquad E_{rxn} = -1.23\ V$$

Scheme 2. Standard Hydrogen Electrode Potential Half Reaction

$$2H^+_{(aq)} + 2e^- \rightarrow H_2 \quad E = 0\ V$$

reduction. Every half reaction has a potential assigned to it that is referenced to the standard hydrogen electrode. The standard hydrogen electrode undergoes the half reaction shown in Scheme 2 and is assigned a potential of 0 V.

The catalyst within a cell that splits water is called the oxygen-evolving complex (OEC). The OEC uses a Mn_4O_4Ca cluster to oxidize water to oxygen and release electrons that reduce $NADP^+$ into NADPH. Other catalysts that can oxidize water are first row spinel and perovskite metal oxides and precious metals and their oxides. The former require moderate overpotentials and very basic solutions (pH 13-15) and the latter have similar efficiencies, but require very acidic solutions (pH <1) (2). An overpotential is the difference between the amount of current used to complete a reaction and how much current is needed theoretically. For every electrochemical reaction done the smallest overpotential possible is desired because that would make the reaction the most efficient.

There are very few catalysts that oxidize water under neutral conditions. Pt electrodes can reduce neutral water along with some precious metal oxides when operated electrocatalytically (2). Sutin et. al. reported a Co^{2+} catalyst that oxidized water to O_2 at neutral pH. In that paper they use $Ru(bpy)_3^{3+}$ and they believe the Co^{2+} goes through a Co^{4+} intermediate before forming H_2O_2 and regenerating Co^{2+} (4). This paper reports an oxygen-evolving catalyst that forms in situ in neutral aqueous phosphate solutions containing Co^{2+}.

It has been shown that Co^{2+} ions in the presence of oxidants in neutral phosphate solutions catalyze the oxidation of water to O_2. In these reactions cobalt oxides precipitate out and cause the yields of the reactions to diminish. This paper proposes that if the precipitates were still catalytically active there would be no drop off in production with the formation of solid cobalt oxides.

Cyclic voltammetry was performed on an aqueous solution containing phosphate and cobalt ions. An oxidation wave was observed at E_p=1.13 V vs. NHE along with a strong catalytic wave that began at 1.23 V (Figure 1) (2). Cyclic voltammetry is an electrochemical technique that involves a working electrode, a counter electrode, and a reference electrode. The working electrode is the electrode where the reaction of interest takes place whereas the counter electrode is just there to make sure current can flow through the system. The reference electrode is a stable electrode with a well-known potential. The use of a reference electrode allows for the potential of the cell to be determined. Currently there is no way to determine the potential of a cell absolutely, it must be referenced to a known potential.

Bulk electrolysis was performed using an indium tin oxide (ITO) working electrode to minimize the background activity of O_2. When the peak current is reached (>1 mA/cm^2) a dark coating forms on the ITO electrode and effervescence increases rapidly (Figure 1). To rule out the possibility of this effervescence coming from the anion or an impurity in solution the same results were observed with various Co^{2+} salts. These results are due to the formation of an oxygen evolving catalyst on the ITO electrode.

The compound formed on the ITO electrode was analyzed by energy-dispersive x-ray analysis (EDX), microanalytical elemental analysis, and x-ray photoelectron spectroscopy (XPS). The EDX experiment consistently returned Co:P:K ratios between 2:1:1 and 3:1:1 (Figure 2). The microanalytical elemental analysis determined the compound was composed of 31.1% Co, 7.70% P, and 7.71% K which corresponds to a 2.1:1.0:.8 Co:P:K ratio. The XPS spectra contained Co, P, K, In, and Sn. The indium and tin were from the electrode whereas the cobalt, phosphorous and potassium were from the

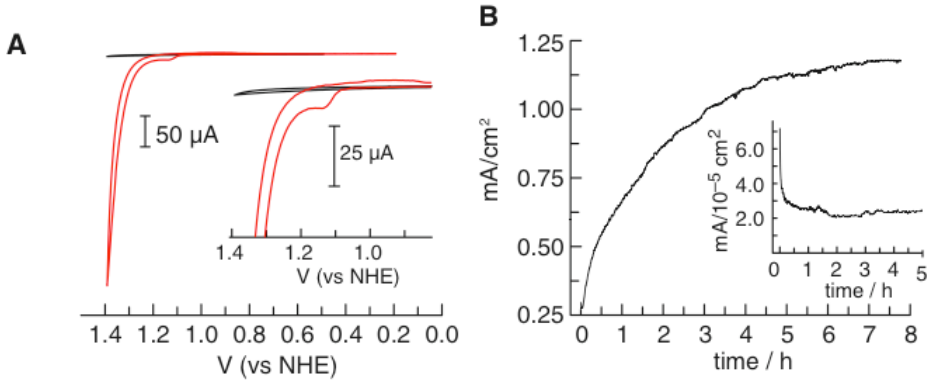

Figure 1. (A) Cyclic voltammagram at pH 7 where the black line is without Co^{2+} ions and the red line is with Co^{2+}. (B) Current density profile for bulk electrolysis at 1.29 V at pH 7 containing Co^{2+}. (Inset) In the absence of Co^{2+}.

compound. There was a phosphorous 2p peak at 133.1 eV that corresponds to phosphate and there were Co 2p peaks at 780.7 and 795.7 eV. These two peaks correspond to typical Co^{2+} or Co^{3+} bound to oxygen. All three of these experiments lead to the conclusion that an amorphous cobalt oxide or hydroxide containing phosphate anion is forming with a ratio of 2:1:1 for Co:P:K.

The next step was to prove that the oxygen being formed was actually coming from the oxidation of water and not something else in the solution. In order to establish this they performed three more experiments in neutral KPi electrolyte without any Co^{2+} present. The first experiment that was done was running the electrolysis in a helium saturated electrolyte containing 14.6% $^{18}OH_2$. The ^{32}O, ^{34}O, and ^{36}O levels were monitored and detected with a relative abundance of 72.9%, 24.9%, and 2.1% respectively. The second experiment run was to test the Faradaic efficiency. A fluorescence-based O_2 sensor was used to detect the amount of O_2 in the headspace of the reaction. The amount of O_2 they detected correlated to the amount expected from the $4e^-$ oxidation of water. In addition the amount of O_2 formed was much greater than the amount of catalyst so it seems that there is not really any decomposition of the catalyst during electrolysis. The third experiment was to make sure the O_2 formed was not coming from the phosphate in the solution. In order to determine this electrolysis was done in solutions only containing the KPi electrolyte and phosphate. After 45 C had gone through the solution a ^{31}P NMR was taken of the solution and there were only single clean peaks. This means that the phosphate was not degrading under electrolysis and therefore was not the source of the O_2 formed during the reaction.

Electrochemical studies were then done on the catalyst to learn more about it. The current density of the catalyst was measured as a function of the overpotential (η). This was graphed as a Tafel plot and appreciable catalytic current can be seen at η=.28 V (Black Dots Figure 3). The current density reaches 1 mA/cm^2 at η=.41 V. This same catalyst was tested under different pH levels and the log of the current density increased linearly until a pH of 8 was reached at which point the increase leveled off. This data was converted to a Tafel plot and it displays Nernstian behavior from pH levels 5-8 (Red Dots Figure 3). The reason for the leveling off of the Tafel plot above pH of 8 may be due to a change in the mechanism.

The KPi electrolyte provides a medium for in situ catalyst formation. The deposition of this catalyst may be driven by the interaction of phosphate and Co^{3+}. It may be possible to form other oxygen-evolving compounds from other metal-anion pairs that form in situ under neutral conditions. A big benefit of in situ formation of a catalyst is that it allows for catalysts to be used in situations too sensitive for a normal catalyst. Another benefit of in situ formation of a catalyst is that it incorporates a self-repair mechanism. A proposed mechanism for this in situ formation involves forming an equilibrium between Co^{2+}-HPO_4 and Co^{3+}-HPO_4. If a catalytic cycle involves an oxidation state that is prone to dissolution, continuous formation of catalyst can happen (2). In this case the oxidation state prone to dissolution is Co^{2+} because it has been shown that Co^{2+} has a much shorter lifetime than Co^{3+} (5). Co^{2+} has a shorter lifetime than Co^{3+} because metals with lower oxidation states react more rapidly.

Overall this article reports a water oxidation catalyst that can be formed in situ from earth-abundant metals at a neutral pH. In order for water splitting chemistry to store the world's energy supply 10^{15} moles of water will have to be split every year. This very large scale may be hard to obtain, but this may be applicable on a smaller scale in a short time period.

The main part of this research that needs to be completed still is characterization of the catalyst. The percent composition of the catalyst is roughly known, but if a more detailed account of what the catalyst actually consisted of could be obtained that would be very useful. A crystal structure would help in many ways such as figuring out a mechanism for the catalysis. ^{31}P NMR was taken to determine the stability of the phosphate in solution, but was not taken of the catalyst itself. This may give some insight into the structure of the catalyst.

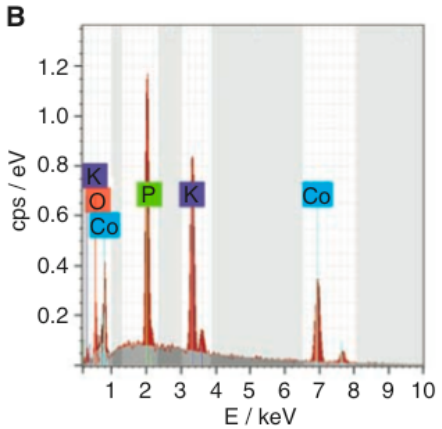

Figure 2. EDX histogram acquired at 12 kV. Counts per second.

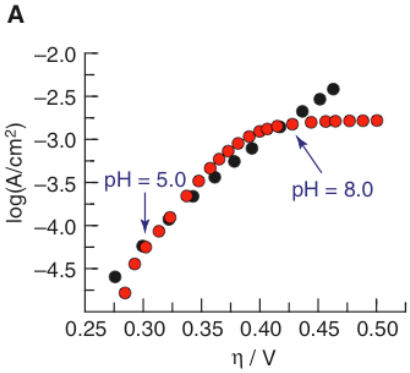

Figure 3. The black circles are a Tafel plot of a catalyst film on the ITO electrode at pH of 7. The red circles are a Tafel plot of the pH data.

References

1. N. S. Lewis, D. G. Nocera, *Proc. Natl. Acad. Sci. U.S.A.* **103**, 15729 (2006).
2. M. W. Kanan, D. G. Nocera, *Science* **321**, 1072 (2008)
3. A. J. Bard, M. A. Fox, *Acc. Chem. Res.* **28**, 141 (1995)
4. B. S. Brunschwig, M. H. Chou, C. Creutz, P. Ghosh, N. Sutin, *J. Am. Chem. Soc.* **105**, 4832 (1983).
5. W. H. Casey, *J. Colloid Interface Sci.* **146**, 586 (1991).

Vol 465|3 June 2010|doi:10.1038/nature09085

LETTERS

Ligand exchanges and selective catalytic hydrogenation in molecular single crystals

Zheng Huang[1], Peter S. White[1] & Maurice Brookhart[1]

Chemical reactions inside single crystals are likely to be highly selective, but examples of single crystal to single crystal (SC–SC) transformations are uncommon, because crystallinity is difficult to retain following the rearrangement of atoms in the solid state[1–19]. The most widely studied SC–SC transformations involve solvent exchange reactions in porous coordination polymers or metal–organic frameworks, which take advantage of the robust polymeric networks of the hosts[2,8,9–11]. Examples of reactions occurring within molecular organic crystals generally involve photo-induced reactions, such as the coupling of alkenes or alkynes within the crystal[1,2,12–15]. For nonporous molecular inorganic or organometallic crystals, single-crystal transformations involving the formation or cleavage of metal–ligand bonds are rare[17–21]; known examples usually involve ligand loss from the single crystal and reversible religation, a process sometimes accompanied by decay of the single crystal to a microcrystalline powder[20,21]. Here we report a series of SC–SC transformations that involve the interchange of multiple small gaseous ligands (N_2, CO, NH_3, C_2H_4, H_2 and O_2) at an iridium centre in molecular single crystals of a pincer Ir(I) complex. The single crystal remains intact during these ligand-exchange reactions, which occur within the crystal and do not require prior ligand extrusion. We reveal a selective catalytic transformation within a nonporous molecular crystal: pincer iridium single crystals ligated with nitrogen, ethylene or hydrogen show selective hydrogenation of ethylene relative to propylene (25:1) when surface sites are passified by CO.

Our interest in using iridium pincer complexes in catalytic reactions[22,23] led to the synthesis of [Ir]-N_2 (see Fig. 1), a square planar Ir(I) complex supported by the bulky, electron-deficient pincer ligand $C_6H_3[OP(C_6H_2(CF_3)_3\text{-}2,4,6)_2]_2$-1,3 (see Supplementary Information). Crystallization of [Ir]-N_2 from toluene gave light-red single crystals that were discovered to undergo SC–SC exchange reactions with small gases to yield [Ir]-CO, [Ir]-NH_3, [Ir]-C_2H_4, [Ir]-$(H)_2(H_2)$ and [Ir]-O_2. Structures of all complexes were established by X-ray diffraction analysis. Table 1 and Supplementary Table 1 summarize all crystal data and selected bond distances and angles; displacement ellipsoid plots (ORTEP) of all structures are shown in Fig. 1.

In mononuclear [Ir]-N_2, nitrogen coordinates to Ir(I) in an end-on mode (Fig. 1) with a N(2)–N(1)–Ir(1) bond angle of 176.5(5)° and a N(1)–N(2) bond distance of 1.106(5) Å (free N_2 = 1.098 Å). Analogous complexes bearing less hindered pincer ligands form dinitrogen-bridged dinuclear complexes, for example $[C_6H_3\text{-}2,6\text{-}(OPtBu_2)_2]Ir\text{–}N{\equiv}N\text{–}Ir[C_6H_3\text{-}2,6\text{-}(OPtBu_2)_2]$ (refs 24, 25). In [Ir]-N_2, the four CF_3-substituted aryl rings form a deep pocket around the Ir centre and prevent dimer formation. Crystals of [Ir]-N_2 have a non-merohedral twinned structure with a rotation of ~180° about the reciprocal axis [0, 0, 1]. (All the other derived structures show this twinning behaviour.) Each unit-cell contains two independent [Ir]-N_2 molecules, related by a crystallographic centre of symmetry, and five toluene molecules (Fig. 2a). One of the toluene molecules is disordered about an inversion centre and is located at the corner of the unit-cell. As depicted in Fig. 2b, the [Ir]-N_2 molecules are stacked along the *a* axis to form channels which are filled with the (disordered) toluene molecules. Along the *b* axis there is a second channel, which is filled with four toluene molecules per unit-cell (Fig. 2c).

Exposure of single crystals of [Ir]-N_2 to 1 atm of CO results in a rapid (<1 min) colour change from light red to orange with retention of the single-crystal morphology. Examination of this crystal by X-ray diffraction revealed that a carbonyl complex, [Ir]-CO, had been formed (Fig. 1). The Ir(1)–C(43) and C(43)–O(44) bond distances are 1.937(5) Å and 1.101(7) Å, respectively, and are consistent with analogous bond lengths in a similar pincer Ir(I)-CO complex[26].

Similar ligand-substitution reactions occur when crystals of [Ir]-N_2 are exposed to ammonia, ethylene or hydrogen. Reaction of [Ir]-N_2 with NH_3 results in a colour change from pale red to dark red in less than 1 min, and formation of [Ir]-NH_3 (Fig. 1). The Ir(1)–N(1) distance of 2.163(8) Å (where numbers in parentheses represent one estimated standard deviation) is close to the Ir–N distance in a similar square planar pincer Ir(I)-NH_3 complex[27]. Treatment of single crystals of [Ir]-N_2 with 1 atm ethylene forms deep-red single crystals of [Ir]-C_2H_4 within a few hours. Ethylene is bound perpendicular to the square plane with Ir(1)–C(43) and Ir(1)–C(44) distances of 2.182(8) Å and 2.168(8) Å. Single crystals of [Ir]-N_2 exposed to H_2 (~1.5 atm) do not show a significant colour change after several days; however, analysis by X-ray diffraction revealed complete loss of nitrogen and formation of an apparent tetrahydride. It is problematic to locate metal-bound hydrogen atoms by X-ray diffraction, so we confirmed the formation of a tetrahydride using solution ^{1}H NMR spectroscopy. Dissolution in toluene-d_8 of crystals exposed to H_2 (135 min) reveal a broad signal at −9.21 p.p.m. (23 °C) in the ^{1}H NMR spectrum, which integrates for four hydrogens. The chemical shift of −9.21 p.p.m. is consistent with similar pincer iridium tetrahydrides[25]. The structure of this tetrahydride is very likely to be an Ir(III) dihydride η^2-dihydrogen complex [Ir]-$(H)_2(H_2)$[28].

[Ir]-N_2, [Ir]-CO, [Ir]-NH_3 [Ir]-C_2H_4, and [Ir]-$(H)_2(H_2)$ all have the same space group and essentially identical lattice parameters. The pincer ligand sets of these systems are superimposable, as are the positions of the toluene molecules in the crystal. Figure 3 shows a superposition of [Ir]-N_2, [Ir]-CO, [Ir]-NH_3, [Ir]-C_2H_4 and [Ir]-$(H)_2(H_2)$, which clearly demonstrates the fidelity of ligand and solvent positions in each of these structures.

Under air, pale-red single crystals of [Ir]-N_2 acquire a dark-green colour in less than 12 h and retain single-crystal morphology. X-ray diffraction analysis revealed loss of N_2 and formation of a monoperoxo Ir(III) complex, [Ir]-O_2. Oxygen binds to Ir in a side-on mode with an O(3)–Ir(1)–O(4) bond angle of 39.3(5)°. The pentacoordinate Ir(III) centre has a distorted trigonal bipyramidal geometry with

[1]Department of Chemistry, University of North Carolina at Chapel Hill, Chapel Hill, North Carolina 27599, USA.

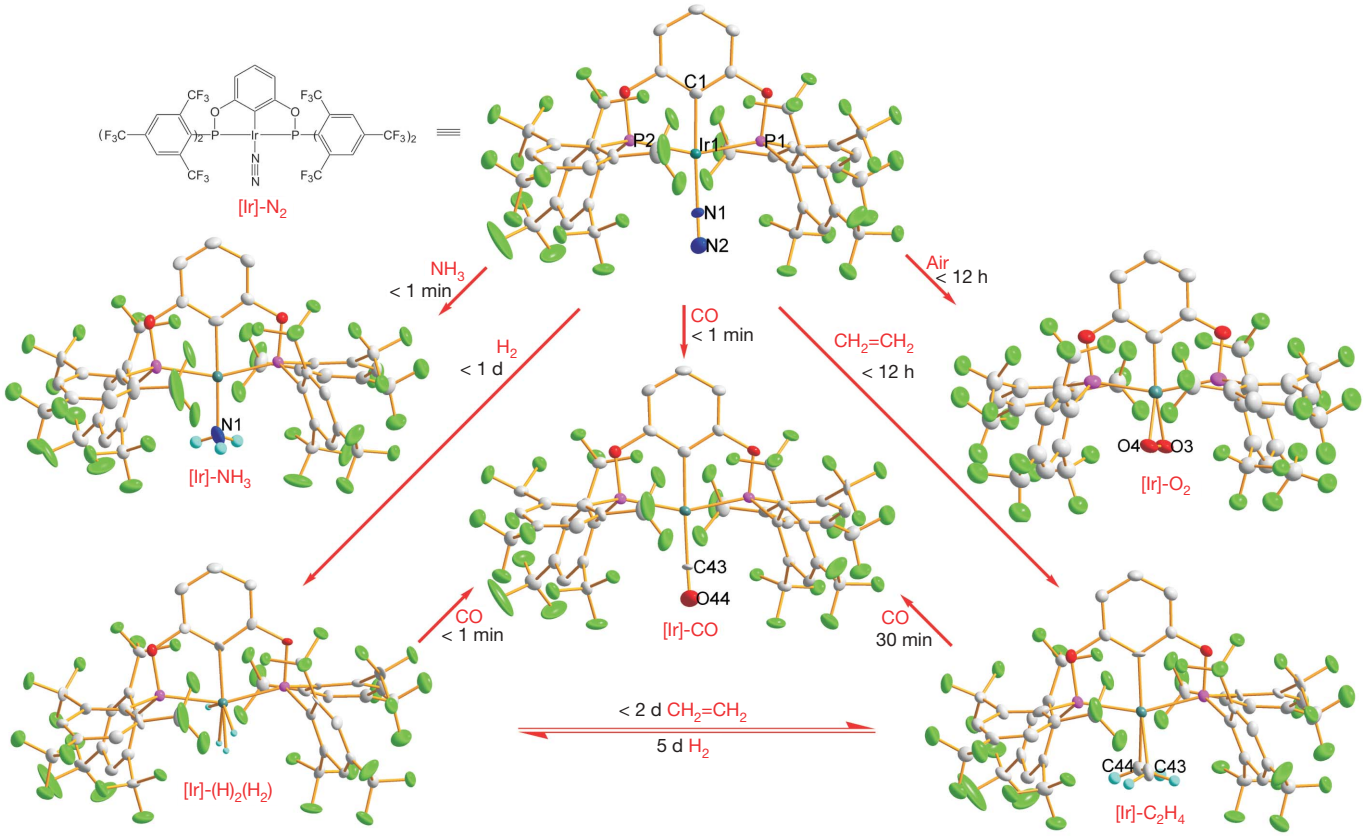

Figure 1 | Single-crystal structures of [Ir]-N_2, [Ir]-CO, [Ir]-NH_3, [Ir]-C_2H_4, [Ir]-$(H)_2(H_2)$, and [Ir]-O_2. Iridium, dark green; phosphorus, pink; fluorine, light green; oxygen, red; nitrogen, dark blue; carbon, grey; hydrogen, light blue. Hydrogen atoms are omitted for clarity, except for those in C_2H_4, NH_3 and H_2 ligands. All SC–SC transformations occur at 25 °C in the presence of 1 atm of gas, except for the transformation of [Ir]-N_2 to [Ir]-$(H)_2(H_2)$, for which 1.5 atm of H_2 was used.

the two P atoms occupying axial positions. The Ir(1)–O(3) and Ir(1)–O(4) bond distances are 2.052(10) Å and 2.024(10) Å, respectively. The O(3)–O(4) bond distance of 1.372(15) Å is typical of peroxo complexes[29]. [Ir]-O_2 is slightly distorted from [Ir]-N_2 compared to the other four systems (Table 1) and is composed of at least three (and possibly further minor, unidentifiable) components as a result of a twin/split structure.

The transformations described above all involve displacement of nitrogen from [Ir]-N_2. Other SC–SC interconversions are possible, depending on the relative binding strengths of the ligands. For example, [Ir]-C_2H_4 converts to [Ir]-CO (~30 min under 1 atm of CO) and [Ir]-$(H)_2(H_2)$ converts to [Ir]-CO (in <1 min under 1 atm of CO). CO has the strongest binding affinity in this series, because none of the other ligands studied displace CO from [Ir]-CO. In addition to X-ray analysis, all ligand-exchange reactions were confirmed by NMR analysis to be quantitative. Following exchange, the excess gaseous ligand was removed under vacuum and crystals were dissolved and analysed by solution NMR spectroscopy. Size selectivity is shown in exchange reactions: exposure of single crystals of [Ir]-N_2 to 1 atm of propylene does not lead to any displacement of nitrogen over the course of five days, but exposure of a toluene-d_8 solution of [Ir]-N_2 to 1 atm of propylene results in complete displacement of nitrogen in 10 min.

Exposure of single crystals of [Ir]-N_2 to high vacuum at 25 °C results in no loss of nitrogen or toluene over one week, whereas displacement of N_2 by CO or NH_3 occurs in minutes. This indicates that ligand exchanges occur within the crystal, not by means of nitrogen loss from the crystal followed by diffusion of CO or NH_3 into the

Table 1 | Crystal data and structure-refinement summary.

	[Ir]-N_2	[Ir]-CO	[Ir]-NH_3	[Ir]-C_2H_4	[Ir]-$(H)_2(H_2)$	[Ir]-O_2
Formula	$C_{59.5}H_{31}F_{36}Ir\ N_2O_2P_2$	$C_{60.5}H_{31}F_{36}\ IrO_3P_2$	$C_{59.5}H_{34}F_{36}\ IrNO_2P_2$	$C_{61.5}H_{35}F_{36}\ IrO_2P_2$	$C_{59.5}H_{35}F_{36}Ir\ O_2P_2$	$C_{59.5}H_{31}F_{36}\ IrO_4P_2$
Crystal system	Triclinic	Triclinic	Triclinic	Triclinic	Triclinic	Triclinic
Space group	P-1	P-1	P-1	P-1	P-1	P-1
a (Å)	12.4720(3)	12.4680(5)	12.4758(5)	12.4844(6)	12.4334(11)	12.769(3)
b (Å)	14.0891(4)	14.1099(6)	14.0658(5)	14.2365(6)	14.0615(12)	13.637(3)
c (Å)	18.6382(5)	18.6021(7)	18.5976(6)	18.5497(9)	18.6354(14)	17.835(3)
α (deg)	108.865(2)	108.852(3)	108.155(2)	108.791(3)	108.879(5)	99.088(13)
β (deg)	99.010(2)	98.939(3)	99.291(3	98.572(3)	98.956(6)	87.194(15)
γ (deg)	97.567(2)	97.635(3)	97.445(3)	98.284(3)	97.594(6)	96.357(17)
V (Å^3)	3002.11(14)	3000.1(2)	3003.56(19)	3020.6(2)	2986.6(4)	3046.3(10)
Z	2	2	2	2	2	2
T (K)	100(2)	100(2)	100(2)	100(2)	100(2)	100(2)
R_1 [$I>2\sigma(I)$]	0.0389	0.0415	0.0556	0.0531	0.0445	0.1090
wR_2 (all data)	0.0866	0.0916	0.1305	0.1313	0.1001	0.2925

Numbers in parentheses indicate one estimated standard deviation. *a*, *b*, *c*, unit-cell parameters; α, β, γ, unit-cell angles; *V*, unit-cell volume; *T*, sample temperature; *Z*, number of formula units in the unit cell; $R_1 = \sum||F_{obs}| - |F_{calc}|| / \sum|F_{obs}|$; $wR_2 = (\sum w(F_{obs}^2 - F_{calc}^2)^2)^{1/2} / \sum wF_{obs}^2$.

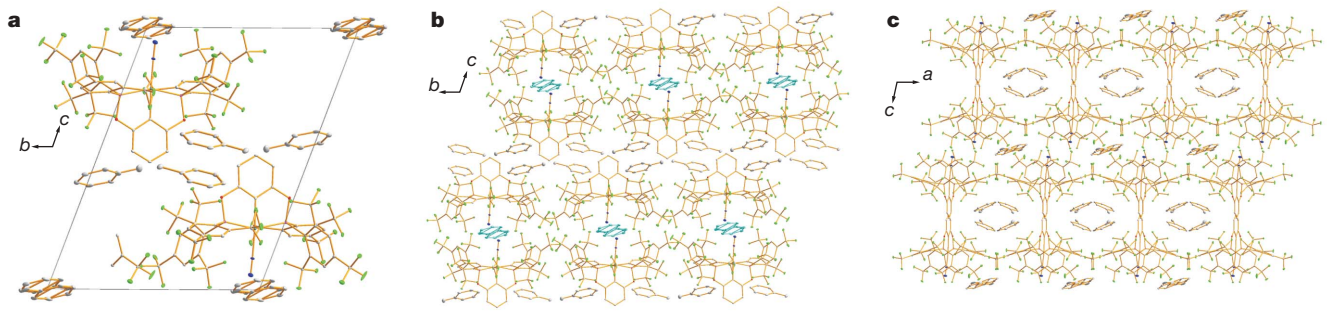

Figure 2 | Unit-cell and stacking diagrams of single-crystal [Ir]-N_2. Colours as in Fig. 1. **a**, Unit-cell of single-crystal [Ir]-N_2 along *a* direction. **b**, Stacking diagram of single-crystal [Ir]-N_2 along *a* direction, showing the disordered toluene (light blue). **c**, Stacking diagram along *b* direction (hydrogen atoms are omitted for clarity).

nitrogen-depleted crystal. Exposure of single crystals of [Ir]-N_2 to toluene-d_8 vapour did not lead to observable toluene-h_8/toluene-d_8 exchange at 25 °C. However, toluene loss can be observed at higher temperatures. For example, heating crystals of [Ir]-N_2 at 75 °C for 30 min, followed by exposure to high vacuum at 75 °C for 1 min results in the complete loss of the disordered toluene, but single-crystallinity is retained. X-ray analysis shows that N_2 is still bound to the Ir centre and the ordered toluene molecules are observed in the same positions as before in the channel along the *b* axis, but that the disordered toluene molecules are absent from the channel along the *a* axis (Supplementary Fig. 3). Heating crystals of [Ir]-N_2 at 75 °C for 5 min followed by exposure to vacuum for 1 min also results in compete loss of disordered toluene, as shown by solution NMR analysis of dissolved crystals. Exposure of such crystals to toluene vapour for 1 day at 25 °C results in recapture of toluene and restoration of the original structure, as shown by X-ray analysis (Supplementary Fig. 4). Although the disordered toluene is more labile than the ordered toluene, longer periods of heating result in loss of both ordered and disordered toluene. It can be fully restored on exposure to toluene vapour (see Supplementary Information). We verified these results by thermogravimetric analysis, which shows toluene loss beginning at 65 °C with nearly complete loss of all toluene by 100 °C (heating rate 5 °C min^{-1}, Supplementary Fig. 6).

These results suggest that ligands enter the crystal via the channel occupied by the disordered toluene, which provides direct access to the Ir–ligand coordination sites. Loss of a tiny fraction of disordered toluene could provide a mechanism for entry by a small ligand, followed by diffusion along the channel by means of successive interchanges with neighbouring toluene molecules. The free volume of the crystal, as estimated by the PLATON program[30] using a modified method (see Supplementary Information), is only ~0.2% (~6 $Å^3$) per unit-cell volume of 3,002 $Å^3$, and supports exclusion of all but the smallest ligands.

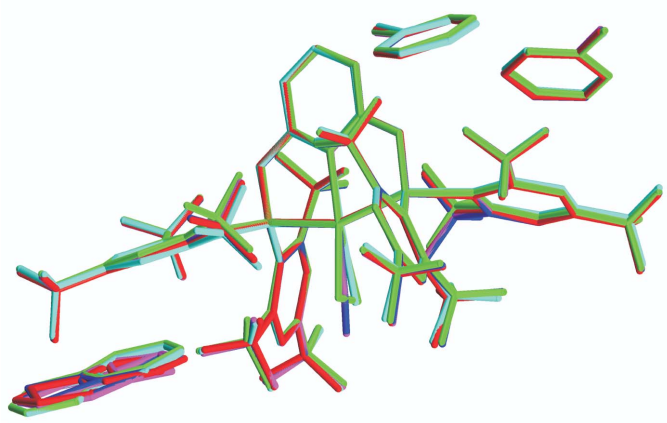

Figure 3 | Superposition of crystal structures. [Ir]-N_2, purple; [Ir]-CO, dark blue); [Ir]-NH_3, light blue; [Ir]-C_2H_4, green; [Ir]-$(H)_2(H_2)$, red.

Single crystals of [Ir]-N_2, [Ir]-C_2H_4 and [Ir]-$(H)_2(H_2)$ are hydrogenation catalysts for gas-phase mixtures of hydrogen and ethylene. For example, treatment of single crystals of [Ir]-N_2 containing 0.6 μmol Ir with ~120 equiv. of ethylene and 200 equiv. of hydrogen (relative to Ir, total pressure ~2.3 atm) at 25 °C produced ethane (95% conversion after 5 h). Heating the system at 75 °C increased the hydrogenation rate and led to more than 99% conversion in 30 min. Catalysts maintain single-crystal morphology throughout the hydrogenation process. The deep-red colour of the crystals suggests [Ir]-C_2H_4 as the dominant catalyst resting state. The crystals show no loss of catalytic activity after three recycles. This hydrogenation of alkenes with organometallic single crystals seems to be unprecedented.

Catalytic hydrogenation of ethylene versus propylene showed selectivity. In initial experiments, single crystals of [Ir]-N_2 or [Ir]-C_2H_4 (0.6 μmol) were treated with ~200 equiv. of hydrogen and 120 equiv. each of ethylene and propylene (total pressure ~3.2 atm). Hydrogenation at 25 °C occurs with a turnover frequency of 5 per minute with formation of ethane and propane in an initial ratio of 1.8:1. In comparison, when an equimolar gaseous mixture of ethylene and propylene was hydrogenated with 10% palladium on carbon, ethane and propane formed in an initial ratio of 1:1, indicating no selectivity for hydrogenation using this heterogeneous catalyst. Given that propylene cannot penetrate the channels of these crystals, this moderate selectivity was surprising and indicated that hydrogenation may occur unselectively at surface or near-surface sites. We reasoned that these sites could be passivated by CO, because CO cannot be displaced in the crystals by either ethylene or hydrogen. Thus, we exposed crystals of [Ir]-N_2 to a CO/N_2 mixture (0.6% vol. CO, 0.5 equiv. relative to Ir) for four days. Using these passivated crystals the rate of hydrogenation is significantly reduced, with negligible turnover at 25 °C, as expected. However, hydrogenation of a mix of 200 equiv. hydrogen/12 equiv. ethylene/120 equiv. propylene at 75 °C (total pressure ~2.4 atm, 1:10 molar ratio of ethylene:propylene) occurred with a turnover frequency of 0.3 per minute and produced an initial ratio (~15% consumption of ethylene) of ethane:propane of 2.5:1, indicating a significant increase in selectivity for ethylene hydrogenation, to 25:1. It seems likely that the small fraction of propylene that undergoes hydrogenation may be occurring at surface or near-surface sites that were not poisoned by CO. The fact that disordered toluene can be ejected from the crystal at 75 °C explains the significant increase in turnover frequency. These iridium complexes carry out catalytic hydrogenation of both ethylene and propylene in solution, but with low selectivity (see Supplementary Information).

In summary, we have observed a series of SC–SC transformations in which small gaseous ligands N_2, CO, NH_3, C_2H_4, H_2 and O_2 undergo rapid exchange at Ir centres in nonporous molecular single

crystals of an iridium(I) pincer complex. Substitutions occur associatively within the crystal and not by ligand loss followed by uptake of the incoming ligand. Most remarkable is that single crystals of [Ir]-N_2, [Ir]-$(H)_2(H_2)$ or [Ir]-C_2H_4 function as alkene-hydrogenation catalysts. When surface and near-surface sites are passivated by treatment with CO, a 25:1 selectivity is observed for hydrogenation of ethylene versus propylene, suggesting that hydrogenation occurs within the crystal. To our knowledge, this is the first demonstration of a catalytic hydrogenation reaction occurring within the interior of an organometallic crystal. The substrate selectivity shown demonstrates the potential for using molecular crystals to carry out selective catalytic reactions.

Received 7 January 2010; accepted 15 April 2010.

1. Foxman, B. M. & Ward, M. D. *Molecules in the Solid State* 534–548 (MRS, 2007).
2. Vittal, J. J. Supramolecular structural transformations involving coordination polymers in the solid state. *Coord. Chem. Rev.* **251,** 1781–1795 (2007).
3. Atwood, J. L., Barbour, L. J., Jerga, A. & Schottel, B. L. Guest transport in a nonporous organic solid via dynamic van der Waals cooperativity. *Science* **298,** 1000–1002 (2002).
4. Cotton, F. A. *et al.* Crystal-to-crystal oxidative deprotonation of a di(μ-hydroxo) to a di(μ-oxo) dimer of dimolybdenum units. *Inorg. Chem.* **46,** 3245–3250 (2007).
5. Hu, C.-H. & Englert, U. Space filling versus symmetry: two consecutive crystal-to-crystal phase transitions in a 2D network. *Angew. Chem. Intl Edn Engl.* **45,** 3457–3459 (2006).
6. Xue, D., Zhang, W., Chen, X. & Wang, H. Single-crystal-to-single-crystal transformation involving release of ridging water molecules and conversion of chain helicity in a chiral three-dimensional metal-organic framework. *Chem. Commun.* 1551–1553 (2008).
7. Iordanidis, L. & Kanatzidis, M. G. Redox-induced "zipper" action in $Rb_2Bi_4Se_7$ and $Cs_2Bi_4Se_7$: coupling of slabs to a three-dimensional framework through single-crystal to single-crystal conversion. *Angew. Chem. Intl Edn Engl.* **39,** 1928–1930 (2000).
8. Kawano, M. & Fujita, M. Direct observation of crystalline-state guest exchange in coordination networks. *Coord. Chem. Rev.* **251,** 2592–2605 (2007).
9. Ghosh, S. K., Kaneko, W., Kiriya, D., Ohba, M. & Kitagawa, S. A bistable porous coordination polymer with a bond-switching mechanism showing reversible structural and functional transformations. *Angew. Chem. Intl Edn Engl.* **47,** 8843–8847 (2008).
10. Haneda, T., Kawano, M., Kawamichi, T. & Fujita, M. Direct observation of the labile imine formation through single-crystal-to-single-crystal reactions in the pores of a porous coordination network. *J. Am. Chem. Soc.* **130,** 1578–1579 (2008).
11. Ghosh, S. K., Zhang, J. & Kitagawa, S. Reversible topochemical transformation of a soft crystal of a coordination polymer. *Angew. Chem. Intl Edn Engl.* **46,** 7965–7968 (2007).
12. Garcia-Garibay, M. A. Molecular crystals on the move: from single-crystal-to-single-crystal photoreactions to molecular machinery. *Angew. Chem. Intl Edn Engl.* **46,** 8945–8947 (2007).
13. Kobatake, S., Takami, S., Muto, H., Ishikawa, T. & Irie, M. Rapid and reversible shape changes of molecular crystals on photoirradiation. *Nature* **446,** 778–781 (2007).
14. Bucar, D. & MacGillivray, L. R. Preparation and reactivity of nanocrystalline cocrystals formed via sonocrystallization. *J. Am. Chem. Soc.* **129,** 32–33 (2007).
15. Warren, M. R. *et al.* Reversible 100% linkage isomerization in a single-crystal to single-crystal transformation: photocrystallographic identification of the metastable [Ni(dppe)(η^1-ONO)Cl] isomer. *Angew. Chem. Intl Edn Engl.* **48,** 5711–5714 (2009).
16. Li, B. *et al.* Solvent-induced transformation of single crystals of a spin-crossover (SCO) compound to single crystals with two distinct SCO centers. *J. Am. Chem. Soc.* **132,** 1558–1566 (2010).
17. Das, S. K. & Supriya, S. Reversible single crystal to single crystal transformation through Fe-O(H)Me/Fe-OH_2 bond formation/bond breaking in a gas-solid reaction at an ambient condition. *J. Am. Chem. Soc.* **129,** 3464–3465 (2007).
18. Libri, S. *et al.* Ligand substitution within nonporous crystals of a coordination polymer: elimination from and insertion into Ag–O bonds by alcohol molecules in a solid–vapor reaction. *Angew. Chem. Intl Edn Engl.* **47,** 1693–1697 (2008).
19. Bezzu, C. G., Helliwell, M., Warren, J. E., Allan, D. R. & McKeown, N. B. Heme-like coordination chemistry within nanoporous molecular crystals. *Science* **327,** 1627–1630 (2010).
20. Albrecht, M., Lutz, M., Spek, A. L. & van Koten, G. Organoplatinum crystals for gas-triggered switches. *Nature* **406,** 970–974 (2000).
21. Lennartson, A., Håkansson, M. & Jagner, S. Cis- and trans-bis(benzoylacetonato)-pyridinecopper(II): co-crystallisation of isomers and reversible pyridine loss with retention of crystallinity. *N. J. Chem.* **31,** 344–347 (2007).
22. Goldman, A. S. *et al.* Catalytic alkane metathesis by tandem alkane dehydrogenation-olefin metathesis. *Science* **312,** 257–261 (2006).
23. Huang, Z. *et al.* Highly active and recyclable heterogeneous iridium pincer catalysts for transfer dehydrogenation of alkanes. *Adv. Synth. Catal.* **351,** 188–206 (2009).
24. Ghosh, R., Kanzelberger, M., Emge, T. J., Hall, G. S. & Goldman, A. S. Dinitrogen complexes of pincer-ligated iridium. *Organometallics* **25,** 5668–5671 (2006).
25. Göttker-Schnetmann, I., White, P. S. & Brookhart, M. Synthesis and properties of iridium bis(phosphinite) pincer complexes (*p*-XPCP)IrH_2, (*p*-XPCP)Ir(CO), (*p*-XPCP)Ir(H)(aryl), and {(*p*-XPCP)Ir}$_2$(μ-N_2} and their relevance in alkane transfer dehydrogenation. *Organometallics* **23,** 1766–1776 (2004).
26. Morales-Morales, D. *et al.* Selective dehydrogenation of alcohols and diols catalyzed by a dihydrido iridium PCP pincer complex. *Can. J. Chem.* **79,** 823–829 (2001).
27. Kanzelberger, M. *et al.* Distinct thermodynamics for the formation and cleavage of N-H bonds in aniline and ammonia. Directly-observed reductive elimination of ammonia from an isolated amido hydride complex. *J. Am. Chem. Soc.* **125,** 13644–13645 (2003).
28. Hebden, T. J. *et al.* Dihydrogen/dihydride or tetrahydride? An experimental and computational investigation of pincer iridium polyhydrides. *Inorg. Chem.* **49,** 1733–1742 (2010).
29. Williams, D. B., Kaminsky, W., Mayer, J. M. & Goldberg, K. I. Reactions of iridium hydride pincer complexes with dioxygen: new dioxygen complexes and reversible O_2 binding. *Chem. Commun.* 4195–4197 (2008).
30. Spek, A. L. Single-crystal structure validation with the program *PLATON*. *J. Appl. Cryst.* **36,** 7–13 (2003).

Supplementary Information is linked to the online version of the paper at www.nature.com/nature.

Acknowledgements This work is financially supported by the National Science Foundation under the auspices of the Centre for Enabling New Technologies through Catalysis (CENTC).

Author Contributions M.B. directed the project. Z.H. carried out all complex syntheses, crystallizations and reactions. P.S.W. carried out single crystal X-ray diffraction experiments and crystal structure determinations. M.B. and Z.H. analysed the data and wrote the manuscript.

Author Information Supplementary crystallographic data for this paper has been deposited at the Cambridge Crystallographic Data Centre under deposition numbers CCDC 728556 to 728561, 729323, 729324 and 759994 to 759996. These data can be obtained free of charge from www.ccdc.cam.ac.uk/data_request/cif. Reprints and permissions information is available at www.nature.com/reprints. The authors declare no competing financial interests. Readers are welcome to comment on the online version of this article at www.nature.com/nature. Correspondence and requests for materials should be addressed to M.B. (mbrookhart@unc.edu).

Ligand exchanges and selective catalytic hydrogenation in molecular single crystals

Review by Tatsiana Haidzinskaya

RECEIVED DATE 11/23/2010

ABSTRACT Single crystal to single crystal (SC–SC) transformations were studied for Ir(I) complex with a pincer ligand. The exchange of small ligands such as N_2, CO, NH_3, C_2H_4, H_2 and O_2 was observed on the metal center. The crystal structure of the complex was retained. The mechanism for the substitution was proposed to be associative with small ligands approaching a metal center via crystal channels. The complex is also capable of selective catalytic hydrogenation, which makes it the first demonstration of a catalytic hydrogenation reaction occurring within the interior of an organometallic crystal.

Chemical transformations of a single crystal are very uncommon because crystallinity is difficult to retain after the reorganization of the atoms in the chemical reactions.[1] The most studied single crystal to single crystal (SC–SC) transformation involves solvent exchange reactions in porous coordination polymers or metal–organic compounds.[2] The removal of solvents without affecting the single crystal nature of the coordination complexes is not necessarily considered as structural transformation. However, many complexes undergo distortion and sliding of network structures, change in conformation and coordination environment during solvation, or desolvation processes.[3] A number of porous rigid coordination polymers often exhibit zeolitic behavior and retain single crystal nature during solvation and desolvation.[4] Kitagawa, Yaghi, Atwood and others have reported that these rigid porous coordination polymers can be used as gas storage materials.[5] The removal of solvents during SC-SC conversion has also been found to accompany by change in magnetic properties,[6] negative thermal expansion[7] and luminescent properties.[8] Another example of single crystal to single crystal (SC–SC) transformations is the formation or cleavage of metal–ligand bonds.[9] These reactions are very rare and sometimes result in the crystal decay with the formation of a microcrystalline powder.[10]

Figure 1. Single-crystal structures of [Ir]-N_2, [Ir]-CO, [Ir]-NH_3, [Ir]-C_2H_4, [Ir]-$(H)_2(H_2)$, and [Ir]-O_2. Iridium, dark green; phosphorus, pink; fluorine, light green; oxygen, red; nitrogen, dark blue; carbon, grey; hydrogen, light blue. Hydrogen atoms are omitted for clarity, except for those in C_2H_4, NH_3 and H_2 ligands. All SC–SC transformations occur at 25 °C in the presence of 1 atm of gas, except for the transformation of [Ir]-N_2 to [Ir]-$(H)_2(H_2)$, for which 1.5 atm of H_2 was used.

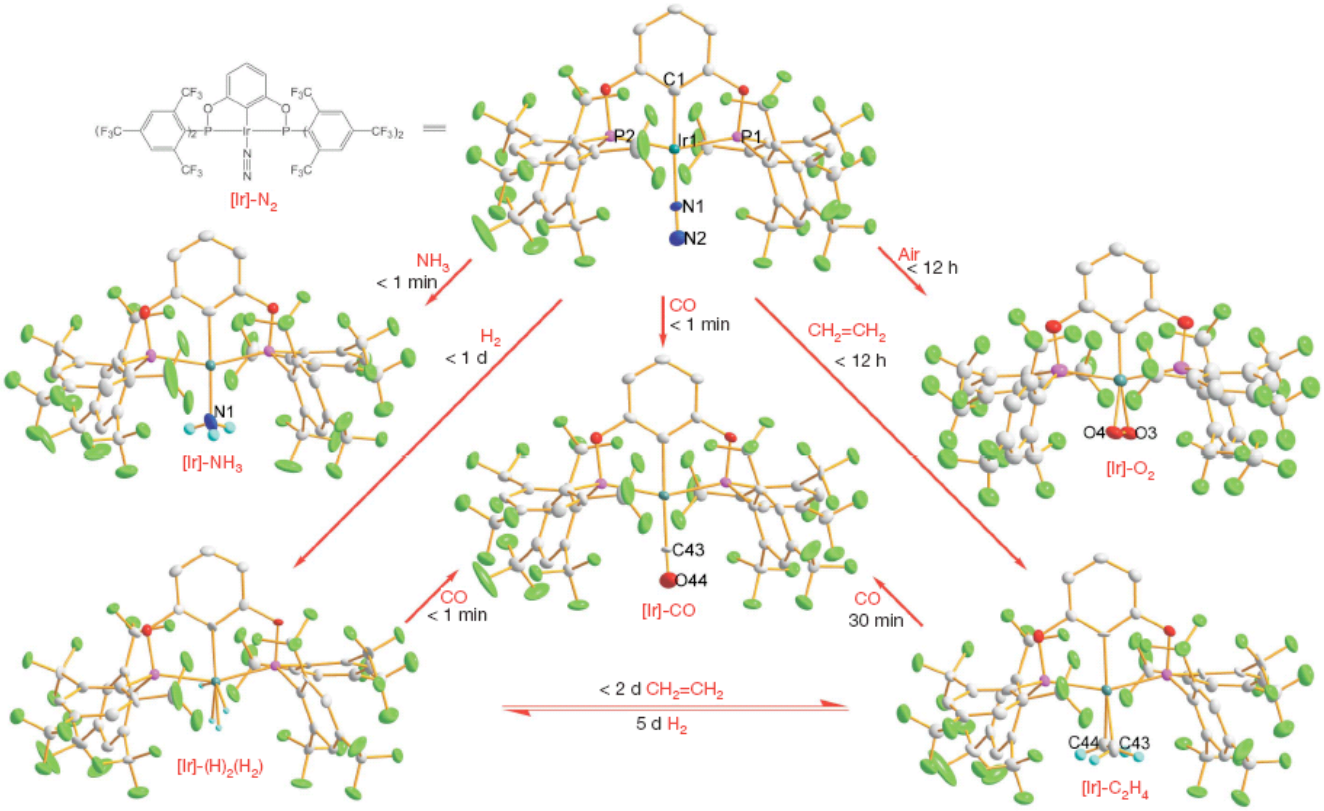

Figure 2. Unit-cell and stacking diagrams of single-crystal [Ir]-N_2. Colors as in Fig. 1. a, Unit-cell of single-crystal [Ir]-N_2 along a direction. b, Stacking diagram of single-crystal [Ir]-N_2 along a direction, showing the disordered toluene (light blue). c, Stacking diagram along b direction (hydrogen atoms are omitted for clarity).

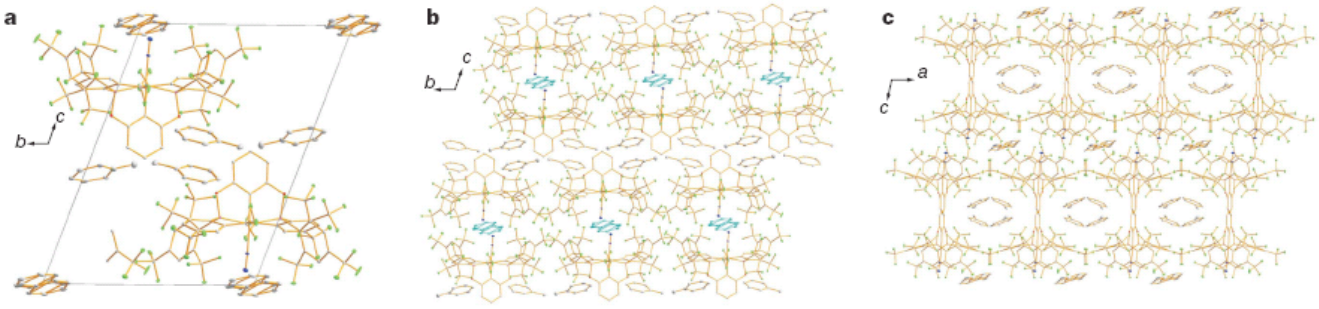

Maurice Brookhart et. al. from the University of North Carolina reported a study on a single crystal of Ir(I) complex with a pincer ligand.[11] The researchers observed the exchange of small ligands such as N_2, CO, NH_3, C_2H_4, H_2 and O_2 on the metal center with the retention of the crystal structure. The scientists also discovered selective catalytic hydrogenation of ethylene to ethane in the presence of propylene when the metal center is ligated with N_2, C_2H_4, H_2 and small amounts of CO. This is the first reported catalytic hydrogenation reaction that occurs within the interior of a molecular single crystal, which opens up the opportunity for the further development of the research area where single crystals could be used as catalysts in the catalytic reactions with high selectivities.

The researchers started the project with the synthesis and characterization of Ir(I) complex with a pincer ligand ligated with nitrogen. [Ir]-N_2 – is a square planar complex, and after the recrystallization from toluene it has a light red color. Bond length and angles are provided in the Table 1. The bulky, electron-deficient pincer ligand $C_6H_3[OP(C_6H_2(CF_3)_3\text{-}2,4,6)_2]_2\text{-}1,3$ with the four CF_3-substituted aryl rings was used to create a pocket and prevent dimerization. Each unit cell contains two molecules of [Ir]-N_2 complex and five molecules of toluene. One molecule of toluene is disordered about an inversion center and located at the corner of a unit cell. The other four solvent molecules are highly ordered (Figure 2).

With [Ir]-N_2 complex in hand, the researchers decided to investigate the possibility of ligand exchange reactions. The crystal was exposed to gaseous small ligands such as CO, NH_3, C_2H_4, H_2 and O_2. In the case of CO, a rapid color change was observed. Within one minute after the exposure to carbon monoxide the complex changed its color from light red to orange. When exposed to NH_3 atmosphere, [Ir]-N_2 complex became dark red in less than one minute; and in case of ethylene, it took several hours for a complex to acquire a deep red color. In all provided examples, the crystal structure was retained and the analysis of the products by X-ray diffraction showed the loss of nitrogen and the formation of [Ir]-CO, [Ir]-NH_3, and [Ir]-C_2H_4 complexes correspondingly. When [Ir]-N_2 complex was exposed to H_2 no color change was observed, but X-ray diffraction and proton NMR confirmed the loss of nitrogen and the formation of a tetra hydride. [Ir]-N_2, [Ir]-CO, [Ir]- NH_3, [Ir]-C_2H_4, and [Ir]-$(H)_2(H_2)$ complexes have the same lattice parameters and the pincer ligand sets are superimposable (Figure 3). Under air, [Ir]-N_2 complex gradually changes color to dark green and the X-ray diffraction analysis shows the formation of a monoperoxo Ir(III) complex. The structure of the complex is distorted and not superimposable with the previously described complexes. The exposure of the [Ir]-N_2 complex to propylene does not lead to the displacement of nitrogen. All ligand displacement transformations were found to be quantitative.

Figure 3. Superposition of crystal structures. [Ir]-N_2, purple; [Ir]-CO, dark blue); [Ir]-NH_3, light blue; [Ir]-C_2H_4, green; [Ir]-$(H)_2(H_2)$, red.

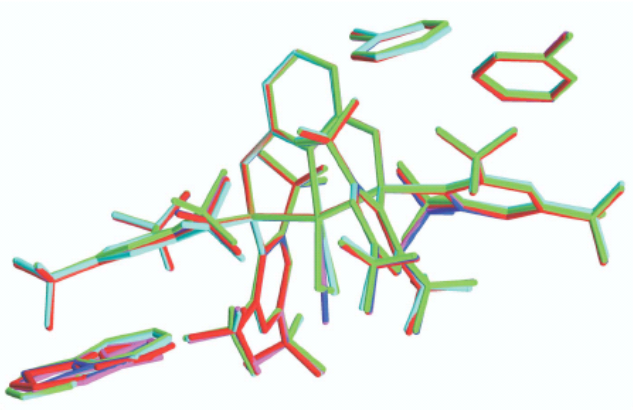

To determine the mechanism of ligand exchange reaction the researchers decided to carry out several experiments by exposing a crystal to vacuum and heat. When the complex was exposed to high vacuum at room temperature for one week the loss of nitrogen or toluene was not observed. It proved that the ligand displacement did not happen through a dissociative mechanism. As we discussed in class, in the dissociative mechanism the metal-ligand bond is fully broken before the new metal-ligand bond is formed. The stability of the complex under vacuum at room temperature proves that the metal-nitrogen bond is relatively strong and does not break spontaneously under reaction conditions. Exposure of a single crystal to toluene-D8 did not lead to observable toluene-H8/toluene-D8 exchange at room temperature as well. When the crystal was heated under vacuum, the complete loss of toluene was observed. The loss of toluene started at 65 ºC with the disordered toluene and at 100 ºC complete loss of toluene was detected. The following exposure of the crystal to the toluene vapor led to the restoration of the original structure. The researchers suggested that ligands enter the crystal via the channel occupied by the disordered toluene. The loss of small amounts of toluene gives a possibility for a small ligand to enter the channel and diffuse through the channel to the ligand metal coordination site.

Because iridium complexes are known to catalyze hydrogenation reactions, the scientists were interested in the catalytic abilities of a single crystal [Ir]-N_2 as a hydrogenation catalyst. The researchers exposed the complex to a

Table 1. *Crystal data and structure-refinement summary.*

	[Ir]-N_2	[Ir]-CO	[Ir]-NH_3	[Ir]-C_2H_4	[Ir]-$(H)_2(H_2)$	[Ir]-O_2
Formula	$C_{59.5}H_{31}F_{36}IrN_2O_2P_2$	$C_{60.5}H_{31}F_{36}IrO_3P_2$	$C_{59.5}H_{34}F_{36}IrNO_2P_2$	$C_{61.5}H_{35}F_{36}IrO_2P_2$	$C_{59.5}H_{35}F_{36}IrO_2P_2$	$C_{59.5}H_{31}F_{36}IrO_4P_2$
Crystal System	Triclinic	Triclinic	Triclinic	Triclinic	Triclinic	Triclinic
Space group	P-1	P-1	P-1	P-1	P-1	P-1
a (A°)	12.4720(3)	12.4680(5)	12.4758(5)	12.4844(6)	12.4334(11)	12.769(3)
b (A°)	14.0891(4)	14.1099(6)	14.0658(5)	14.2365(6)	14.0615(12)	13.637(3)
c (A°)	18.6382(5)	18.6021(7)	18.5976(6)	18.5497(9)	18.6354(14)	17.835(3)
α (deg)	108.865(2)	108.852(3)	108.155(2)	108.791(3)	108.879(5)	99.088(13)
β (deg)	99.010(2)	98.939(3)	99.291(3)	98.572(3)	98.956(6)	87.194(15)
γ (deg)	97.567(2)	97.635(3)	97.445(3)	98.284(3)	97.594(6)	96.357(17)
V (A°3)	3002.11(14)	3000.1(2)	3003.56(19)	3020.6(2)	2986.6(4)	3046.3(10)
Z	2	2	2	2	2	2
T(K)	100(2)	100(2)	100(2)	100(2)	100(2)	100(2)
R1 [I>2s(I)]	0.0389	0.0415	0.0556	0.0531	0.0445	0.1090
wR2 (all data)	0.0866	0.0916	0.01305	0.1313	0.1001	0.2925

mixture of ethylene (120 equivalents) and hydrogen (200 equivalents) at room temperature and obtained ethane in 95 % yield after 5 hours. Increasing the temperature to 75 ºC led to 99% conversion in 30 minutes. This is the first reported catalytic hydrogenation reaction that occurs within the interior of a molecular single crystal. An interest in selective hydrogenation led to another experiment where equimolar mixture of ethylene and propylene under the same conditions gave 1.8:1.0 mixture of ethane to propane. Higher selectivity was expected due to the fact that propylene cannot penetrate the channels of the crystals. It led to the conclusion that hydrogenation occurs not only at the metal center inside the crystal but on the surface and near surface sites of the crystal as well. These sites could be passivated with CO due to the strong binding affinity of the ligand and the observation that ethylene and hydrogen cannot displace CO from the complex. The researchers exposed crystals of [Ir]-N_2 to a CO/N_2 mixture (0.6% vol. CO, 0.5 equiv. relative to Ir) for four days and used these passivated crystals in the hydrogenation reaction. The rate of the reaction was considerably reduced, but the selectivity was increased to 25:1 ratio of ethane to propane. The rate of the reaction can be increased by heating the reaction mixture with reduction of selectivity.

In conclusion, the scientists observed ligand exchange transformations in nonporous molecular single crystals of an iridium (I) pincer complex. The proposed mechanism of this associative exchange is via crystal channels occupied by toluene. The complex is also capable of selective hydrogenation, which, according to the authors, makes it the first demonstration of a catalytic hydrogenation reaction occurring within the interior of an organometallic crystal. For the future directions, I would suggest the researchers to search for another transition metal complex capable of selective hydrogenation inside the crystal. I would test Rh, Co, Ru, Os, Pd, Pt complexes for similar transformations. I believe it would be necessary to enlarge the size of the crystal channels to increase the substrate scope of the reaction. It can be achieved by using larger ligands, such as tris-pyrazolyl borate, or solvent molecules, such as mesitylene or 1,3,5-triisopropylbenzene. Larger channels might provide the opportunity for selective hydrogenation of larger molecules, for example, butene and propene. To check if the selectivity is based solely on the size of the ligands I would recommend to run the hydrogenation reaction of ethylene and propylene in solution. If no selectivity is observed, crystal channels are responsible for the selectivity. I also suggest running the hydrogenation reaction with alkynes. Selective hydrogenation of acetylene in the presence of propyne may be of scientific interest as well.

REFERENCES

1. Atwood, J. L.; Barbour, L. J.; Jerga, A.; Schottel, B. L. *Scienc*e **2002**, 298,1000–1002.
2. Vittal, J. J. *Coord. Chem. Rev*. 2007, 251, 1781–1795.
3. a) Dobrzanska, L.; Lloyd G. O.; Esterhuysen, C.; Barbour, L. J. *Angew Chem. Int. Ed*. **2006**, 45, 5856. b) Dobrzanska L., Lloyd G.O., Raubenheimer H. G., Barbour L. J., *J. Am. Chem. Soc*. **2005**, 127, 13134. c) Dobrza´ska, L.; Lloyd, G.O.; Raubenheimer, H. G.; Barbour L. J. *J. Am. Chem. Soc*. **2006**, 128, 698. d) Okubo, T.; Asami, A.; Noro, S.; Yoshitomi, T.; Kitagawa, S.; Ishii, T.; Matsuzaka, H.; Seki, K. *Angew. Chem. Int. Ed*, **1999**,. 38, 140.
4. Kitagawa, S.; Uemura, K. *Chem. Soc. Rev*. **2005**, 34, 109.
5. a) Kitagawa, S.; Noro, S.; Nakamura, T.; Takayoshi, T. *Chem. Commun*. **2006**, 701. b) Yaghi, O. M. *Angew. Chem. Int. Ed*. **2005**, 44, 4670. c) Atwood, J. L.; Barbour, L. J.; Jerga, A.; Schottel, B. L., *Science*, **2002**, 298, 1000.
6. Kurmoo, M.; Kumagai, H.; Chapman, K. W.; Kepert, C. J. *Chem. Commun*. **2005**, 3012.
7. Pretsch, T.; Chapman, K. W.; Halder, G. J.; Kerpert, C. J. *Chem. Commun*. **2006**, 1587.
8. Wong, K.-L.; Law, G.-L.; Yang, Y.-Y.; Wong, W.-T. *Adv. Mater. 18* **2006**, 1051.
9. a) Das, S. K.; Supriya, S. *J. Am. Chem. Soc*. **2007**, 129, 3464–3465. b) Libri S. *Angew. Chem. Int. Ed* **2008**, 47, 1693–1697. c) Bezzu, C. G.; Helliwell, M.; Warren, J. E.; Allan, D. R.; McKeown, N. B. *Science*, **2010**, 327, 1627–1630.
10. Albrech, M.; Lutz, M; Spek, A. L. *Nature* **2000**, 406, 970–974.
11. Huang, Z.; White, P. S.; Brookhart, M. *Nature* **2010**, 465, 598-60

the ion trap, which alters the spectrum of the emitted photons and degrades the quantum interference, reduces the average fidelity by less than 1%.

The entangling gate central to this teleportation protocol is a heralded, probabilistic process. The net probability for coincident detection of two emitted photons is given by $P_{gate} = (p_{Bell})[p_\pi \eta T_{fiber} T_{optics} \xi(\Delta\Omega/4\pi)]^2 \approx 2.2 \times 10^{-8}$, where $p_{Bell} = 0.25$ accounts for the detection of only one out of the four possible Bell states; $p_\pi = 0.5$ is the fraction of photons with the correct polarization (half are filtered out as being produced by σ decays); $\eta = 0.15$ is the quantum efficiency of each PMT; $T_{fiber} = 0.2$ is the coupling and transmission of each photon through the single-mode optical fiber; $T_{optics} = 0.95$ is the transmission of each photon through the other optical components; $\xi = 1 - 0.005 = 0.995$, where 0.005 is the branching ratio into the $^2D_{3/2}$ level; and $\Delta\Omega/4\pi = 0.02$ is the solid angle of light collection. The attempt rate of 75 kHz is currently limited by the time of the state preparation microwave pulse, resulting in about one successful teleportation event every 12 min. However, the expression for P_{gate} reveals multiple ways to substantially increase the success rate. The most dramatic increase would be achieved by increasing the effective solid angle of collection, which, for instance, could be accomplished by surrounding each ion with an optical cavity. Although improvements that increase the success probability of the gate operation can enhance scalability, even with a low success probability this gate can still be scaled to more complex systems (*16*).

The fidelity obtained in the current experiment is evidence of the excellent coherence properties of the photonic frequency qubit and the "clock" state atomic qubit. Together, these complementary qubits provide a robust system for applications in quantum information. The teleportation scheme demonstrated here could be used as the elementary constituent of a quantum repeater. Moreover, the entangling gate implemented in this protocol may be used for scalable measurement-based quantum computation.

References and Notes

1. W. K. Wootters, W. H. Zurek, *Nature* **299**, 802 (1982).
2. C. H. Bennett *et al.*, *Phys. Rev. Lett.* **70**, 1895 (1993).
3. H.-J. Briegel, W. Dür, J. I. Cirac, P. Zoller, *Phys. Rev. Lett.* **81**, 5932 (1998).
4. D. Gottesman, I. L. Chuang, *Nature* **402**, 390 (1999).
5. D. Bouwmeester *et al.*, *Nature* **390**, 575 (1997).
6. D. Boschi, S. Branca, F. De Martini, L. Hardy, S. Popescu, *Phys. Rev. Lett.* **80**, 1121 (1998).
7. A. Furusawa *et al.*, *Science* **282**, 706 (1998).
8. J. F. Sherson *et al.*, *Nature* **443**, 557 (2006).
9. Y.-A. Chen *et al.*, *Nat. Phys.* **4**, 103 (2008).
10. L.-M. Duan, M. D. Lukin, J. I. Cirac, P. Zoller, *Nature* **414**, 413 (2001).
11. M. Riebe *et al.*, *Nature* **429**, 734 (2004).
12. M. D. Barrett *et al.*, *Nature* **429**, 737 (2004).
13. M. Riebe *et al.*, *N. J. Phys.* **9**, 211 (2007).
14. S. Massar, S. Popescu, *Phys. Rev. Lett.* **74**, 1259 (1995).
15. S. J. van Enk, N.Lütkenhaus, H. J. Kimble, *Phys. Rev. A* **75**, 052318 (2007).
16. L.-M. Duan *et al.*, *Phys. Rev. A* **73**, 062324 (2006).
17. R. Van Meter, K. M. Itoh, T. D. Ladd, http://arxiv.org/abs/quant-ph/0507023.
18. P. Maunz *et al.*, *Nat. Phys.* **3**, 538 (2007).
19. D. L. Moehring *et al.*, *Nature* **449**, 68 (2007).
20. S. Olmschenk *et al.*, *Phys. Rev. A* **76**, 052314 (2007).
21. D. N. Matsukevich, P. Maunz, D. L. Moehring, S. Olmschenk, C. Monroe, *Phys. Rev. Lett.* **100**, 150404 (2008).
22. M. J. Madsen *et al.*, *Phys. Rev. Lett.* **97**, 040505 (2006).
23. B. B. Blinov, D. L. Moehring, L.-M. Duan, C. Monroe, *Nature* **428**, 153 (2004).
24. C. K. Hong, Z. Y. Ou, L. Mandel, *Phys. Rev. Lett.* **59**, 2044 (1987).
25. Y. H. Shih, C. O. Alley, *Phys. Rev. Lett.* **61**, 2921 (1988).
26. S. L. Braunstein, A. Mann, *Phys. Rev. A* **51**, R1727 (1995).
27. C. Simon, W. T. M. Irvine, *Phys. Rev. Lett.* **91**, 110405 (2003).
28. J. B. Altepeter, E. R. Jeffrey, P. G. Kwiat, in *Advances in Atomic, Molecular, and Optical Physics*, P. Berman, C. Lin, Eds. (Elsevier, San Diego, CA, 2006), vol. 52, pp. 105–159.
29. J. L. O'Brien *et al.*, *Phys. Rev. Lett.* **93**, 080502 (2004).
30. M. Horodecki, P. Horodecki, R. Horodecki, *Phys. Rev. A* **60**, 1888 (1999).

31. This work is supported by the Intelligence Advanced Research Projects Activity (IARPA) under Army Research Office contract, the NSF Physics at the Information Frontier program, and the NSF Physics Frontier Center at JQI.

14 October 2008; accepted 19 December 2008
10.1126/science.1167209

Femtosecond XANES Study of the Light-Induced Spin Crossover Dynamics in an Iron(II) Complex

Ch. Bressler,[1] C. Milne,[1] V.-T. Pham,[1] A. ElNahhas,[1] R. M. van der Veen,[1,2] W. Gawelda,[1,2]* S. Johnson,[2] P. Beaud,[2] D. Grolimund,[2] M. Kaiser,[1,2] C. N. Borca,[2] G. Ingold,[2] R. Abela,[2] M. Chergui[1]†

X-ray absorption spectroscopy is a powerful probe of molecular structure, but it has previously been too slow to track the earliest dynamics after photoexcitation. We investigated the ultrafast formation of the lowest quintet state of aqueous iron(II) tris(bipyridine) upon excitation of the singlet metal-to-ligand-charge-transfer (^{1}MLCT) state by femtosecond optical pump/x-ray probe techniques based on x-ray absorption near-edge structure (XANES). By recording the intensity of a characteristic XANES feature as a function of laser pump/x-ray probe time delay, we find that the quintet state is populated in about 150 femtoseconds. The quintet state is further evidenced by its full XANES spectrum recorded at a 300-femtosecond time delay. These results resolve a long-standing issue about the population mechanism of quintet states in iron(II)-based complexes, which we identify as a simple ^{1}MLCT→^{3}MLCT→^{5}T cascade from the initially excited state. The time scale of the ^{3}MLCT→^{5}T relaxation corresponds to the period of the iron-nitrogen stretch vibration.

There is a large class of iron(II)-based molecular complexes that exhibit two electronic states closely spaced in energy: a low-spin (LS) singlet and a high-spin (HS) quintet state. They therefore manifest spin crossover (SCO) behavior, wherein conversion from a LS ground state to a HS excited state (or the reverse) can be induced by small temperature or pressure changes or by light absorption (*1*, *2*). The SCO phenomenon has been much studied using steady-state (*2*) and ultrafast (*3*–*6*) optical spectroscopies, with the goal of identifying the elementary steps leading to formation of the HS state. A representative energy level diagram of all Fe(II)-based complexes is shown in Fig. 1 (*7*). The main difference between them concerns the absolute energies of states, not their energetic ordering (*2*). All crystallographic studies point to an Fe-N bond elongation by ~0.2 Å in the HS compared to the LS state (*1*, *2*). Theoretical studies show that the Fe-N bond length of the singlet and triplet metal-centered (MC) ^{1,3}T states lies halfway between those of the LS and HS states (*7*). Obviously, accessing the HS excited state by absorption of light from the LS ground state is forbidden by the spin selection rules. Therefore, the doorway to the HS state is ideally via the singlet metal-to-ligand-charge-transfer (^{1}MLCT) that exhibits strong absorption bands in the visible spectrum, or via the weakly absorbing and lower-lying ^{1,3}T states (*1*, *2*). The time scale and the route going from the initially excited ^{1}MLCT state to the lowest-lying quintet state are still the subject of debate. Steady-state spectroscopic studies at cryogenic temperatures showed that excitation into the MC ^{1,3}T states leads to population of the $^5T_2$ state with a quantum efficiency of ~80% (*2*). Researchers therefore concluded that the relaxation cascade from the ^{1}MLCT state to the HS $^5T_2$ state proceeds via the intermediate ^{1,3}T states. However, for excitation of the ^{1}MLCT state, the relaxation process was reported to occur with 100% efficiency at both 10 K (*2*) and at room

[1]Ecole Polytechnique Fédérale de Lausanne, Laboratoire de Spectroscopie Ultrarapide, ISIC, FSB-BSP, CH-1015 Lausanne, Switzerland. [2]Swiss Light Source, Paul-Scherrer Institut, CH-5232 Villigen PSI, Switzerland.

*Present address: Laser Processing Group, Instituto de Optica, Consejo Superior de Investigaciones Científicas, Serrano 121, E-28006 Madrid, Spain.

†To whom correspondence should be addressed. E-mail: Majed.chergui@epfl.ch

temperatures (*8*, *9*), thus questioning the involvement of the intermediate ^{1,3}T states. Ultrafast laser studies established that the relaxation cascade from the initially excited ^{1}MLCT state to the lowest excited quintet state $^5T_2$ is complete in <1 ps (*3*–*5*), but this result was indirectly inferred, as neither the intermediate MC states nor the final $^5T_2$ state have spectroscopic transitions in the region of the probe (>350 nm). McCusker and co-workers (*6*) proposed that the ^{1}MLCT state relaxes to a manifold of strongly mixed singlet and triplet MC states down to the quintet state, the latter being considered to be the only one clearly defined by its spin quantum number S. However, the steady-state spectroscopic studies of Hauser and co-workers (*2*) point to a clear classification of all MC states according to their spin character, thus excluding strong state mixings.

Iron(II)-tris(bipyridine) ($[Fe^{II}(bpy)_3]^{2+}$), which is the molecule studied here, serves as a model system for the family of Fe(II)-based SCO complexes. Early events of the relaxation cascade in aqueous $[Fe^{II}(bpy)_3]^{2+}$ were recently investigated using femtosecond resolved fluorescence and transient absorption by Gawelda *et al.* (*5*) upon 400-nm excitation of the ^{1}MLCT state. They observed a prompt (~30 fs) intersystem crossing (ISC) to the ^{3}MLCT state, followed by a departure from this state within ~120 fs (Fig. 1B). The subsequent steps and the arrival into the HS state were not observed directly, and the final step of the photocycle, the radiationless HS→LS transition, was identified via the recovery of the ground-state bleach with its 665-ps lifetime. For 400-nm excitation, the relaxation cascade from the initially excited ^{1}MLCT state to the HS state implies dissipation of 2.6 eV of energy in <1 ps and, were it to proceed via the intermediate MC states, it would entail a back electron transfer, followed by at least three ISC events, as well as an Fe-N bond elongation by 0.2 Å. This elongation was recently measured by x-ray absorption spectroscopy (XAS) studies with 50- to 100-ps resolution on $[Fe^{II}(tren(py)_3)]^{2+}$ (*10*) and $[Fe^{II}(bpy)_3]^{2+}$ (*11*, *12*) in solution. The structural change manifests itself through substantial modifications of the x-ray absorption near-edge structure (XANES) at the Fe K-edge, which we exploit in the present study of the ultrafast light-induced SCO of aqueous $[Fe^{II}(bpy)_3]^{2+}$.

So far, most x-ray studies with subpicosecond time resolution have used diffraction to investigate strain, coherent phonon dynamics, or melting phenomena in solid materials (*13*–*15*). Scattering does not require wavelength tunability, and sources of (monochromatic) femtosecond x-ray pulses (obtained by plasma emission from metal targets struck by intense ultrashort laser pulses) have readily been available for some time now. Diffraction is also a collective phenomenon in crystals, delivering rather strong signals. For chemical and biological systems that may be disordered and diluted in solution, x-ray absorption spectroscopy is a more suitable probe (*12*, *16*, *17*). However, it requires rather stable sources of tunable ultrashort x-rays. Subpicosecond x-ray plasma sources have been implemented for time-resolved XAS studies on the few picoseconds (*18*) to tens of picoseconds time scale, but their use is challenging because of their poor shot-to-shot stability and low fluxes (*19*, *20*). Synchrotron sources (*12*, *17*) deliver very stable radiation with reasonable fluxes, although the pulse durations lie in the 50- to 150-ps range. The recently developed slicing scheme (*21*) has allowed the extraction of tunable femtosecond x-ray pulses from a synchrotron and was first implemented for soft x-ray absorption studies of the electronic changes resulting from the photo-induced ultrafast insulator-metal phase transition in VO_2 bulk crystals (*22*) and the ultrafast demagnetization dynamics in solid nickel (*23*). For structural determination, hard x-rays (>2 keV) are better suited, and the recent implementation of the slicing scheme for 5 to 20 keV radiation at the Swiss Light Source (SLS, PSI-Villigen) (*24*) opens the possibility of carrying out ultrafast XANES studies on dilute molecular systems in liquids. By applying this technique, we have succeeded in following the structural changes in real time upon visible light excitation of aqueous $[Fe^{II}(bpy)_3]^{2+}$, and moreover we have unraveled the mechanism of the ultrafast spin crossover in this class of molecules.

Briefly (*25*), a 100-μm-thick free-flowing liquid jet of an aqueous solution of 50 mM $[Fe^{II}(bpy)_3]^{2+}$ was excited by an intense 400-nm laser pulse (115-fs pulse width, repetition rate 1 kHz), and a tunable femtosecond hard x-ray pulse from the slicing source was used to probe the system in transmission mode at 2 kHz. The flux of the femtosecond x-ray source was about 10 photons per pulse at 7 keV. We recorded the transient difference absorption spectra by alternating detection of signals from the laser-excited and the unexcited sample, thus achieving a precise intrinsic energy calibration that compensates for

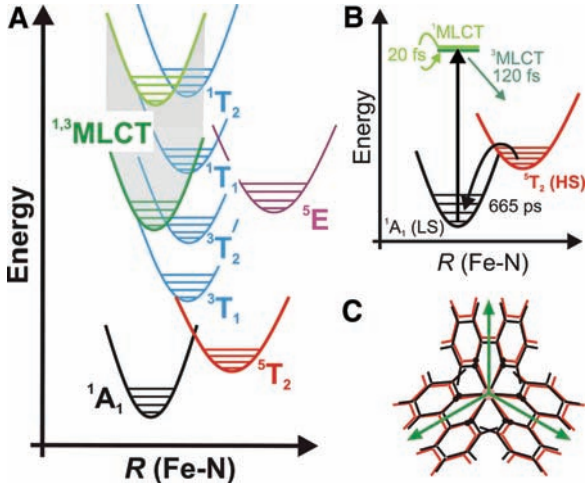

Fig. 1. (**A**) Representative potential energy curves of Fe(II)-based SCO complexes as a function of the Fe-N bond distance (*7*). The manifold of MLCT states is shown as a shaded area. $[Fe^{II}(bpy)_3]^{2+}$ has predominantly O_h symmetry with a trigonal (D_3) distortion. The MC states are represented by their symmetry character (A, T, and E) in the D_3 group: the LS $^1A_1$ ground state has a completely filled $e^4a_1^2$ configuration (deriving from the t_{2g}^6 subshell in O_h symmetry), whereas the antibonding e (e_g in O_h symmetry) orbital is empty. Per electron that is promoted from the t_{2g} subshell to the e_g subshell (for easier reading we will use the O_h nomenclature hereafter), the metal-ligand bond length increases by as much as 0.1 Å (*1*, *7*). For the series of $^{1,3}T(t_{2g}^5e_g)$ states, the Fe-N bond length is expected to lie between the values observed for the ground and the high-spin $^5T_2$ ($t_{2g}^4e_g^2$) states. (**B**) Relaxation cascade as determined by ultrafast laser spectroscopy upon excitation of aqueous $[Fe(bpy)_3]^{2+}$ at 400 nm (*5*). The intermediate MC states are not shown because they are optically silent in the region >350 nm and were therefore not observed in (*5*). (**C**) For the $[Fe(bpy)_3]^{2+}$ complex, the Fe-N bond length is 1.97 Å in the low-spin $^1A_1(t_{2g}^6)$ ground state (*32*) but increases by 0.2 Å in the high-spin $^5T_2$ ($t_{2g}^4e_g^2$) state, as determined by picosecond XAS experiments (*11*).

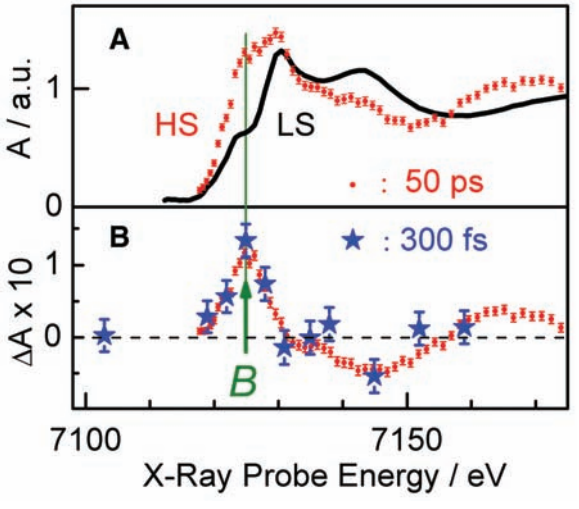

Fig. 2. (**A**) Fe K-edge XANES spectrum of the LS state of aqueous $[Fe^{II}(bpy)_3]^{2+}$ (black trace) and of the HS quintet state (red dots). The latter is determined from the LS spectrum and the transient spectrum (B) measured at a time delay of 50 ps after laser excitation at 400 nm (*11*). (**B**) Transient XANES spectrum (difference in x-ray absorption between the laser-excited sample and the unexcited sample) recorded 50 ps after laser excitation at 400 nm (red dots) (*11*). Note the increase in absorption at the so-called B-feature. The blue stars represent the transient spectrum recorded at a time delay of 300 fs in the present work. Error bars, ±1 SD (*25*).

drifts of the laser or synchrotron energies and fluxes. The time resolution was <250 fs (*25*).

Figure 2A shows the Fe K-edge XANES spectra of aqueous $[Fe^{II}(bpy)_3]^{2+}$ in its ground (LS) and excited (HS) state. The spectrum of the latter was retrieved from the LS spectrum and the difference spectrum recorded 50 ps after laser excitation (red dots in Fig. 2B) (*11*). The strongest increase in absorption upon LS to HS conversion occurs at the so-called B-feature (arrow in Fig. 2), which was previously identified as a structure-sensitive above-ionization multiple-scattering resonance (*26*). The increase in intensity of the B-feature is concomitant with the increase in Fe-N bond distance upon LS to HS conversion, reflecting a well-established correlation between edge absorption intensity and bond distance [see, e.g., (*27*)]. For the present system, this correlation was confirmed (fig. S1) by a simulation of the XANES spectrum using the Minuit XANES (MXAN) code (*11*, *28*), which additionally shows a nearly linear relationship between the Fe-N bond elongation and the intensity of the B-feature. The B-feature intensity is therefore a signature of the Fe-N bond elongation, and it allows us to distinguish the various states that can be grouped by their similar Fe-N bond distances: (i) the LS ground and the ^{1,3}MLCT states; (ii) the ^{1,3}T states, which exhibit an elongation of 0.1 Å relative to the ground state (*7*); and (iii) the ^{5}T state, which exhibits a 0.2 Å elongation (*11*). Based on this correlation, we analyze the observed light-induced changes at the B-feature as a function of the time delay between the optical pump pulse and the x-ray probe pulse in the femtosecond to picosecond time domain.

Figure 3 shows the transient signal at the B-feature as a function of time delay (the inset shows an expanded region out to 10 ps). It is characterized by a steep rise followed by a plateau beyond 250 to 300 fs, which suggests that the system has reached the HS state within this time frame. This suggestion is confirmed by the energy scan recorded at a time delay of 300 fs (blue stars in Fig. 2B), which agrees with the transient absorption spectrum recorded at 50-ps time delay. Considering a simple four-level kinetic model $^1A_1 \rightarrow {}^1$MLCT$\rightarrow {}^3$MLCT$\rightarrow {}^5$T, we simulated the signal with no adjustable parameters, assuming (i) an optical/x-ray cross-correlation of 250 fs; (ii) the ^{1}MLCT and ^{3}MLCT decay times measured in (*5*) (Fig. 1B); (iii) the cross sections at the B-feature for the LS and HS states (Fig. 2A), as well as for the intermediate ^{1,3}T states, derived from the relationship between the Fe-N bond elongation and the B-feature intensity (*25*); and (iv) the absorption cross section of the MLCT state(s). For the latter, based on our previous study of the analogous $[Ru^{II}(bpy)_3]^{2+}$ molecule (*29*), the MLCT and LS XANES are expected to be similar, except for a shift to higher energies of the MLCT XANES spectrum, due to the oxidation of the central metal atom (over the time the system remains in the MLCT manifold). At the Fe K-edge, this oxidation state shift amounts to at most +2 eV based on a study of Fe(II)- and Fe(III)-hexacyanide (*30*).

Figure 3B shows the simulated time evolution of the signal due to the various states, including (solid curves) and excluding (dashed curves) the MLCT states, as well as the resulting total signal (red traces). The blue shift of the MLCT spectrum should lead to an initial decrease in absorption of the signal, which we do not observe. The simulations (green trace in Fig. 3B) confirm that our pump-probe correlation time brings this initial signal decrease below our experimental sensitivity, thus accounting for its absence in the data. Also, we note that time zero is hardly affected by inclusion of the signal due to the MLCT state, and its value changes by at most 40 fs when comparing the simulations with and without the (temporary) oxidation shift. Finally, introducing the ^{1,3}T state(s) can reproduce the data only for a fitted relaxation time of <60 fs (*25*). Such a short lifetime, however, is unrealistic because it corresponds to the period of high frequency modes of the system, which in addition would need to be shared among the ^{1,3}T states that all have potential curves with identical equilibrium distances and curvatures along the Fe-N coordinate (Fig. 1A). Consequently, the agreement between the experimental and the simulated time trace (Fig. 3A) implies that the rise time (~150 fs) of the x-ray absorption of the HS state corresponds to the decay of the ^{3}MLCT state (*5*). Thus, the population of the ^{3}MLCT state proceeds to the quintet state directly and bypasses the intermediate ^{1,3}T states. Furthermore, the derived relaxation time scale corresponds to the period of the Fe-N stretch mode, which lies in the 130- to 160-fs range for all Fe(II)-based complexes, according to Raman studies (*31*). Therefore, here the observation of the structural dynamics allows us to unambiguously unravel the population relaxation pathway.

Because the ^{3}MLCT state lies about 1.5 eV above the quintet state (Fig. 1), the latter is populated in high vibrational levels. However, we do not observe vibrational cooling in the quintet state, because XANES spectroscopy is in general not very sensitive to Debye-Waller factors, which reflect the uncertainty in atomic coordinates due to thermal motion.

The general picture of the light-induced SCO process that emerges from this study becomes very simple and is summarized in Fig. 1B. The full cascade reduces a two-step ISC process, ^{1}MLCT$\rightarrow {}^3$MLCT$\rightarrow {}^5$T. The bypassing of the intermediate ^{1,3}T states resolves the issue of multiple ultrafast ISC steps among states that are quasiparallel with respect to the Fe-N coordinate (Fig. 1A). Dissipation of the energy difference in the ultrafast cascade is accounted for by storage of vibrational energy in the quintet state. Finally, the unit quantum efficiency of the SCO process from the ^{1}MLCT state into the quintet state makes sense in the context of excluding any leakage back to the ground state (*9*) through the bypassing of the ^{1,3}T states.

Considering that $[Fe^{II}(bpy)_3]^{2+}$ is a model system for all Fe(II)-based SCO complexes, we believe that our results are of general validity to this family. These results also underscore the power of ultrafast x-ray absorption spectroscopy for the study of molecular structural dynamics of dilute systems. In the present case, resolving the structural dynamics unravels the pathways of spin and electronic relaxation.

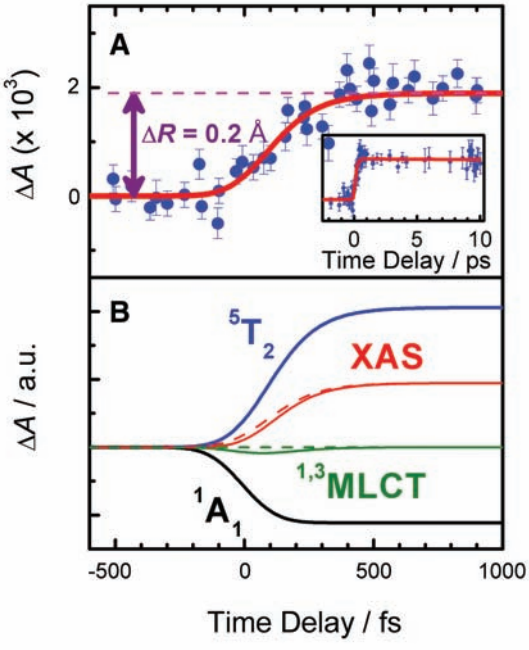

Fig. 3. (**A**) Time scan of the signal (blue points) at the B-feature (at 7126 eV) (Fig. 2B) as a function of laser pump/x-ray probe time delay after excitation of aqueous $[Fe^{II}(bpy)_3]^{2+}$ at 400 nm. The inset shows a long time scan up to a 10-ps time delay. The red trace is the simulated signal assuming a simple four-step kinetic model $^1A_1 \rightarrow {}^1$MLCT$\rightarrow {}^3$MLCT$\rightarrow {}^5$T to describe the spin conversion process [see (B)]. The vertical arrow displays the expected effect of the elongation of 0.2 Å for the Fe-N bond elongation ΔR between the LS and HS states. Error bars, ±1 SD (*25*). (**B**) Simulated transient absorption traces of the individual states (black, green, and blue) and total (red) trace based on a four-step kinetic model $^1A_1 \rightarrow {}^1$MLCT$\rightarrow {}^3$MLCT$\rightarrow {}^5$T, with the ^{1}MLCT$\rightarrow {}^3$MLCT intersystem crossing taking place in 20 to 30 fs and the depopulation of the ^{3}MLCT state taking place in 120 fs, as determined by ultrafast fluorescence and transient absorption studies (*5*). Neglect of the absorption decrease due to the MLCT states (dashed traces) does not affect the final simulated signal. The kinetics were convoluted with a cross-correlation of 250 fs between laser and x-ray pulse.

References and Notes

1. P. Gutlich, H. A. Goodwin, *Top. Curr. Chem.* **233**, 1 (2004).
2. A. Hauser, *Top. Curr. Chem.* **234**, 155 (2004).
3. J. K. McCusker *et al.*, *J. Am. Chem. Soc.* **115**, 298 (1993).
4. J. E. Monat, J. K. McCusker, *J. Am. Chem. Soc.* **122**, 4092 (2000).
5. W. Gawelda *et al.*, *J. Am. Chem. Soc.* **129**, 8199 (2007).
6. C. Brady, J. J. McGarvey, J. K. McCusker, H. Toftlund, D. N. Hendrickson, *Top. Curr. Chem.* **235**, 1 (2004).
7. B. Ordejon, C. de Graaf, C. Sousa, *J. Am. Chem. Soc.* **130**, 13961 (2008).
8. C. Creutz, M. Chou, T. L. Netzel, M. Okumura, N. Sutin, *J. Am. Chem. Soc.* **102**, 1309 (1980).
9. M. A. Bergkamp, C. K. Chang, T. L. Netzel, *J. Phys. Chem.* **87**, 4441 (1983).
10. M. Khalil *et al.*, *J. Phys. Chem. A* **110**, 38 (2006).
11. W. Gawelda *et al.*, *Phys. Rev. Lett.* **98**, 057401 (2007).
12. C. Bressler, R. Abela, M. Chergui, *Z. Kristallogr.* **223**, 307 (2008).
13. A. Cavalleri, R. W. Schoenlein, *Top. Appl. Phys.* **92**, 309 (2004).
14. M. Bargheer, N. Zhavoronkov, M. Woerner, T. Elsaesser, *Chem. Phys. Chem.* **7**, 783 (2006).
15. K. J. Gaffney, H. N. Chapman, *Science* **316**, 1444 (2007).
16. L. X. Chen, *Angew. Chem. Int. Ed.* **43**, 2886 (2004).
17. C. Bressler, M. Chergui, *Chem. Rev.* **104**, 1781 (2004).
18. F. Raksi *et al.*, *J. Chem. Phys.* **104**, 6066 (1996).
19. I. V. Tomov, J. Chen, X. Ding, P. M. Rentzepis, *Chem. Phys. Lett.* **389**, 363 (2004).
20. T. Lee, Y. Jiang, C. G. Rose-Petruck, F. Benesch, *J. Chem. Phys.* **122**, 084506 (2005).
21. R. W. Schoenlein *et al.*, *Science* **287**, 2237 (2000).
22. A. Cavalleri *et al.*, *Phys. Rev. Lett.* **95**, 067405 (2005).
23. C. Stamm *et al.*, *Nat. Mater.* **6**, 740 (2007).
24. P. Beaud *et al.*, *Phys. Rev. Lett.* **99**, 174801 (2007).
25. Materials and methods are available as supporting material on *Science* Online.
26. V. Briois, P. Sainctavit, G. J. Long, F. Grandjean, *Inorg. Chem.* **40**, 912 (2001).
27. H. Dau, P. Liebisch, M. Haumann, *Anal. Bioanal. Chem.* **376**, 562 (2003).
28. M. Benfatto, A. Congiu-Castellano, A. Daniele, S. D. Longa, *J. Synchrotron Radiat.* **8**, 267 (2001).
29. W. Gawelda *et al.*, *J. Am. Chem. Soc.* **128**, 5001 (2006).
30. A. Bianconi, in *X-ray Absorption Principles, Applications, Techniques of EXAFS, SEXAFS and XANES*, D. C. P. Koningsberger, R. Prins, Eds. (Wiley, New York, 1988), pp. 573–662.
31. J. P. Tuchagues, A. Bousseksou, G. Molnar, J. J. McGarvey, F. Varret, *Top. Curr. Chem.* **235**, 85 (2004).
32. S. Dick, *Z. Kristallogr., New Cryst. Struct.* **213**, 356 (1998).

33. This work was funded by the Swiss National Science Foundation (FNRS), 110464, 107956, 620-066145, and 105239, and by Staatssekretariat für Bildung und Forschungcontract COST D35 C06.0016. We are very grateful to A. Hauser (Geneva) for providing us with the samples, as well as for many useful discussions. We also thank M. Benfatto (Rome) for providing us with the MXAN code and for useful discussions.

Supporting Online Material

www.sciencemag.org/cgi/content/full/1165733/DC1
Materials and Methods
Fig. S1
References

25 June 2008; accepted 1 December 2008
Published online 11 December 2008;
10.1126/science.1165733
Include this information when citing this paper.

Complementary Active Sites Cause Size-Selective Reactivity of Aluminum Cluster Anions with Water

Patrick J. Roach,[1] W. Hunter Woodward,[1] A. W. Castleman Jr.,[1]* Arthur C. Reber,[2] Shiv N. Khanna[2]

The reactions of metal clusters with small molecules often depend on cluster size. The selectivity of oxygen reactions with aluminum cluster anions can be well described within an electronic shell model; however, not all reactions are subject to the same fundamental constraints. We observed the size selectivity of aluminum cluster anion reactions with water, which can be attributed to the dissociative chemisorption of water at specific surface sites. The reactivity depends on geometric rather than electronic shell structure. Identical arrangements of multiple active sites in Al_{16}^-, Al_{17}^-, and Al_{18}^- result in the production of H_2 from water.

Metal clusters possess electronic shells that result from quantum confinement of the nearly free valence electrons (*1*–*3*). Because the shell structures of clusters and atoms are similar, shell-filling concepts from traditional valence bond theory can be applied to the description of clusters (*4*, *5*). The result of a chemical interaction may then be explained through the energy minimization that results when a cluster closes an incomplete electronic shell (closed shell n = 2, 8, 18, 20, 34, 40, …), either by direct ionization or through the formation of a covalent or ionic bond (*3*–*11*). A cluster can therefore be assigned as a superatom analog of a specific group of the periodic table on the basis of the difference between its valence electron count and the number of electrons required to fill the nearest superatomic shell (*8*–*11*).

The previously reported size-selective reactions of Al clusters with O_2 (*4*, *6*–*11*) result from the superatomic electronic structure. However, the observed selective reactivity of Al cluster anions with water is inconsistent with the closing of superatom shells. For example, Al_{23}^- and Al_{37}^- are both considered by the superatom model to have rare gas–like closed electronic shells (*4*) yet adsorb water molecules, whereas Al_{14}^- and Al_{46}^- have open electronic shells but do not adsorb water molecules (fig. S1) (*12*). We investigated what combination of geometric and electronic features could account for this observed reactivity. We found that pure Al cluster anions of certain sizes harbor distinct active sites in which a pair of adjacent Al atoms is responsible for the dissociative chemisorption of water. The complementary active site consists of one Al atom that acts as a Lewis acid and a second Al atom that acts as a Lewis base. The ability of an adjacent pair of different elements to promote similar chemical activity is known in metal oxides (*13*) and at the interface of dissimilar metals (*14*) because of the different electron affinity of each element. In the current case, however, we show that the conditions required for reactivity are met in certain clusters that consist of only a single element. Understanding how a specific shape or size will affect the affinity of a metal cluster toward a specific reagent may facilitate future efforts to design either stable or reactive materials for specific technological applications (*15*–*18*).

Reactions between water (*12*) and anionic Al clusters comprising 7 to 60 atoms (Fig. 1) were observed under multicollisional conditions in a fast-flow reactor (fig. S2) (*12*). When water was introduced into the fast-flow reactor, products were observed that we have assigned as adducts of Al anion clusters with water. Most clusters adsorbed one or more water molecules with varying intensity, whereas no adducts were observed for other species (fig. S1) (*12*). The distinct differences in the reactivity of similarly sized clusters suggests that small differences in electronic and geometric structure play an important role in determining the reactivity of aluminum nanostructures with water.

Al_{12}^- is the smallest cluster that reacts to form a product of observable intensity (Fig. 2A); thus, we analyzed this species by a first-principles approach within a gradient-corrected density functional formalism (*12*). The initial interaction we considered between a water molecule and an Al cluster anion was the nucleophilic attack of water on the Al surface. This reaction requires the donation of lone-pair electrons from water to the lowest unoccupied molecular orbital (LUMO) of the cluster (or LUMO+1 in odd-electron species, as the lone pair interacts most strongly with levels where both spin states are unoccupied) where the probability density of the vacant orbital protrudes out from the cluster structure into vacuum (*19*–*22*). Previous rules proposed by Chrêtien *et al.* (*23*) suggest that the susceptibility of a specific species to a nucleophilic reactant is increased as the relative energy of a cluster's LUMO decreases, as compared to other species (fig. S3A) (*12*). Although the observation of a strong $Al_{12}H_2O^-$ product peak (the LUMO energy of Al_{12}^- is a

[1]Departments of Chemistry and Physics, Pennsylvania State University, University Park, PA 16802, USA. [2]Department of Physics, Virginia Commonwealth University, Richmond, VA 23284, USA.

*To whom correspondence should be addressed. E-mail: awc@psu.edu

Femtosecond XANES Study of the Light-Induced Spin Crossover Dynamics in an Iron(II) Complex

Yuan Hu

Brown Laboratories, Department of Chemistry and Biochemistry, University of Delaware, Newark, Delaware 19716

RECEIVED DATE (automatically inserted by publisher); E-mail: yuanhu@udel.edu

Recently, a new technique--femtosecond optical pump/x-ray probe is been employed to investigated the ultrafast formation of the lowest quintet state of aqueous iron(II) tris(bipyridine) upon excitation of the singlet metal-to-ligand-charge-transfer (^{1}MLCT) state based on x-ray absorption near-edge structure (XANES).

There is a long-standing issue[1-12] about the population mechanism of the singlet state (low spin state) to the quintet state (high spin state) in iron(II)-based complexes. X-ray absorption spectroscopy with subpicosecond time resolution, has been used as a powerful probe of molecular structure to uncover the mechanism, which turns out to be too slow to track the earliest dynamics after photoexcitation.

Chergui and his coworkers solve this issue.

They have used the femtosecond optical pump/x-ray probe technique based on x-ray absorption near-edge structure (XANES), to investigate the ultrafast formation of the lowest quintet state of aqueous iron(II) tris(bipyridine) $[Fe^{II}(bpy)_3]^{2+}$ upon excitation of the singlet metal-to-ligand-charge-transfer (^{1}MLCT) state. The observation of the structural dynamics allows them to unambiguously unravel the population relaxation pathway. They found that the quintet state is populated in about 150 femtoseconds, which was evidenced by its full XANES spectrum recorded at a 300-femtosecond time delay. They identify it as a simple ^{1}MLCT→^{3}MLCT→^{5}T cascade from the initially excited state.

As it is concerned, a lot of metal complexes exhibit two electronic states: a high-spin (HS) state and a low-spin (LS) state, which mainly depends on the difference between the splitting energy (Δ) and the pair energy (P). When the two energies are close to each other, an interconversion of the spin states of the complex can occur. This phenomenon is called Spin Crossover (SCO).

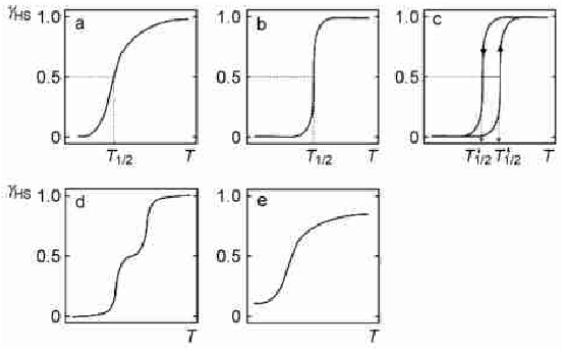

Figure 1. The principal types of spin transition curves (high spin fraction γHS vs temperature T) : (a) gradual ; (b) abrupt ; (c) with hysteresis ; (d) two steps; (e) incomplete[13]

There are several types of SCO phenomenon depicted in Figure 1, in which γ_{HS} (the high-spin molar fraction) is plotted vs. Temperature. The figure shows a gradual spin transition (Figure 1a), an abrupt transition (Figure 1b), an abrupt transition with hysteresis (Figure 1c), a two-step transition (Figure 1d), and an incomplete transition (Figure 1e).

The SCO complexes are very useful, since the spin states of complexes can be easily changed as a result of external stimuli such as a variation of temperature, pressure, light irradiation or an influence of a magnetic field.[14] They have an ideal inherent molecular bistability (HS and LS) in which a single molecule or an assembly of molecules can be used as active elements in novel thermal switches, optical switches or information memory devices, since the bistability leads to changes in the colour of the material and major magnetic changes[15].

A larger class of iron(II)-based complexes are found processing the SCO property. Iron is the first row transition metal. The iron(II) has 6 d-electrons. The splitting energy (Δ) of octahedral structure between e_g and t_{2g} is very small. The iron(II)-based molecular complexes exhibit two electronic states: a high-spin (HS) state and a low-spin (LS) (scheme 1). The spin multiplicity of HS state is quintet, and the one of LS state is singlet. According to the multiplicity, the HS state is paramagnetic and the LS state is diamagnetic (Figure 2).

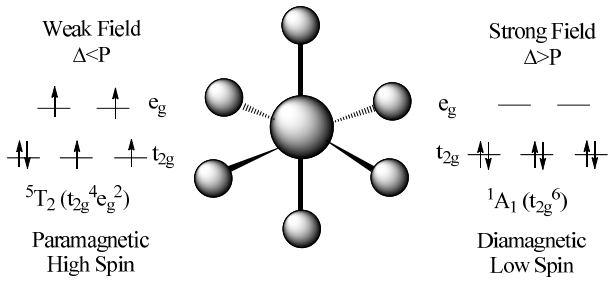

Figure 2. The iron(II)-based molecular complexes exhibit two electronic states

Spin selection rules tell us transitions between states of different spin multiplicities are forbidden. That is to say, the transition from singlet LS to quintet HS is forbidden by selection rules, since they have different spin multiplicities.

Figure 3 is Tanabe-Sugano diagram for a transition metal ion with d^6 electrons. From the lecture we know that, $^5T_2$→^5E, $^1A_1$→$^1T_1$, $^1A_1$→$^1T_2$ are allowed. They have the same spin multiplicity.

As the spin multiplicity changes in SCO, the mechanism of the SCO here turns out to be a big issue.

However, there is another way to the HS state, which is via the singlet metal-to-ligand-charge-transfer (^{1}MLCT) which may exhibit strong absorption bands in the visible spectrum with molar

absorptivity about 1,000~50,000 $M^{-1}\cdot cm^{-1}$, or via the weakly absorbing and lower-lying $^{1,3}T$ states.[7, 13] The time scale and the route(going from the initially excited $^{1}MLCT$ state to the lowest-lying quintet state) are the subject of debate. X-ray absorption spectroscopy (XAS) is used to discover the mechanism, but the time resolution is subpicosecond, which has turned out to be too slow to track the earliest dynamics after photoexcitation.

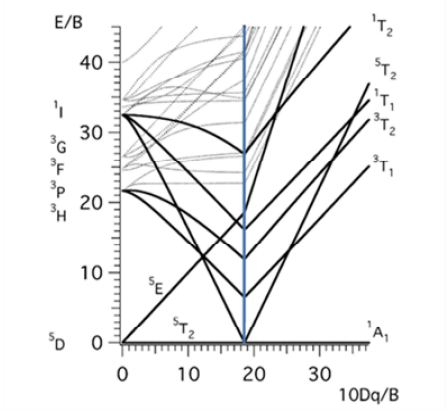

Figure 3. Tanabe-Sugano diagram for a transition metal ion with d^6 electrons.

In the class, we have learned that, XANES affords the metal oxidation state and coordination environment. The spin multiplicity affects the coordination environment. So HS and LS display different spectra (figure 4A).

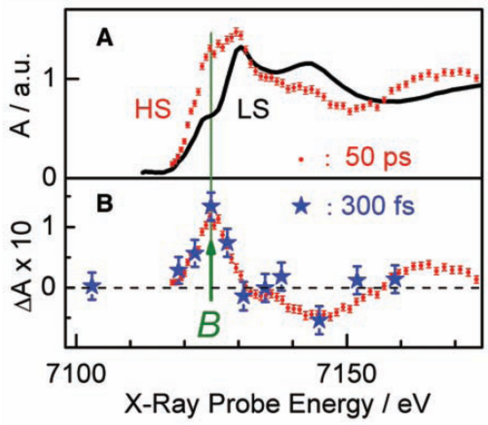

Figure 4A. The Fe K-edge XANES spectra of aqueous $[Fe^{II}(bpy)_3]^{2+}$ in its ground (LS) and excited (HS) state.
Figure 4B. The spectrum of the latter was retrieved from the LS spectrum and the difference spectrum recorded 50 ps after laser excitation (red dots in Figure 4B).[10] (50 PS = 50,000 FS)

By applying femtosecond x-ray pulses, the structural changes in real time upon visible light excitation of aqueous iron(II)-tris(bipyridine) ($[Fe^{II}(bpy)_3]^{2+}$), which serves as a model system for the family of Fe(II)-based SCO complexes are followed , and the mechanism of the ultrafast spin crossover in this class of molecules is unraveled.

The most significant consequences of SCO are the changes in metal-to-ligand bond distances. Usually, HS state has a larger volume than LS state. When the spin multiplicity changes from LS to HS, the metal-to-ligand bonds will be elongated, due to the population of the e_g orbitals which have a slight antibonding character. X-ray crystallography can be used to measure the bond distances between the metal and the ligands, which give insight into the spin state of the complex.[16]

The strongest increase in absorption intensity upon LS to HS conversion is called B-feature (arrow in Figure 4)[17-31] which complies with the increase in Fe-N bond distance[10].

Figure 4A shows the XANES of Fe(II) from excited (HS) state to its ground (LS), and Figure 4B shows the XANES of the complex excited from its ground (LS) to excited (HS) state spectrum which is recorded at 300 fs and 50 ps after laser excitation (red dots in Figure 4B)[10]. That means the complex exhibits HS state within 300 fs, as the spectrum at 300 fs is the same as that at 50 ps, which is a long time equal to 50,000 fs.

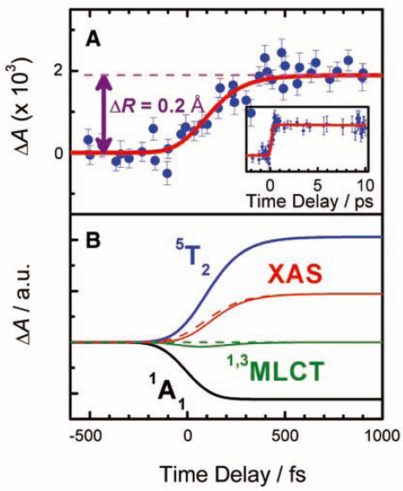

Figure 5A. Time scan of the signal (blue points) at the B-feature as a function of laser pump/x-ray probe time delay after excitation of aqueous $[Fe^{II}(bpy)_3]^{2+}$ at 400 nm.
Figure 5B. Simulated transient absorption traces of the individual states (black, green, and blue) and total (red) trace based on a four-step kinetic model $^{1}A_1 \rightarrow {}^{1}MLCT \rightarrow {}^{3}MLCT \rightarrow {}^{5}T$, with the $^{1}MLCT \rightarrow {}^{3}MLCT$ intersystem crossing taking place in 20 to 30 fs and the depopulation of the $^{3}MLCT$ state taking place in 120 fs, as determined by ultrafast fluorescence and transient absorption studies.

Figure 5A shows the transient signal at the B-feature as a function of time delay (the inset shows an expanded region out to 10 ps). It is characterized by a steep rise followed by a plateau beyond 250 to 300 fs, which suggests that the system has reached the HS state within this time frame. And this result is confirmed by the energy scan recorded at a time delay of 300 fs in Fig 4A.

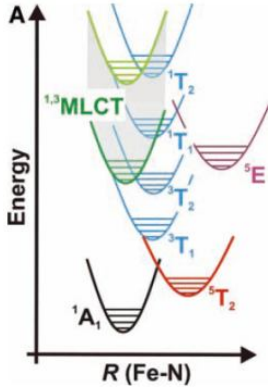

Figure 6. Representative potential energy curves of Fe(II)-based SCO complexes as a function of the Fe-N bond distance.

From figure 6, several ways to accomplish the change of spin states could be assumed. Chergui and his coworkers have investigated all of the possible ways by simulated transient absorption traces of the individual states (black, green, and blue) and total (red) trace based on a four-step kinetic model $^1A_1 \rightarrow {}^1MLCT \rightarrow {}^3MLCT \rightarrow {}^5T$ (fig 5B).

Consequently, the agreement between the experimental and the simulated time trace (Figure 5A) implies that the rise time (~150 fs) of the x-ray absorption of the HS state corresponds to the decay of the ^{3}MLCT state.

The observation of the structural dynamics allows Chergui and his coworkers to unambiguously unravel the population relaxation pathway. They summarized the general picture of the light-induced SCO process that emerges from this study in Figure 7.

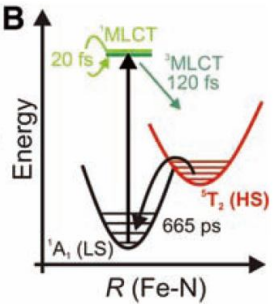

Figure 7. Relaxation cascade as determined by ultrafast laser spectroscopy upon excitation of aqueous $[Fe^{II}(bpy)_3]^{2+}$ at 400 nm.

The full cascade reduces a two-step Intersystem crossing (ISC) process $^1MLCT \rightarrow {}^3MLCT \rightarrow {}^5T$. ISC is a process involving a transition between two electronic states with different spin multiplicity.

Their results are thought to be of general validity to all Fe(II)-based SCO complexes, since $[Fe^{II}(bpy)_3]^{2+}$ is a model system. They also proved a powerful new method can be employed in the future study of molecular structural dynamics of dilute systems.

REFERENCES

(1). Creutz, C.; Chou, M.; Netzel, T. L.; Okumura, M.; Sutin, N. *J. Am. Chem. Soc.* **1980**, *102*, 1309-1319.
(2). Bergkamp, M. A.; Chang, C. K.; Netzel, T. L. *J. Phys. Chem.* **1983**, *87*, 4441-4446.
(3). McCusker, J. K.; Walda, K. N.; Dunn, R. C.; Simon, J. D.; Magde, D.; Hendrickson, D. N. *J. Am. Chem. Soc.* **1993**, *115*, 298-307.
(4). Monat, J. E.; McCusker, J. K. *J. Am. Chem. Soc.* **2000**, *122*, 4092-4097.
(5). Brady, C.; McGarvey, J. J.; McCusker, J. K.; Toftlund, H.; Hendrickson, D. N. In *Spin Crossover in Transition Metal Compounds Iii*; Springer-Verlag Berlin: Berlin, **2004**; *Vol. 235*, p 1-22.
(6). Gutlich, P.; Goodwin, H. A. In *Spin Crossover in Transition Metal Compounds I*; Springer-Verlag Berlin: Berlin, **2004**; *Vol. 233*, p 1-47.
(7). Hauser, A. In *Spin Crossover in Transition Metal Compounds Ii*; Springer-Verlag Berlin: Berlin, **2004**; *Vol. 234*, p 155-198.
(8). Khalil, M.; Marcus, M. A.; Smeigh, A. L.; McCusker, J. K.; Chong, H. H. W.; Schoenlein, R. W. *J. Phys. Chem. A* **2006**, *110*, 38-44.
(9). Gawelda, W.; Cannizzo, A.; Pham, V. T.; van Mourik, F.; Bressler, C.; Chergui, M. *J. Am. Chem. Soc.* **2007**, *129*, 8199-8206.
(10). Gawelda, W.; Pham, V.-T.; Benfatto, M.; Zaushitsyn, Y.; Kaiser, M.; Grolimund, D.; Johnson, S. L.; Abela, R.; Hauser, A.; Bressler, C.; Chergui, M. *Phys. Rev. Lett.* **2007**, *98*, 057401.
(11). Ordejon, B.; de Graaf, C.; Sousa, C. *J. Am. Chem. Soc.* **2008**, *130*, 13961-13968.
(12). Bressler, C.; Abela, R.; Chergui, M. *Z. Kristallogr.* **2008**, *223*, 307.
(13). Gütlich, P.; Goodwin, H. A. *Top. Curr. Chem.*, **2004** , *233* : 1-47
(14). Gütlich, P.; Goodwin, H. A. *Spin Crossover in Transition Metal Compounds I*; Springer-Verlag, **2004**.
(15). Gütlich, P.; Goodwin, H. A. *Spin Crossover in Transition Metal Compounds III*; Springer-Verlag: New York, **2004**; *Vol. 3*.
(16). Graaf, C. d.; Sousa, C. *Chem. Eur. J.* **2010**, *16*, 4550-4556.
(17). Briois, V.; Sainctavit, P.; Long, G. J.; Grandjean, F. *Inorg. Chem.* **2001**, *40*, 912-918.
(18). Raksi, F.; Wilson, K. R.; Jiang, Z.; Ikhlef, A.; Cote, C. Y.; Kieffer, J.-C. *J. Chem. Phys.***1996**, *104*, 6066-6069.
(19). Schoenlein, R. W.; Chattopadhyay, S.; Chong, H. H.; nbsp; W.; Glover, T. E.; Heimann, P. A.; Shank, C. V.; Zholents, A. A.; Zolotorev, M. S. *Science* **2000**, *287*, 2237-2240.
(20). Benfatto, M.; Congiu-Castellano, A.; Daniele, A.; Longa, S. D. *J. Synchrot. Radiat.* **2001**, *8*, 267-269.
(21). Dau, H.; Liebisch, P.; Haumann, M. *Anal. Bioanal. Chem.* **2003**, *376*, 562-583.
(22). Bressler, C.; Chergui, M. *Chem. Rev.* **2004**, *104*, 1781-1812.
(23). Chen, L. X. *Angew. Chem. Int. Ed.* **2004**, *43*, 2886-2905.
(24). Tomov, I. V.; Chen, J.; Ding, X.; Rentzepis, P. M. *Chem. Phys. Lett.* **2004**, *389*, 363-366.
(25). Tuchagues, J. P.; Bousseksou, A.; Molnar, G.; McGarvey, J. J.; Varret, F. In *Spin Crossover in Transition Metal Compounds Iii*; Springer-Verlag Berlin: Berlin, 2004; Vol. 235, p 85-103.
(26). Lee, T.; Jiang, Y.; Rose-Petruck, C. G.; Benesch, F. *J. Chem. Phys.* **2005**, *122*, 084506.
(27). Bargheer, M.; Zhavoronkov, N.; Woerner, M.; Elsaesser, T. *Chem. Phys. Chem.* **2006**, *7*, 783-792.
(28). Gawelda, W.; Johnson, M.; de Groot, F. M. F.; Abela, R.; Bressler, C.; Chergui, M. *J. Am. Chem. Soc.* **2006**, *128*, 5001-5009.
(29). Beaud, P.; Johnson, S. L.; Streun, A.; Abela, R.; Abramsohn, D.; Grolimund, D.; Krasniqi, F.; Schmidt, T.; Schlott, V.; Ingold, G. *Phys. Rev. Lett.* **2007**, *99*, 174801.
(30). Gaffney, K. J.; Chapman, H. N. *Science* **2007**, *316*, 1444-1448.
(31). Bressler, C.; Milne, C.; Pham, V.-T.; ElNahhas, A.; van der Veen, R. M.; Gawelda, W.; Johnson, S.; Beaud, P.; Grolimund, D.; Kaiser, M.; Borca, C. N.; Ingold, G.; Abela, R.; Chergui, M. *Science* **2009**, *323*, 489-492.

Multinuclear palladium compounds containing palladium centers ligated by five silicon atoms

Shigeru Shimada[†‡], Yong-Hua Li[†], Yoong-Kee Choe[§], Masato Tanaka[¶], Ming Bao[†‖], and Tadafumi Uchimaru[§]

[†]Research Institute for Innovation in Sustainable Chemistry, National Institute of Advanced Industrial Science and Technology (AIST), Tsukuba Central 5, 1-1-1 Higashi, Tsukuba, Ibaraki 305-8565, Japan; [§]Research Institute for Computational Sciences, National Institute of Advanced Industrial Science and Technology (AIST), Tsukuba Central 2, 1-1-1 Umezono, Tsukuba, Ibaraki 305-8568, Japan; and [¶]Chemical Resources Laboratory, Tokyo Institute of Technology, Nagatsuta, Midori-ku, Yokohama 226-8503, Japan

Edited by Jack Halpern, University of Chicago, Chicago, IL, and approved March 12, 2007 (received for review January 17, 2007)

Palladium (Pd) generally prefers low oxidation states. So far, no stable Pd compound with a +5 oxidation state is known. Here, we report two multinuclear Pd compounds containing Pd centers ligated by five silicon (Si) atoms. A thermal condensation reaction of [{1,2-$C_6H_4(SiMe_2)(SiH_2)$}$Pd^{II}(Me_2PCH_2CH_2PMe_2)$] (Me = methyl) afforded two stereoisomers of dinuclear Pd^{II} compounds and a trinuclear Pd compound as major products and a tetranuclear Pd compound as a minor product. The structures of the four Pd compounds were confirmed by single-crystal x-ray structure analysis. The dinuclear Pd compounds have a dimeric structure of [{1,2-$C_6H_4(SiMe_2)(SiH)$}$Pd^{II}(Me_2PCH_2CH_2PMe_2)$] connected through a Si–Si single bond formed by dehydrogenation of two molecules of the starting compound. The trinuclear and tetranuclear Pd compounds proved to have Pd centers bonded to five Si atoms with normal Pd–Si single-bond distances. Theoretical calculations of the trinuclear and tetranuclear Pd compounds accurately reproduced their x-ray structures and suggested that all of the Pd–Si bonds of the central Pd atoms have a relatively high single-bond character.

transition metal | hydrosilanes | oxidation states

Palladium (Pd) compounds provide useful catalysts for organic transformations to produce a wide range of organic compounds such as pharmaceuticals, agrochemicals, and organic materials for various applications (1, 2). Organopalladium compounds, typical intermediates in Pd-catalyzed organic transformations, generally prefer low formal oxidation states such as 0 and +2. Only relatively recently has the importance of organopalladium compounds with a +4 formal oxidation state been recognized (3, 4). The first stable organopalladium compounds with this +4 formal oxidation state, $Pd^{IV}(C_6F_5)_2Cl_2$(L–L) (L–L = bidentate neutral ligands), were isolated in 1975 (5); then, alkylpalladium(IV) species were also isolated and intensively studied (3, 6). However, an organopalladium compound with a formal oxidation state exceeding +4 has never been identified. On the other hand, highly electronegative fluorine ligands reportedly can produce +5 and +6 oxidation states in inorganic Pd compounds, although such species are unstable and have not been well characterized (7, 8). Electrochemical formation of PdO_3 is also suggested (9). It is also known that more electropositive ligands such as hydride and silyl ligands can form stable transition-metal compounds with high formal oxidation states such as $K_2Re^{VII}H_9$, $(Me_5C_5)Ir^{V}H_4$, and $(Me_5C_5)M^{V}(H)_2(SiEt_3)_2$ (M = Co, Rh, Ir) (10–14).

We have found that sterically less demanding chelating silyl ligands are useful in stabilizing silyl transition-metal compounds with high formal oxidation states (15) and reported silylpalladium(IV) (16) and silylnickel(IV) compounds (17). During our effort to synthesize silyl group 10 transition-metal compounds with formal oxidation states exceeding +4, we obtained a trinuclear Pd compound **1** (Fig. 1), which has a central Pd atom ligated by six Si atoms (18). X-ray structure analysis of compound **1** showed a possible Si–Si bonding interaction between two pairs of Si atoms and lead to two possible structural descriptions, **1a** (six Pd–Si single bonds, formal oxidation state +6) and **1b** (two Pd–Si single bonds and two Si–Si σ-bonds coordinating to the Pd atom, formal oxidation state +2) (18, 19). Theoretical calculations for compound **1** suggested that **1b** more appropriately represented the bonding structure of this compound than did **1a** (20, 21). In this article, we describe two multinuclear Pd compounds, each of which has a Pd center ligated by five Si atoms. X-ray structure analysis as well as theoretical calculations suggested that each Pd–Si bond of the central Pd atoms has a relatively high single-bond character.

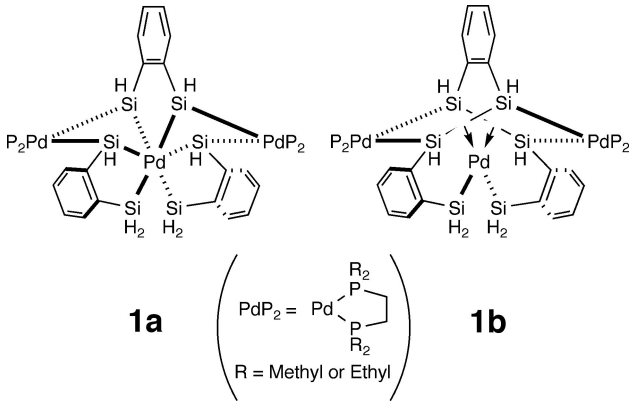

Fig. 1. Two structural description of compound **1**.

Results and Discussion

The trinuclear Pd compound **1** was synthesized by the thermal condensation reaction of three molecules of Pd(II) compound [{1,2-$C_6H_4(SiH_2)_2$}$Pd^{II}(R_2PCH_2CH_2PR_2)$] **2**. We simply modified the structure of the starting Pd compound **2** by putting two methyl groups on one of the two Si atoms. Because the Si–C bonds are much less reactive toward transition metals than are Si–H bonds, the modified compound [{1,2-$C_6H_4(SiMe_2)(SiH_2)$}Pd^{II}(dmpe)] **3** [dmpe = 1,2-bis(dimethylphosphino)ethane] was expected not to produce a compound similar to **1**.

A thermal condensation reaction of compound **3**, which was prepared by the reaction of 1,2-$C_6H_4(SiMe_2H)(SiH_3)$ (22) with

Author contributions: S.S. and M.T. designed research; S.S., Y.-H.L., Y.-K.C., M.B., and T.U. performed research; S.S. analyzed data; and S.S. and Y.-K.C. wrote the paper.

The authors declare no conflict of interest.

This article is a PNAS Direct Submission.

Abbreviations: AIM, atoms in molecule; DME, 1,2-dimethoxyethane; dmpe, 1,2-bis(dimethylphosphino)ethane.

Data deposition: The atomic coordinates have been deposited in the Cambridge Structural Database, Cambridge Crystallographic Data Centre, Cambridge CB2 1EZ, United Kingdom (CSD reference nos. 626200–626203).

[‡]To whom correspondence should be addressed. E-mail: s-shimada@aist.go.jp.

[‖]Present address: State Key Laboratory of Fine Chemicals, Dalian University of Technology, 158 Zhongshan Road, Dalian 116012, China.

This article contains supporting information online at www.pnas.org/cgi/content/full/0700450104/DC1.

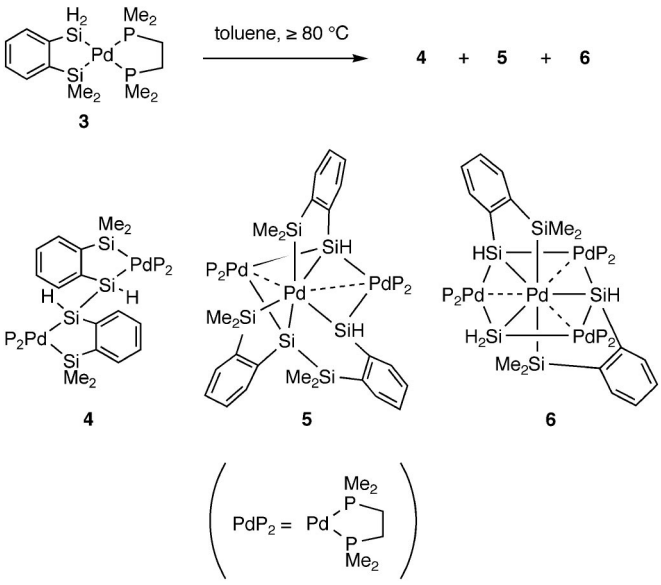

Fig. 2. Synthesis of compounds **4**–**6**.

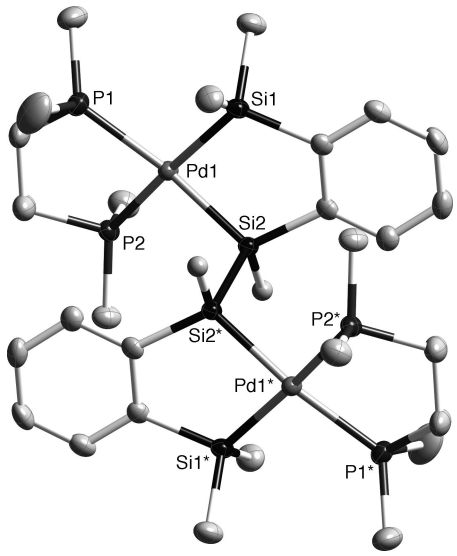

Fig. 3. Thermal ellipsoid plots (50% probability level for Pd, P, Si, and C atoms) of *meso*-**4** determined by single-crystal x-ray diffraction. Hydrogen atoms on the carbon atoms are omitted for clarity.

$[Pd(PEt_3)_2(dmpe)]$, took place at 80°C or higher (Fig. 2). At 80°C in toluene, dinuclear compound **4** with a new Si–Si single bond was initially formed as a mixture of two stereoisomers as judged by ^1H and ^{31}P NMR spectroscopy. The structures of the two stereoisomers were confirmed to be *meso*- and *dl*-isomers by x-ray structure analysis (*vide infra*). With continued heating at 80°C for 2 days, trinuclear compound **5** started to emerge, and ^{31}P NMR spectroscopy identified four signals with equal intensities for this compound. A separate experiment in an NMR tube heated at 100°C for 6 days afforded compounds **4** (*meso*- and *dl*-isomers in a 7:3 ratio) and **5** as the main products. The reaction slowed gradually, and the conversion of **3** reached ≈70% after 6 days. The yields of **4** and **5** estimated by ^1H NMR integration were 55% and 39%, respectively, based on the converted **3**. Compounds **4** and **5** were isolated by fractional solvent extraction/crystallization procedures. During the attempts to isolate and crystallize compound **5**, a tiny amount of minor product, tetranuclear compound **6**, was unexpectedly obtained as single crystals. Although compound **6** was formed in a low yield, the existence of **6** in the reaction mixture was easily confirmed by ^1H NMR spectroscopy in tetrahydrofuran (THF)-d_8, in which some of the signals of **6** were well separated from those of other compounds. The estimated yields of compound **6** in the reaction mixture varied (1–5%) depending on the reaction conditions. The product distribution largely depended on the concentration and reaction temperature. Higher concentration and higher reaction temperature favor the formation of **5** and **6**.

The structures of the two isomers of **4**, **5**, and **6**, respectively, were unambiguously determined by the x-ray structure analysis. Figs. 3 and 4, respectively, show the molecular structures of *meso*- and *dl*-**4**. The Pd–Si, Pd–P, and Si–Si bond distances in *meso*- and *dl*-**4** (Table 1) were all in their typical ranges.

Fig. 5*a* shows the molecular structure of **5**, and its structural features are as follows. The central Pd atom, Pd1, no longer retains the chelating phosphine ligand as is the case in **1** but instead is ligated by five Si atoms. The geometry of the $Pd1(Si)_5$ moiety may be described as highly distorted, square-based pyramidal with Si5 at the apical position. The five Pd1–Si bond distances range from 2.2903(8) to 2.4015(8) Å (Table 2) and are comparable to typical Pd–Si single-bond distances [2.26–2.45 Å] (Cambridge Structural Database, Version 5.27, November 2005). These distances contrast with those in compound **1**, in which four are long [2.437(3)–2.562(3) Å, average 2.483(3) Å for **1** bearing dmpe ligands]. One (Si6) of the six Si atoms in **5** is not bonded to Pd1 but forms a Si–Si single bond (Si3–Si6) with a common distance [2.3414(12) Å]. In compound **1**, there are two short Si···Si contacts [2.488(4)-2.589(4) Å], whereas compound **5** has no such short Si···Si contact [the shortest Si···Si contact is 2.8919(13) Å, Si3···Si5]. The Pd···Pd distances [2.7677(3) and 2.7996(3) Å] suggest possible weak interatomic interactions. Another unique feature of compound **5** is that one (Si1) of the Si atoms is pentacoordinate. As mentioned above, the Pd1–Si1 distance is comparable to common Pd–Si single-bond distances, but the Pd2–Si1 [2.5273(10) Å] and Pd3–Si1 [2.5966(9) Å] bond distances are much longer than is common.

The molecular structure of compound **6** is shown in Fig. 5*b*. Compound **6** is crystallographically C_2-symmetric. The geometry of the $Pd1(Si)_5$ moiety can be described as distorted trigonal bipyramidal [or hexagonal bipyramidal for the $Pd1(Si)_5(Pd)_3$ moiety]. Five atoms (Pd1, Pd2, Pd2*, Pd3, and Si1) locate on the same plane, whereas two Si atoms (Si2 and Si2*) deviate from the plane by 0.59 Å. The Pd1–Si1, Pd1–Si2(Si2*), and Pd1–Si3(Si3*) bond distances of 2.3265(13), 2.2944(9), and 2.4357(10) Å, respectively, are similar

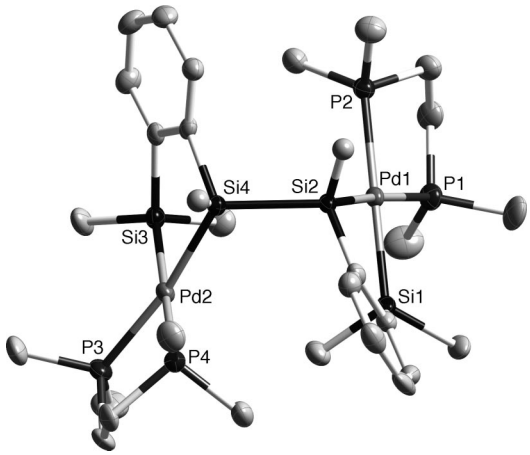

Fig. 4. Thermal ellipsoid plots (50% probability level for Pd, P, Si, and C atoms) of *dl*-**4** determined by single-crystal x-ray diffraction. Hydrogen atoms on the carbon atoms are omitted for clarity.

Table 1. Selected bond distances (Å) for compounds *meso*- and *dl*-4

Bond	*meso*-4	*dl*-4
Pd1–Si1	2.3634(10)	2.3713(16)
Pd1–Si2	2.3405(9)	2.3626(14)
Pd2–Si3		2.3632(17)
Pd2–Si4		2.3613(15)
Pd1–P1	2.3307(10)	2.3259(16)
Pd1–P2	2.3391(9)	2.3465(15)
Pd2–P3		2.3277(17)
Pd2–P4		2.3402(15)
Si–Si	2.3720(13)	2.355(2)

to those of common Pd–Si single bonds. The axial Pd1–Si3(Si3*) bond distances are relatively long; this is partly because the two axial Si atoms [Si3 and Si3*] locate *in trans* to each other, and the strong trans-influence (or structural trans-effect) of Si atoms lengthens the Pd–Si bond distances (23). The three equatorial Si atoms (Si1, Si2, and Si2*) are pentacoordinate, like Si1 in compound **5**. The Pd–Si distances for the outer Pd atoms [2.5124(5)–2.6093(9) Å] are much longer than those of common Pd–Si single bonds.

Although it is difficult and less meaningful to assign a formal oxidation state for each atom in cluster-type compounds (19, 20), an unusual +5 formal oxidation state may be assigned to the central Pd atoms (Pd1) in **5** and **6**, if each Pd1–Si bond is simply counted to increase the formal oxidation state of Pd1 by +1. Therefore, we carried out density functional theory calculations for **5** and **6** to obtain further information about the structures of compounds **5** and **6**. We also further evaluated the bonding of **5** and **6**, using Mayer's bond order analysis (24) and Bader's atoms in molecule (AIM) analysis (25); the former was used for the bonding analysis of compound **1** (20), and the latter searches for bond critical points and indicates the existence of a chemical bond between two atoms sharing the bond critical point. Both calculated structures of **5** and **6** accurately reproduced the x-ray structures of **5** and **6**. Table 2 summarizes selected bond distances obtained from x-ray analysis and density functional theory calculations and Mayer bond orders for **5** and **6** [see supporting information (SI) Tables 4 and 5 for Cartesian coordinates for the calculated structures of **5** and **6**, and see SI Tables 6 and 7 for further lists of Mayer bond orders for **5** and **6**]. For compound **5**, the bond orders of the five Pd1–Si bonds (0.67–0.77) are higher than the highest value (0.63) calculated for the Pd–Si bonds of the central Pd atom in compound **1** (20). The total bond orders of the five Pd1–Si bonds (3.63) is also higher than that of the six central Pd–Si bonds (3.32) in **1** (20). The calculated bond orders and the bond distances determined by x-ray analysis suggest that the five Pd1–Si bonds in **5** have a relatively high single-bond character. The bonds between the pentacoordinate Si1 and terminal Pd atoms (Pd2 and Pd3) have lower bond orders (average 0.50), as expected from the long bond distances. The total (3.59) and individual bond orders (0.67–0.75) of the five Pd1–Si bonds in **6** are at a level similar to those of **5**, suggesting that the five Pd1–Si bonds in **6** also have a relatively high single-bond character. The six outer Pd–Si bonds in **6** have lower bond orders (average 0.48), as expected from the long bond distances.

Because attempted AIM analysis on compounds **5** and **6** failed as a result of its inability to find bond critical points for the C–H bonds of the benzene rings of **5** and **6**, we carried out AIM analysis on model systems **M5** and **M6** (Fig. 6*a*; see also SI Figs. 7 and 8), which were constructed by removing carbon atoms from **5** and **6**, respectively. The Cartesian coordinates of core regions were fixed, while the positions of the substituted hydrogen atoms were optimized. Thus, the nature of the chemical bonds of the core regions in the model compounds **M5** and **M6** should be the same as those in the real systems. AIM analysis on **M5** and **M6** was successful and indicated the existence of bond critical points in all Pd1–Si bonds of **M5** and **M6** (Fig. 6*b*). This result also supports the bonding nature of Pd1–Si bonds of compounds **5** and **6**. Mayer bond order analysis (Table 2) suggested a possible weak bonding interaction between Pd atoms in compounds **5** and **6** (bond order = 0.20–0.22) and also between Si3 and Si5 atoms (bond order = 0.28) in compound **5**, although the Si3···Si5 distance is long. AIM analyses on the model compounds showed the existence of bond critical points only between Pd atoms in **M6** but not between Pd atoms or Si3 and Si5 atoms in **M5**.

The formation of silylpalladium compounds with unusual Pd centers ligated by five Si atoms represents one of interesting features of Si ligands in transition metal chemistry. Although interest in the chemistry of transition metal compounds with Si ligands is rapidly growing (26), the field is still at the initial stage of development compared with the organometallic chemistry of transition metals. We believe Si ligands will provide further unique chemistry of transition metals and lead to the development of unique catalyses.

Materials and Methods

All manipulations of air-sensitive materials were carried out under a nitrogen atmosphere by using standard Schlenk tube techniques

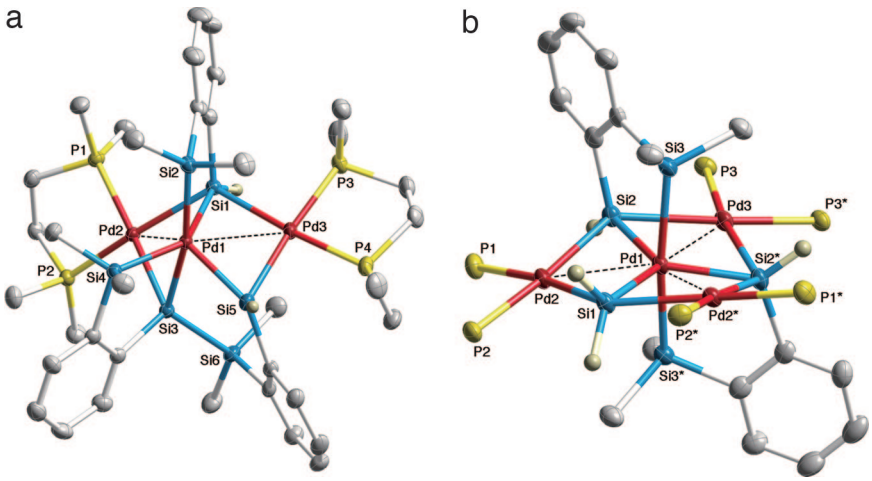

Fig. 5. Thermal ellipsoid plots (50% probability level for Pd, P, Si, and C atoms) of compound **5** (*a*) and compound **6** (*b*) determined by single-crystal x-ray diffraction. Hydrogen atoms on the carbon atoms (for **5** and **6**) and carbon atoms on the phosphorus atoms (for **6**) are omitted for clarity.

Table 2. Experimental (x-ray diffraction) and calculated bond distances and Mayer bond orders for compounds 5 and 6

Bond	Distance, Å		Bond order
	Experimental	Calculated	
	Compound 5		
Pd1–Si1	2.3526(11)	2.401	0.672
Pd1–Si2	2.4015(8)	2.457	0.747
Pd1–Si3	2.3385(8)	2.384	0.709
Pd1–Si4	2.3464(11)	2.405	0.729
Pd1–Si5	2.2903(8)	2.326	0.769
Pd2–Si1	2.5273(10)	2.564	0.542
Pd2–Si3	2.3832(9)	2.443	0.628
Pd3–Si1	2.5966(9)	2.652	0.455
Pd3–Si5	2.4033(11)	2.439	0.668
Pd1–Pd2	2.7996(3)	2.939	0.200
Pd1–Pd3	2.7677(3)	2.899	0.211
Si3···Si5	2.8919(13)	2.928	0.280
	Compound 6		
Pd1–Si1	2.3265(13)	2.349	0.673
Pd1–Si2 or Pd1–Si2*	2.2944(9)	2.32	0.747
Pd1–Si3 or Pd1–Si3*	2.4357(10)	2.508	0.713
Pd2–Si1 or Pd2*–Si1	2.5124(5)	2.572	0.519
Pd2–Si2 or Pd2*–Si2*	2.5781(10)	2.621	0.460
Pd3–Si2 or Pd3–Si2*	2.6093(9)	2.649	0.449
Pd1–Pd2 or Pd1–Pd2*	2.7332(3)	2.815	0.204
Pd1–Pd3	2.7013(4)	2.804	0.218

or in a glovebox filled with argon or nitrogen. Toluene-d_8, THF-d_8, and benzene-d_6 were distilled from Na/benzophenone ketyl. All other anhydrous solvents were purchased from Kanto Chemicals or Aldrich and degassed before use. ^{1}H (499.1 MHz), ^{29}Si (99.1 MHz), and ^{31}P (202.0 MHz) NMR spectra were recorded on a JEOL LA500 spectrometer. Chemical shifts are given in parts per million, using external references [tetramethylsilane (0 ppm) for ^{1}H and ^{29}Si, and 85% H_3PO_4 (0 ppm) for ^{31}P] or residual solvent signal for the ^{1}H NMR in THF-d_8 (the residual solvent signal at lower field position was set to 3.60 ppm), and coupling constants are reported in hertz.

Synthesis of [{1,2-C_6H_4(SiMe$_2$)(SiH$_2$)}Pd(dmpe)], 3. A toluene solution (5 ml) of $Pd(PEt_3)_4$ (300 mg, 0.52 mmol) and dmpe (78 mg, 0.52 mmol) was stirred at room temperature overnight. Volatiles were removed under vacuum to leave $Pd(PEt_3)_2$(dmpe) as a viscous solid. To the solid was added toluene (5 ml) and 1,2-C_6H_4(SiMe$_2$H)(SiH$_3$) (87 mg, 0.52 mmol) at 0°C. During the addition of 1,2-C_6H_4(SiMe$_2$H)(SiH$_3$), a small amount of gas evolution was observed. Then the mixture was stirred at room temperature for 12 h under a nitrogen atmosphere. Removal of the volatiles under vacuum and washing the residual solid with hexane gave **3** in 72% yield (157 mg) as a pale brown powder. The product is practically pure and used for the following reactions without further purification. ^{1}H NMR (toluene-d_8) δ 0.73 (t, 6H, $J_{P\text{-}H}$ = 2), 0.92–1.04 (m, 16H), 5.57 (t, 2H, $J_{P\text{-}H}$ = 10, $J_{Si\text{-}H}$ = 158), 7.32 (t, 1H, $J_{H\text{-}H}$ = 7), 7.36 (t, 1H, $J_{H\text{-}H}$ = 7), 7.82 (d, 1H, $J_{H\text{-}H}$ = 7), 8.07 (d, 1H, $J_{H\text{-}H}$ = 7). ^{31}P NMR (toluene-d_8) δ 13.2 (br). ^{29}Si{^{1}H} NMR (toluene-d_8, dept) δ −17.7 (d, $J_{P\text{-}Si}$ = 137, ($J_{H\text{-}Si}$ = 158), *Si*H$_2$). The measurement parameters were adjusted to the silicon atoms with directly bound hydrogen atoms. The $J_{H\text{-}Si}$ value was determined by ^{1}H-coupled spectrum. ^{29}Si{^{1}H} NMR (toluene-d_8, inept) δ 31.8 (d, $J_{P\text{-}Si}$ = 145, *Si*Me$_2$). The measurement parameters were adjusted to the silicon atoms with two methyl groups. Anal. Calcd. for $C_{14}H_{28}P_2PdSi_2$: C, 39.95; H, 6.71. Found C, 40.14; H, 6.65.

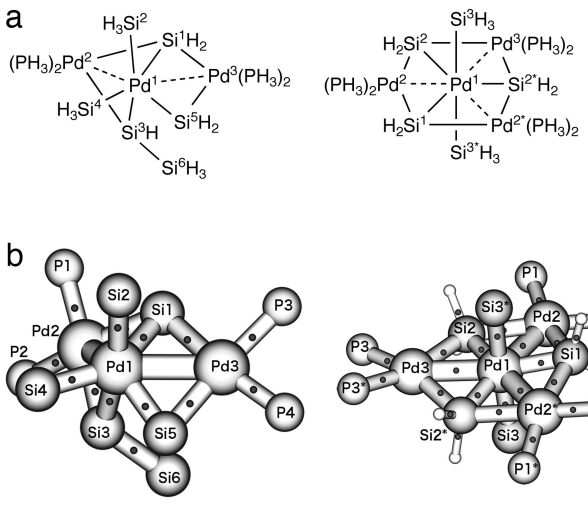

Fig. 6. AIM analysis. (*a*) Structure of model compounds **M5** and **M6**. (*b*) AIM analysis results for model compounds **M5** and **M6**. Some of hydrogen atoms are omitted for clarity. Dots between the atoms represent the bond critical points.

Thermal Condensation Reaction of 3. ***Isolation of compounds 4 and 5.*** A toluene solution (10 ml) of **3** (507 mg, 1.20 mmol) was heated in an

Table 3. Calculated and observed ^{29}Si NMR chemical shifts [δ (ppm)] of compounds 5 and 6

Si	Compound **5**		Compound **6**	
	Calculated	Observed	Calculated	Observed
Si1	122.1	130.9	101.6	103.0
Si2 (Si2*)	25.8	25.0	147.0 (147.1)	139.3
Si3 (Si3*)	194.8	173.1	24.6 (24.5)	19.0
Si4	43.5	38.7	—	—
Si5	202.7	210.7	—	—
Si6	−32.1	−21.1	—	—

The atomic numbering refers to that in Fig. 5.

oil bath at 90°C for 44 h, at 95°C for 51 h, and then at 100°C for 47 h. After cooling to room temperature, volatiles were removed under vacuum to give crude solid products. NMR measurement of the crude products showed that the conversion of **3** was ≈68% and the formation of **4** (≈39%, *meso*-**4**/*dl*-**4** = 72/28) and **5** (≈23%) as major products. The crude products were dissolved in THF (≈20 ml) and filtered through a membrane filter (Sartorius Minisart SRP 15, no. 17573). The filtrate was evacuated to remove volatiles, and the remaining solid was extracted with hexane (3 × 4 ml) and hexane/toluene mixture (1/1, 3 × 3 ml), leaving a solid mixture mainly consisting of **4** and **5**. The solid was dissolved in toluene (20 ml) by heating at 100°C for a few minutes. After cooling to room temperature, the supernatant was transferred to another Schlenk tube to remove a small amount of undissolved materials on the bottom. A few crystals of **4** were added to the solution to induce crystallization, and the mixture was kept at room temperature for 1 day to give almost colorless crystals of **4**. The supernatant was removed by decantation, and the remaining crystals were washed with toluene (1 × 1 ml and 2 × 0.5 ml) and hexane (1 × 0.5 ml and 2 × 1 ml) and dried under vacuum to give 65 mg of **4** (*meso*-**4**:*dl*-**4** = 78:22). The supernatant was evacuated to remove the solvent, and the resulting solid was dissolved in 16 ml of 1,2-dimethoxyethane (DME) by heating in an oil bath at 100°C for a few minutes. Keeping the solution at room temperature for 1 day gave orange-red crystals of **5** containing DME as a cocrystallization solvent. The supernatant was removed by decantation, and the remaining crystals were washed with DME and hexane to give 27 mg (6%) of **5**. The separated supernatant was evacuated to remove the solvent, and the resulting solid was recrystallized from toluene to give additional **4** (58 mg). Total isolated yield of **4** was 24%. Compound **4**: ^{1}H NMR (benzene-d_6, 4:1 mixture of *meso*- and *dl*-isomers) δ 0.43 (d, 6H of *meso*-isomer, $J_{P\text{-}H}$ = 3); 0.69–1.15 (m, 38H of *meso*-isomer and 44H of *dl*-isomer); 5.62 (ddd, 2H of *dl*-isomer, $J_{P\text{-}H}$ = 4, 8, 23, Si-*H*); 5.86 (ddd, 2H of *meso*-isomer, $J_{P\text{-}H}$ = 5, 8, 19, Si-*H*); 7.21–7.37 (m, 4H of *meso*-isomer and 4H of *dl*-isomer); 7.67 (d, 2H of *meso*-isomer, $J_{H\text{-}H}$ = 7); 7.81 (d, 4H of *dl*-isomer, $J_{H\text{-}H}$ = 8); 8.07 (d, 2H of *meso*-isomer, $J_{H\text{-}H}$ = 7). ^{31}P NMR (benzene-d_6, 4:1 mixture of *meso*- and *dl*-isomers) δ value 10.2 (d, *meso*-isomer, $J_{P\text{-}P}$ = 13); 10.6 (d, *dl*-isomer, $J_{P\text{-}P}$ = 15); 10.9 (d, *meso*-isomer, $J_{P\text{-}P}$ = 13); 13.3 (d, *dl*-isomer, $J_{P\text{-}P}$ = 15). Anal. calcd. for $C_{28}H_{54}P_4Pd_2Si_4$: C, 40.04; H, 6.48. Found C, 40.43; H, 6.48. Compound **5.** ^{1}H NMR (THF-d_8) δ −0.10 (s, 3H, SiCH_3), −0.08 (s, 3H, SiCH_3), −0.03 (s, 3H, SiCH_3), 0.07 (d, 3H, $J_{P\text{-}H}$ = 8, PCH_3), 0.13 (d, 3H, $J_{P\text{-}H}$ = 7, PCH_3), 0.20 (d, 3H, $J_{P\text{-}H}$ = 9, PCH_3), 0.43 (d, 3H, $J_{P\text{-}H}$ = 8, PCH_3), 0.45 (s, 3H, SiCH_3), 0.70 (s, 3H, SiCH_3), 0.72 (s, 3H, SiCH_3), 1.44 (d, 3H, $J_{P\text{-}H}$ = 7, PCH_3), 1.54 (d, 3H, $J_{P\text{-}H}$ = 9, PCH_3), 1.59 (d, 3H, $J_{P\text{-}H}$ = 7, PCH_3), 1.61 (d, 3H, $J_{P\text{-}H}$ = 8, PCH_3), 1.50 - 1.85 (m, 8H, PCH_2CH_2P), 6.86–6.90 (m, 2H), 7.00–7.11 (m, 4H), 7.15 (dt, 1H, $J_{H\text{-}H}$ = 1 and 7), 7.37–7.40 (m, 1H), 7.45–7.49 (m, 1H), 7.60–7.67 (m, 2H), 7.76–7.85 (m, 2H), 8.01 (d, 1H, $J_{H\text{-}H}$ = 7 Hz). ^{31}P{^{1}H} NMR (THF-d_8) δ 15.7 (dd, $J_{P\text{-}P}$ = 10 and 31), 17.3 (dd, $J_{P\text{-}P}$ = 12 and 29), 18.9 (dd, $J_{P\text{-}P}$ = 10 and 29), 21.0 (dd, $J_{P\text{-}P}$ = 12 and 31). ^{29}Si{^{1}H} NMR (THF-d_8, nne) δ −21.1 (d, $J_{P\text{-}Si}$ = 6, Si6), 25.0 (s, Si2 (or Si4)), 38.7 (d, $J_{P\text{-}Si}$ = 18, Si4 (or Si2)), 129.8–132.0 (m, Si1), 173.1 (d, $J_{P\text{-}Si}$ = 113, Si3), 210.7 (ddd, $J_{P\text{-}Si}$ = 12, 34, 122, Si5). The assignment is based on the coupling pattern of the signals as well as the prediction by the theoretical calculations (Table 3). IR (KBr pellet, cm^{-1}) 1999 (Si–H), 1972 (Si–H). Anal. calcd. for $C_{36}H_{64}P_4Pd_3Si_6{\cdot}C_4H_{10}O_2$ C, 40.08; H, 6.22. Found C, 40.27; H, 6.23.

Isolation of compound 6. A toluene solution (100 ml) of **3** (910 mg, 2.16 mmol) was heated in an oil bath at 100°C for 6 days. The estimated molar ratio of **3**/**4** (two isomers)/**5**/**6** by ^{1}H NMR spectroscopy was 73/19/7.7/0.3 at this stage. The solution was evacuated to reduce the volume to ≈40 ml and then was heated in an oil bath at 100°C for 58 h. The estimated molar ratio of **3**/**4** (two isomers)/**5**/**6** by ^{1}H NMR spectroscopy was 48/34/17/1 at this stage. The mixture was evacuated to dryness and washed with hexane (2 × 7 ml and 3 × 5 ml) to leave solid materials. The solid was dried under vacuum, dissolved in toluene (7 ml), and heated in an oil bath at 100°C for 84 h. The estimated molar ratio of **3**/**4** (two isomers)/**5**/**6** by ^{1}H NMR spectroscopy was 29/38/30/3 at this stage. The mixture was evacuated to dryness and reacted with 1,2-C_6H_4($SiMe_2H$)(SiH_3) (111 mg, 0.67 mmol) in THF (10 ml) at 40°C for 11 h [this hydrosilane selectively reacted with compound **4** to form an unidentified product(s), which has much higher solubility in hexane than does **4** and can be easily removed from the mixture by solvent extraction]. The mixture was evacuated to dryness and washed with hexane (4 × 5 ml), hexane/toluene (3/2) mixture (4 × 5 ml), and hexane/toluene (1/1) mixture (3 × 7 ml). The residue was dissolved in THF (20 ml), filtered through a membrane filter (Sartorius Minisart SRP 15, no. 17573), and evacuated to dryness to give yellow-brown solid (179 mg). ^{1}H and ^{31}P NMR spectroscopy showed that the solid consisted of **5** and **6** in a 92:8 molar ratio. Fortunately, compound **6** has higher solubility in DME but much lower solubility in diethyl ether than does **5**. The solid was extracted with DME (6 ml) to give a mixture of **5** and **6** in a 3:4 molar ratio and to leave pure **5** (153 mg, 19% yield). Then, the mixture (after evacuation) was extracted with diethyl ether (1 × 3 ml, 1 × 2 ml, 1 × 1 ml) to leave compound **6** with >80% purity by ^{1}H and ^{31}P NMR spectroscopy (9 mg). Compound **6**: ^{1}H NMR (THF-d_8) δ −0.48 (s, 6H, SiCH_3), −0.37 (s, 6H, SiCH_3), 0.03 (d, 6H, $J_{P\text{-}H}$ = 7, PCH_3), 1.36–1.40 (m, 12H, PCH_3), 1.48–1.51 (m, 6H, PCH_3), 1.56–1.58 (m, 6H, PCH_3), 1.68 (d, 6H, $J_{P\text{-}H}$ = 7, PCH_3), 1.50–1.90 (m, 12H, PCH_2CH_2P), 6.06 (tt, 2H, $J_{P\text{-}H}$ = 7 and 20, SiH_2), 6.62 (t, 2H, $J_{H\text{-}H}$ = 7, aromatic H), 6.91 (t, 2H, $J_{H\text{-}H}$ = 7, aromatic H), 6.94 (d, 2H, $J_{H\text{-}H}$ = 7, aromatic H), 7.76–7.93 (br m, 2H, Si*H*), 7.89 (d, 2H, $J_{H\text{-}H}$ = 7, aromatic H). The assignments of SiH_2 and Si*H* signals are based on the coupling patterns of the signals and the prediction by the theoretical calculations. ^{31}P{^{1}H} NMR (THF-d_8) δ 11.7–12.6 (m), 14.1 (s). ^{29}Si{^{1}H} NMR (THF-d_8, dept) δ 102.0–103.9 (m, Si1), 138.1–140.5 (m, Si2 and Si2*). The measurement parameters were adjusted to the silicon atoms with directly bound hydrogen atoms. The assignments of the signals are based on the prediction by the theoretical calculations (Table 3). ^{29}Si{^{1}H} NMR (THF-d_8, inept) δ 19.0 (s, Si3 and Si3*). The measurement parameters were adjusted to the silicon atoms with two methyl groups.

X-Ray Data Collection, Structure Determination, and Refinement. For details on x-ray data collection, structure determination, and refinement for compounds *meso*-**4**, *dl*-**4**, **5**, and **6**, see *SI Materials and Methods* and *SI Data Set*.

Computational Details. The calculations for geometry optimizations, vibrational frequency analysis, NMR chemical shifts, Mayer's bond-order analysis, and AIM analysis were carried out with the Gaussian 03 program package (27). For further details on computations, see *SI Materials and Methods*.

Y.-H.L. thanks the Japan Society for the Promotion of Science for a postdoctoral fellowship. This work was supported by Ministry of Education, Science, Sports, and Culture (Japan) Grants-in-Aid for Scientific Research 15350037 and 05F05666.

1. Tsuji J (2004) *Palladium Reagents and Catalysts* (Wiley, Chichester, UK).
2. Malleron J-L, Fiaud J-C, Legros J-Y (1997) *Handbook of Palladium-Catalyzed Organic Reactions* (Academic, San Diego).
3. Canty AJ (1992) *Acc Chem Res* 25:83–90.
4. Elsevier CJ (1999) *Coord Chem Rev* 185/186:809–822.
5. Uson R, Fornies J, Navarro R (1975) *J Organomet Chem* 96:307–312.
6. Byers PK, Canty AJ, Skelton BW, White AH (1986) *J Chem Soc Chem Commun*, 1722–1724.
7. Timakov AA, Prusakov VN, Drobyshevskii YV (1982) *Russ J Inorg Chem* 27:1704–1705.

8. Sokolov VB, Drobyshevskii YV, Prusakov VN, Ryzhkov AV, Khoroshev SS (1976) *Proc Acad Sci USSR* 229:503–505.
9. Chausse V, Regull P, Victori L (1987) *J Electroanal Chem* 238:115–128.
10. Abrahams SC, Ginsberg AP, Knox K (1964) *Inorg Chem* 3:558–567.
11. Gilbert TM, Bergman RG (1983) *Organometallics* 2:1458–1460.
12. Fernandez MJ, Maitlis PM (1982) *J Chem Soc Chem Commun*, 310–311.
13. Fernandez MJ, Maitlis PM (1983) *Organometallics* 2:164–165.
14. Brookhart M, Grant BE, Lenges CP, Prosenc MH, White PS (2000) *Angew Chem Int Ed* 39:1676–1679.
15. Shimada S, Tanaka M (2006) *Coord Chem Rev* 250:991–1011.
16. Shimada S, Tanaka M, Shiro M (1996) *Angew Chem Int Ed Engl* 35:1856–1858.
17. Shimada S, Rao MLN, Tanaka M (1999) *Organometallics* 18:291–293.
18. Chen WZ, Shimada S, Tanaka M (2002) *Science* 295:308–310.
19. Crabtree RH (2002) *Science* 295:288–289.
20. Sherer EC, Kinsinger CR, Kormos BL, Thompson JD, Cramer CJ (2002) *Angew Chem Int Ed* 41:1953–1956.
21. Aullón G, Lledós A, Alvarez S (2002) *Angew Chem Int Ed* 41:1956–1959.
22. Shimada S, Rao MLN, Hayashi T, Tanaka M (2001) *Angew Chem Int Ed* 40:213–216.
23. Coe BJ, Glenwright SJ (2000) *Coord Chem Rev* 203:5–80.
24. Mayer I (1983) *Chem Phys Lett* 97:270–274.
25. Bader RFW (1991) *Chem Rev* 91:893–928.
26. Corey JY, Braddock-Wilking J (1999) *Chem Rev* 99:175–292.
27. Frisch MJ, Trucks GW, Schlegel HB, Scuseria GE, Robb MA, Cheeseman JR, Montgomery JA, Jr, Vreven T, Kudin KN, Burant JC, *et al.* (2004) Gaussian 03 (Gaussian, Inc, Wallingford, CT), Revision C.02.

The first examples of multinuclear Pd^{V} supported by silicon atoms

Jesse R. McAtee *

Department of Chemistry and Biochemistry University of Delaware, Newark Delaware 19716

RECEIVED DATE (automatically inserted by publisher); E-mail jmcatee@udel.edu

Abstract: The condensation of three [{1,2-$C_6H_4(SiH_2)_2$}$Pd^{II}(R_2PCH_2CH_2PR_2)$] molecules had previously been reported to give rise to a complex which was originally reported as having a +4 oxidation state on Palladium (Pd). Since then it has been assigned a formal Pd^{II} oxidation, however, due to the difference of reactivity of hydro-silanes and alkyl-silanes the condensation of three units of [{1,2-$C_6H_4(SiH_2)(SiMe_2)$}$Pd^{II}(R_2PCH_2CH_2PR_2)$] gave rise to 3 new complexes of unique structure. For the first time we report two multinuclear compounds with a +5 oxidation state on Palladium.

Palladium IV and other Pd species of high oxidation state have been of great interest to many chemists in the last five years.[1] While the existence of Pd^{IV} has been reported in the literature for over three decades,[2] it has not been until recently that stable complexes have been well characterized.[3-9] Due to the reactive nature of palladium in high oxidation states there has been relatively few species isolated. There are also many works containing Pd^{IV} proposed intermediates (many of which are stable enough for thorough characterization) that with or without heating can undergo reductive elimination.[6-9] The Pd^{IV} species have been of great interest due to the prospects of a Pd^{II}-Pd^{IV} catalytic cycle similar to the well established and accepted Pd^{0}-Pd^{II} catalytic cycle. Most of the Pd^{IV} complexes described have either been supported by halogens and chelating ligands such as 2-phenylpyridine and 1,2-disilylbenzenes.

Scheme 1. Synthesis of **2** with Two Representations of the Structure of **2.**

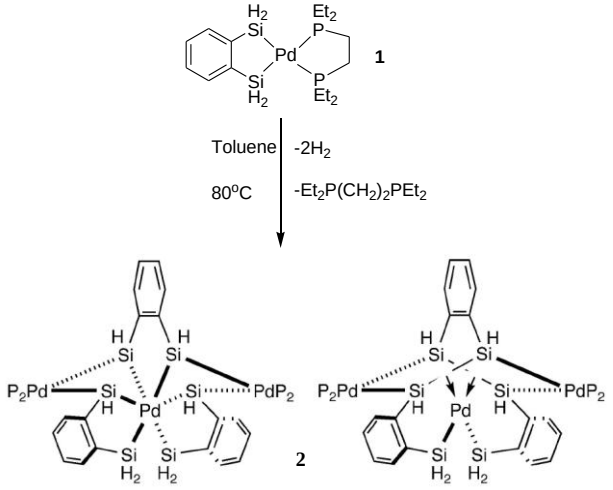

Two decades ago Canty described the interest of applying the chemistry of Pd^{IV} beyond the known complexes supported by chelating nitrogen donor ligands to those supported by other ligands or phosphines due to their predominant role in Pd^{0}-Pd^{II} catalytic cycles.[10] Herein is the description of **2**, **4**, **5**, and **6** which contain not only high oxidation state, but are complexes supported by ligands other than nitrogen donor ligands, namely silanes. The complexes described may give further understanding of the unusual bonding nature of the metalloid silicon in varying electronic states.

The condensation of three molecules of [{1,2-$C_6H_4(SiH_2)_2$}$Pd^{II}(R_2PCH_2CH_2PR_2)$] **1** gives rise to **2** which after much scrutiny by the scientific community has been given a formal oxidation state of +2.The bonding interactions between the Si-Si bond and metal center is of particular interest and worthy of complex analysis. Similarly the condensation of **3** initially gave rise to **4,** and when this dinuclear compound was heated further to 80°C for 48h, the formation of **5** occurred. During purification **6** was found as a single crystal, which was later confirmed by ^{1}HNMR as being in the crude mixture in low amounts. The formation of **4** arises from a new Si-Si bond, and contains two typical square-planar Pd^{II} metal centers. The bonding interactions in **2** can now be described as square-planar like, but the mode of bonding is quite atypical and worthy of some discussion.

Scheme 2. Synthesis of **4**, **5**, and **6**.

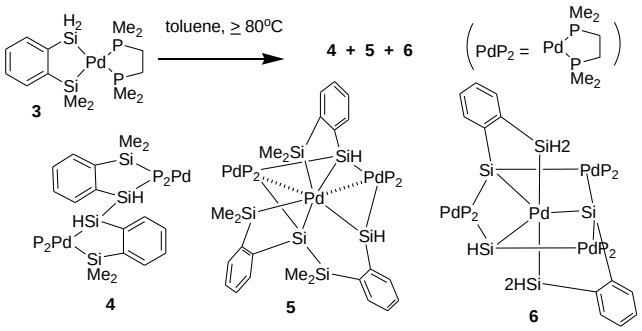

Compounds have been prepared that have a tautomeric relationship between the η^2 form and oxidative addition to the metal to the silicon-hydrogen bond of a silane (Figure 1a).[11] Palladium has been seen to activate di-silanes presumably by a similar mechanism, activating a Si-Si bond to undergo interesting chemical reactions.[12, 13] If it is viewed that the Si-Si bond is σ donating to Pd in **2**, there is the possibility that the empty σ^* orbital on silicon could accept electrons from the *d*xz and *d*yz orbitals given appropriate geometry and overlap, which are indeed present in the molecule.[14] This may account for the low bond order with respect to both Si-Si and Si-Pd

bonds. This back-bonding phenomena is present in some simple organic silicon containing molecules such as tetrasilylamine $(H_3Si)_3N$. The planar geometry of this molecule is accounted for by the sharing of the filled 2*pz* orbital on nitrogen to the empty 3*d* orbital on each of the Si atoms caused by good overlap (Figure 1b) .[15] It has also been shown that given the proper substituents on silicon, a transannular bond can be formed intramolecular between nitrogen and silicon (Figure 1c).[16]

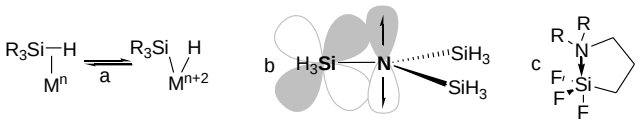

Figure 1. Bonding Interactions of Silicon. (a) Tautomerization of Si-H-metal bond, (b) Lone pair to empty *d* orbital contribution gibing rise to planar molecule, (c) The N→Si transannular bonding of quasisilatranes.

The bonding nature of this unique complex may be nonlinear similar to a description by Bater.[17] He showed that in diborane (also in a metalloid species) the density of the electrons is bent inward to maximize their efficiency of the electron deficient species (Figure 2). The overall geometry of **2** can be described as a near square planar Pd^{II} species if arrows are drawn from the centroid (cen) of the Si-Si bonds to the palladium. This gives a planar coordination with Si-Pd-Si, Si-Pd-cen, and cen-Pd-cen angles all close to 90° which sum to 360°.[14]

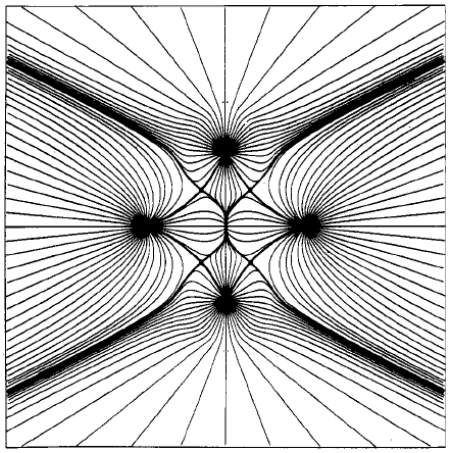

Figure 2. Vector of Charge Distribution about Diborane. Note the bond paths linking the two equatorial protons to the axial borons are bent inward so to maximize efficiency in the electron deficient heterocycle.

While the bond order for this molecule is arguably greater than two, it would be unconventional to assign a higher oxidation state when the molecule contains many elements of a Pd^{II} complex. A common method for giving a numerical value for bond order is Meyer's bond order (MBO) analysis.[18] It is an exceptionally strong tool for the determination of bonds in many organic compounds. The way chemists commonly depict bonds on paper may correlate little to the values calculated for metalloids like silicon and boron. For example Boron-Boron, Boron-Nitrogen, and Boron-Hydrogen bonds gave MBOs less than 0.5 in B_2H_6 and B_3NH_3.[18] This may not be unexpected in the case of the ammonium borane complex where the interaction can be drawn as a complexing arrow. Values of under 0.5 for B-H bonds however may suggest that without alterations of parameters to compensate for such non-classical electronic valences, MBOs can vary.

Modifications or additional variables have commonly been invoked to explain bond order. In the early description of a chemical bond by Pauling a bond order was describes as equal to the exponential of ((the difference of a bond from its common value) over a variable).[19] The common value for a bond is based on averages of measured distances and the variable is appropriately fitted.

Similar to this MBOs also change nonlinearly with regard to distance, so a small distance can account for a drastic change in order. Tanaka and coworkers deemed "typical Pd-Si single bond distances" to be (2.26-2.45 Å) after computation using Cambridge Structural Database for their pool of molecules. Experimental values of 2.4357 and 2.2944 Å gave MBOs of 0.71 and 0.75 respectivly.[3] Perhaps there are other factors to be considered when looking at Pd-Si bonds which can account for the observed distances.

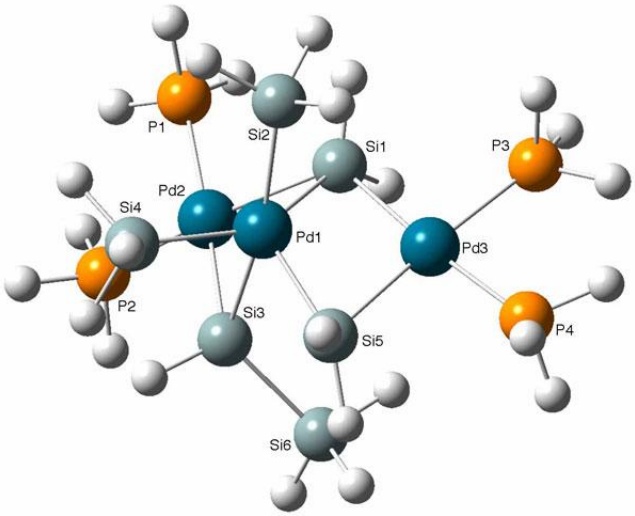

***Figure 3*:** Structure of Compounds **5.**

Ligands that give Structural Trans Effects (STEs) are strong σ donors and anionic silyl ligands are known to exhibit some of the largest STEs to opposing ligands in both square planar and octahedral complexes.[20] In the report of the first hexa-valent Pd^{IV} complex, Tanaka noted a larger STE from silicon than from phosphorus in compound **6**.[5] Compounds **5** and **6** contain two opposing silicon ligands which may be expected to have the longest of the Pd-Si distances. However, this is only true of one of the two Si atoms in **5**. This may be due to the Si3-Pd1 bond being a bridge of three metallacycles and the rings' conformations adding additional force to draw the Si atom slightly closer to the Pd center than the opposing ligand.

Typically the STE is thought of as acting by strong electron donation into the *d* orbital on the metal and in effect lengthening the opposing bond interacting with the same *d* orbital. When the geometry is atypical as in **5,** which can be described as highly distorted square based pyramidal, the STE of the equatorial ligands is difficult to propose. Complex **6**, having a distorted hexoganal-bipyrimidal structure, also lacks linearly opposing geometry about the equatorial ligands and

their Pd-Si bond distances are all slightly shorter than the middle of the typical range.

An aspect of **5** which is unique is one of the Si atoms. Besides it bridging 3 metals (μ_3), Si1(Figure 3) has an expanded octet with 5 bonds; making it formally a silicate. One might expect the Pd1-Si1 bond to be slightly longer due to the greater electron density about the Si nucleus. That bond distance seems to remain consistent while the lengths between the Si1-Pd2 and Si1-Pd3 are substantially longer to compensate. Compound **6** also contains silicates, Si1, Si2 and Si2', all located around the distorted hexagon perpendicular to the pseudo-axis.

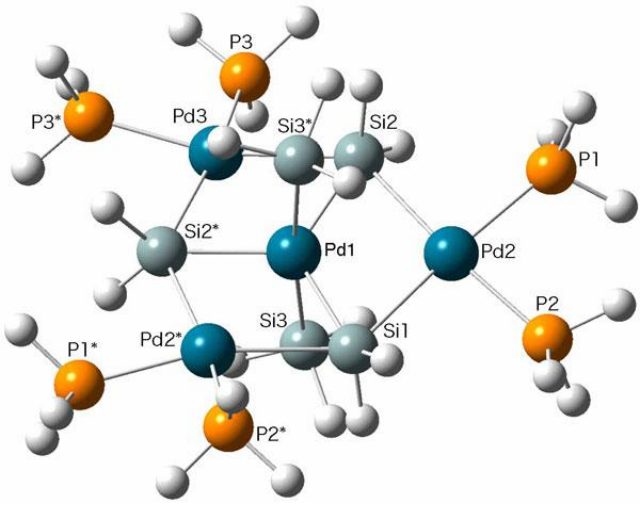

***Figure 4*:** Structure of Compounds **6.**

Compounds **5** and **6** both contain five Pd-Si bonds that are within the bond distances of typical Pd-Si single bonds. Ultimately one can draw single bonds from each silicon and count each Pd-Si bond to increase the oxidation state of palladium to +5. There are no short distances between adjacent Si atoms, so no side-on σ donation can be proposed. The central Pd^{V} metals are the first reported, and their existence greatly expands our understanding of the electronic versatility of silicon and palladium. The synthesis of similar complexes of high oxidation state on palladium but without the presence of multiple metal centers would be even more profound. Certainly the multiple metal centers have influence in stabilizing the central metal and DFT calculations for the HOMO of **2** have shown the HOMO to be a hybrid between σ bonds on silicon, d_{xy} orbitals on the outer Pd metals, and d_z^2 orbital on the central Pd atom.[21]

Sanford's work with Pd^{II}-Pd^{IV} catalytic cycles and stable Pd^{IV} organometallic complexes has shown stable high oxidation states on Pd are possible and can be useful in synthetic chemistry.[6-9] The work described above gives examples of Pd^{V} complexes which are not only higher in oxidation state than what was commonly considered possible for transient species, but compounds stable enough for isolation. Future work relating to the work described above could include exploration of other silicon ligands or other ligands to support high oxidation states of palladium, developing Si-Si bond forming chemistry by reductive elimination of Pd^{V} species which might give Pd^{III} species, attempt to isolate a Pd^{III} species, development of unique catalysts using Pd^{V} intermediates, and development of new algorithms, variables, or modifications of MBO giving a normalized unit for typical boron and silicon bond lengths; to adjust for the unique bonding nature of metalloids.

Refrences

(1) Sehnal, P.; Taylor, R.; Fairlamb, I. *Chem. Rev.* **2010**, 110, 824.
(2) Timakov, A.A.; Prusakov, V,N.; Drobyshevskii, Y.V. *Russ. J. Inorg. Chem.* **1982**, 27,1704.
(3) Shimada, S.; Li, Y. H.; Choe, Y. K.; Tanaka, M.; Bao, M.; Uchimaru, T. *PNAS* ***2007,*** 104, 7758.
(4) Chen, W.; Shimada, S.; Tanaka, M. *Science,* **2002**, 295, 308.
(5) Shigeru, S.; Tanaka, M.; Shiro, M. *Angew. Chem. Int. Ed.* **1996**, 35, 1856-1858.
(6) Ball, N. D.; Sanford, M. S. *J. Am. Chem. Soc.* **2009**, 131, 3796.
(7) Ball, N. D.; Kampf, J. W.; Sanford, M. S. *J. Am. Chem. Soc.* **2010** 132, 2878.
(8) Arnold, P. L.; Sanford, M. S.; Pearson, S. M. *J. Am. Chem. Soc.* **2009,** 131, 13912.
(9) Whitfield, S. R.; Sanford, M. S. *J. Am. Chem. Soc.* **2007**, 127, 15142.
(10) Canty, A.J. *Acc. Chem. Res.* **1992**, 25,83.
(11) Luo, X. L. J.; Kubas, G. J.; Burns, C. J.; Bryan, J. C.; Unkefer, C. J. *J. Am. Chem. Soc.***1995** 117, 1159.
(12) Williams, N. A.; Uchimaru, Y.; Tanaka, M. *Dalton Trans.* **2003**, 236.
(13) McNeill, E.; Barder, T. E.; Buchwald, S. L. *Org. Lett.* **2007**, 9, 3785.
(14) Aullon, G.; Lledos, A.; Alvarez, S. *Angew. Chem. Int. Ed.* **2002**, 41, 1956.
(15) Anderson, D. G.; Rankin, D. W. H.; Robertson, H. E.; Gundersen, G.; Seip, R. *J. Chem. Soc. Dalton. Trans.* **1990**, 1, 161.
(16) Koryukov, A. A.; Lyssenko, K. A.; Antipin, M. Y.; Grebneva, E. A.; Albanov, A. I.;Trofimova, O. M.; Zel'bst, E. A.; Voronkov, M. G. *J. Organomet. Chem.* **2008**, 607.
(17) Bader, R. F. W. *Chem. Rev.* **1991** 91, 893.
(18) Bridgeman, A. J.; Cavigliasso, G.; Ireland, L. R.; Rothery, J. *J. Chem. Soc. Dalton. Trans.* **2001**, 13, 2095.
(19) Pauling, L. *The Nature of the Chemical Bond*, Cornell University Press, New York, 1960.
(20) Coe, B. J.; Glenwright, S. J. *Coord. Chem. Rev.* **2000**, 203, 5.
(21) Sherer, E. C.; Kinsinger, C. R.; Kormos, B.L.; Thompson, J. D.; Cramer, C.J. *Angew. Chem. Int. Ed.* **2002**, 41, (11), 1953-1956.

nature chemistry

ARTICLES

PUBLISHED ONLINE: 29 MARCH 2009 | DOI: 10.1038/NCHEM.162

A diiron(IV) complex that cleaves strong C–H and O–H bonds

Dong Wang[1], Erik R. Farquhar[1], Audria Stubna[2], Eckard Münck[2]* and Lawrence Que, Jr[1]*

The controlled cleavage of strong C–H bonds such as those of methane poses a significant and industrially important challenge for chemists. In nature, methane is oxidized to methanol by soluble methane monooxygenase via a diiron(IV) intermediate called Q. However, the only two reported diiron(IV) complexes have activities towards C–H bonds that fall far short of the activity of this biological catalyst. In this paper, we model the chemistry of MMO-Q by generating an oxo-bridged diiron(IV) complex by electrochemical oxidation. This species is a more effective oxidant. It can attack C–H bonds as strong as 100 kcal mol^{-1} and reacts with cyclohexane 100- to 1,000-fold faster than mononuclear Fe^{IV}=O complexes of closely related ligands. Strikingly, this species can also cleave the strong O–H bonds of methanol and *t*-butanol instead of their weaker C–H bonds, representing the first example of O–H bond activation for iron complexes.

The controlled cleavage of strong C–H bonds such as those of methane remains an elusive goal and one of great industrial and practical importance. In nature, methane hydroxylation occurs by oxygen activation through the action of soluble and particulate methane monooxygenases (MMOs) found in methane-metabolizing bacteria[1–4]. The much better characterized soluble MMOs have a non-haem diiron active site that reacts with O_2 to produce an oxo-bridged diiron(IV) oxidant called **Q** that effects the transformation[5–8]. The generation of a diiron(IV) complex that can oxidize strong C–H bonds thus represents an appealing challenge for synthetic chemists.

To date, only two types of (μ-oxo)diiron(IV) complexes have been characterized. The first example, represented by two complexes of tetraamido macrocyclic ligands (TAMLs) characterized by Ghosh *et al.*[9], is stable at room temperature, but no oxidation chemistry involving C–H bond cleavage has been reported. The second example, reported by Xue *et al.*[10], uses the neutral tetradentate N4 ligand tris(3,5-dimethyl-4-methoxypyridylmethyl)amine to form $[Fe^{IV}_2(\mu\text{-}O)_2(N4)_2]^{4+}$ and serves as a synthetic precedent for the $Fe^{IV}_2(\mu\text{-}O)_2$ core proposed for MMO-**Q**. This complex is stable for only 1 hour at −40 °C and can attack the weak C–H bonds of dihydroanthracene. These (μ-oxo)diiron(IV) complexes thus exhibit reactivities that fall far short of that associated with the diiron active site of soluble MMO. In this study, we report a much more strongly oxidizing (μ-oxo)diiron(IV) complex, obtained by electrochemical oxidation of its (μ-oxo)diiron(III) precursor, that is capable of cleaving not only the strong C–H bonds of cyclohexane but also the even stronger O–H bonds of aliphatic alcohols.

The starting point for this study is $[Fe^{III}_2O(L)_2]^{2+}$ (**1**), a (μ-oxo)diiron(III) complex of L, where L is *N*,*N*-bis-(3′,5′-dimethyl-4′-methoxypyridyl-2′-methyl)-*N*′-acetyl-1,2-diaminoethane. Its structure (Fig. 1a) shows that L acts as a pentadentate ligand with an N_4O donor set, where the N_4 subset binds to one iron centre and the oxygen atom coordinates to the other iron site. This structure resembles that of a recently described complex of a closely related ligand[11], both having a (μ-oxo)diiron(III) unit that is supported by two carboxamido bridges. The fact that the bridging moieties are connected to the terminal ligands results in smaller Fe–(μ-O)–Fe angles than are typically found for closely related (μ-oxo)bis(μ-carboxylato)diiron(III) complexes[12], and these (μ-oxo)bis(μ-carboxamido)diiron(III) complexes have the shortest Fe–Fe distances (approximately 3 Å) in this class of complexes.

Cyclic voltammetry (CV) of **1** in CH_3CN at room temperature reveals the presence of two redox waves (Fig. 2a). Scanning anodically from 0 V versus the ferrocenium/ferrocene couple ($Fc^{+/0}$) elicits an oxidative wave with a peak potential $E_{p,a} = +1.07$ V versus $Fc^{+/0}$; scan reversal below 1.2 V gives rise to a reductive wave with a peak potential $E_{p,c} = +0.33$ V, which is not observed unless the oxidative wave at +1.07 V is also present. A similarly large separation of the oxidative and reductive waves was observed by Wieghardt and co-workers[13] in the one-electron oxidation of related (μ-oxo)bis(μ-carboxylato)diiron(III) complexes. Although not strictly reversible according to CV criteria (for example, reversibility requires a peak separation between $E_{p,a}$ and $E_{p,c}$ of approximately 0.06 V), these one-electron redox transformations are reversible according to spectropotentiometric and chemical methods. More interestingly, increasing the potential above 1.20 V in the CV experiment on **1** reveals a second redox process (Fig. 2a) with a half-wave potential $E_{1/2} = +1.50$ V versus $Fc^{+/0}$; in this case, the separation between the oxidative and reductive waves ($\Delta E = 0.07$ V) approaches that expected for reversible CV behaviour. These results suggest that **1** can be oxidized in two one-electron steps to attain a diiron(IV) oxidation state.

Controlled potential bulk electrolysis has been used in this study to prepare sufficient amounts of the oxidized species for detailed spectroscopic characterization. The complex **1** exhibits optical features at 370 nm ($\varepsilon = 3{,}400$ M^{-1} cm^{-1}), 432 nm ($\varepsilon = 2{,}200$ M^{-1} cm^{-1}), 508 nm ($\varepsilon = 730$ M^{-1} cm^{-1}) and 680 nm ($\varepsilon = 180$ M^{-1} cm^{-1}) (Fig. 2b, dotted line), the latter two bands being characteristic of a (μ-oxo)diiron(III) complex with an Fe–O–Fe angle of approximately 130° (refs 12 and 14). Electrolysis of **1** at potentials above +0.70 V versus $Fc^{+/0}$ in CD_3CN at −40 °C produces a dark-red species **2** with absorbance maxima at 550 nm ($\varepsilon = 1800$ M^{-1} cm^{-1}) and 878 nm ($\varepsilon = 770$ M^{-1} cm^{-1}) (Fig. 2b, solid line). These features resemble those reported by Wieghardt and co-workers[13] in the one-electron oxidation of (μ-oxo)bis(μ-carboxylato)diiron(III) complexes to generate iron(III)iron(IV) derivatives. The complex **2** is stable for several days at −40 °C, and can be re-reduced to regenerate **1** in quantitative yield either electrochemically by shifting to a potential below

[1]Department of Chemistry and Center for Metals in Biocatalysis, University of Minnesota, Minneapolis, Minnesota 55455, USA, [2]Department of Chemistry, Carnegie Mellon University, Pittsburgh, Pennsylvania 15213, USA. *e-mail: emunck@cmu.edu; larryque@umn.edu

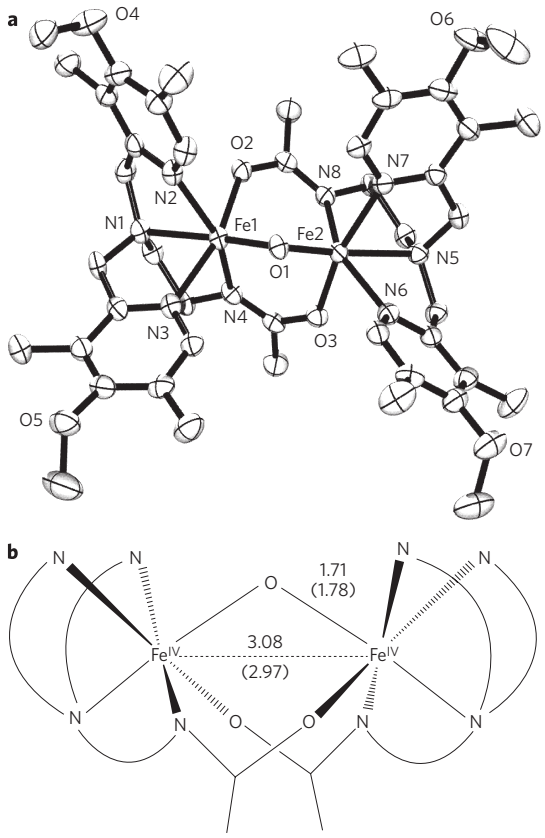

Figure 1 | Structures of the complexes 1 and 3. a, ORTEP plot of $[Fe^{III}{}_2O(L)_2]^{2+}$ (**1**) with thermal ellipsoids drawn at the 50% probability level. Carbon atoms shown are not labelled, and hydrogen atoms are omitted for clarity. Selected distances and angles: Fe1–O1: 1.795(16) Å; Fe1–O2: 2.007(16) Å; Fe1–N1: 2.237(2) Å; Fe1–N2, N3: 2.157(2) Å; Fe1–N4: 2.088(2) Å; Fe1–Fe2: 3.007(3) Å; Fe1–O1–Fe2: 113.68(8)°. **b**, Schematic representation of the structure of **3** with labelled Fe–Fe and Fe–O distances (in Å) determined by EXAFS analysis. Values in parentheses are the corresponding distances in **1** (see also Table 1).

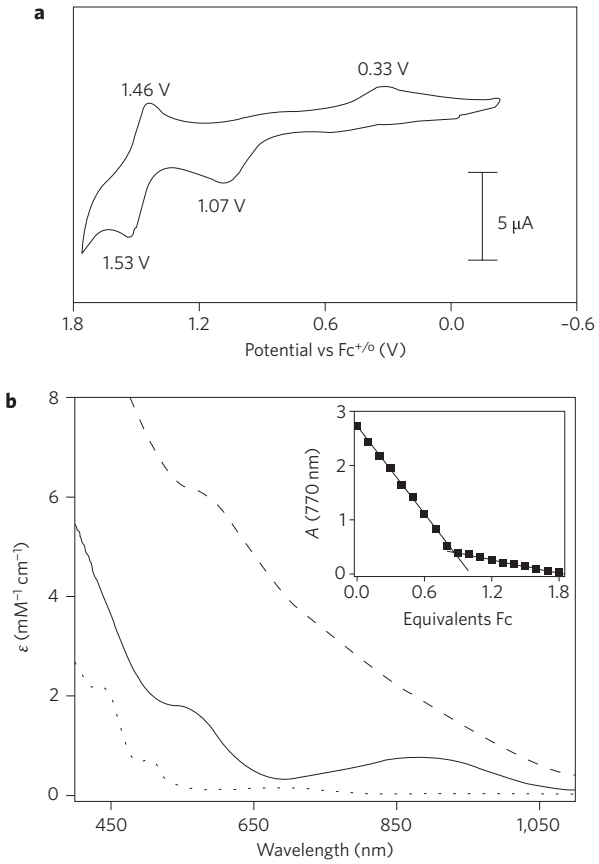

Figure 2 | Characterization of complexes 1, 2 and 3. a, Cyclic voltammetry of **1** in CH_3CN at room temperature with 0.10 M KPF_6 as the supporting electrolyte at a scan rate of 100 mV s^{-1}. Peak potentials are shown next to each peak. **b**, Ultraviolet/visible spectra of the Fe^{III}–O–Fe^{III} complex **1** (dotted line), the Fe^{III}–O–Fe^{IV} species **2** (solid line) and the Fe^{IV}–O–Fe^{IV} complex **3** (dashed line) taken in CD_3CN at −40 °C. The inset shows ferrocene titration of 1 mM **3** monitored at 770 nm.

+0.70 V or chemically by the addition of one equivalent of ferrocene. Thus, the oxidation of **1** to **2** is reversible. Counting charge during the oxidative electrolysis reveals the extraction of one electron from **1**, consistent with the reductive titration. Thus, **2** is a one-electron-oxidized derivative of **1**.

Increasing the bulk electrolysis potential to +1.70 V after the formation of **2** in CD_3CN at −40 °C affords a black species **3** with no distinct absorption bands (Fig. 2b, dashed line). The complex **3** is much less stable than **2**, but its half-life of about 1 hour at −40 °C is sufficiently long to allow its spectroscopic characterization. It is formed in 85% yield, as indicated by Mössbauer spectroscopy (see below) and reductive titration (Fig. 2b, inset), where the addition of 0.85 equivalent of ferrocene converts **3** to **2**. Thus, **3** is a two-electron-oxidized derivative of **1**. The time required to accumulate **3** is much longer than that for complete conversion of **1** to **2**, and the yield of **3** is greater with CD_3CN as solvent in place of CH_3CN (85% versus only 30%) and with KPF_6 as electrolyte in place of a quaternary ammonium salt—substitutions that minimize the number of potentially oxidizable C–H bonds in the electrolysis medium.

X-ray absorption spectroscopy demonstrates that oxidation of **1** to **2** and **3** occurs at the iron centres. As shown in Fig. 3a and Table 1, the Fe K-edge exhibits a progressive blue shift from **1** to **2** to **3**, the total upshift of 1.5 eV being in accord with a stepwise increase in the oxidation state of the diiron unit in this series. Extended X-ray absorption fine structure (EXAFS) analysis (Fig. 3b and Supplementary Fig. S1; Table 1 and Supplementary Tables S2–S4) reveals further structural details. For **1**, the respective Fe–N/O and Fe–C distances of 2.11 and 3.07 Å are as expected for the ligand L bound to a high-spin iron(III) centre. These distances decrease by 0.15 and 0.2 Å in **2** and **3**, respectively, which is consistent with the iron centres in these complexes undergoing a transition to low spin on oxidation. There are additional features in the EXAFS results that are assignable to the Fe–O–Fe unit. The Fe–μ-O distance of 1.78 Å in **1** decreases to 1.71 Å in **2** and **3**; the latter distances compare favourably with those of the two crystallographically characterized $[Fe^{IV}{}_2(O)(TAML)_2]^{2-}$ complexes (1.7284(8) and 1.744(3) Å)[9]. The Fe–Fe distance increases from 2.97 Å in **1** to 3.07 Å in **2** and 3.08 Å in **3**. The changes in Fe–Fe distance are comparable to the 0.05–0.08 Å increase observed on one-electron oxidation of $[Fe^{III}M^{III}(\mu\text{-}O)(\mu\text{-}O_2CR)_2(Me_3TACN)_2]^{2+}$ (M = Fe or Cr; TACN = 1,4,7-triazacyclononane) and $[Fe^{III}Fe^{IV}(\mu\text{-}O)_2(N4)_2]^{3+}$ (refs 10,13). These results suggest strongly that the (μ-oxo)bis(μ-carboxamido)diiron core is maintained on oxidation (Fig. 1b).

Mössbauer studies also show that oxidation occurs at the iron centres. The 4.2 K zero-field Mössbauer spectrum of **1** exhibits a single quadrupole doublet with parameters and high-field behaviour typical of an antiferromagnetically coupled (μ-oxo)diiron(III) unit, as expected (Table 1). On oxidation to **2** and **3**, the isomer shifts decrease substantially to values near 0 mm s^{-1} (Table 1), indicating that the high-spin iron(III) sites of **1** convert to low-spin iron centres. The corresponding spectrum of **3** (Fig. 4a) also exhibits a single quadrupole doublet representing 85–90% of the iron

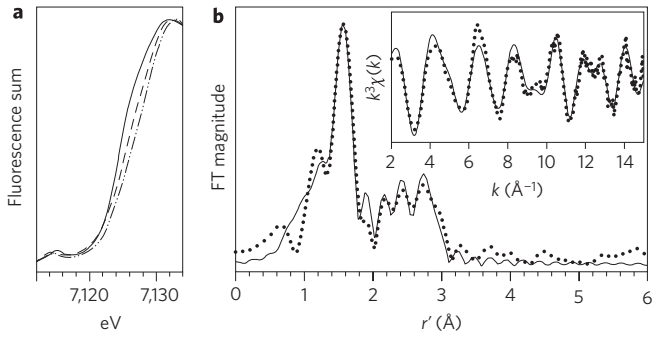

Figure 3 | X-ray absorption spectra of complexes 1, 2 and 3. **a**, X-ray absorption edge spectra of **1** (solid line), **2** (dashed line), and **3** (dot-dashed line), showing the blueshift of the Fe K-edge transition with progressive oxidation of the iron centres. **b**, Fourier transform of the Fe K-edge EXAFS data ($k^3\chi(k)$) and unfiltered EXAFS spectra ($k^3\chi(k)$, inset) of **3**, where k is the photoelectron wave vector, $\chi(k)$ is the X-ray absorption cross-section and r' is the Fe–X distance plus phase shift. Experimental data are shown by dotted lines and fits by solid lines. The Fourier transform range is $k = 2.0$–15.0 Å^{-1}. The fit parameters are shown in bold italics in Supplementary Table S4.

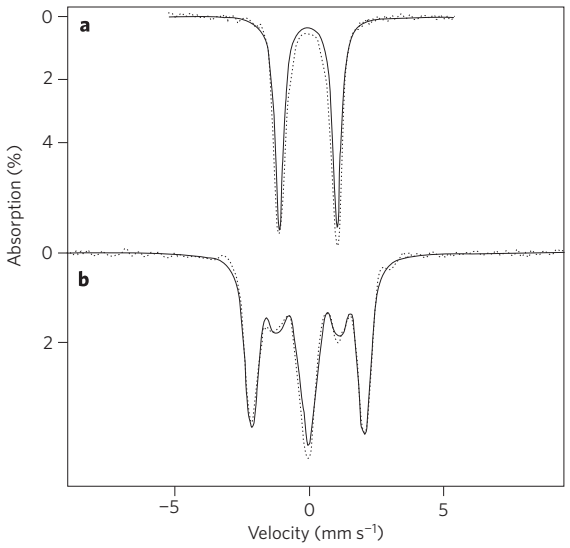

Figure 4 | 4.2 K Mössbauer spectra of 3. a, 45 mT; **b**, 8 T. Dotted lines represent experimental data points, and the solid lines are spectral simulations assuming an $S = 0$ ground state and two equivalent Fe sites with $\delta = -0.05$ mm s^{-1}, $\Delta E_Q = 2.14$ mm s^{-1} and asymmetry parameter $\eta = 0.9$.

in the sample with parameters ($\Delta E_Q = 2.14$ mm s^{-1} and $\delta = -0.05$ mm s^{-1}). These parameters are nearly identical to those of $[Fe^{IV}_2(\mu\text{-}O)_2(N4)_2]^{4+}$, where the individual iron sites are $S = 1$ (ref. 10). The 8.0 T spectra of **3** (Fig. 4b) and $[Fe^{IV}_2(\mu\text{-}O)_2(N4)_2]^{4+}$ both lack paramagnetic hyperfine structure, indicating antiferromagnetic coupling between the two Fe^{IV} sites to provide a dimer ground state with $S = 0$. Given the likely N_4O_2 ligand set, we assume that the local sites of **3** have $S_1 = S_2 = 1$, in accord with observations of $S = 1$ ground states for other $Fe^{IV}(N_4O_2)$ complexes[15,16].

The complex **3** has the highest redox potential (+1.50 V versus $Fc^{+/0}$) among the three types of (μ-oxo)diiron(IV) complexes synthesized thus far, being respectively 1.7 and 0.7 V more positive than those of $[Fe^{IV}_2(\mu\text{-}O)(TAML)_2]^{2-}$ and $[Fe^{IV}_2(\mu\text{-}O)_2(N4)_2]^{4+}$ (refs 9,10). The redox potential of **3** is also more positive than the value of +0.90 V versus $Fc^{+/0}$ determined for $[Fe^{IV}(O)(N4Py)]^{2+}$ (N4Py = *N*,*N*-bis(2-pyridylmethyl)-bis(2-pyridyl)methylamine)[17], a complex with a terminal Fe=O unit that has been found to cleave the C–H bonds of cyclohexane[18]. Thus, **3** should be a fairly powerful oxidant.

Reactivity studies demonstrate that **3** can cleave C–H bonds with bond dissociation energies D_{C-H} as high as 100 kcal mol^{-1}, and the logarithm of the second-order rate constants normalized on a per hydrogen basis ($\log k'_2$) for these oxidations correlates inversely with the strength of the C–H bonds being cleaved (Fig. 5). In all cases studied, hydrocarbon oxidation results in the quantitative reduction of **3** to **2** (Supplementary Fig. S2), demonstrating that **3** acts as a one-electron oxidant. Cyclohexane ($D_{C-H} = 99.3$ kcal mol^{-1}) is oxidized by **3** with a second-order rate constant $k_2 = 8.1 \times 10^{-2}$ M^{-1} s^{-1} at 10 °C, whereas the oxidation rate for cyclohexane-d_{12} ($D_{C-D} = 100.6$ kcal mol^{-1}) is a factor of 3.5 smaller (Supplementary Fig. S3). This kinetic isotope effect (KIE) of 3.5 shows that C–H bond cleavage is an important component of the rate-determining step. However, the observed formation of **2**, but not its conjugate acid, suggests that protonated **2** is a strong acid and readily loses the proton acquired in the hydrogen-atom abstraction step.

Gas chromatographic analysis of the products of cyclohexane oxidation under anaerobic conditions shows the formation of cyclohexene and 1,3-cyclohexadiene in respective yields of 13% and 9% (but no cyclohexanol or benzene), accounting for 63% of the oxidizing equivalents available in the conversion of **3** to **2** (Supplementary Table S6). The oxidizing equivalents unaccounted for may be ascribed to the self-decay of **3**, which has a first-order rate constant of 0.003 s^{-1}, which is about a factor of 3 smaller than the pseudo-first-order decay constant of 0.01 s^{-1} observed in the presence of 0.1 M cyclohexane. For comparison, we have also investigated the oxidations of cyclohexene and 1,3-cyclohexadiene by **3** independently under the same experimental conditions as above. Because of their much weaker C–H bonds, these substrates react very rapidly with **3** and quantitatively afford **2** in both reactions. Cyclohexene and 1,3-cyclohexadiene are respectively converted to 1,3-cyclohexadiene and benzene in 47% and 45% yields per diiron(IV) unit, which account for at least 90% of the oxidizing equivalents in each reaction. The absence of hydroxylated products in the reactions above suggests that C–O bond formation after the initial hydrogen-abstraction step may be disfavoured owing to the bridging nature of the oxo atom and the consequent requirement for cleavage of two Fe–O bonds to form the alcohol product. Instead, dehydrogenation occurs either by abstraction of the β-hydrogen atom of the alkyl radical by a second diiron(IV) centre or by electron transfer from the alkyl radical to another diiron(IV) molecule to generate the cation, followed by loss of a proton from the β-carbon atom[19–21]. Thus, **3** acts as a hydrocarbon dehydrogenating agent, rather than as a hydroxylating agent (Fig. 6).

Table 1 | X-ray absorption and Mössbauer spectroscopic data for $[Fe_2O(L)_2]^{n+}$.

Complex	Edge energy (eV)	*r*(Fe-μ-O) (Å)	*r*(Fe-N) (Å)	*r*(Fe-C) (Å)	*r*(Fe-Fe) (Å)	δ (mm s^{-1})	ΔE_Q (mm s^{-1})
1	7,124.1	1.78	2.11	3.07	2.97	0.45	1.30
2	7,124.9	1.70	1.96	2.89	3.07	0.07*	1.57
3	7,125.6	1.71	1.96	2.88	3.08	−0.05	2.14

*Complex **2** is a valence-delocalized $Fe^{III}Fe^{IV}$ complex that yields one doublet with $\delta = 0.07$ mm s^{-1} at 120 K; a more detailed description of this interesting complex will be presented in a future publication.

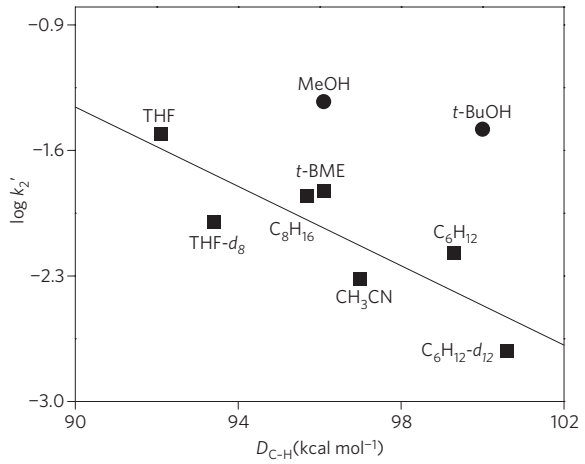

Figure 5 | Oxidative reactivity study of 3 in CD_3CN at 10 °C. The solid line represents the best linear fit correlating the log k_2' values for the reactions of hydrocarbons with **3** (filled squares) with their C–H bond dissociation energies. k_2' is the normalized second-order rate constant (the second-order rate constant k_2 divided by the number of equivalent C–H bonds on the substrate that may be attacked by **3**). For methanol (MeOH) and *t*-butanol (*t*-BuOH), the filled circles represent the values assuming that a C–H bond is attacked. THF(-d_8), (deuterated)-tetrahydrofuran; *t*-BME, *t*-butyl methyl ether; C_6H_{12}(-d_{12}), (deuterated)-cyclohexane; C_8H_{16}, cyclooctane. D_{C-H} values were obtained from refs 18, 24 and 39.

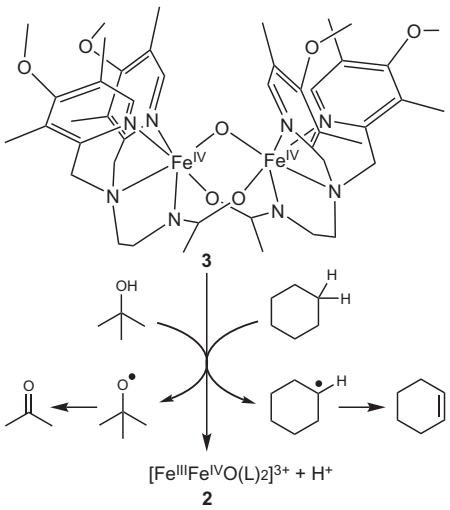

Figure 6 | Reaction scheme of 3 in its oxidation of cyclohexane and *t*-butanol. Complex **3** acts as a one-electron oxidant that cleaves a C–H bond of cyclohexane and the O–H bond of *t*-butanol.

Interestingly, the aliphatic alcohols methanol (D_{C-H} = 96.1 kcal mol^{-1}) and *t*-butanol (D_{C-H} = 100 kcal mol^{-1}) also serve as substrates for oxidation by **3**, with respective k_2 values of 0.14 and 0.30 M^{-1} s^{-1}. These values, when normalized on a per-hydrogen basis, fall well above the line for the linear correlation shown in Fig. 5. Kinetic studies of methanol and *t*-butanol with different degrees of deuteration (Supplementary Figs S4 and S5, respectively) show that changing the C–H bonds to C–D bonds does not affect their respective oxidation rates. However, deuteration of the O–H bond results in a KIE of 1.4–1.5. Thus, oxidation of these alcohols seems to proceed via O–H, rather than C–H, bond cleavage.

The notion of O–H bond cleavage by **3** is supported by ^{1}H-NMR spectroscopic analysis of the *t*-butanol oxidation products under anaerobic conditions, revealing the formation of acetone ($\delta = 2.1$) and 2-methylpropene ($\delta = 1.73$, 6H; $\delta = 4.67$, 2H) in respective yields of 50% and 40% (Supplementary Table S7). Cleavage of the *t*-butanol O–H bond should yield a *t*-butoxyl radical that would decay readily to acetone via the well-documented β-scission pathway[22]. On the other hand, 2-methylpropene derives from acid-promoted dehydration of *t*-butanol via the *t*-butyl cation[23]. The protons needed for this transformation are generated in the course of bulk electrolysis from oxidation of the solvent as mentioned above. Unfortunately, we cannot find an appropriate base that is able to neutralize these protons before substrate addition but is not readily oxidized by **3**. However, in support of our proposal, a comparable yield of 2-methylpropene (but no acetone) is observed when **3** is first reduced to **2** by 1 equivalent of ferrocene before the addition of *t*-butanol.

Both alcohols have D_{O-H} values greater than 105 kcal mol^{-1} (105.2 and 106.3 kcal mol^{-1} for methanol and *t*-butanol, respectively)[24], and these O–H bonds are cleaved by **3** instead of the weaker C–H bonds in the molecule. Indeed, on a per-hydrogen basis, the O–H bond of *t*-butanol is cleaved by **3** about 50 times faster than a C–H bond of cyclohexane, which has a D_{C-H} comparable to that of the C–H bonds of *t*-butanol. Similarly, **3** reacts 10 times faster with the O–H bond of methanol than with a C–H bond of cyclooctane. Given the high redox potential of **3**, it may react by electron transfer from one of the non-bonding oxygen orbitals of the substrate, instead of the hydrogen atom transfer (HAT) process typically associated with C–H bond cleavage. However, having an oxygen atom in the substrate is apparently insufficient to trigger this alternative mechanism, because the oxidation rates of both THF and *t*-butyl methyl ether (*t*-BME) fall nicely on the line correlating log k_2' and D_{C-H} (Fig. 5). We therefore propose that for alcohol oxidation, proton transfer from the O–H group is coupled with the electron abstraction from the O atom. Such a proton-coupled electron transfer mechanism would be consistent with the observation of an O–H/O–D KIE that is smaller than for C–H bond cleavage (Fig. 6).

The complex **3** is thus unique among iron-based oxidants in its ability to cleave both strong C–H and O–H bonds. Table 2 compares rate constants for **3** and selected mononuclear oxoiron(IV) complexes. The complex **3** differs from the other complexes listed in the table in having a bridging oxo group instead of a terminal oxo group. Of note is the significantly larger second-order rate constant for cyclohexane oxidation by **3** at 10 °C compared with those obtained at 25 °C for $[Fe^{IV}(O)(Bn\text{-}TPEN)]^{2+}$ and $[Fe^{IV}(O)(N4Py)]^{2+}$ (ref. 18). Even without accounting for the 15 °C temperature difference, **3** is still respectively over two and three orders of magnitude more effective at oxidizing cyclohexane than $[Fe^{IV}(O)(Bn\text{-}TPEN)]^{2+}$ and $[Fe^{IV}(O)(N4Py)]^{2+}$. The latter two complexes are the most reactive of the oxoiron(IV) complexes that have been isolated or generated in high yield. This greater reactivity of **3** may derive from its much higher redox potential.

On the other hand, **3** seems to be less reactive than $[Fe^{IV}(O)(OH_2)_5]^{2+}$, a transient species trapped from the reaction of $[Fe^{II}(OH_2)_6]^{2+}$ and O_3 at pH 1 (Table 2)[25]. Owing to its short half-life, $[Fe^{IV}(O)(OH_2)_5]^{2+}$ has only been characterized by its ultraviolet and Mössbauer spectral properties[26]. Its $Fe^{IV/III}$ potential has been estimated to be comparable to that of **3** on the basis of its ability to oxidize chloride ion[27], but $[Fe^{IV}(O)(OH_2)_5]^{2+}$ reacts with CH_3CN more rapidly than **3** by a factor of more than two orders of magnitude. An important difference between **3** and $[Fe^{IV}(O)(OH_2)_5]^{2+}$ is the spin state of the individual iron centres, the former being $S = 1$ and the latter $S = 2$. A number of density functional theory calculations suggest that high-spin oxoiron(IV) centres have lower activation barriers for C–H bond cleavage[28–31], and the greater C–H bond cleavage activity of $[Fe^{IV}(O)(OH_2)_5]^{2+}$ supports this notion.

The complex **3** also differs from the Fe=O complexes listed in Table 2 in its preference to cleave the O–H bonds of methanol

Table 2 | Second-order rate constants ($M^{-1}\,s^{-1}$) for the reactions of iron(IV) complexes*.

Complexes†	$E_{1/2}$ ($Fe^{IV/III}$) (vs $Fc^{+/0}$)	Fe spin state	Cyclo-C_6H_{12}	CH_3CN	Methanol	*t*-butanol	Ref.
3 (10 °C)	1.50	$S=1$	0.081 [C–H, 3.5]	0.014	0.14 [O–H, 1.5]	0.30 [O–H, 1.4]	This work
$[Fe(O)(Bn\text{-}TPEN)]^{2+}$ (25 °C)	>0.90	$S=1$	3.9×10^{-4}	2×10^{-6} ‡ [C–H, 4]	2.8×10^{-3} § [C–H, 8]	NA	18,32
$[Fe(O)(N4Py)]^{2+}$ (25 °C)	0.90	$S=1$	5.5×10^{-5}	2×10^{-7} ‡	4.4×10^{-4} § [C–H, 7]	NA	17,18,32
$[Fe(O)(OH_2)_5]^{2+}$ (25 °C)	~1.4‖	$S=2$	NA¶	4.1 [C–H, 4.1]	572 [C–H, 4.4]	60	25,27
MMO-**Q** (25 °C)	NA	$S=2$	$(3\text{–}4)\times10^4$ for CH_4				36,37

NA, not available.
*KIE values (where available) are shown in square brackets.
†Bn-TPEN, *N*-benzyl-*N*,*N*′,*N*′-tris(2-pyridylmethyl)-1,2-diaminoethane; N4Py, *N*,*N*-bis(2-pyridylmethyl)-bis(2-pyridyl)methylamine.
‡ Estimated from $t_{1/2}$ values in CH_3CN solvent from ref. 18 or 32.
§ Data obtained at 40 °C from ref. 32.
‖ It has not been possible to establish the $Fe^{IV/III}$ potential for $[Fe(O)(OH_2)_5]^{2+}$ by electrochemical means because of its very short lifetime; the value given here is an estimate from ref. 27 based on its ability to oxidize Cl^- ion.
¶ No oxidation rate has been reported for cyclohexane or any other hydrocarbon because of the immiscibility of such substrates with the aqueous medium in which $[Fe(O)(OH_2)_5]^{2+}$ is generated.

and *t*-butanol, rather than their C–H bonds. This difference is strikingly demonstrated by the observation of C–H/C–D KIEs of 4–8 for methanol oxidation by the three oxoiron(IV) complexes[25,32] and the absence of a KIE for oxidation by **3**. Instead, for methanol and *t*-butanol oxidation by **3**, there is a small but measurable O–H/O–D KIE. Why **3** should specifically target the O–H bond instead of the weaker C–H bonds of the alcohol is not clear, and will be the subject of further investigation.

In conclusion, we have generated and characterized a novel diiron(IV) complex **3** with a redox potential +1.50 V versus $Fc^{+/0}$, the highest $Fe^{IV/III}$ potential determined electrochemically to date[9,10,13,17,33–35]. This high potential suggests that **3** should be a powerful oxidant. Indeed, **3** can cleave the strong C–H bonds of cyclohexane, whereas $[Fe^{IV}_2(\mu\text{-}O)_2(N4)_2]^{4+}$, a complex that serves as the synthetic precedent for the $Fe^{IV}_2(\mu\text{-}O)_2$ core proposed for MMO-**Q** (ref. 10), can only attack the weak C–H bonds of dihydroanthracene. Furthermore, **3** reacts much faster with cyclohexane than do mononuclear Fe^{IV}=O complexes of closely related ligands. Unexpectedly, we find that **3** preferentially cleaves the stronger O–H bonds of methanol and *t*-butanol instead of their C–H bonds, representing the first example of O–H bond activation for iron complexes. However, the rate of cyclohexane oxidation by **3** is still orders of magnitude smaller than the rate of oxidation of methane by the diiron(IV) intermediate **Q** of MMO[36,37]. This reactivity gap may arise from a difference in the spin states of the individual iron centres in the complexes ($S=1$ for **3** and $S=2$ for **Q**). The complex **3** also differs from MMO-**Q** in that it carries out substrate dehydrogenation rather than hydroxylation. From this perspective, the action of **3** more closely resembles that of fatty acid desaturases, which, like MMO, also have diiron active sites and are thus proposed to generate diiron(IV) oxidants in their catalytic cycle[38]. As discussed for **3** above, the difference in the reactivities of MMO and the fatty acid desaturases may hinge on the relative ease by which C–O bond formation between the incipient alkyl radical and the Fe–OH unit (that is, oxygen rebound) can take place relative to electron transfer between them[19–21], and the results for **3** can help us understand how different but related enzyme active sites can modulate the outcome of substrate oxidation. Lastly, our intriguing results demonstrate that complexes with very high $Fe^{IV/III}$ potential can be generated in high yield and characterized spectroscopically, and they set the stage for future efforts aimed at more efficient hydrocarbon oxidation by synthetic iron complexes.

Received 26 November 2008; accepted 16 February 2009; published online 29 March 2009

References

1. Hanson, R. S. & Hanson, T. E. Methanotrophic bacteria. *Microbiol. Rev.* **60,** 439–471 (1996).
2. Wallar, B. J. & Lipscomb, J. D. Dioxygen activation by enzymes containing binuclear non-heme iron clusters. *Chem. Rev.* **96,** 2625–2657 (1996).
3. Merkx, M. *et al.* Dioxygen Activation and methane hydroxylation by soluble methane monooxygenase: A tale of two irons and three proteins. *Angew. Chem. Int. Ed.* **40,** 2782–2807 (2001).
4. Balasubramanian, R. & Rosenzweig, A. C. Structural and mechanistic insights into methane oxidation by particulate methane monooxygenase. *Acc. Chem. Res.* **40,** 573–580 (2007).
5. Lee, S.-K., Fox, B. G., Froland, W. A., Lipscomb, J. D. & Münck, E. A transient intermediate of the methane monooxygenase catalytic cycle containing an $Fe^{IV}Fe^{IV}$ cluster. *J. Am. Chem. Soc.* **115,** 6450–6451 (1993).
6. Liu, K. E. *et al.* Kinetic and spectroscopic characterization of intermediates and component interactions in reactions of methane monooxygenase from *Methylococcus capsulatus* (Bath). *J. Am. Chem. Soc.* **117,** 10174–10185 (1995).
7. Nesheim, J. C. & Lipscomb, J. D. Large kinetic isotope effects in methane oxidation catalyzed by methane monooxygenase: Evidence for C–H bond cleavage in a reaction cycle intermediate. *Biochemistry* **35,** 10240–10247 (1996).
8. Shu, L. *et al.* An $Fe^{IV}_2O_2$ diamond core structure for the key intermediate Q of methane monooxygenase. *Science* **275,** 515–518 (1997).
9. Ghosh, A. *et al.* Catalytically active μ-oxodiiron(IV) oxidants from iron(III) and dioxygen. *J. Am. Chem. Soc.* **127,** 2505–2513 (2005).
10. Xue, G. *et al.* A synthetic precedent for the $[Fe^{IV}_2(\mu\text{-}O)_2]$ diamond core proposed for methane monooxygenase intermediate **Q**. *Proc. Natl Acad. Sci. USA* **104,** 20713–20718 (2007).
11. Xu, J.-Y. *et al.* Iron(III) complexes with the ligand *N*′,*N*′-bis[(2-pyridyl)-methyl]ethylenediamine (uns-penp) and its amide derivative *N*-acetyl-*N*′,*N*′-bis[(2-pyridyl)methyl]ethylenediamine (acetyl-uns-penp). *Eur. J. Inorg. Chem.* 1601–1610 (2006).
12. Kurtz, D. M. Jr Oxo- and hydroxo-bridged diiron complexes: A chemical perspective on a biological unit. *Chem. Rev.* **90,** 585–606 (1990).
13. Slep, L. D. *et al.* Mixed-valent $\{Fe^{IV}(\mu\text{-}O)(\mu\text{-carboxylato})_2Fe^{III}\}^{3+}$ core. *J. Am. Chem. Soc.* **125,** 15554–15570 (2003).
14. Norman, R. E. *et al.* (μ-Oxo)(μ-carboxylato)diiron(III) complexes with distinct iron sites. Consequences of the inequivalence and its relevance to dinuclear iron–oxo proteins. *J. Am. Chem. Soc.* **112,** 1554–1562(1990).
15. Jackson, T. A. *et al.* Axial ligand effects on the geometric and electronic structures of nonheme oxoiron(IV) complexes. *J. Am. Chem. Soc.* **130,** 12394–12407 (2008).
16. Rohde, J. U. *et al.* Nonheme oxoiron(IV) complexes of tris(2-pyridylmethyl)amine with *cis*-monoanionic ligands. *Inorg. Chem.* **45,** 6435–6445 (2006).
17. Collins, M. J., Ray, K. & Que, L. Jr Electrochemical generation of a nonheme oxoiron(IV) complex. *Inorg. Chem.* **45,** 8009–8011 (2006).
18. Kaizer, J. *et al.* Nonheme $Fe^{IV}O$ complexes that can oxidize the C–H bonds of cyclohexane at room temperature. *J. Am. Chem. Soc.* **126,** 472–473 (2004).
19. Kumar, D., de Visser, S. P., Sharma, P. K., Cohen, S. & Shaik, S. Radical clock substrates, their C–H hydroxylation mechanism by cytochrome P450, and other reactivity patterns: What does theory reveal about the clocks' behaviour? *J. Am. Chem. Soc.* **126,** 1907–1920 (2004).
20. Kumar, D., de Visser, S. P. & Shaik, S. Oxygen economy of cytochrome P450: What is the origin of the mixed functionality as a dehydrogenase-oxidase

enzyme compared with its normal function? *J. Am. Chem. Soc.* **126,** 5072–5073 (2004).
21. Jin, Y. & Lipscomb, J. D. Desaturation reactions catalyzed by soluble methane monooxygenase. *J. Biol. Inorg. Chem.* **6,** 717–725 (2001).
22. Griller, D. & Ingold, K. U. Free-radical clocks. *Acc. Chem. Res.* **13,** 317–323 (1980).
23. Vollhardt, K. P. C. The reactions of alcohols and the chemistry of ethers, in *Organic Chemistry* 308–358 (W. H. Freeman, 1987).
24. Luo, Y.-R. in *Comprehensive Handbook of Chemical Bond Energies* 255–369 (Taylor & Francis, 2007).
25. Pestovsky, O. & Bakac, A. Reactivity of aqueous fe(IV) in hydride and hydrogen atom transfer reactions. *J. Am. Chem. Soc.* **126,** 13757–13764 (2004).
26. Pestovsky, O. *et al.* Aqueous Fe^{IV}=O: Spectroscopic identification and oxo group exchange. *Angew. Chem. Int. Ed.* **44,** 6871–6874 (2005).
27. Jacobsen, F., Holcman, J. & Sehested, K. Reactions of the ferryl ion with some compounds found in cloud water. *Int. J. Chem. Kinet.* **30,** 215–221 (1998).
28. Shaik, S., Hirao, H. & Kumar, D. Reactivity of high-valent iron–oxo species in enzymes and synthetic reagents: A tale of many states. *Acc. Chem. Res.* **40,** 532–542 (2007).
29. Sastri, C. V. *et al.* Axial ligand tuning of a nonheme iron(IV)–oxo unit for hydrogen atom abstraction. *Proc. Natl Acad. Sci. USA* **104,** 19181–19186 (2007).
30. Decker, A. *et al.* Spectroscopic and quantum chemical studies on low-spin Fe^{IV}=O complexes: Fe–O bonding and its contributions to reactivity. *J. Am. Chem. Soc.* **129,** 15983–15996 (2007).
31. Bernasconi, L., Louwerse, M. J. & Baerends, E. J. The role of equatorial and axial ligands in promoting the activity of non-heme oxidoiron(IV) catalysts in alkane hydroxylation. *Eur. J. Inorg. Chem.* 3023–3033 (2007).
32. Klinker, E. J. High-valent iron compounds supported by pentadentate ligands. PhD thesis, Univ. Minnesota–Twin Cities (2007).
33. Berben, L. A. & Peters, J. C. Dimanganese and diiron complexes of a binucleating cyclam ligand: Four-electron, reversible oxidation chemistry at high potentials. *Inorg. Chem.* **47,** 11669–11679 (2008).
34. Berry, J. F., Bill, E., Bothe, E., Neese, F. & Wieghardt, K. Octahedral non-heme oxo and non-oxo Fe(IV) complexes: An experimental/theoretical comparison. *J. Am. Chem. Soc.* **128,** 13515–13528 (2006).
35. Zheng, H., Yoo, S. J., Münck, E. & Que, L. Jr The flexible $Fe_2(\mu\text{-}O)_2$ diamond core: A terminal iron(IV)–oxo species generated from the oxidation of a bis(μ-oxo)diiron(III) complex. *J. Am. Chem. Soc.* **122,** 3789–3790 (2000).
36. Brazeau, B. J. & Lipscomb, J. D. Kinetics and thermodynamics of methane monooxygenase compound **Q** formation and reaction with substrates. *Biochemistry* **39,** 13503–13515 (2000).
37. Valentine, A. M., Stahl, S. S. & Lippard, S. J. Mechanistic studies of the reaction of reduced methane monooxgyenase hydroxylase with dioxygen and substrates. *J. Am. Chem. Soc.* **121,** 3876–3887 (1999).
38. Fox, B. G., Lyle, K. S. & Rogge, C. E. Reactions of the diiron enzyme stearoyl-acyl carrier protein desaturase. *Acc. Chem. Res.* **37,** 421–429 (2004).
39. Luo, Y.-R. in *Comprehensive Handbook of Chemical Bond Energies* 19–147 (Taylor & Francis, 2007).

Acknowledgements

This work was supported by NIH Grants EB-001475 (E.M.) and GM-38767 (L.Q.) and NIH Graduate Traineeship GM-08700 (E.R.F.). XAS data were collected on beamlines 7-3 and 9-3 at the Stanford Synchrotron Radiation Lightsource (SSRL), a national user facility operated by Stanford University on behalf of the US Department of Energy, Office of Basic Energy Sciences. The SSRL Structural Molecular Biology Program is supported by the Department of Energy, Office of Biological and Environmental Research, and by the National Institutes of Health, National Centre for Research Resources and the Biomedical Technology Program. We thank M. Latimer and A. Aranda for technical support and advice during XAS data collection. We also thank V.G. Young Jr and the X-ray Crystallographic Laboratory of the University of Minnesota for expert assistance in the crystal structure determination.

Author contributions

D.W., E.M. and L.Q. conceived and designed the experiments; D.W., E.R.F. and A.S. performed the experiments; D.W., E.R.F., A.S. and E.M. analysed the data; D.W., E.R.F., A.S., E.M. and L.Q. wrote the paper. All authors discussed the results and commented on the manuscript.

Additional information

Supplementary information accompanies this paper at www.nature.com/naturechemistry. Reprints and permission information is available online at http://npg.nature.com/reprintsandpermissions/. Correspondence and requests for materials should be addressed to E.M. and L.Q.

A diiron(IV) complex that cleaves strong C–H and O–H bonds

Dong Wang, Erik R. Farquhar, Audria Stubna, Eckard Mu¨nck* and Lawrence Que, Jr*

Reviewed by Allen Pistner

*[1]Department of Chemistry and Center for Metals in Biocatalysis, University of Minnesota, Minneapolis, Minnesota 55455, USA, [2]Department of Chemistry,Carnegie Mellon University, Pittsburgh, Pennsylvania 15213, USA. *e-mail: emunck@cmu.edu; larryque@umn.edu.*

Cleavage of C-H bonds is a difficult process to be completed artificially. This is accomplished in Nature using methane monooxygenase that has a diiron(IV) intermediate called Q. The diiron(IV) complex presented here models the structure of the MMO-Q to be able to cleave C-H bonds. The presented system is has been able to cleave C-H bonds as strong as 100 kcal mol^{-1} and able to react with cyclohexane at a much higher rate than reported mononuclear Fe(IV)=O systems. This complex has also shown the ability to cleave O-H bonds, which is the first iron complex to do so

Controlling the cleavage of a C-H bond is a difficult task to perform. There are potential uses for a synthetic system that is able to selectively cleave a C-H bond that would be able to be adapted to industry. Efficient systems in Nature have shown the potential to perform such transformations, such as methane monooxygenase (MMOs). Methanotrophs are able to use a diiron(IV) intermediate of the MMOs called Q that is able to convert methane to methanol for energy.[1] A conversion such as this could have industrial applications as well as the ability to reduce the release of the potent greenhouse gas.

The previous work that has been performed using diiron(IV) complexes is very limited. There have been only two previously reported structures, as seen in Figure 1. The first put forth by Ghosh *et al*[2] used the tetraamido macrocycle ligands (TAMLs), which provide the complex with high stability and is able to maintain the (μ-oxo)diiron(IV) core (Figure 1a). The reactivity of this complex was shown to be able to catalytically transfer oxygen to PPh_3. This complex was also able to oxidize benzyl alcohols to the aldehyde selectively, without forming any carboxylic acid groups through a two-electron type reaction. The complex reacts with the efficiency to covert 60 equivalents of benzyl alcohol to the aldehyde with 1 equivalent of the diiron(IV) complex. Cyclic voltammetry of the compound revealed that it goes through a reversible one-electron transfer making the complex Fe^{IV}-O–Fe^{III}. Although able to perform oxidation reactions of alcohols and PPh_3 this complex does not display any C-H activation, which is the overall goal of the research presented in this current paper.

The second of the previous compounds that has been reported with the (μ-oxo)diiron(IV) core (Figure 1b). The reactive compound is formed from the bulk electrolysis of a $Fe^{III}Fe^{IV}$ precursor. The diiron(IV) compound is able to be formed with electrolysis at 900 mV for an hour giving a relative stable compound that is able to characterized. The reactivity of the compound was limited compared to that of MMO-Q. The difference was attributed by the author as having a nitrogen rich environment around the Fe-O diamond core, where as nature has an oxygen rich environment around the diiron(IV) core of the MMO-Q. The high spin state of the diiron(IV) core of MMO-Q is also a notable difference between the natural and synthetic versions. This was further confirmed using DFT calculations that the oxidative power of the complex is increased with the inclusion of high spin states of iron(IV). The spin state of a metal has been talked about in great detail during class. The factors that affect the spin state of a metal are the oxidation state, number of orientation of ligand and the type of ligand. The oxidation of the system proposed is Fe(IV) which is achieved only through electrolysis with these systems. The ligands in the compound are mostly pyridine type rings as well as amines and oxygen. Given the oxidation state and the rather strong field ligands it is of no real

Figure 1. Three reported (μ-oxo)diiron(IV) compounds.

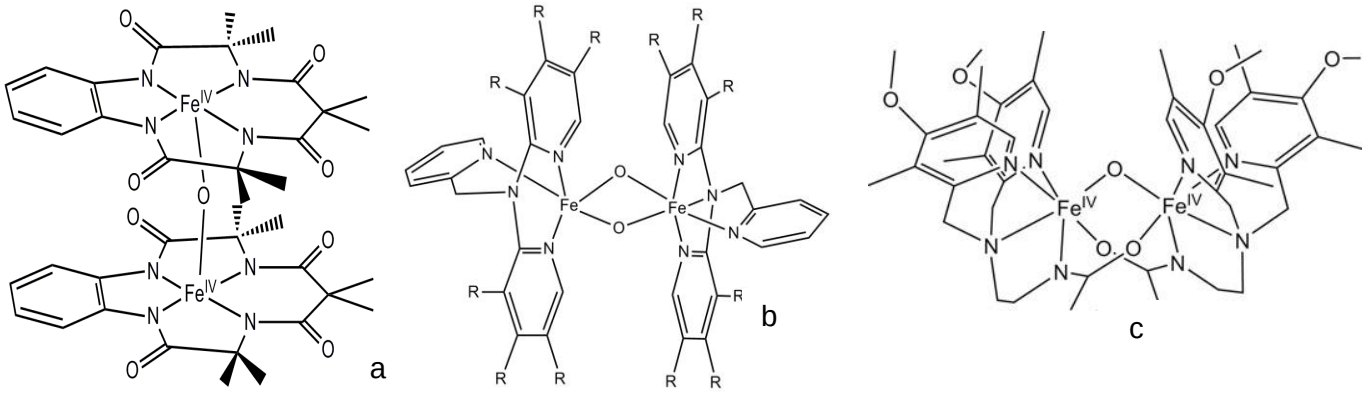

Figure 2. CV of **1** in CH_3CN at room temperature.

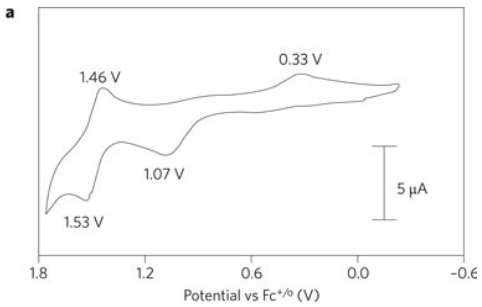

surprise that the spin state of the iron atoms are low spin in this complex.

In this current paper, the complex describes shows improved reactivity toward the cleavage of C-H bonds. The complex begins as a (μ-oxo)diiron(III) (**1**) which is a pentadentate ligand, donating with four nitrogen atoms and one oxygen.

The analysis begins with cyclic voltammetry, which is scanned anodically with ferrocene as the standard, as seen in Figure 2. Two redox waves were observed with the first oxidation at $E_{p,a}$ = +1.07 V with the corresponding reductive peak at $E_{p,c}$ = +0.33 V on the return sweep. The large difference between the peaks limits the transformation and not considered to be reversible. The second oxidative peak observed while scanning anodoically was at $E_{p,a}$ = +1.53 V with the corresponding reductive wave at $E_{p,c}$ = +1.46 V. The difference between the peaks is 0.07 V, which is approaching the 0.06 V CV criteria to identify a transition as being reversible.

The result of the CV is that species **1** is able to go through a one-electron transfer to make iron(IV)iron(III) derivative (**2**). Complex **2** is stable at -40 °C for several days if the potential remains above +0.70 V and can regenerate complex **1** if the potential is dropped below +0.70 V in quantitative yield, making this transformation a reversible process.

Redox chemistry is a topic that was discusses during the course and the determination of the favorability of oxidation and reduction. Cyclic voltammetry, which was also discussed, is an application of using redox chemistry to determine the potential at which the electron transfers is able to take place. This is done by measuring the current while the potential of the electrode is swept between the boundaries that are set. This allows for the determination of the potential needed to either oxidize or reduce a given compound as seen above and can help determine the potential for bulk electrolysis as well

The conversion of complex **2** to complex **3** (Figure 1c), the diiron(IV) species can be accomplished using bulk electrolysis with a potential of +1.70 V. Complex **3** was stable enough for spectroscopic characterization, however the half life was reported as about 1 hour at -40 °C. The conversion of **2** to **3** is also less efficient than the conversion for **1** to **2**. The yield was reported as 85% but is solvent dependent. The best results were seen using CD_3CN in place of acetonitrile. The electrolyte was limited to KPF_6 rather than quaternary-ammonium salts to limit the C-H bonds in the solution.

The structure was solved using extended X-ray absorption fine structure (EXAFS) analysis allowing for the determination of the distances between the iron atoms as well as the bond lengths of the Fe-O-Fe between the different complexes. The distances are higher in complex **1** as it is in high spin state, where as the distances are shorter in the low spin states of iron in **2** and **3**. The oxidation states were further confirmed using Mossbauer studies.

The reactivity of the active complex **3** was studied through kinetic isotope effects (KIE). The studies revealed that **3** has the ability to cleave relatively strong C-H bonds that are around 100 kcal mol^{-1}. The KIE of 3.5 showed that the cleavage of the C-H bond is a large part of the rate determining step of the reaction. The study also revealed the formation of complex **2** after cleavage of the C-H bond. This indicated that **3** acts through a one electron donation for the bond cleavage. The formation of **2** is seen and not the conjugate acid, showing that the hydrogen is lost from the complex into the solution.

The products of the reaction were monitored as cyclohexane was reacted with **3**. The products that were seen were cyclohexene and 1,3-cyclohezadiene in poor yields. There was no formation of benzene or cyclohexanol. Further studies were performed with using cyclohexene and 1,3-cyclohexadiene as reactants. The cyclohexene was converted to 1,3-cycloheadiene in 47% yield, while the 1,3-cyclohexadiene was converted to benzene in 45% yield. The products of the reactions are the result of C-H bond cleavage with no showing of alcohol products. The authors propose two mechanisms for the formation of the products. The first is the initial formation of the alkyl radical which is followed by the removal of a β-hydrogen of the alkyl radical by a second diiron(IV) center. The other proposed mechanism is the electron transfer from the alkyl radical to the diiron(IV) center to create a cation, which then loses a proton at the β-position to form the double bond.

Figure 3. Oxidative reactivity of **3**.

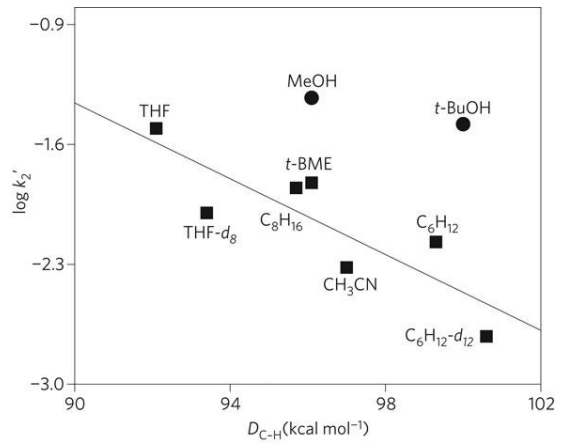

Figure 4. Reaction Scheme of **3** with cyclohexane and t-butanol.

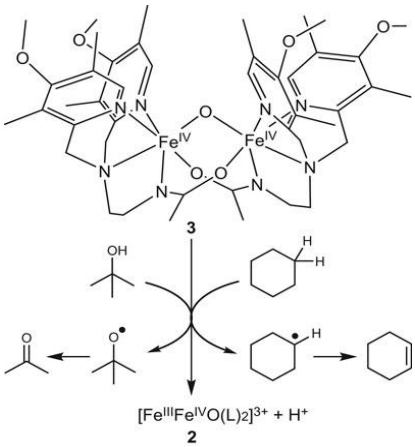

Table 1. Second-order rate constants for he reactions with iron(IV) complexes.

Complexes	$E_{1/2}$ ($Fe^{IV/III}$) (vs $Fc^{+/0}$)	Fe spin state	Cyclo-C_6H_{12}	CH_3CN	Methanol	t-butanol	Ref
3	1.50	S = 1	0.081 [C-H], 3.5	0.014	0.14 [O-H, 1.5]	0.30 [O-H, 1.4]	
$[Fe(O)(Bn\text{-}TPEN)]^{2+}$	>0.90	S=1	3.9×10^{-4}	2×10^{-6} [C-H, 4]	2.8×10^{-3}	NA	4,5
$[Fe(O)(N4Py)]^{2+}$	0.90	S=1	5.5×10^{-5}	2×10^{-7}	4.4×10^{-4} [C-H, 7]	NA	6,7
$[Fe(O)(OH_2)_5]^{2+}$	~1.4	S=2	NA	4.1 [C-H, 4.1]	572 [C-H, 4.4]	60	8
MMO-Q	NA	S=2	$(3\text{-}4)\times10^4$ for CH_4				

The study of **3** with the reaction of aliphatic alcohols such as methanol and *t*-butanol also gave interesting results. The KIE studies were performed first with the deuteration of the C-H bonds, which showed no impact on the kinetics of the reaction. The deuteration of the O-H bonds however, showed a KIE of 1-1.5, which leads to the interpretation that the reaction goes through the O-H bond cleavage rather than the cleavage of C-H.

The products of the reaction of **3** with *t*-butanol were monitored using ^{1}H NMR, where the formation of acetone and 2-methylpropene was seen. The reaction is proposed to go through the formation of the radical at the oxygen and then lead to the formation of acetone. They propose that the alcohol proton transfer from the O-H is coupled with the loss of an electron from the oxygen from a non-bonding orbital (Figure 4).

The formation of the 2-methylpropene indicates that a competing reaction is taking place. This is proposed to be caused by the electrolysis of the solvent to give the protons needed to make the *t*-butyl cation that undergoes dehydrogenation. This would be avoided if the solution would be able to buffered to prevent the reaction of the protons with the *t*-butanol, however, the authors have not been successful in finding a base that would not be oxidized by complex **3**.

In Table 1 are listed iron species that have been characterized and have shown the ability to perform similar chemistry as that of complex **3**. The first is $[Fe(O)(Bn\text{-}TPEN)]^{2+}$ complex that uses the pentadentate ligand as a form of nonheme oxoiron(IV) complex.[4] This compound has shown too active in C-H activation but in much lower rates. This complex hydroxylates alkanes rather than the one-electron transfer mechanism put forth by the authors of this paper.

The second complex is another nonheme pentadentate ligand that forms the complex $[Fe(O)(N4Py)]^{2+}$.[5] This compound again uses the oxoiron(IV) structure, however the compound is activate through electrolysis from the Fe^{II} species through a two-electron transfer. This differs from the previous compound that activated from Fe^{III} by electrolysis. The reactivity of this system is lower than that of the recent report as well as the previous mononuclear system.

The third mononuclear Fe^{IV} complex that is compared is $[Fe(O)(OH_2)_5]^{2+}$, which is different from the others in that it has a high spin state at the iron center. This high spin state allows for a greater rate of reactivity, which is seen in acetonitile, methanol and t-butanol. The shortcoming of this complex is that the stability of the complex is limited and being immiscible in nonpolar solutions like that of cyclohexane. The activated iron(IV) complex is accessed using a two electron process, but due to the instability of the complex the potential at which the Fe^{III}/Fe^{IV} transformation has not been fully established.

The reactivity of MMO-Q with the rate constant for the reaction with methane is still greatly above that of the synthesized compounds. This structure still provides a synthetic target in which to pursue in order to achieve the desired goal of C-H activation.

Kinetics and rate laws were another topic that was covered in class and although KIEs were not specifically discussed, understanding the general scheme of kinetics allows for understand of the meaning.

The overall goal of the research is rather well defined, with the pursuit of a structure that is comparable to that of the active intermediate MMO-Q. In the current work the authors propose a compound that is relatively reactive, however lacks in stability as well as high rates of reactivity. The reactivity of the mononuclear iron(IV) complex and the MMO-Q is much higher than that of the other complexes, which can be possibly correlated to the high spin state of the iron. Therefore the overall goal of the research should be in the direction of a stable high spin diiron(IV) complex that is stable enough to be used as a C-H activator.

In the current paper the only solvent that is used for the cyclic voltammetry is deuterated acetonitrile because of the need to a solvent that does not contain C-H bonds. It would be interesting to see the effects of other solvents, whether it be other deuterated solvents or a solvent such as carbon tetrachloride that also does not contain C-H bonds.

The ability to determine an acceptable base that can be used to keep the reaction neutral but not provide other potential C-H bonds to be cleaved is a challenge that should be investigated further. This may provide better results as well as future applications in the next systems that will be designed for the cleavage of C-H bonds.

References

1. Merkx, M. et al. Dioxygen Activation and methane hydroxylation by soluble methane monooxygenase: A tale of two irons and three proteins. *Angew. Chem. Int. Ed.* **40**, 2782–2807 (2001).
2. Ghosh, A. et al. Catalytically active m-oxodiiron(IV) oxidants from iron(III) and dioxygen. *J. Am. Chem. Soc.* **127**, 2505–2513 (2005).
3. Xue, G. et al. A synthetic precedent for the $[Fe^{IV}_2(m\text{-}O)_2]$ diamond core proposed for methane monooxygenase intermediate Q. *Proc. Natl Acad. Sci. USA* **104**, 20713–20718 (2007).
4. Kaizer, J. et al. Nonheme $Fe^{IV}O$ complexes that can oxidize the C–H bonds of cyclohexane at room temperature. *J. Am. Chem. Soc.* **126**, 472–473 (2004).
5. Collins, M. J., Ray, K. & Que, L. Jr Electrochemical generation of a nonheme oxoiron(IV) complex. *Inorg. Chem.* **45**, 8009–8011 (2006).
6. Pestovsky, O. & Bakac, A. Reactivity of aqueous fe(IV) in hydride and hydrogen atom transfer reactions. *J. Am. Chem. Soc.* **126**, 13757–13764 (2004).
7. Jacobsen, F., Holcman, J. & Sehested, K. Reactions of the ferryl ion with some compounds found in cloud water. *Int. J. Chem. Kinet.* **30**, 215–221 (1998).
8. Valentine, A. M., Stahl, S. S. & Lippard, S. J. Mechanistic studies of the reactionof reduced methane monooxgyenase hydroxylase with dioxygen and substrates. *J. Am. Chem. Soc.* **121**, 3876–3887 (1999).

but creates increased mass transport losses at current densities of >0.1 A cm^{-2}. It is clear from these results that improvements in electrode mass transport properties are required to overcome this performance loss.

The results of 100-hour durability tests in fuel cells using hydrogen/oxygen and hydrogen/air as anode/cathode gases are shown in fig. S4. Relative to the stable current densities obtained by Bashyam and Zelenay (*32*) for tests performed under the same conditions (0.2 A cm^{-2} with H_2/O_2 at 0.5 V; 0.13 to 0.14 A cm^{-2} with H_2/air at 0.4 V), the initial current densities produced by the catalyst in this work (0.75 A cm^{-2} with H_2/O_2 at 0.5 V; 0.58 A cm^{-2} with H_2/air at 0.4 V) were much higher and remained higher throughout the 100-hour period, with final values of 0.33 A cm^{-2} with H_2/O_2 at 0.5 V and 0.36 A cm^{-2} with H_2/air at 0.4 V.

The best NPMC in this work has a much higher initial activity, but less stability, than those prepared by Bashyam and Zelenay according to a nonpyrolytic method based on a cobalt salt and polypyrrole deposited on carbon black (*32*). Continued research must now focus on improving the stability of these NPMCs and optimizing their cathode mass-transport properties.

References and Notes

1. H. A. Gasteiger, S. S. Kocha, B. Sompalli, F. T. Wagner, *Appl. Catal. B* **56**, 9 (2005).
2. H. A. Gasteiger, J. E. Panels, S. G. Yan, *J. Power Sources* **127**, 162 (2004).
3. R. Jasinski, *Nature* **201**, 1212 (1964).
4. J. P. Dodelet, in *N4-Macrocyclic Metal Complexes*, J. H. Zagal, F. Bedioui, J. P. Dodelet, Eds. (Springer, New York, 2006), pp. 83–147.
5. S. Gupta, D. Tryk, I. Bae, W. Aldred, E. Yeager, *J. Appl. Electrochem.* **19**, 19 (1989).
6. M. Yuasa *et al.*, *Chem. Mater.* **17**, 4278 (2005).
7. N. P. Subramanian *et al.*, *J. Power Sources* **157**, 56 (2006).
8. E. B. Easton, A. Bonakdarpour, J. R. Dahn, *Electrochem. Solid State Lett.* **9**, A463 (2006).
9. R. Z. Yang, A. Bonakdarpour, E. B. Easton, P. Stoffyn-Egli, J. R. Dahn, *J. Electrochem. Soc.* **154**, A275 (2007).
10. J. Maruyama, I. Abe, *Chem. Commun.* **2007**, 2879 (2007).
11. T. E. Wood, Z. Tan, A. K. Schmoeckel, D. O'Neill, R. Atanasoski, *J. Power Sources* **178**, 510 (2008).
12. A. Garsuch, K. MacIntyre, X. Michaud, D. A. Stevens, J. R. Dahn, *J. Electrochem. Soc.* **155**, B953 (2008).
13. T. Schilling, M. Bron, *Electrochim. Acta* **53**, 5379 (2008).
14. A. H. C. Sirk, S. A. Campbell, V. I. Birss, *J. Electrochem. Soc.* **155**, B592 (2008).
15. J. Maruyama, N. Fukui, M. Kawaguchi, I. Abe, *J. Power Sources* **182**, 489 (2008).
16. V. Nallathambi, J.-W. Lee, S. P. Kumaraguru, G. Wu, B. N. Popov, *J. Power Sources* **183**, 34 (2008).
17. U. I. Koslowski, I. Abs-Wurmbach, S. Fiechter, P. Bogdanoff, *J. Phys. Chem. C* **112**, 15356 (2008).
18. J. Maruyama, J. Okamura, K. Miyazaki, Y. Uchimoto, I. Abe, *J. Phys. Chem. C* **112**, 2784 (2008).
19. J. M. Ziegelbauer *et al.*, *J. Phys. Chem. C* **112**, 8839 (2008).
20. F. Jaouen, F. Charreteur, J. P. Dodelet, *J. Electrochem. Soc.* **153**, A689 (2006).
21. F. Jaouen, M. Lefèvre, J. P. Dodelet, M. Cai, *J. Phys. Chem. B* **110**, 5553 (2006).
22. F. Jaouen, J. P. Dodelet, *J. Phys. Chem. C* **111**, 5963 (2007).
23. F. Jaouen, A. M. Serventi, M. Lefevre, J. P. Dodelet, P. Bertrand, *J. Phys. Chem. C* **111**, 5971 (2007).
24. F. Jaouen, S. Marcotte, J. P. Dodelet, G. Lindbergh, *J. Phys. Chem. B* **107**, 1376 (2003).
25. F. Charreteur, F. Jaouen, S. Ruggeri, J. P. Dodelet, *Electrochim. Acta* **53**, 2925 (2008).
26. See supporting material on *Science* Online.
27. U. S. Department of Energy, Technical Plan: Fuel Cells, 2007 (www1.eere.energy.gov/hydrogenandfuelcells/mypp/pdfs/fuel_cells.pdf).
28. F. Charreteur, S. Ruggeri, F. Jaouen, J. P. Dodelet, *Electrochim. Acta* **53**, 6881 (2008).
29. F. Jaouen, J. P. Dodelet, *Electrochim. Acta* **52**, 5975 (2007).
30. M. Lefèvre, J.-P. Dodelet, *Electrochim. Acta* **53**, 8269 (2008).
31. Although detailed cost analysis of these Fe-based electrocatalysts was not performed, their principal elements are carbon, nitrogen, and iron and they require no expensive precursors or processing steps. Their manufacturing cost is conservatively estimated to be at least two orders of magnitude lower than that of current Pt-based ORR catalysts for PEMFCs.
32. R. Bashyam, P. Zelenay, *Nature* **443**, 63 (2006).

33. Supported by General Motors of Canada and the Natural Sciences and Engineering Council of Canada. The Cabot Corporation provided the carbon black. U.S. patent application US 61/112,844 related to this work was filed on 10 November 2008.

Supporting Online Material

www.sciencemag.org/cgi/content/full/324/5923/71/DC1
Materials and Methods
SOM Text
Figs. S1 to S4
Tables S1 and S2
References

19 December 2008; accepted 9 February 2009
10.1126/science.1170051

Consecutive Thermal H_2 and Light-Induced O_2 Evolution from Water Promoted by a Metal Complex

Stephan W. Kohl,[1] Lev Weiner,[2] Leonid Schwartsburd,[1] Leonid Konstantinovski,[2] Linda J. W. Shimon,[2] Yehoshoa Ben-David,[1] Mark A. Iron,[2] David Milstein[1]*

Discovery of an efficient artificial catalyst for the sunlight-driven splitting of water into dioxygen and dihydrogen is a major goal of renewable energy research. We describe a solution-phase reaction scheme that leads to the stoichiometric liberation of dihydrogen and dioxygen in consecutive thermal- and light-driven steps mediated by mononuclear, well-defined ruthenium complexes. The initial reaction of water at 25°C with a dearomatized ruthenium (II) [Ru(II)] pincer complex yields a monomeric aromatic Ru(II) hydrido-hydroxo complex that, on further reaction with water at 100°C, releases H_2 and forms a cis dihydroxo complex. Irradiation of this complex in the 320-to-420–nanometer range liberates oxygen and regenerates the starting hydrido-hydroxo Ru(II) complex, probably by elimination of hydrogen peroxide, which rapidly disproportionates. Isotopic labeling experiments with $H_2{}^{17}O$ and $H_2{}^{18}O$ show unequivocally that the process of oxygen–oxygen bond formation is intramolecular, establishing a previously elusive fundamental step toward dioxygen-generating homogeneous catalysis.

The design of efficient catalytic systems for splitting water into H_2 and O_2, driven by sunlight without the use of sacrificial reductants or oxidants, is among the most important challenges facing science today, underpinning the long-term potential of hydrogen as a clean, sustainable fuel (*1*, *2*). In this context, it is essential to enhance our basic understanding of the fundamental chemical steps involved in such processes (*3*–*17*). Of the two parts of the water-splitting cycle, the oxidation half-cycle to form O_2 presents the greatest challenge. Well-defined metal complexes that catalyze water oxidation to dioxygen are rare and generally require a sacrificial strong oxidant. The molecular mechanisms of such systems, including that of the intensively studied "blue dimer" *cis*,*cis*-$[(bpy)_2(H_2O)Ru^{III}ORu^{III}(OH_2)(bpy)_2]^{4+}$ (*3*, *11*, *12*), are generally thought to involve metal oxo intermediates and bimolecular steps, but clarification of the fundamental chemical principles responsible for O–O bond formation remains a considerable challenge. In addition, a major challenge faced by hydrogen and oxygen photogeneration systems based on soluble metal complexes is that for a viable system, the two half-cycles must be combined, avoiding the use of sacrificial oxidants and reductants. We present here a ruthenium-mediated reaction sequence that, in a stepwise stoichiometric manner, generates hydrogen thermally and oxygen photochemically, involves well-defined complexes, and demonstrates the feasibility of unimolecular O–O bond formation at a single metal center.

[1]Department of Organic Chemistry, The Weizmann Institute of Science, Rehovot 76100, Israel. [2]Department of Chemical Research Support, The Weizmann Institute of Science, Rehovot 76100, Israel.

*To whom correspondence should be addressed. E-mail: david.milstein@weizmann.ac.il

We have previously reported that the non-aromatic pincer Ru(II) complex **1** (Fig. 1) is a powerful catalyst for the coupling of alcohols to form esters with the liberation of H_2 (*18*) and for the dehydrogenative coupling of alcohols with amines to produce amides (*19*). We have now studied the reactivity of this complex with water. The addition of one equivalent of water to a solution of **1** in tetrahydrofuran (THF) at room temperature immediately led to ligand aromatization with quantitative formation of the *trans* hydrido-hydroxo complex **2** (Fig. 1), which we isolated and fully characterized (*20*). This compound is probably formed by a mechanism involving coordination of water at the vacant coordination site trans to the hydride ligand, followed by proton migration to the side arm. This unique water activation process involves cooperation between the metal and the ligand and no change in the metal oxidation state (*21*).

Characteristic spectroscopic features in the ^1H nuclear magnetic resonance (NMR) spectrum of **2** are the large downfield shift of the hydride ligand resonance from –26.5 parts per million (ppm) (d, $^2J_{PH}$ = 25.5 Hz) in **1** to –14.9 ppm (d, $^2J_{PH}$ = 27.5 Hz) and a doublet at –1.4 ppm ($^3J_{PH}$ = 2.3 Hz) assigned to the hydroxo ligand. If one equivalent of D_2O is used instead of H_2O, one deuterium atom is incorporated at the side-arm benzylic carbon, leading to a broad peak (because of unresolved small $^2J_{HD}$ and $^2J_{PD}$) at 2.8 ppm in the ^2H NMR spectrum; the OD group gives rise to a signal at –1.2 ppm (complex **2-*D*$_2$**, Fig. 1). These reactions are reversible. Placing the solid under vacuum or heating it in benzene solution at 65°C resulted in water elimination to quantitatively yield the starting complex **1**. Direct spectroscopic evidence for coordination of the hydroxo group to the metal center was obtained by adding one equivalent of $H_2{}^{17}O$ to **1** in THF. The oxygen atom in the labeled complex **2-*^{17}O*** exhibits a singlet at 32.43 ppm in the ^{17}O NMR spectrum (in THF). Coupling ($^2J_{OP}$, $^2J_{OC}$) of the ^{17}O atom (s = 5/2) with the adjacent ligands leads to broadening of the signal in the ^{31}P NMR spectrum at 112.14 ppm and the appearance of a more complicated signal for the carbonyl ligand in the $^{13}C\{^1H\}$NMR spectrum (δ = 209.27 ppm). The doublet in the ^1H NMR spectrum (δ = 14.78 ppm) assigned to the hydride ligand in the trans position is not affected.

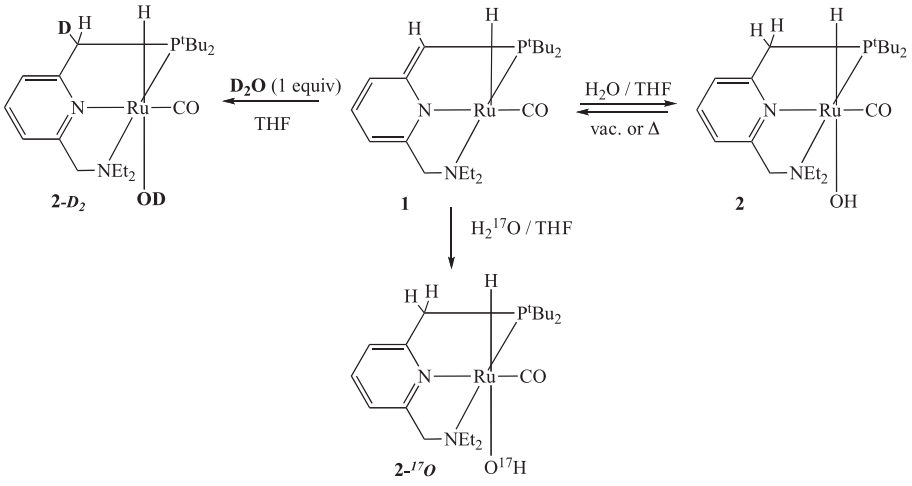

Fig. 1. Reactions of water with complex **1.** Et, ethyl.

Repeating the reaction in benzene by adding an excess of water to **1** resulted in formation of colorless crystals at the interface between the water and benzene layers. X-ray diffraction analysis of the isolated solid (**2.*nH$_2$O***) shows a distorted octahedral coordination geometry at ruthenium (Fig. 2). The Ru–O–H nonlinear angle [103(3)] indicates repulsion between the oxygen lone pairs and d electrons of the complex (*22*, *23*). The crystals are composed of alternating layers of the metal complex, benzene, and water. The hydroxo groups of the complex are involved in hydrogen bonding with the water layer (figs. S4 to S6). These crystals are stable below 10°C and release the solvated water at room temperature.

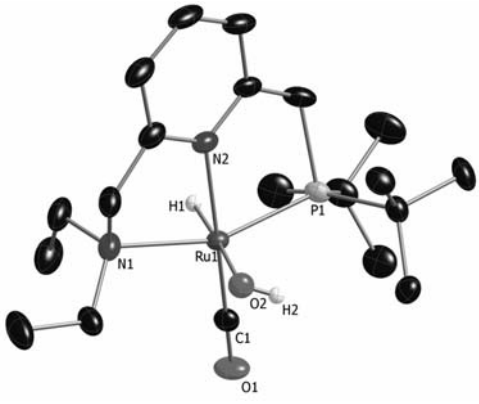

Fig. 2. Structure of the *trans* hydrido-hydroxo complex **2.*nH$_2$O*** (ellipsoids shown at 50% probability level). Hydrogen atoms are shown only for the hydride and hydroxo ligands. The water and benzene layers are omitted for clarity. Selected bond distances (in angstroms) and angles (in degrees): Ru1–H1, 1.54(3); Ru1–C1, 1.820(3); Ru1–N2, 2.097(2); Ru1–N1, 2.241(2); Ru1–O2, 2.261(2); Ru1–P1, 2.2653(8); N2–Ru1–C1, 173.02(10); N1–Ru1–P1, 159.12(7); H1–Ru1–O2, 171.9(13); N2–Ru1–O2, 86.94(8); N1–Ru1–O2, 82.44(9); Ru1–O2–H2, 103(3).

Heating complex **2** (or **2.*nH$_2$O***) in refluxing water for 3 days resulted in evolution of H_2 with concomitant formation of the green *cis* dihydroxo complex **3** (Fig. 3). The gas was collected in a burette, and hydrogen was detected by the reaction of a sample of the gas phase with $(PEt_3)_3IrCl$ to form *mer-cis*-$(PEt_3)_3Ir(H)_2Cl$ (*24*). H_2 was quantified with gas chromatography (GC) (yield: 37%). The NMR yield of the complex **3** was 45%. Some unreacted **2.*nH$_2$O*** (25%) remained, the rest being unidentified products. This reaction may proceed by electrophilic attack by water on the hydride ligand. Pure **3** was independently prepared by reaction of **2.*nH$_2$O*** with N_2O (*25*, *26*): N_2O was bubbled into a THF solution of **2.*nH$_2$O*** for 10 min at room temperature, after which the solution was stirred overnight and turned green. We isolated and fully characterized the result-

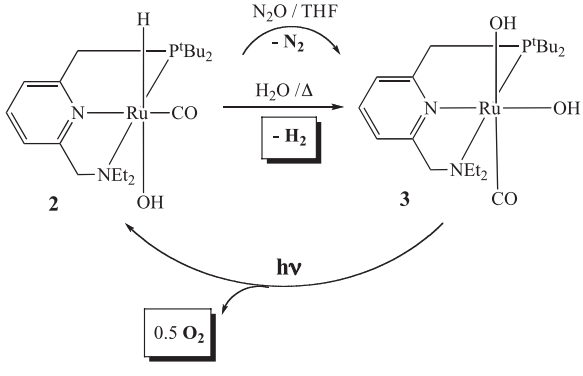

Fig. 3. Thermal activation of water by the hydrido-hydroxo complex **2** with liberation of H_2, independent synthesis of the dihydroxo complex **3** using N_2O, and O_2 formation upon photolysis of **3** regenerating complex **2.** *h*, Planck's constant; ν, frequency.

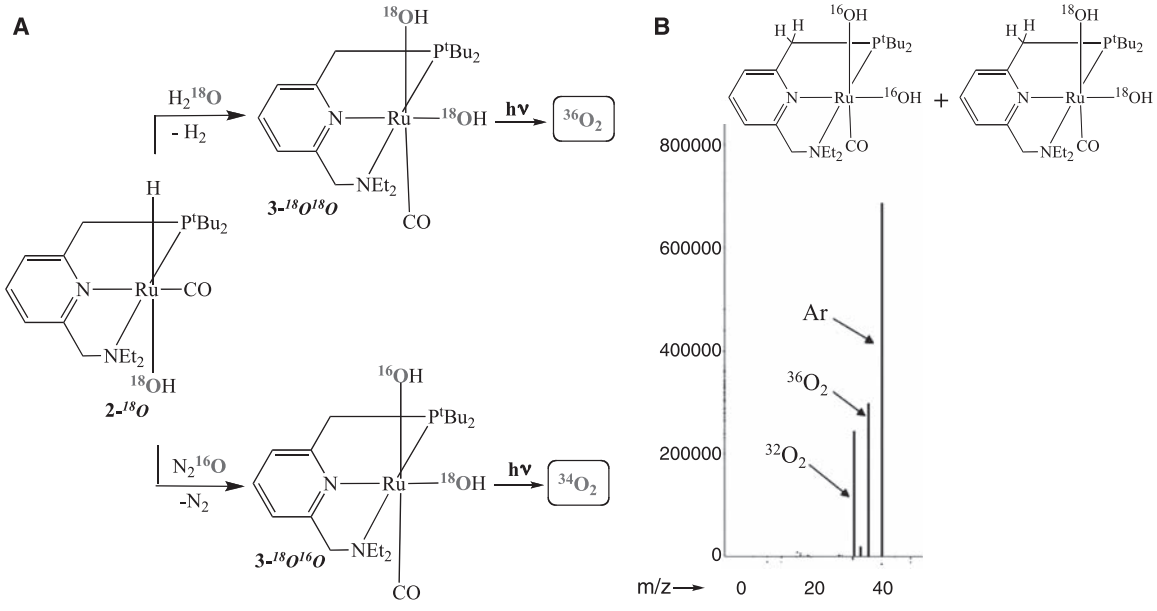

Fig. 4. Photolysis of isotopically labeled dihydroxo complexes. (**A**) Synthesis and photolysis of complexes **3-^{18}O^{18}O** and **3-^{18}O^{16}O**. (**B**) Mass spectrum of a gaseous extract from the photolytic reaction of equimolar amounts of **3-^{18}O^{18}O** and **3-^{16}O^{16}O**, showing virtually no crossover.

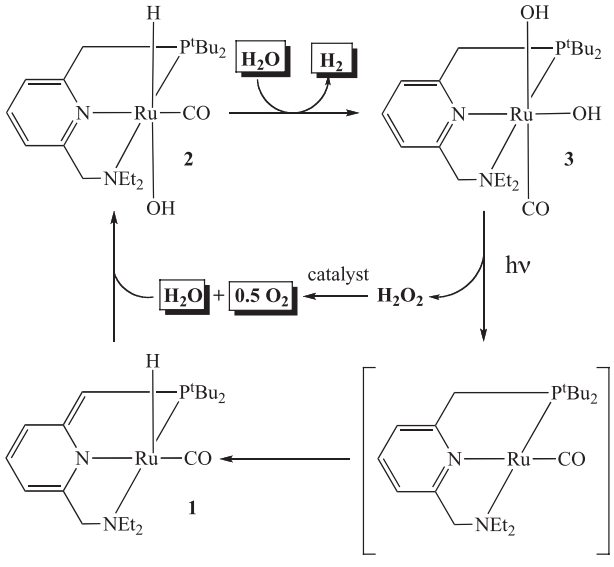

Fig. 5. Proposed mechanism for the formation of H_2 and O_2 from water.

ant green microcrystalline solid **3** (60% yield). It is stable in a THF solution up to 65°C but decomposes into unidentified products at 102°C in dioxane. The $^{31}P\{^1H\}$ NMR spectrum of **3** shows a singlet at 94.0 ppm, representing an upfield shift of 14 ppm relative to the corresponding singlet of complex **2**. The two tert-butyl (^{t}Bu) groups of P^{t}Bu$_2$ give rise to different signals in both the ^1H and $^{13}C\{^1H\}$NMR spectra, and the ethyl groups of NEt$_2$ are also nonequivalent, indicating C_1 symmetry and a cis dihydroxo arrangement. The hydroxo ligands give rise to a broad signal at –7.4 ppm in the ^1H NMR spectrum and absorb at 3413 cm^{-1} in the infrared (IR) spectrum. The carbonyl ligand exhibits a doublet at 207.4 ppm ($^2J_{PC}$ = 16.1 Hz) in the $^{13}C\{^1H\}$ NMR spectrum and absorbs at 1923 cm^{-1} in the IR spectrum. The main peak in the mass spectrum (electrospray ionization) at mass/charge ratio (m/z) = 453 (100) can be assigned to the cation $[M - OOH]^+$ and the peak at m/z = 469 (18) is characteristic for $[M - OH]^+$. Elemental analysis agrees with the calculated values for our posited structure.

We next studied the stability of complex **3** on exposure to light. Irradiation of THF or aqueous solutions of **3** under N_2 or Ar with a 300-W halogen lamp filtered through perspex (*27*) over 2 days resulted in a color change from green to greenish-yellow, accompanied by O_2 evolution. NMR of the solution showed that besides unreacted **3** (33%), the hydrido-hydroxo complex **2.*n*H$_2$O** (45%) was formed, in addition to some unidentified by-products (22%), most probably phosphine oxides (Fig. 3). The liberated gas was identified as dioxygen by GC–mass spectrometry (GC-MS) and by the reaction with $(PEt_3)_3IrCl$ to form the dioxygen complex $(PEt_3)_3Ir(O_2)Cl$ (*20*). This specific and very sensitive reaction was also used for quantification (*20*). The yield of the detected dioxygen formed from the reaction in water was 23% (34% based on reacted **3**). When irradiation of aqueous solutions of **3** was performed under argon flow to remove the generated O_2, clean conversion of **3** (49%, the rest being unreacted **3**) to **2.*n*H$_2$O** (49%) was observed, with no by-products being formed, indicating that the unidentified by-products are a result of reaction with the generated dioxygen.

To verify that O_2 was released from the dihydroxo complex, a labeled complex bearing two ^{18}OH groups (**3-^{18}O^{18}O**) was prepared using $H_2{}^{18}O$ (Fig. 4). The ^{18}O-H stretching vibration is shifted in the IR spectrum to lower energy by 14 wavenumbers, to 3399 cm^{-1}, whereas all NMR spectra are identical to those of **3**. Upon irradiation (*27*) of **3-^{18}O^{18}O** in H_2O, $^{36}O_2$ was formed as the major dioxygen product, as confirmed by GC-MS (Fig. 4A and fig. S3A). No exchange between **3-^{18}O^{18}O** and $H_2{}^{16}O$ was observed, indicating that no substantial Ru-OH dissociation took place.

An important question is whether the O–O bond formation process is intra- or intermolecular. To address this issue, we prepared the isotopically mixed-labeled dihydroxo complex **3-^{18}O^{16}O** by treatment of **2-^{18}O** with $N_2{}^{16}O$ (Fig. 4A). Upon photolysis, $^{34}O_2$ was formed predominantly with only small amounts of $^{32}O_2$ and $^{36}O_2$ observed (observed ratio $^{32}O_2$:$^{34}O_2$:$^{36}O_2$, 3.8:16.2:1) (fig S3B) (*20*). Moreover, we performed a crossover experiment involving photolysis of equimolar amounts of complexes **3-^{18}O^{18}O** and **3-^{16}O^{16}O**, resulting in formation of $^{36}O_2$ and $^{32}O_2$ with only a small amount of $^{34}O_2$ (observed ratio $^{32}O_2$:$^{34}O_2$:$^{36}O_2$, 13.1:1:15.6) (Fig. 4B). Thus, our results unambiguously show that the O-O

bond formation process in this system is intramolecular and involves a single metal center.

We suggest that upon photolysis, complex **3** liberates hydrogen peroxide in a reductive elimination step (*28*, *29*), which then catalytically disproportionates into O_2 and water (Fig. 5). Our labeling studies show that, if H_2O_2 is indeed an intermediate in the O_2 generation process, then O_2 is formed by two electron oxidation of H_2O_2 without scission of the O–O bond, as reported for the reaction catalyzed by the enzyme catalase (*30*).

The metal-to-ligand charge transfer (MLCT) band of **3** has an absorbance maximum in the ultraviolet-visible (UV-Vis) spectrum in water at wavelength $\lambda = 380$ nm (extinction coefficient $\varepsilon = 8157\ cm^{-1}M^{-1}$). Weaker absorptions appear at $\lambda = 459$ nm ($\varepsilon = 2045\ cm^{-1}M^{-1}$) and $\lambda = 716$ nm ($\varepsilon = 505\ cm^{-1}M^{-1}$) (fig. S2). The theoretical UV-Vis spectrum (of the NMe_2, PMe_2 model of **3**) in water was determined by time-dependent density functional theory (TDDFT) (figs S8 and S9 and table S5). When a 400-nm filter was used, the yield of produced O_2 decreased to only 8 to 10%. Together with filtration of wavelengths of $\lambda < 320$ nm by the perspex filter, this observation is in line with an effective spectral range corresponding to the MLCT band of **3** (320 to 420 nm).

Unlike the dihydroxo complex **3**, the hydrido-hydroxo complex **2** was stable toward irradiation with a 300-W halogen lamp for 2 days, with or without the perspex filter, and did not release O_2. This observation is in line with an intramolecular, mononuclear O–O bond formation mechanism.

Because the intermediacy of H_2O_2 might give rise to hydroxyl radicals, via a Fenton-type reaction (*31*), we employed the spin trap 5,5-dimethyl-1-pyrroline-1-oxide (DMPO) (*32*) to detect them. Electron paramagnetic resonance spectra did provide evidence for DMPO-OH adducts (fig. S7A). However, it is clear that these hydroxyl radicals are not substantially involved in O_2 production (as the isotopic labeling experiments would have resulted in scrambling). Thus, in the presence of the OH radical scavenger *tert*-butanol (*33*), no hydroxyl radicals were observed, whereas the amount of O_2 formed remained unchanged. Further evidence supporting hydrogen peroxide as the source of hydroxyl radicals, and that the hydroxyl radicals are not the source of the produced O_2, was obtained from experiments with the enzyme catalase, which is an extremely efficient catalyst for the disproportionation of hydrogen peroxide to O_2 and water by a non-radical mechanism. If H_2O_2 were the source of hydroxyl radicals, its interception by catalase would retard their formation. When irradiation of **3** was performed in the presence of catalase, only traces of hydroxyl radicals were observed (fig. S7C), whereas the amount of O_2 produced remained almost unchanged (actually slightly increased). Thus, we believe that H_2O_2 forms photolitically from **3** and undergoes disproportionation to O_2 and water, with only a marginal amount of it forming hydroxyl radicals, perhaps by a Fenton-type reaction. As expected, no OH radicals were detected when the hydrido-hydroxo complex ***2.nH$_2$O*** was irradiated.

Combining the separate stoichiometric reactions presented here gives rise to a stepwise cycle in which H_2 and O_2 are released in consecutive steps, and the starting Ru complex is regenerated (Fig. 5). The cycle starts with the *trans* hydrido-hydroxo complex ***2.nH$_2$O*** that reacts with water under refluxing conditions, evolving H_2 and forming the *cis* dihydroxo complex **3**. The second step is light-induced. Irradiating **3** may release hydrogen peroxide by reductive elimination, probably forming a Ru(0) intermediate, which converts to **1** by migration of a proton from the methylene group of the phosphorus side arm to the ruthenium center to form a hydride ligand with coincident dearomatization of the pyridine ring (*34*, *35*). The liberated hydrogen peroxide is then rapidly catalytically decomposed into dioxygen and water. A possible catalyst for this latter reaction is complex **1**. The addition of a very dilute THF solution of **1** to a THF solution of hydrogen peroxide at room temperature resulted in immediate O_2 evolution, as detected by GC-MS and by reaction with $(PEt_3)_3IrCl$ (*20*). In the last step of the cycle, the water reacts readily with **1** to form the starting complex **2**.

We believe that our studies indicate a distinct approach toward a complete cycle for the generation of dihydrogen and dioxygen from water catalyzed by metal complexes and show that light-induced O–O bond formation can be intramolecular and need not necessarily involve bimolecular mechanisms, dinuclear complexes, and metal oxo intermediates.

References and Notes

1. N. S. Lewis, D. G. Nocera, *Proc. Natl. Acad. Sci. U.S.A.* **103**, 15729 (2006).
2. V. Balzani, A. Credi, M. Venturi, *ChemSusChem* **1**, 26 (2008).
3. R. A. Binstead, C. W. Chronister, J. Ni, C. W. Hartshorn, T. J. Meyer, *J. Am. Chem. Soc.* **122**, 8464 (2000).
4. J. H. Alstrum-Acevedo, M. K. Brennaman, T. J. Meyer, *Inorg. Chem.* **44**, 6802 (2005).
5. T. A. Betley, Q. Wu, T. Van Voorhis, D. G. Nocera, *Inorg. Chem.* **47**, 1849 (2008).
6. J. K. Hurst, *Coord. Chem. Rev.* **249**, 313 (2005).
7. M. Yagi, M. Kaneko, *Chem. Rev.* **101**, 21 (2001).
8. W. Ruttinger, G. C. Dismukes, *Chem. Rev.* **97**, 1 (1997).
9. I. Romero *et al.*, *Inorg. Chem.* **47**, 1824 (2008).
10. Z. Deng, H.-W. Tseng, R. Zong, D. Wang, R. Thummel, *Inorg. Chem.* **47**, 1835 (2008).
11. J. K. Hurst, J. L. Cape, A. E. Clark, S. Das, C. Qin, *Inorg. Chem.* **47**, 1753 (2008).
12. X. Yang, M.-H. Baik, *J. Am. Chem. Soc.* **128**, 7476 (2006).
13. J. T. Muckerman, D. E. Polyansky, T. Wada, K. Tanaka, E. Fujita, *Inorg. Chem.* **47**, 1787 (2008).
14. N. D. McDaniel, F. J. Coughlin, L. L. Tinker, S. Bernhard, *J. Am. Chem. Soc.* **130**, 210 (2008); and references therein.
15. Y. V. Geletii *et al.*, *Angew. Chem. Int. Ed.* **47**, 3896 (2008); and references therein.
16. J. Limburg *et al.*, *Science* **283**, 1524 (1999).
17. S. Chakraborty, T. J. Wadas, H. Hester, R. Schmehl, R. Eisenberg, *Inorg. Chem.* **44**, 6865 (2005).
18. J. Zhang, G. Leitus, Y. Ben-David, D. Milstein, *J. Am. Chem. Soc.* **127**, 10840 (2005).
19. C. Gunanathan, Y. Ben-David, D. Milstein, *Science* **317**, 790 (2007).
20. Experimental details are available as supporting material on *Science* Online.
21. DFT calculations on a model system (with PMe_2, NMe_2 groups) at the PCM(H_2O)-M06/SDB-cc-pVDZ//M06/SDD(d) level indicate that the Gibbs free energy change (ΔG) = –5.4 kcal/mol for H_2O coordination and ΔG = –5.7 kcal/mol and $\Delta G^{\ddagger}$ = 9.4 kcal/mol for the subsequent proton migration. Addition of a bridging water molecule as part of the proton-transfer transition state lowers the barrier to $\Delta G^{\ddagger} = 3.6$ kcal/mol. According to this DFT calculation, the D atom would selectively transfer to the same side of the double bond as the hydroxo ligand, but we have not yet demonstrated this experimentally.
22. P. E. M. Siegbahn, M. R. A. Blomberg, M. Svenson, *J. Phys. Chem.* **97**, 2564 (1993).
23. D. Milstein, J. C. Calabrese, I. D. Williams, *J. Am. Chem. Soc.* **108**, 6387 (1986).
24. O. Blum, D. Milstein, *J. Am. Chem. Soc.* **117**, 4582 (1995).
25. Reaction of a Ru(H)(OH) complex with N_2O was reported to yield a $Ru(OH)_2$ complex (*26*). We found that bubbling N_2O into a solution of the crystalline material ***2.nH$_2$O*** (rather then **2**) avoided the formation of impurities.
26. A. W. Kaplan, R. G. Bergman, *Organometallics* **17**, 5072 (1998).
27. We used a filter made of polymethylmethacrylate (perspex, thickness = 1 cm) during the irradiation. This material absorbs UV light at wavelengths shorter than $\lambda = 320$ nm. Irradiation without perspex gave more by-products, and dioxygen was formed in only 19% yield.
28. Photochemically induced reductive elimination of HOCl from a $Pt^{(IV)}(Cl)(OH)$ complex was suggested (*29*).
29. Y. Nakabayashi *et al.*, *Chem. Eur. J.* **13**, 3980 (2007).
30. S. Kato, T. Ueno, S. Fukuzumi, Y. Watanabe, *J. Biol. Chem.* **279**, 52376 (2004).
31. C. Walling, *Acc. Chem. Res.* **8**, 125 (1975).
32. M. A. Grela, M. E. J. Coronel, A. J. Colussi, *J. Phys. Chem.* **100**, 16940 (1996).
33. J. von Sonntag, E. Mvula, K. Hildenbrand, C. von Sonntag, *Chem. Eur. J.* **10**, 440 (2004).
34. For such a proton migration process with a PNP-Ir(I) complex, see (*35*).
35. E. Ben-Ari, G. Leitus, L. J. W. Shimon, D. Milstein, *J. Am. Chem. Soc.* **128**, 15390 (2006).

36. This project was supported by the Israel Science Foundation, the Petroleum Research Fund administered by the American Chemical Society, the programme for Deutsch-Israelische Partnerschaft, and the Helen and Martin Kimmel Center for Molecular Design. S.W.K. thanks the Humboldt Foundation for a Feodor Lynen Postdoctoral Fellowship. D.M. holds the Israel Matz Professorial Chair of Organic Chemistry. We thank M. Feller for fruitful discussions, A. Tishbee and R. Kramer for performing mass spectroscopy, A. Khenkin and H. Weissman for carrying out GC-MS and GC measurements, and E. Shirman for photon flux measurements. Structural parameters for ***2.nH$_2$O*** are available free of charge from the Cambridge Crystallographic Data Centre under identification number CCDC-681749.

Supporting Online Material

www.sciencemag.org/cgi/content/full/324/5923/74/DC1
Materials and Methods
SOM Text
Figs. S1 to S9
Tables S1 to S5
References

17 November 2008; accepted 13 February 2009
10.1126/science.1168600

chem 651
final presentation
Zhou Qi

Consecutive Thermal H_2 and Light-Induced O_2 Evolution from Water Promoted by a Metal Complex

Stephan W. Kohl[a], Lew Weiner[b], Leonid Schwartsburd[a], Lenoid Konstantinovski[b], Linda J. W. Shimon[b], Yehoshoa Ben David[a], Mark A. Iron[b], David Milstein[a].

a Department of organic chemistry, The Weizmann Instituteof Science, Rehovot 76100, Israel. b Department of chemical research support, The Weizmann Instituteof Science, Rehovot 76100, Israel.

E-mail: david.milstein@weizmann.ac.il

ABSTRACT By using a structurally well-defined Ru(II) pincer complex, water had been successfully decomposed into H_2 and O_2 in sequence. Experimental data show O_2 releasing through an intramolecular procedure on the single metal complex center.

Global energy demanding is facing huge increase for the next decades. As conservative speculation, the total amount of global energy need will be doubled in the mid 21 century, while tripled by 2100 [1]. In light of this context, looking for more reliable energy source with enormous storage would be an imperative mission. As both the academic and industrial divisions longer endeavored research domain, more effective transfer, store and utilize solar energy has been pushing steady toward our final goal – replace our energy demand by the endlessly solar power.

As a tutorial instruction, Richard Eisenberg briefly described three normal strategies of utilizing solar energy [2]. Our first principle is to transfer light into electronic energy, photovoltaic devices, for example. The second one is kind of indirect pathway; however, still constitute an important force of modern energy supply market – the bio-fuels made from naturally photosynthesis products. For the last strategy, and most studied in chemistry labs, is how to split water molecules into O_2 and H_2.

Chemically speaking, water molecule, with CAS register Number 7732-18-5, is one of the most simplest compounds consist of only two H-atoms and one O-atom. The O-H bond energy is about119 kcal/mol. When electronically dissociation of water happens, the following two half-reactions happened: cathode, $4\ H^+ + 4\ e^- = 2\ H_2$, $E_c = 0\ V - 0.059\ V$ pH (NHE, Normal Hydrogen Electrode); Anode, $O_2 + 4\ e^- + 4\ H^+ = 2\ H_2O$, $E_a = 1.23\ V - 0.059\ V$ pH (NHE). Practically, the second half reaction is much more challenge than the first one as it requires simultaneously breaking down four O-H bond with four electrons transfer.

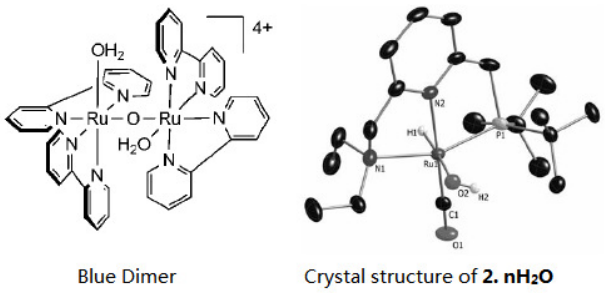

Figure 1. structure of Blue dimer and Crystal 2.nH_2O

In order to solve that problem, large volume of study has been operated. The most importance discovery should be the so-called "blue dimer" [3] (cis, cis-$[(bpy)_2(H_2O)Ru^{III}ORu^{III}(OH_2)(bpy)_2]^{4+}$, bpy = 2,2′-bipyridine, Figure 1). Even these kind of d^5-Ru(III) species showed increased turnover number of O_2 evolution reaction, the mechanism of how O_2 been released are still elusive. Besides, for sake of continuously splitting water molecule, the two half reaction has to be combined together, otherwise an equivalent reductant or oxidant will be necessity.

Here, a striking work [4] from Milstein's group state the first time of consecutive H_2 and O_2 generation promoted by Ru-pincer liangd complexes. This work is done by a straightforwardly observation and certification process. However, through the authors' detailed analysis, a unimolecular O-O bond formation within a single metal complex can be deduced.

Basically, this work has some precursor research concerning the ability of non-aromatic pincer Ru(II)-PNN complex **1**. In the author's former works, compound **1** was found to be able to help constructing esters and amides from alcohols and amine dehydrogenative coupling [5] (Scheme 1). So, what will happen if putting together two equivalent water molecules?

Scheme 1. Precedent work by Milstein's group

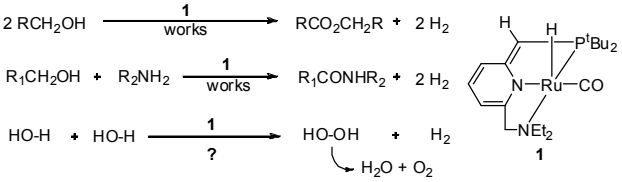

Step 1: Water activation by non-aromatic Ru(II) complexes **1**.

Experimental data shows the non-aromatic pincer Ru(II) complex**1** would undergo a special way of react with H_2O (Scheme 2). The OH group will add trans to hydride in compound **1**, while H-atom add to the ligand side chain to form an aromatic trident ligand, see compound **2**. Structure of 2 can be further confirmed by the product 2-D and 2-O[17] which obtained by reaction **1** with D_2O and H_2O[17], respectively. Feature of this process is the center metal remain to be Ru(II). Besides, x-ray diffraction analysis of compound **2. nH$_2$O** crystal demonstrate a distorted octahedral coordination geometry, implicit a chiral metal complex (Figure 1).

Step 2: Thermal H_2 generation. Heat **2** in water would generate H_2 gas at 45% percent yield after three days. This reaction may work through hydrolysis process of Metal hydride which renders H_2 and Metal hydroxide (Scheme 3). Similar reaction also happened between **2** and N_2O. Here, by NMR analysis, both two

tetra-butyl and ethyl group in the ligand arm show different chemical shifts, thus, the real geometry of **3** should be chiral which only possible when the two OH groups adopts cis position.

Scheme 2. H_2O activation by Ru^{II} complex **1**

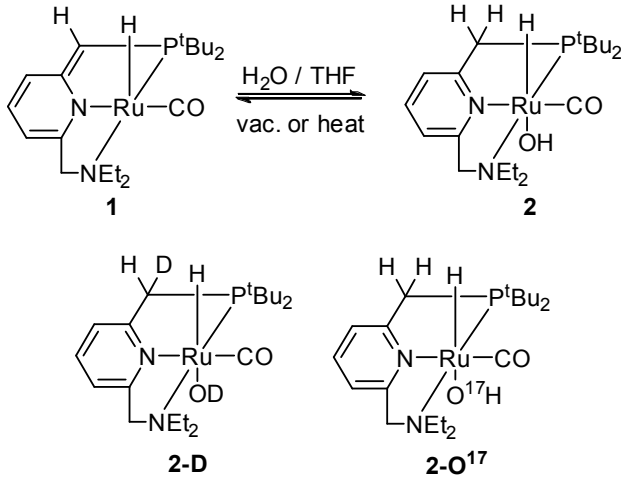

Scheme 3. Thermal Generation of H_2 from complex 2 and water

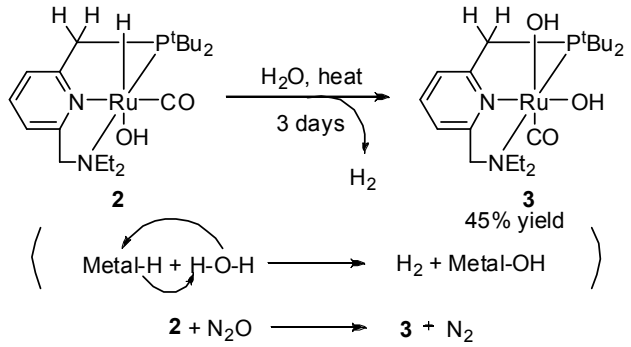

Step 3: photochemical induced O_2. After obtain cis-dihydroxyl Ru(II) complex **3** (Scheme 4), the author expose it to light. When argon flow was used upon the reaction, 49% conversion of **3** can be achieved. Here, the author utilize isotope labeling experiment to detect where O_2 was formed. By analysis the ratio of different allotrope of oxygen gas, the only reasonable explanation is an intramolecular O-O bond formation pathway, which never been envisioned before (Scheme 5). Analyzing the composition of O_2 collected after expose labeled species to light, the author found that major product of intramolecular O-O formation has been obtained in both cases. Moreover, in the cross over experiment, only tiny amount of $^{34}O_2$ was detected which further support the intramolecular O_2 evolution process.

Scheme 4. Photochemical evolution of O_2

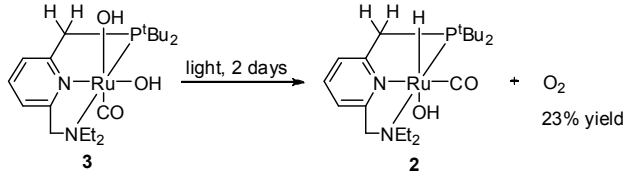

Finally, the three steps mentioned about composed the following postulated mechanism of this water splitting reaction (Scheme 6). As we can seen, after releasing H_2 by gas, O_2 evolution happened in presence of light (320-400 nm).

In addition to the geometry analysis, the author also applied the metal-to-ligand charge transfer (MLCT) analysis in determine the way of O_2 releasing procedure, both of which are connect to what we learned on the course.

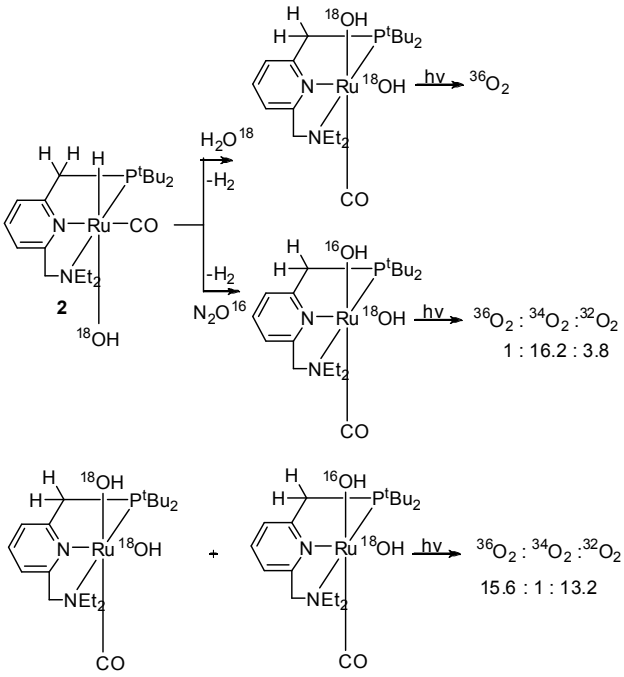

Scheme 5. Isotope labeling experiments for studying O_2 generation process

Scheme 6. Proposed Mechanism

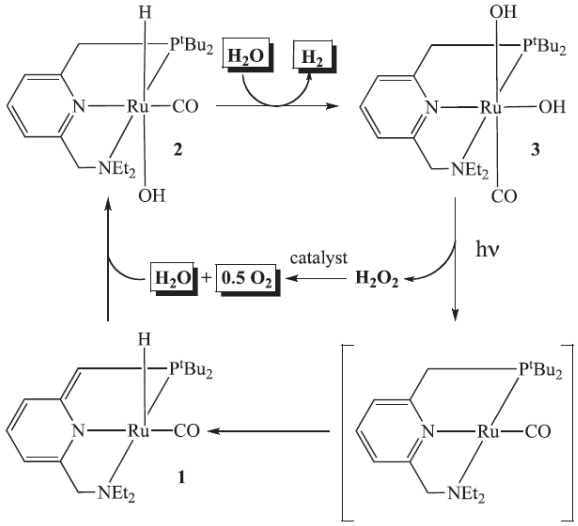

This work greatly induced people's interest in figuring out the detailed mechanism of the reaction. Michael B. Hall and Fang Wei Hai's groups published their DFT calculation result toward the reaction pathway soon afterward [6a-6b], both of which give some interesting supplementary comment based on their calculations, for example, endothermic H_2O_2 formation (6b). On

the other hand, deeper research into the ligand dearomatization-aromatization effect had also been calculated by Kazunari Yoshizawa group [6c].

To sum up, Kohl's work rendered us with both novel ideas of water splitting and challenges. Through this work, we can see that by appropriate ligand design, we can avoid using stochimetric reductant or oxidant to combining the two half reactions together and using different strategy in H_2 and O_2 evolution. Moreover, experimental analysis such as NMR (^{1}H, ^{13}C, ^{17}O, ^{31}P, 2-dimentional), x-ray Diffraction, GC, GC-MS, IR, UV-VIS, EPR (electron paramagnetic resonance spectroscopy) have all turn out to be the tools. It hints that we should consider more about how to greatly utilize the gears at hand.

However, this work still suffered some shortcomings, like low yield and long reaction time (5 days for a complete reaction cycle). In addition to that, how to find a more effective catalyst to lower the catalyst loading would be a potential breakthrough point of this type of reaction.

References

(1) Cook, T. R.; Dogutan, D. K.; Reece, S. Y.; Surendranath, Y.; Teets, T. S.; Nocera, D. G. *Chem. Rev.* **2010**, 110, 6474-6502.
(2) Eisenberg, R. *Science*, **2009**, 324, 44-45.
(3) Gersten, S. W.; Samuels, G. J.; Meyer, T. J. *J. Am. Chem. Soc.* **1982**, 104, 4030-4032.
(4) Kohl, S. W.; Weiner, L.; Schwartsburd, L.; Konstantinovski, L.; Shimon, L. J.; Ben-David, Y.; Iron, M. A.; Milstein, D. *Science*, **2009**, 324, 74-77.
(5) (a) Zhang, J.; Leitus, G.; Ben-David, Y.; Milstein, D. *J. Am. Chem. Soc.* **2005**, *127*, 10840-10841. (b) Gunanathan, C., Ben-David, Y.; Milstein, D. *Science*, **2007**, 317, 790-792.
(6) (a)Yang, X. Z.; Hall, M. B.; *J. Am. Chem. Soc.* **2010**, 132, 120-130. (b) Yue, C.; Fang, W. H. *J. Phys. Chem. A*, **2010**, 114, 10334-10338. (c) Li, J.; Shiota, Y., Yoshizawa, K. *J. Am. Chem. Soc.* **2009**, 131, 13584-13585.

Electrocatalytic CO_2 Conversion to Oxalate by a Copper Complex

Raja Angamuthu,[1] Philip Byers,[1] Martin Lutz,[2] Anthony L. Spek,[2] Elisabeth Bouwman[1]*

Global warming concern has dramatically increased interest in using CO_2 as a feedstock for preparation of value-added compounds, thereby helping to reduce its atmospheric concentration. Here, we describe a dinuclear copper(I) complex that is oxidized in air by CO_2 rather than O_2; the product is a tetranuclear copper(II) complex containing two bridging CO_2-derived oxalate groups. Treatment of the copper(II) oxalate complex in acetonitrile with a soluble lithium salt results in quantitative precipitation of lithium oxalate. The copper(II) complex can then be nearly quantitatively electrochemically reduced at a relatively accessible potential, regenerating the initial dinuclear copper(I) compound. Preliminary results demonstrate six turnovers (producing 12 equivalents of oxalate) during 7 hours of catalysis at an applied potential of −0.03 volts versus the normal hydrogen electrode.

Research toward carbon dioxide fixation enjoys much attention at present, as a result of the alarming reports that link global warming and its potentially devastating effects with the steadily increasing concentration of CO_2 in the atmosphere. Chemical activation of carbon dioxide could help to reduce its concentration in the atmosphere while at the same time exploiting it as a carbon feedstock for the production of useful organic compounds (*1*–*5*). Transition-metal complexes, especially of copper and zinc (*6*, *7*), as well as simple salts such as lithium hydroxide monohydrate and soda-lime (mixture of sodium and calcium hydroxides) are well known for their assistance in the stoichiometric transformation of carbon dioxide to carbonate salts (*8*–*17*). Mixtures of glycol and amines (glycol-amine) as well as coordination complexes of polyamines have been reported to bind CO_2 reversibly through the formation of carbamates (*8*, *15*, *17*, *18*). In contrast, reductive conversion of CO_2 into useful products of industrial significance such as formaldehyde, formic acid, methanol, or oxalic acid has proven more challenging to achieve selectively (*19*, *20*).

The one-electron reduction of CO_2 into the $CO_2^{\bullet-}$ radical anion occurs at potentials as high as –1.97 V versus NHE (normal hydrogen electrode) in *N*,*N*-dimethylformamide, and the $CO_2^{\bullet-}$ may further react to form CO, carbonate, formate, or oxalate (*19*–*21*). Selective production of oxalate would be much preferred because dimethyl oxalate is a useful feedstock, for example, for the production of methyl glycolate. The assistance of transition-metal complexes appears mandatory to direct the reactivity of the $CO_2^{\bullet-}$ radical anion toward a specific product, in addition to optimizing electrochemical parameters such as current density. Moreover, the inner-sphere electron-transfer mechanisms that proceed with most transition metal systems result in less-negative reduction potentials, which may improve overall thermodynamic favorability of the reduction, assuming there is an accessible way to liberate the product after the electron-transfer reaction (*20*). Reductive coupling of CO_2 to form the oxalate dianion has been accomplished by electrochemical methods, including outer-sphere electron transfer using mercury or lead electrodes and inner-sphere electron transfer using transition-metal complexes or anion radicals of aromatic hydrocarbons, esters, and nitriles as electrocatalysts (*20*–*22*). Mechanistic understanding of the metal-catalyzed reduction of CO_2 to C_2 or C_3 fragments is also highly relevant for an improved understanding of the natural photosynthetic transformation of atmospheric CO_2 to functionalized C_3 molecules (3-phosphoglycerate).

We herein report a copper complex, which spontaneously captures and reductively couples CO_2 from the air selectively, yielding an oxalate-bridged copper(II) tetramer in acetonitrile solution. Moreover, we have found that this copper system can be used repeatedly as a catalyst for the reductive coupling of CO_2 to oxalate upon electrochemical reduction. The reduction of the copper(II) complex occurs at a readily accessible potential that is nearly 2 V less negative than that required for outer-sphere reduction of CO_2 to $CO_2^{\bullet-}$.

The ligand HL [*N*-(2-mercaptopropyl)-*N*,*N*-bis(2-pyridylmethyl)amine] was designed for the synthesis of biomimetic models for nickel-containing superoxide dismutase. In addition to studies with nickel salts, reactions were performed with copper and zinc for comparison. Upon mixing of equimolar amounts of $Cu(acac)_2$ (Hacac is acetylacetone), the ligand HL, and HBF_4 in acetonitrile at room temperature, we obtained a yellow-colored solution, in which as expected the thiolate-containing ligand was oxidized by the copper(II) ion. The solution was analyzed with positive-ion electrospray ionization mass spectroscopy (ESI-MS); a prominent signal at mass/charge (*m*/*z*) ratio of 335.91 showed an isotopic distribution envelope matching that calculated for the dinuclear copper(I) complex $\mathbf{[1]}^{2+}$ (Fig. 1) (*23*). This complex $\mathbf{[1]}^{2+}$ can also be synthesized by the reaction of the preoxidized disulfide ligand with two equivalents of $[Cu(CH_3CN)_4]BF_4$ in dry acetonitrile. This yellow-colored solution turned greenish-blue upon exposure to air; over the course of 3 days crystals formed, which we isolated in 72% yield and analyzed by x-ray diffraction. We observed a tetranuclear copper(II) structure $[Cu^{II}_2(L\text{-}L)(\mu\text{-oxalato-}\kappa^4O^1,O^2:O^3,O^4)]_2(BF_4)_4$ {$\mathbf{[2]}(BF_4)_4$, Fig. 1}, with bridging oxalate anions that must originate from CO_2 in the air. A positive-ion ESI-MS spectrum acquired from the acetonitrile solution is consistent with this molecular struc-

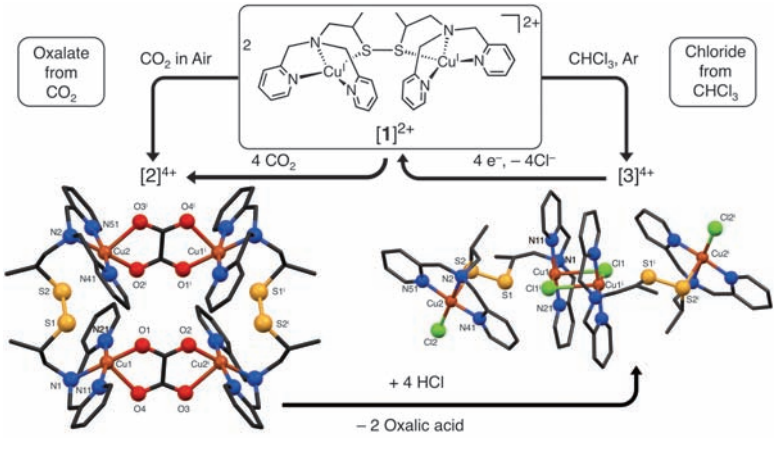

Fig. 1. Schematic overview of the formation and reactivity of the complexes $\mathbf{[1]}^{2+}$, $\mathbf{[2]}^{4+}$, and $\mathbf{[3]}^{4+}$. Cu, brown; N, blue; S, yellow; O, red; Cl, green; C, black. BF_4 anions, solvent molecules, and hydrogen atoms are omitted for clarity. Selected (average) bond lengths (Å) for $\mathbf{[2]}^{4+}$: Cu–O_{eq}, 1.963(2); Cu–O_{ax}, 2.283(2); Cu–N_{py}, 1.991(2); Cu–N_{amine}, 2.026(2); S1–S2, 2.0423(16); Cu1···S1, 2.9837(12); Cu2···S2, 2.9731(12); Cu1···Cu2, 5.3205(6); Cu1···Cu2^{i}, 5.4295(6). Selected (average) bond lengths (Å) for $\mathbf{[3]}^{4+}$: Cu1–Cl1^{i} 2.2479(6); Cu2–Cl2 2.2440(7); Cu1–Cl1 2.8589(6); Cu–N_{py}, 1.984(1); Cu–N_{amine}, 2.052(2); S1–S2, 2.0388(11); Cu1···S1, 3.0036(9); Cu2–S2, 2.7343(7); Cu1···Cu1^{i}, 3.5677(5); Cu1···Cu2, 6.1248(4). Symmetry operation i; $1-x$, $1-y$, $1-z$. Estimated standard deviations in the last digits are given in parentheses. Further details are provided in (*23*).

[1]Leiden Institute of Chemistry, Gorlaeus Laboratories, Leiden University, Post Office Box 9502, 2300 RA Leiden, Netherlands. [2]Bijvoet Center for Biomolecular Research, Crystal and Structural Chemistry, Utrecht University, Padualaan 8, 3584 CH Utrecht, Netherlands.

*To whom correspondence should be addressed. E-mail: bouwman@chem.leidenuniv.nl

ture, showing a prominent signal at *m/z* of 379.35 (figs. S9 and S10). We thus found that the initial Cu(I) complex is oxidized by CO_2 rather than O_2. Indeed, purging carbon dioxide into a solution of complex $[1]^{2+}$ results in the formation of the tetranuclear oxalate-bridged complex $[2]^{4+}$, which was fully characterized by Fourier transform infrared spectroscopy (FT-IR), ESI-MS, and elemental analysis. That carbon dioxide is the origin of the oxalate dianion was proven with the use of $^{13}CO_2$; the resulting copper(II) complex showed a signal at *m/z* of 381.06 (fig. S11). The reaction of $[1]^{2+}$ in an O_2 atmosphere under strict exclusion of CO_2 resulted in a deep green solution containing a copper(II) compound with a molecular ion peak at *m/z* = 361.16 in positive ion ESI-MS that is consistent with the expected dihydroxo complex of molecular formula $[Cu^{II}(L\text{-}L)Cu^{II}(\mu\text{-}OH)_2(H_2O)]^{2+}$(fig. S12).

In the solid state, $[2]^{4+}$ consists of a cyclic centrosymmetric dimer of two dinuclear moieties bridged by two oxalato dianions (fig. S13). Each dinuclear moiety consists of two crystallographically independent copper(II) ions. The two copper(II) ions within the asymmetric unit bind to the same disulfide ligand and are separated by 5.3205 ± 0.0006 [5.3205(6)] Å. The copper ions are situated in square-pyramidal environments, with the three nitrogen donors of the meridionally coordinated dipicolylamine unit occupying three corners of the basal plane. One of the oxygens from the bridging oxalato dianion is situated at the fourth corner of the basal plane, with another oxygen from the same oxalato dianion occupying the apical position. However, for both copper ions one of the disulfide sulfur atoms can be regarded as a sixth ligand at meaningful axial distances of 2.9837(12) and 2.9731(12) Å. (Further parameters are provided in table S1.)

In an attempt to crystallize the original complex $[1]^{2+}$, chloroform was let to diffuse into the initial reaction mixture containing the copper(I) complex in an argon atmosphere. Interestingly, this yielded the unexpected tetranuclear compound $[ClCu^{II}(L\text{-}L)Cu^{II}(\mu\text{-}Cl)]_2(BF_4)_4$ {$[3](BF_4)_4$, Fig. 1} with bridging and terminal chloride anions that can only originate from chloroform (*24*). The solid-state structure of $[3]^{4+}$ was obtained by x-ray diffraction from a blue crystal of $[3](BF_4)_4$. The molecular structure of $[3]^{4+}$ is confirmed by a positive-ion ESI-MS spectrum of the compound acquired from acetonitrile solution, which shows a prominent signal at *m/z* = 370.71 (figs. S14 and S15). Complex $[3]^{4+}$ is a linear centrosymmetric dimer of two dinuclear moieties bridged by two chloride anions (figs. S16 and S17). The two copper(II) ions within the asymmetric unit are bound to the same disulfide ligand and are separated by 6.1248(4) Å. The copper ions in $[3]^{4+}$ are situated in pentacoordinate environments resembling those in complex $[2]^{4+}$; the thioether sulfur and the chloride donors replace the oxalato oxygen donors in $[2]^{4+}$.

Inspired by this finding, we explored whether complex $[2]^{4+}$ could be converted to this chloride complex $[3]^{4+}$ by treatment with HCl, in the process liberating the CO_2-derived oxalic acid.

Addition of four equivalents of hydrochloric acid to an acetonitrile solution of $[2](BF_4)_4$ indeed leads to elimination of oxalic acid with concurrent formation of $[3](BF_4)_4$ as confirmed by ESI-MS and elemental analysis. The electrochemical reduction of $[3](BF_4)_4$ occurs at the cathodic peak potential (E_{pc}) of +0.06 V versus NHE (fig. S18), producing a copper(I) complex that selectively produces complex $[2]^{4+}$ upon reaction with CO_2. This result stimulated us to explore the possibility of using the copper/disulfide-ligand system as an electrocatalyst for the selective reduction of CO_2.

To that end, we undertook electrochemical reduction of complex $[3]^{4+}$ by using controlled potential coulometry and monitored the process by using electronic absorption spectroscopy. The copper complex $[3](BF_4)_4$ (0.9 g, 0.5 mmol) was dissolved in 100 ml of 0.1 M tetrabutylammonium hexafluoridophosphate in acetonitrile; the solution was then reduced at +0.03 V versus NHE. A current drop was observed after 195 C of charge was passed, the quantity expected for a one-electron reduction of each copper ion. The disappearance of the characteristic *d-d* transition band (~670 nm) of $[3]^{4+}$ during electrolysis confirmed the formation of a copper(I) species (fig. S19). The resulting yellow-colored solution was shown by ESI-MS to contain the dinuclear copper(I) complex $[1]^{2+}$ (fig. S20). The cyclic voltammogram of this solution showed a reversible oxidation process at the anodic peak potential (E_{pa}) of +0.81 V versus NHE (fig. S21).

Bubbling carbon dioxide into this solution turned the color greenish-blue, indicating the formation of complex $[2]^{4+}$ as confirmed by ESI-MS analysis of the solution. The cyclic voltammogram of $[2]^{4+}$ produced in this reaction sequence was identical to that of the independently synthesized and isolated $[2]^{4+}$ and showed an irreversible reduction process at –0.03 V versus NHE (fig. S22). The bulk electrolysis experiment was then repeated under the same conditions but with use of lithium perchlorate as the supporting electrolyte in a CO_2-saturated acetonitrile solution. These conditions resulted in the precipitation of lithium oxalate as the generated copper(I) complex spontaneously reacted with the CO_2 available in the solution to form oxalate (fig. S23). In order to quantify the selectivity of our electrocatalyst, we halted electrolysis after passing 195 C of charge (the charge expected for a one-electron reduction of each copper ion), purged the solution with CO_2, and removed the lithium oxalate precipitate by filtration under an argon atmosphere. The 24-mg (0.24-mmol) yield of lithium oxalate [as confirmed by ESI-MS spectrometry, nuclear magnetic resonance (NMR), and FT-IR spectroscopy, figs. S24 and S25] corresponded to nearly quantitative current efficiency (96%) for formation of the desired product. The remaining blue-colored solution was shown to contain the dinuclear copper(II) complex $[(CH_3CN)Cu^{II}(L\text{-}L)Cu^{II}(CH_3CN)]^{4+}$ $[4]^{4+}$ as characterized by ESI-MS spectrometry (fig. S26). We proceeded to saturate this solution with argon to remove the remaining CO_2 and then subjected it to a second electrolysis run; 185 C of charge was consumed before the current dropped, indicating regeneration of nearly 95% of the copper(I) complex.

Fig. 2. Formation of $[4]^{4+}$ from $[2]^{4+}$ or $[3]^{4+}$.

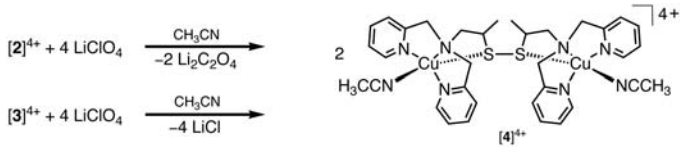

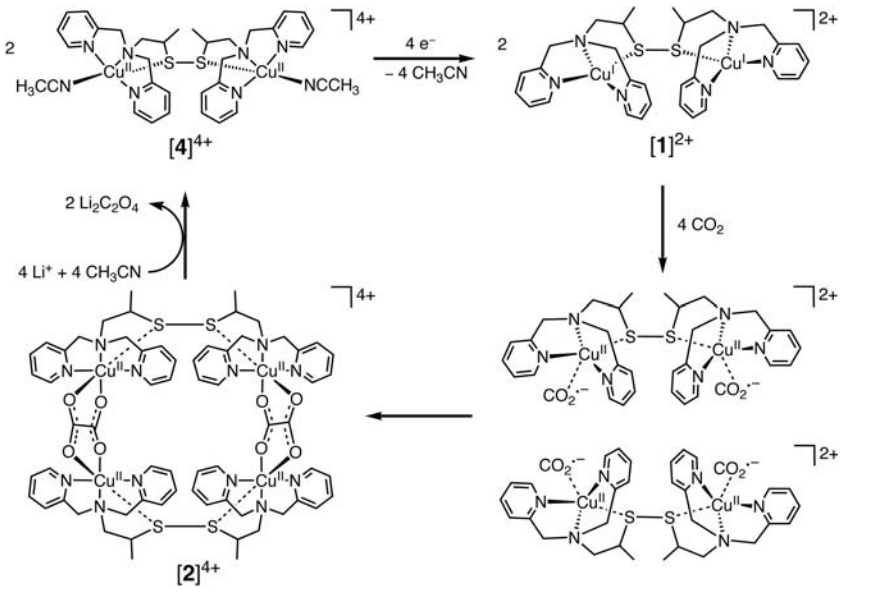

Fig. 3. Proposed electrocatalytic cycle for oxalate formation.

Both complexes $[2]^{4+}$ and $[3]^{4+}$ upon mixing with $LiClO_4$ in acetonitrile yield $[4]^{4+}$ as confirmed by ESI-MS spectrometry (Fig. 2 and figs. S27 and S28). Therefore, in another attempt to use the complex $[2]^{4+}$ as an electrocatalyst in this reaction, the electrochemical cell containing an acetonitrile solution of complex $[2]^{4+}$ and lithium perchlorate (as supporting electrolyte) was stirred to precipitate all the available oxalate. Then the solution was electrolyzed at –0.03 V versus NHE with continuous purging of CO_2. The consumption of current continued linearly for more than 3.3 hours, consuming three equivalents of charge (12 electrons) per four copper ions, with concurrent crystallization of lithium oxalate. Thereafter, the rate of the reaction gradually decreased as the crystallized lithium oxalate started to cover the electrode surface, thereby hampering electron transfer (fig. S29). In total, the electrocatalysis could be extended for more than 7 hours, with consumption of 6 equivalents of charge (24 electrons) and generating 12 equivalents of oxalate per molecule of $[2]^{4+}$.

We have thus devised an electrocatalytic system based on a copper coordination compound that is able to activate and convert CO_2 selectively into oxalate at readily accessible potentials, in the simple but very effective catalytic cycle shown in Fig. 3. The finding that a copper(I) system is oxidized by CO_2 rather than O_2 implies that the selective binding of CO_2 to the copper(I) ions offers a low-energy pathway for the formation of the $CO_2^{\bullet-}$ radical anion. The copper(II) oxalate complex $[2]^{4+}$ is thermodynamically favored; the binding of CO_2 to the Cu(I) centers in $[1]^{2+}$ and the formation of oxalate appears to be highly selective and relatively rapid. Because of the low solubility of lithium oxalate in acetonitrile, the release of the oxalate dianion from $[2]^{4+}$ in the presence of lithium perchlorate is instantaneous, generating the complex $[4]^{4+}$. Therefore, for the current system the electrocatalytic reduction of the copper(II) ion to copper(I) appears to be rate-limiting. The precipitation of the lithium oxalate formed during the reaction onto the electrode surface hampers efficient electron transfer. Tuning the redox potential of the copper complex by altering the ligand structure with a variety of substituents, immobilization of the complex onto the electrode surface, and improved methods for the removal of oxalate may result in improved efficiency of the catalytic system. We believe that our studies will instigate further development of coordination complexes for catalytic CO_2 sequestration, its selective conversion and use as fuels such as methanol or as feedstock in the synthesis of useful organic compounds.

References and Notes

1. T. Reda, C. M. Plugge, N. J. Abram, J. Hirst, *Proc. Natl. Acad. Sci. U.S.A.* **105**, 10654 (2008).
2. M. Aresta, A. Dibenedetto, *Dalton Trans.* **2007**, 2975 (2007).
3. D. P. Schrag, *Science* **315**, 812 (2007).
4. T. Sakakura, J. C. Choi, H. Yasuda, *Chem. Rev.* **107**, 2365 (2007).
5. C. S. Song, *Catal. Today* **115**, 2 (2006).
6. S. Youngme, N. Chaichit, P. Kongsaeree, G. A. van Albada, J. Reedijk, *Inorg. Chim. Acta* **324**, 232 (2001).
7. G. A. van Albada, I. Mutikainen, O. Roubeau, U. Turpeinen, J. Reedijk, *Inorg. Chim. Acta* **331**, 208 (2002).
8. J. Notni, S. Schenk, H. Görls, H. Breitzke, E. Anders, *Inorg. Chem.* **47**, 1382 (2008).
9. B. Sarkar, B. J. Liaw, C. S. Fang, C. W. Liu, *Inorg. Chem.* **47**, 2777 (2008).
10. B. Verdejo *et al.*, *Eur. J. Inorg. Chem.* **2008**, 84 (2008).
11. J. M. Chen, W. Wei, X. L. Feng, T. B. Lu, *Chem. Asian J.* **2**, 710 (2007).
12. A. Company *et al.*, *Inorg. Chem.* **46**, 9098 (2007).
13. R. P. Doyle *et al.*, *Dalton Trans.* **2007**, 5140 (2007).
14. M. Fondo, A. M. García-Deibe, N. Ocampo, J. Sanmartín, M. R. Bermejo, *Dalton Trans.* **2007**, 414 (2007).
15. B. Verdejo *et al.*, *Inorg. Chem.* **45**, 3803 (2006).
16. R. Johansson, M. Jarenmark, A. F. Wendt, *Organometallics* **24**, 4500 (2005).
17. E. García-España, P. Gaviña, J. Latorre, C. Soriano, B. A. Verdejo, *J. Am. Chem. Soc.* **126**, 5082 (2004).
18. H. J. Himmel, *Eur. J. Inorg. Chem.* **2007**, 675 (2007).
19. E. E. Benson, C. P. Kubiak, A. J. Sathrum, J. M. Smieja, *Chem. Soc. Rev.* **38**, 89 (2009).
20. J. M. Savéant, *Chem. Rev.* **108**, 2348 (2008).
21. C. Amatore, J. M. Savéant, *J. Am. Chem. Soc.* **103**, 5021 (1981).
22. Y. Kushi, H. Nagao, T. Nishioka, K. Isobe, K. Tanaka, *J. Chem. Soc. Chem. Commun.* **1995**, 1223 (1995).
23. Synthesis and characterization details are provided as supporting material on *Science* Online.
24. A similar reactivity of coordination complexes with chloroform has been observed and reported before; see, for example, (*25*).
25. I. M. Angulo *et al.*, *Eur. J. Inorg. Chem.* **2001**, 1465 (2001).

26. This work was supported by the Leiden Institute of Chemistry. X-ray crystallographic work was supported (M.L. and A.L.S.) by the Council for the Chemical Sciences of The Netherlands Organization for Scientific Research (CW-NWO). J. Reedijk and M. T. M. Koper are gratefully acknowledged for stimulating discussions. P.B. (Ithaca College, New York) was involved in the project through a summer exchange program. Crystallographic data for $[2](BF_4)_4$ and $[3](BF_4)_4$ have been deposited with the Cambridge Crystallographic Data Center under reference numbers 717726 and 717727.

Supporting Online Material

www.sciencemag.org/cgi/content/full/327/5963/313/DC1
Materials and Methods
SOM Text
Figs. S1 to S30
Tables S1 and S2
References

19 June 2009; accepted 25 November 2009
10.1126/science.1177981

Ligand-Enabled Reactivity and Selectivity in a Synthetically Versatile Aryl C–H Olefination

Dong-Hui Wang, Keary M. Engle, Bing-Feng Shi, Jin-Quan Yu*

The Mizoroki-Heck reaction, which couples aryl halides with olefins, has been widely used to stitch together the carbogenic cores of numerous complex organic molecules. Given that the position-selective introduction of a halide onto an arene is not always straightforward, direct olefination of aryl carbon-hydrogen (C–H) bonds would obviate the inefficiencies associated with generating halide precursors or their equivalents. However, methods for carrying out such a reaction have suffered from narrow substrate scope and low positional selectivity. We report an operationally simple, atom-economical, carboxylate-directed Pd(II)-catalyzed C–H olefination reaction with phenylacetic acid and 3-phenylpropionic acid substrates, using oxygen at atmospheric pressure as the oxidant. The positional selectivity can be tuned by introducing amino acid derivatives as ligands. We demonstrate the versatility of the method through direct elaboration of commercial drug scaffolds and efficient syntheses of 2-tetralone and naphthoic acid natural product cores.

Unactivated carbon–hydrogen (C–H) bonds are among the simplest and most common structural motifs in naturally occurring organic molecules, and, as such, they are ideal targets for chemical transformations. Although C–H bonds are generally unreactive, during the past several decades transition metal catalysis has emerged as an effective means of converting unactivated C–H bonds into carbon–heteroatom and carbon–carbon (C–C) bonds (*1*–*5*). This technology has proven to be valuable in natural products synthesis, where several distinct C–H functionalization strategies have been exploited (*6*–*12*).

Traditionally, C–C bonds between aryl and olefinic fragments have been forged through the Pd-catalyzed Mizoroki-Heck reaction, which couples aryl halides or triflates with olefins (Fig. 1A). Considering the prominence of this transformation in organic synthesis (*13*), Pd-catalyzed olefination of aryl C–H bonds has the potential to emerge as a powerful platform for more direct access to carbogenic cores of complex molecules (Fig. 1, A and E), particularly in cases in which the position-selective introduction of a halide is problematic. However, the few pioneering examples of Pd-catalyzed C–H olefination in total synthesis to date are restricted to specific cases, generally including electron-rich heterocycles, such as indoles and pyrroles, and/or

Scripps Research Institute, 10550 North Torrey Pines Road, La Jolla, CA 92037, USA.

*To whom correspondence should be addressed. E-mail: yu200@scripps.edu

A Review of Electrocatalytic Conversion of CO_2 to Oxalate by a Copper Complex.

Tian Qiu

Department of Chemistry and Biochemistry, University of Delaware

RECEIVED DATE 11/24/2010; Email Address: tianqiu@udel.edu

ABSTRACT Worldwide green house effect caused by the significant release of carbon dioxide owning to fossil fuel combustion demands effective measures to lower down the concentration of carbon dioxide in our living environment. A considerable researches focusing on the conversion of carbon dioxide has been done. This article generally reviews several earlier trials of carbon dioxide conversion and introduces a new electrocatalytic way to reduce carbon dioxide to oxalate using a copper/disulfide complex. The reduction process is highly selective, effective and costs fewer energy input compared to most process reported before. Cyclic voltammogram is used to study the reduction qualitatively and potential coulometry is use to study the reduction quantitatively.

The tremendous emission of carbon dioxide (CO_2) due to the major reliance of fossil fuel combustion causes the global warming during the past few decades. Capturing CO_2 from form the atmosphere and then exploiting it as stock chemicals is a good strategy to mitigate the climate change while at the same time generating fuel resources. The biggest obstacle to transform CO_2 into useful chemicals is its low energy level as raw material[1-4]. Extensive efforts to activate CO_2 chemically have been made. Few research groups use transition metal complexes, especially copper[5-12], zinc[11,13,14], and nickel[15] to convert CO_2 to carbonate (CO_3^{2-}) salts, which is a helpful way to undergo CO_2 fixation. One group had synthesized a Pd complex which is reactive toward CO_2 insertion[16]. A carbamylation produced by atmospheric CO_2 assisted by a complexed metal ion and amino groups in the environment[17] and a formation of carbamate molecules by reaction of amides of main group elements (such as Li or Mg) with CO_2 [18] are also reported.

Compared to stoichiometrically binding CO_2, reducing CO_2 to industrial significant products such as CO, methanol, formaldehyde, formic acid and oxalic acid is more meaningful but challenging. People tried to perform direct electrochemical reduction of CO_2 on various metal elctrodes[19]. This is, however, considered not a practical strategy. Because according to the equilibrium potentials in water for a series of CO_2 reductions and their variations with pH shown in Figure 1, the reduction in neutral system could happen only if extra electrical energy is put in. Furthermore, the fact is even more disappointing since the reduction process of CO_2 requires to form $CO_2^{\bullet-}$ radical anion as an early step, and the standard potential for the formation of the anion radical $CO_2^{\bullet-}$ is -1.90 V vs SCE in water, which means to overcome a great overpotential owing to the kinetic barrier caused by the large HOMO-LUMO gap in the molecule.[19] The electrochemical reduction of CO_2 catalyzed by metal complexes has attracted continuous attention over past decades because they help to mediate CO_2 reduction at less negative potentials[20]. From Figure.1, it is obvious that the reduction potential to CO and $HCOO^-$ is relatively less negative in a neutral system. So early researches are mainly focused on producing CO or $HCOO^-$ using transition metal, such as Rh[21], Co[22] and Ru[23] catalysts. Later growing interest is put in catalyzing the electrochemical reduction of CO_2 accompanied by C-C bond formation. Not only first row metal complexes are reported to be active electrocalaysts, for example following a series Ni-dppm-Ligand clusters have been studied[24], a PVA/$[Ni(dppm)_2Cl_2]$-coated Pt electrode was reported to electrocatalyse CO_2 reduction to oxalate at -1.1V vs SCE[25], but also a rhodium disulfide complex assisted oxalate formation at -1.50V vs SCE with a 60% current efficiency[26] and a iridium disulfide complex catalysed oxalate formation at -1.30V (vs Ag/AgCl) with a nearly 60% current efficiency.[27]

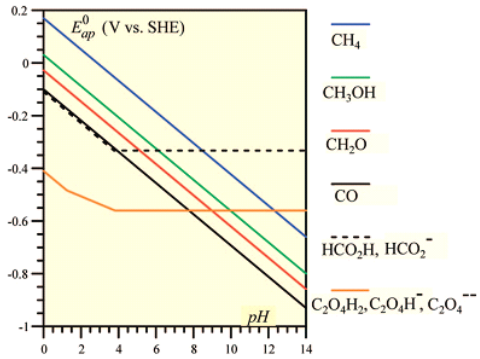

Figure 1. CO_2 reduction standard potential vs. pH .

The above listed researches were all done decades ago and facing a major problem of not able to lower the external electrical energy input during the reduction process to a readily accessible one. Nevertheless, several practical experiences are provided with respect to improve the favorability of the conversion of CO_2 into oxalate. First, the studies reveal that metal-disulfide clusters have good selectivity of producing oxalate in the electrochemical CO_2 reduction. This is probably due to the a strong interaction between S_2^{2-} and the metal centers, which tends to remove electron density from the S-S π^* antibonding orbitals toward metal d orbitals. This assists metals to dump electron density to CO_2 during redox process, meanwhile leading to a strengthened S-S bond which lowers the overall molecule energy after the electron transfer process. Second, the electrochemical processes all happen in anhydrous conditions to exclude H+ ions, which favors a further reduction of protonated $CO_2^{\bullet-}$ then forming products like formic acid instead of oxalate. Third, to drive the reduction reaction of CO_2 to oxalate forward, keeping removing the forming oxalate out of the reaction system is helpful. One can manage to do that

with the usage of chemicals that can produce oxalate containing precipitate.

In this paper, the group has developed a new electrocatalytic cycle of high selective CO_2 to oxalate reduction by a copper complex at much less negative potential than former researches. The reductive copper(I) complex $[1]^{2+}$(Figure. 2) was prepared by mixing of a HL ligand(Figure. 3) with one equivalent of $Cu(acac)_2$ (Hacac is acetylacetone) and HBF_4 in acetonitrile. $[1]^{2+}$ was characterized with positive-ion electrospray inoization mass spectroscopy (ESI-MS). When exposure the yielding solution to air, it spontaneously captures and reduce CO_2 while itself turning to a tetranuclear copper(II) structure$[2]^{4+}$(Figure. 2), which is fully characterized by Fourier transform infrared spectroscopy, ESI-MS and elemental analysis. The experiment to react the copper(I) complex with pure O_2 resulted in a totally different product from that carried out in the air, which confirms a better reactivity with CO_2 over O_2 of the compound. Adding four equivalents of hydrochloric acid to an acetonitrile solution of $[2](BF_4)_4$ results in another compound $[3](BF_4)_4$(Figure. 2) as confirmed by ESI-MS analysis and elemental analysis. The discovery of $[2]^{4+}$ will easily eliminate the oxalate can be attribute to an unexpected formation of crystal $[3]^{4+}$ containing newly formed Cu-Cl bridging bonds in the attempt to crystallize $[1]^{2+}$ with chloroform. Conducting electrochemical reduction of $[3](BF_4)_4$ at +0.03V to produce the initial $[1]^{2+}$ complex yields the expected result confirmed by ESI-MS analysis.

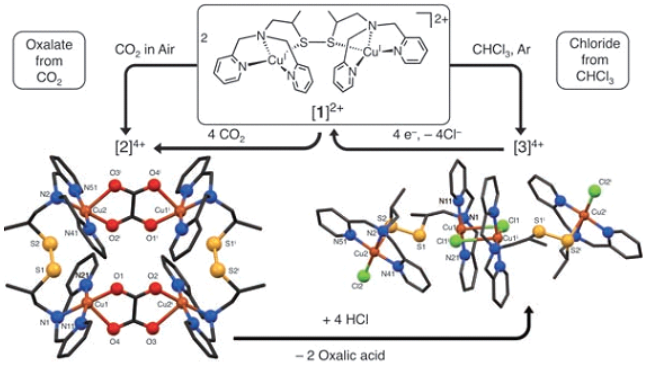

Figure 2 Schematic overview of the formation and reactivity of the complexes $[1]^{2+}$, $[2]^{4+}$(consists tow dimers), and $[3]^{4+}$. Each dimer in $[2]^{4+}$ consists two copper(II) ions situated in square-pyramidal environments with three N and one O(from the oxalate) donors on the basal plane and one O(another from the oxalate) at the apical position.

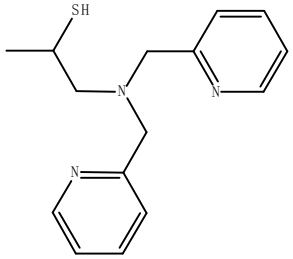

Figure 3 [N-(2-mecaptopropyl-N,N-bis(2-pyridylmethyl)amine], ligand.

The cyclic voltammongrams of the copper(II) complex $[3]^{4+}$ and the oxalate containing copper(II) structure $[2]^{4+}$is showed in Figure 4. In The cyclic voltammogram of complex$[3]^{4+}$ showed a cathodic peak current of $Cu^{2+/+}$ at +0.06V vs SCE indicating the close of a complete redox circle of the copper/disulfide-ligand electrocatalyse CO_2 reduction system. Besides, the cyclic votammogram of complex$[2]^{4+}$ showed a irreversible reduction process at -0.03V vs SCE indicating that the $C_2O_4^{2-}$ anion falls apart when copper is reduced, which provide a potential prospect to realize the redox circle that an apt method is need to remove the releasing $C_2O_4^{2-}$ thus providing a driving force of the whole redox.

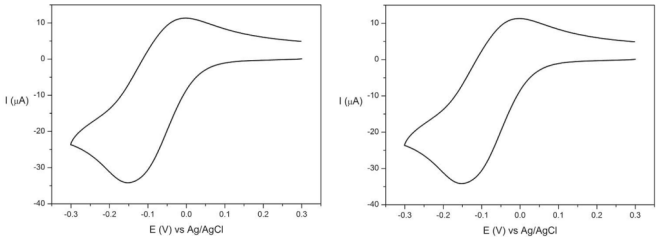

Figure 4. The cyclic voltammograms(measured in identical condition) of complex$[3]^{4+}$ (left) and complex$[2]^{4+}$ (right).

Therefore, the design of the redox cycle is revised by the induction of lithium perchlorate into the system. Firstly, the salt solution supports the electrolyte in the CO_2-saturated acetonitrile solution. Secondly, Li+ and ClO_4^{2-}'s reduction potential do not fall into the range of the potential applied for the electrochemical CO_2 reduction. Thirdly, Li_2ClO_4 as a precipitate lowers the concentration of the reduction product, thus contributes to the thermodynamic favorability of the reduction. Forth, the knowing the solid weigh helps to quantify the reaction, due to which a measurement of current efficiency and catalyst regenerate percentage is conducted using controlled potential coulometry. The corresponding results indicate a 96% current efficiency in this conversion which is much more improved compared to historical reseaches[26-27]. In addition, a 95% regeneration of copper(I) complex shows a minor consumption of the catalyst. The practicality of this CO_2 reduction cycle can be reflected by the success of more than 7 hours' electrocatalysis experiment. Herein, a proposed electrocatalytic mechanism of the CO_2 conversion is showed in Figure 5.

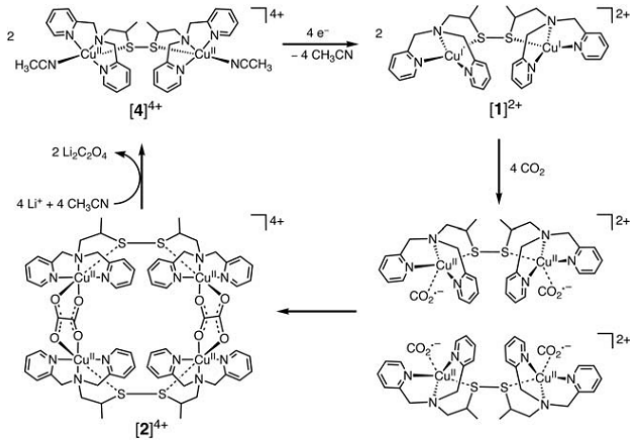

Figure 5. A possible electrocatalytic mechanism for oxalate formation.

The high selectivity and reaction efficiency can be interpreted from the follow aspects. Metal complexes show great advantage to mediate CO_2 reduction at less negative potentials. The electron transfer process accompanies with the Cu-O bonds formation and break, which follows the inner-sphere electron transfer mechanism. The exchange of ligand determines the rate of inner sphere electron transfer. Cu(I) has a d^{10} electron configuration, which is labile and favors fast reaction. The disulfide part of the ligand is very electron rich and tend to push electron density toward Cu which is also electron rich and further helps to donate electron to CO_2. Meanwhile, the low solubility of lithium oxalate assists the breakage of Cu-O bonds and moves the equilibrium toward reducing more CO_2 to oxalate. These effects add up together result in a lower barrier of forming metal-carbon dioxide radical anion intermediate and improves the reaction rate, also cuts down the consumption of additional energy input.

The new electrocatalytic method developed in this paper makes a great leap forward in the whole development of the electrochemically reduce carbon dioxide. It not only performs an extraordinary high selectivity and great thermodynamic favorablity of CO_2 reduction over O_2 in atmosphere by using commonly used copper complex, and using a much less negative potential to accomplish the reduction cycle, but also improves the current efficiency to a significant extent. It gives the industrial application of the carbon dioxide conversion a promising future. Nevertheless, the system still carries some inherent shortages with respect to the reduction rate. Since the rate of reduction of CO_2 gradually slowed due to the deposition of solid lithium oxalate on the electrode, a low cost method for the clearance of the precipitate on the electrode or a better way for the removal of oxalate need to be invested efforts on. In addition, this study provides us a vision of designing metal complexes ahead target on different reduction missions of the carbon dioxide. Researches can be focused on trying other metals or altering the ligand structure with various substituents to improve the function of the catalyst or develop a practical way to convert carbon dioxide to other useful organic fuels.

ACKNOWLEDGMENT The author acknowledge Peng Wang and Jiaming Lin for helpful discussion relating to this project. The authors thank Professor Rosenthal for helpful instruction.

REFERENCES

(1) Aresta, M.; Dibenedetto, A. Dalton Trans. 2007, 2975 -2992.
(2) Schrag D. P. Science 2007,315, 812 -813.
(3) Sakakura T.; Choi J. C.; Yasuda H. Chem. Rev. 2007,107,2365-2387.
(4) Song C. S.; Catal. Today 2006,115, 2-32.
(5) Youngme S.; Chaichit N.; Kongsaeree P.; van Albada G. A.; Reedijk J. Inorg. Chim. Acta 2001,324, 232-240.
(6) van Albada G. A.; Mutikainen, I.; Roubeau O.; Turpeinen U.; Reedijk J. Inorg. Chim. Acta 2002,331, 208-215.
(7) Verdejo B. et al. Eur. J. Inorg. Chem. 2008,84-97.
(8) Chen J. M.; Wei W.; Feng X. L.; Lu T. B. Chem. Asian J. 2007,2,710-719.
(9) Company A. et al. Inorg. Chem. 2007,46, 9098-9110.
(10) Doyle R. P. et al. Dalton Trans. 2007, 5140-5147.
(11) Verdejo B. et al. Inorg. Chem. 2006,45, 3803-3815.
(12) García-España E.; Gaviña P.; Latorre J.; Soriano C.; Verdejo B. A. J. Am. Chem. Soc. 2004,126, 5082-5083
(13) Notni J.; Schenk S.; Görls H.; Breitzke H.; Anders E. Inorg. Chem. 2008,47, 1382-1390.
(14) Sarkar B.; Liaw B. J.; Fang C. S.; Liu C. W. Inorg. Chem. 2008,47, 2777-2785.
(15) Fondo M.; García-Deibe A. M.; Ocampo N.; Sanmartín J.; Bermejo M. R. Dalton Trans. 2007, 414-416.
(16) Johansson R.; Jarenmark M.; Wendt A. F. Organometallics 2005,24, 4500-4502.
(17) García-España E.; Gaviña P.; Latorre J.; Soriano C.; Verdejo B. A. J. Am. Chem. Soc. 2004,126, 5082-5803.
(18) Himmel H. J. Eur. J. Inorg. Chem. 2007, 675-683.
(19) Ikeda S.; Takagi T.; Ito K. Bull. Chem. Soc. Jpn. 1987,60,2517-2522.
(20) Benson E. E.; Kubiak C. P.; Sathrum A. J.; Smieja J. M. Chem. Soc. Rev. 2009,38, 89-99.
(21) Calabrese J.C.; Herskovitz T.; Kinney J. B. J. Am. Chem. Soc. 1983,105,5914.
(22) Gambarotta S,; Arena F.; Floriani C.; Zanazzi P. F. J. Am. Chem. Soc. 1982,104,5082.
(23) Tanaka H.; Nagao H.; Tanaka K. Inorg. Chem. 1992,31,1971.
(24) Ali M. M.; Sato H.; Mizukawa T.; Tsuge K.; Haga M.; Tanaka K. J. Chem. Soc., Chem. Commun. 1998, 249.
(25) Christensen P. A.; Jiggins S. J. J. Electroanalaytial Chem. 1995,387,127-132.
(26) Kushi Y.; Nagao H.; Nishioka T.; Isobe K.; Tanaka K. Chem. Lett. 1994,2175-2178.
(27) Kushi T.; Nagao H.; Nishioka T.; Isobe K.; Tanaka K. J. Chem. Soc. Chem. Commun. 1995,1223-1224.

longitudes; in panels B and C, obtained just 6 days apart, the ring appears to be consistently brightest at longitudes leading (to the right of) Portia, which can be identified in the figure as R2's bright interior neighbor. If R2 arises from a belt of macroscopic bodies, then the brighter clumps might be transient phenomena arising when embedded parent bodies collide; a similar process is believed to be at work in Saturn's clumpy F ring (*18*–*21*).

Discussion. Dynamical simulations of the closely packed inner uranian moons reveal that they will perturb each other into crossing orbits at million-year time scales (*3*). The discovery of Cupid orbiting so close to Belinda substantially exacerbates the stability problem (*22*). Our new findings provide a clearer picture of this rapidly and chaotically evolving system. The largest moons show orbital changes within decades; these subtle variations can, over time, lead to orbital collisions and disruptions. So close to the Roche limit, one might expect to find one or more debris belts within this evolving system; R2 is likely to be one such example. Mab and R1 are distant enough to be unaffected by the dynamical turmoil within the Portia group, but the mysterious orbital variations of Mab suggest that it may play a part in the underlying interactions. It is as yet unclear whether related phenomena are at work within Uranus's main ring system.

The rings and smaller moons listed in Tables 1 and 2 have probably changed quite substantially since the time of the dinosaurs, and perhaps even since the time of the Roman Empire. Uranus does not host a swarm of independent moons and rings, but instead features a closely coupled dynamical system that rivals the other known ring-moon systems in its subtlety and complexity.

References and Notes

1. B. A. Smith *et al.*, *Science* **233**, 43 (1986).
2. E. Karkoschka, *Icarus* **151**, 69 (2001).
3. M. J. Duncan, J. J. Lissauer, *Icarus* **125**, 1 (1997).
4. See supporting material on *Science* Online.
5. M. R. Showalter, J. J. Lissauer, *IAU Circ. 8194* (2003).
6. M. R. Showalter, J. J. Lissauer, *IAU Circ. 8209* (2003).
7. E. Karkoschka, *Icarus* **151**, 51 (2001).
8. W. M. Owen Jr., S. P. Synnott, *Astron. J.* **93**, 1268 (1987).
9. R. A. Jacobson, *Astron. J.* **115**, 1195 (1998).
10. J. A. Burns, D. P. Hamilton, M. R. Showalter, in *Interplanetary Dust*, E. Grün, B. A. S. Gustafson, S. F. Dermott, H. Fechtig, Eds. (Springer-Verlag, Berlin, 2001), pp. 641–725.
11. J. A. Burns et al., in *Jupiter: The Planet, Satellites and Magnetosphere*, F. Bagenal, Ed. (Cambridge Univ. Press, Cambridge, 2004), pp. 241–262.
12. M. R. Showalter, J. N. Cuzzi, *Icarus* **103**, 124 (1993).
13. H. B. Throop, L. W. Esposito, *Icarus* **131**, 152 (1998).
14. J. J. Lissauer, R. G. French, *Icarus* **146**, 12 (2000).
15. A. L. Broadfoot *et al.*, *Science* **233**, 74 (1986).
16. J. E. Colwell, L. W. Esposito, *Icarus* **86**, 530 (1990).
17. J. E. Colwell, L. W. Esposito, *J. Geophys. Res.* **97**, 10227 (1992).
18. J. N. Cuzzi, J. A. Burns, *Icarus* **74**, 284 (1988).
19. M. R. Showalter, *Science* **282**, 1099 (1998).
20. F. Poulet, B. Sicardy, P. D. Nicholson, E. Karkoschka, J. Caldwell, *Icarus* **144**, 135 (2000).
21. J. M. Barbara, L. W. Esposito, *Icarus* **160**, 161 (2002).
22. J. A. Meyer, personal communication.

23. Support for this publication was provided by NASA through proposals GO-9823, GO-10102, and GO-10274 from the Space Telescope Science Institute, which is operated by the Association of Universities for Research in Astronomy under NASA contract NAS5-26555. Additional support was provided by NASA's Planetary Geology and Geophysics Program (M.R.S.). We thank A. Roman and R. Gilliland for their extensive support in the planning and execution of our HST observations.

Supporting Online Material

www.sciencemag.org/cgi/content/full/1122882/DC1
Materials and Methods
Tables S1 to S3
Movie S1

21 November 2005; accepted 15 December 2005
Published online 22 December 2005;
10.1126/science.1122882
Include this information when citing this paper.

REPORTS

Electrodes with High Power and High Capacity for Rechargeable Lithium Batteries

Kisuk Kang,[1] Ying Shirley Meng,[1] Julien Bréger,[2] Clare P. Grey,[2] Gerbrand Ceder[1]*

New applications such as hybrid electric vehicles and power backup require rechargeable batteries that combine high energy density with high charge and discharge rate capability. Using ab initio computational modeling, we identified useful strategies to design higher rate battery electrodes and tested them on lithium nickel manganese oxide [$Li(Ni_{0.5}Mn_{0.5})O_2$], a safe, inexpensive material that has been thought to have poor intrinsic rate capability. By modifying its crystal structure, we obtained unexpectedly high rate-capability, considerably better than lithium cobalt oxide ($LiCoO_2$), the current battery electrode material of choice.

Rechargeable Li batteries offer the highest energy density of any battery technology, and they power most of today's portable electronics. Although most electronics require only moderately high charge/discharge rates, newer applications, such as regenerative braking in hybrid electric vehicles (HEVs), power backup, and portable power tools, require both high energy and high power density (i.e., the ability to charge and discharge very fast), which has been difficult to accomplish with Li batteries. Cathode electrodes in rechargeable Li batteries store Li^+ and electrons by the concurrent insertion of Li^+ in a crystal structure and the reduction of a transition-metal ion (*1*). Good electrode materials therefore have high reversible storage capacity for Li (to obtain long battery life per unit weight or volume of the battery) and rapid solid-state Li^+ and electron transport. Reasonable charge/discharge times require that, at room temperature, Li^+ ions can diffuse over micrometer distances in a matter of an hour (minutes for HEV technology). Hence, materials with very fast Li diffusivity are needed to produce batteries capable of satisfying high power demands in new applications. In this report, we use ab initio computational modeling to identify the basic energy barrier that limits Li^+-ion hopping in a prototypical layered electrode structure and use the insights gained from these calculations to synthesize a material with substantially better rate capability.

Many current (e.g., $LiCoO_2$ in today's batteries) and potential intercalation electrodes have the layered structure shown in Fig. 1A, consisting of layers of transition-metal cations separated from Li layers by oxygen. In this structure, Li is coordinated octahedrally by oxygens but diffuses from site to site by hopping through intermediate tetrahedral sites (Fig. 1B) (*2*). Previous work has identified the tetrahedral site as being close to the maximum-energy position along the path between octahedral sites (*3*). Because Li hops require thermal energy fluctuations, the hopping rate decreases exponentially with the energy of the activated state, and small reductions in this activation energy can lead to substantial improvement of the Li diffusion and of the rate at which an electrode can be charged or discharged. At room temperature, a reduction of activation energy of only 57 meV increases the rate of Li migration by a factor of 10 [$\exp(-57\ \text{meV}/kT) \sim 10$]. The energy required for a Li^+ ion to cross the activated

[1]Center for Materials Science and Engineering and Department of Materials Science and Engineering, Massachusetts Institute of Technology, 77 Massachusetts Avenue, Cambridge, MA 02139, USA. [2]Department of Chemistry, State University of New York, Stony Brook, NY 11794–3400, USA.

*To whom correspondence should be addressed. E-mail: gceder@mit.edu

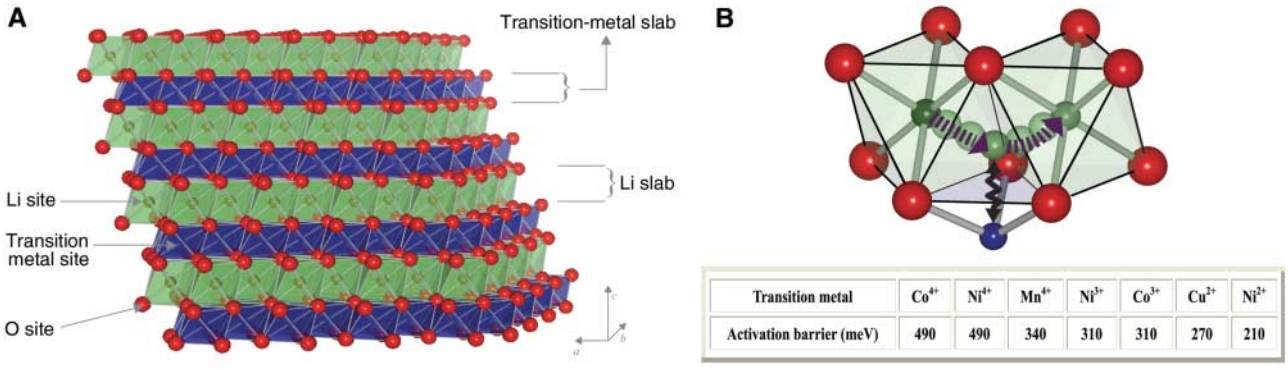

Transition metal	Co^{4+}	Ni^{4+}	Mn^{4+}	Ni^{3+}	Co^{3+}	Cu^{2+}	Ni^{2+}
Activation barrier (meV)	490	490	340	310	310	270	210

Fig. 1. (**A**) The structure of $Li(Ni_{0.5}Mn_{0.5})O_2$ consists of layers of transition metal (Ni and Mn) separated from Li layers by oxygen. In materials made by a conventional high-temperature synthesis, partial exchange of Li and Ni ions is always observed, which contracts the space through which Li can move. (**B**) Li moves from one octahedral site to another by passing through an intermediate tetrahedral site where it encounters strong repulsion from a nearby transition-metal cation. The table shows the activation barrier for Li motion for various transition metals near the activated state. Values were calculated by GGA DFT for various chemistries and Li contents.

state is likely to depend on the size of the tetrahedral site (strain effect) as well as on the electrostatic interaction between Li^+ in the activated state and the transition-metal cation directly below it (Fig. 1B). Hence, a strategy to increase Li diffusivity should focus on reducing these two contributions to the activation energy.

Using ab initio calculations performed in the generalized gradient approximation to density functional theory (GGA DFT), we can gauge the effect of both the strain and electrostatic contributions to the activation energy. The table in Fig. 1B shows the calculated energy for a Li^+ ion in the tetrahedral site with various other cations in the face-sharing octahedron adjoining it. Clearly, a low-valent transition metal such as Ni^{2+} is beneficial to the Li diffusion. The reduction from Co^{3+} (currently used) to Ni^{2+} leads to a hopping rate that is higher by a factor of 54 [$\sim\exp(100\ meV/kT)$]. Hence, a material such as $Li(Ni^{2+}_{0.5}Mn^{4+}_{0.5})O_2$, in which half the Li^+-activated states come in contact with Ni^{2+}, should have substantially higher Li diffusivity at the early stage of charging than the currently used battery material $LiCoO_2$, in which all the pathways are in contact with Co^{3+}. Because the number of high-rate pathways is well above the percolation limit, the presence of low-rate pathways (in contact with Mn^{4+}) in $LiNi_{0.5}Mn_{0.5}O_2$ should not substantially reduce the Li diffusivity. It is expected that the benefit of Ni^{2+} is noticeable until the charging level is so high that the Ni^{2+} pathways do not percolate anymore.

$LiNi_{0.5}Mn_{0.5}O_2$ is fundamentally different from the currently used electrode material, $LiCoO_2$, in which Co can only exchange one electron, and removal of all Li leads to an unstable material containing only highly oxidized Co^{4+} ions. In comparison, the transition-metal layer in $Li(Ni_{0.5}Mn_{0.5})O_2$ is bifunctional, with Ni^{2+} acting as a double redox-active center (*4*–*7*) and Mn^{4+} providing stability to the host structure (*8*). Although the distinctive electronic properties of $Li(Ni_{0.5}Mn_{0.5})O_2$ have been shown to result in high battery capacity for this material at very low charge/discharge rates (*4*, *5*, *9*, *10*), this capacity advantage over current electrode materials completely disappears at commercially interesting rates, in apparent contradiction to the predictions made based on the calculations (Fig. 1B). Our calculations were performed for materials with an ideal layered structure. However, in all $Li(Ni_{0.5}Mn_{0.5})O_2$ materials synthesized thus far, perfect separation between Li and transition-metal cations into alternating layers could not be achieved, with all materials exhibiting 8 to 12% exchange of Li and Ni (*4*, *5*, *9*, *10*). Calculations were, therefore, performed to explore the effect of Li/Ni site exchange on the Li mobility. Figure 2 shows ab initio computations of the activation energy as a function of the distance between the oxygen layers on each side of the plane of Li^+ ions (Fig. 2). As this layer-to-layer distance grows, the space in the activation site increases. It is clear that more space between these oxygen layers substantially reduces the activation energy for Li motion. These calculations also clearly point to the Li/Ni disorder as the reason $Li(Ni_{0.5}Mn_{0.5})O_2$ has not yet lived up to its high rate potential. The solid lines show the calculated O-O interlayer spacing for a material with 8.3% of Li-Ni site disorder. The dashed lines give the equivalent spacing for a hypothetical material with no Li/Ni disorder. Our calculations indicate that the Li slab space reduces from 2.64 to 2.62 Å when 8.3% of transition metal is present in the Li layer. Li motion is so sensitive to the spacing between oxygen layers that this very small change ($\sim$0.02 Å) results in a 20- to 30-meV increase in the activation barrier. More important, Li/Ni disorder greatly limits the opening of the Li slab space upon delithiation (i.e., on charging the battery). The Li slab space expands during the early stages of delithiation as a result of the removal of O^{2-}-Li^+-O^{2-} bonds across the slab, leading to faster Li motion. Whereas the Li slab space increases from 2.64 to 2.74 Å in a perfect layered system, calculations indicate that it only increases from 2.62 to 2.69 Å when 8.3% Ni ions are present in the Li layer. These observations clearly

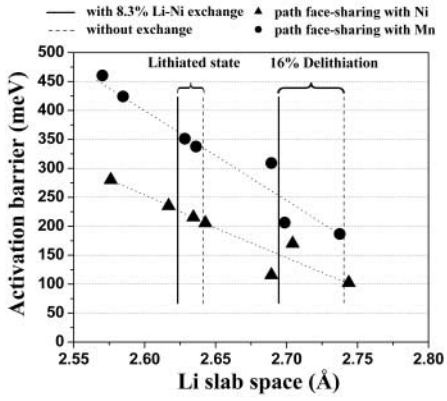

Fig. 2. Calculated activation barrier for Li migration in $Li(Ni_{0.5}Mn_{0.5})O_2$ as a function of the Li slab space. Triangles and circles represent the activated state that face-shares with Ni and Mn, respectively. The activation barriers have been calculated for a hypothetically perfect layered system, for a system with 8.3% excess Ni present in the Li layer without a change in the transition-metal layer, and for a system with 8.3% Li-Ni exchange.

indicate that the diffusivity of Li should be greatly improved by reducing the Li/transition-metal (Ni) exchange in $Li(Ni_{0.5}Mn_{0.5})O_2$, a fact that has already been noticed experimentally in $LiNiO_2$ and $LiTiS_2$ compounds (*11*, *12*).

Although Li-containing materials prepared through traditional high-temperature synthesis routes contain substantial Li/Ni disorder and are, therefore, unlikely to be high-rate electrodes, better ordering can be expected in $Na(Ni_{0.5}Mn_{0.5})O_2$ because the larger size difference between Na^+ and Ni^{2+} or Mn^{4+} creates a larger driving force for separating the alkali ions and the transition-metal ions in discrete layers. We have previously shown that the driving force for layering is likely to be increased if a larger ion, such as Na^+, is used instead of Li^+ because of the increased size mismatch between Na^+ and transition-metal ions such as Ni^{2+} (*13*). Na compounds can be trans-

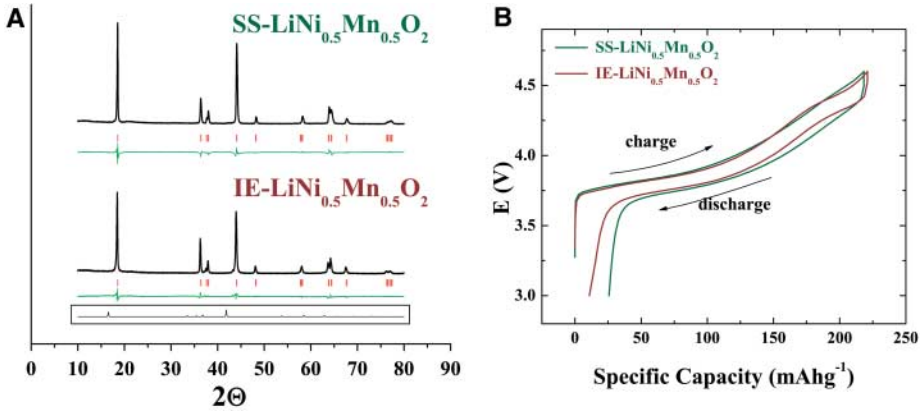

Fig. 3. (**A**) XRD patterns of SS-Li($Ni_{0.5}Mn_{0.5}$)O_2 (top) and IE-Li($Ni_{0.5}Mn_{0.5}$)O_2 (bottom). The observed pattern, the calculated peak positions, and the difference between the two patterns are shown for each XRD pattern. The bottom inset is the XRD pattern of the Na precursor. The precursor peak is not observed after ion exchange. The Rietveld refinement of SS-Li($Ni_{0.5}Mn_{0.5}$)O_2 (in R-3m) gives c = 14.2820(14) Å, a = 2.8850(1) Å, and z = 0.25736(37); the Ni-Li exchange = 10.9%, with R_p = 13.6 and R_{wp} = 15.3. The refinement of IE-Li($Ni_{0.5}Mn_{0.5}$)O_2 gives c = 14.3437(8) Å, a = 2.8924(1) Å, and z = 0.25907(21); the Ni-Li exchange = 4.3%, with R_p = 7.08 and R_{wp} = 8.74. (**B**) First charge/discharge curves of IE-Li($Ni_{0.5}Mn_{0.5}$)O_2 and SS-Li($Ni_{0.5}Mn_{0.5}$)O_2 within the voltage window of 3.0 to 4.6 V at C/20 rate.

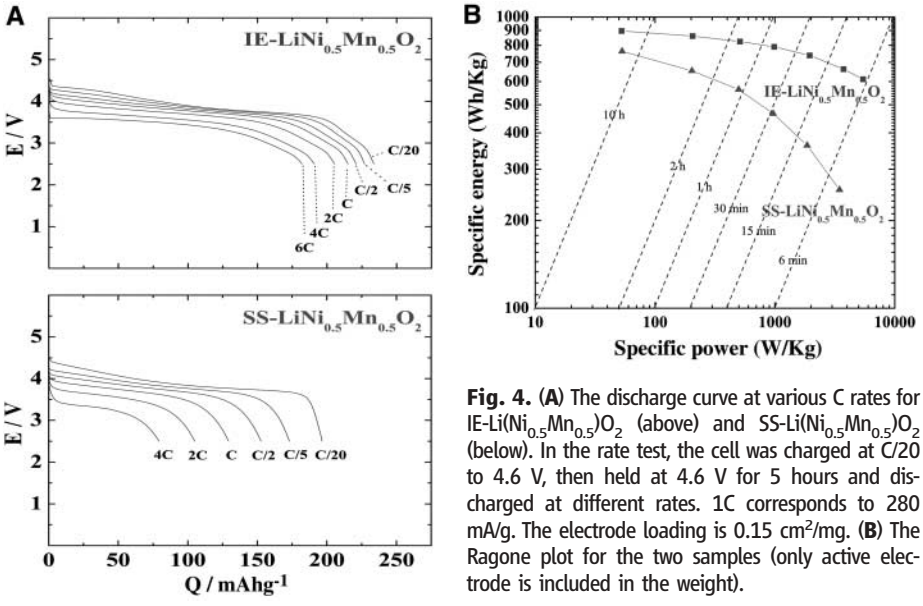

Fig. 4. (**A**) The discharge curve at various C rates for IE-Li($Ni_{0.5}Mn_{0.5}$)O_2 (above) and SS-Li($Ni_{0.5}Mn_{0.5}$)O_2 (below). In the rate test, the cell was charged at C/20 to 4.6 V, then held at 4.6 V for 5 hours and discharged at different rates. 1C corresponds to 280 mA/g. The electrode loading is 0.15 cm^2/mg. (**B**) The Ragone plot for the two samples (only active electrode is included in the weight).

formed to well-layered Li compounds by ion exchange of Na^+ for Li^+ (*14*–*16*). Ion exchange is a soft chemical approach performed at relatively low temperature so that only Na^+ is replaced by Li^+, keeping the rest of the structure intact. We have indeed obtained a well-layered material with excellent performance by ion-exchanging Li for Na in Na($Ni_{0.5}Mn_{0.5}$)O_2. Details of the synthesis procedure are given in the Supporting Online Material (*17*).

The x-ray diffraction (XRD) pattern of the Li($Ni_{0.5}Mn_{0.5}$)O_2 obtained by ion exchange [IE-Li($Ni_{0.5}Mn_{0.5}$)O_2] is shown in Fig. 3A. For comparison, we also show Li($Ni_{0.5}Mn_{0.5}$)O_2 synthesized through a conventional solid-state reaction [SS-Li($Ni_{0.5}Mn_{0.5}$)O_2]. The refined structural parameters for SS-Li($Ni_{0.5}Mn_{0.5}$)O_2 are in good agreement with the literature (*4*, *9*, *10*, *18*–*20*). Noticeably, there is a substantial increase in the c-lattice parameter from 14.28 Å in SS-Li($Ni_{0.5}Mn_{0.5}$)O_2 to 14.34 Å in IE-Li($Ni_{0.5}Mn_{0.5}$)O_2. The c-lattice parameter is perpendicular to the layers in the structure of Fig. 1, and its increase signifies an increase in the space around the Li layer. Defining the Li slab space as the average distance between the oxygen layers around the Li layer, the Li slab space increases from 2.59 Å in SS-Li($Ni_{0.5}Mn_{0.5}$)O_2 to 2.65 Å in IE-Li($Ni_{0.5}Mn_{0.5}$)O_2. Given the computational results in Fig. 2, IE-Li($Ni_{0.5}Mn_{0.5}$)O_2 should therefore have a substantially higher Li diffusivity. The small quantitative disagreement with the calculated slab spaces is typical for modern ab initio approaches. No Na precursor peaks are visible in the XRD, and only about 0.3 weight percent of Na could be detected by inductively coupled plasma (ICP) measurement in IE-Li($Ni_{0.5}Mn_{0.5}$)O_2, which implies that the ion exchange of Na and Li is complete.

Rietveld refinement of the XRD gives Li/Ni exchanges of 10.9% and 4.3%, respectively, in the SS-Li($Ni_{0.5}Mn_{0.5}$)O_2 and IE-Li($Ni_{0.5}Mn_{0.5}$)O_2. Because the site occupancies obtained by Rietveld refinement can be somewhat inaccurate as a result of preferential texture of the sample, and when refining occupancies for multiple cations on the same crystallographic site, the Li/Ni exchange was independently verified by solid state ^{6}Li magic angle spinning nuclear magnetic resonance (MAS NMR). Quantitative analysis of the 1450–parts per million peak in the NMR spectrum, which is known to correspond to Li in a transition-metal site (*21*), reveals that Li-Ni exchange is even lower, about 0.5% (*17*). This suggests that our strategy to obtain a better layered structure with larger slab space is successful.

Electron microscopy revealed plate-shaped crystals of about 1 μm for IE-Li($Ni_{0.5}Mn_{0.5}$)O_2, whereas the SS-Li($Ni_{0.5}Mn_{0.5}$)O_2 forms cubic particles of about 0.5 μm (*17*). The anisotropic shape of the crystallites offers further evidence for the more layered structure of IE-Li($Ni_{0.5}Mn_{0.5}$)O_2.

Figure 3B shows the first charge and discharge profiles of IE-Li($Ni_{0.5}Mn_{0.5}$)O_2 and SS-Li($Ni_{0.5}Mn_{0.5}$)O_2 tested in an electrochemical cell at a rate corresponding to fully charging the theoretical capacity of the material in 20 hours (C/20). Whereas the charge/discharge behavior of IE-Li($Ni_{0.5}Mn_{0.5}$)O_2 is very similar to that of SS-Li($Ni_{0.5}Mn_{0.5}$)O_2 below 4 V, the plateau at 4.3 V is more pronounced in IE-Li($Ni_{0.5}Mn_{0.5}$)O_2. Because the 4.3-V plateau is observed at about x = 0.6 to 0.7 [Li_{1-x}($Ni_{0.5}Mn_{0.5}$)O_2], it could be caused by Li-vacancy ordering (*22*). The absence of transition metals in the Li layer is likely to enhance Li-vacancy ordering.

Figure 4A shows that, despite its larger particle size, the rate capability of IE-Li($Ni_{0.5}Mn_{0.5}$)O_2 is superior to that of SS-Li($Ni_{0.5}Mn_{0.5}$)O_2. Although the performance of the materials is similar at low rates, IE-Li($Ni_{0.5}Mn_{0.5}$)O_2 retains much higher capacity at high rates than does SS-Li($Ni_{0.5}Mn_{0.5}$)O_2. Even at a 6C rate (one charge of 280 mAh/g in 10 min), IE-Li($Ni_{0.5}Mn_{0.5}$)O_2 delivers a discharge capacity of 183 mAh/g. There is no published data available for a rate as high as 6C, but comparison with the best electrochemical data published for this material so far [135 mAh/g at a 397 mA/g rate (*9*)] confirms that we have developed a material with substantially improved performance.

For practical applications, the trade-off between power (rate) and energy density is important and is often represented in a Ragone plot (Fig. 4B). Most Li-battery materials show a substantial decrease in specific energy as one draws more current from them, making them less useful in applications such as EV (electric vehicle), HEV, and power tools, where high charge and

discharge rates are required. Figure 4B shows that IE-Li($Ni_{0.5}Mn_{0.5}$)O_2 clearly retains its energy storage capacity even at the very high rate required for those applications. At a 6-min charge/discharge rate, IE-Li($Ni_{0.5}Mn_{0.5}$)O_2 delivers almost double the energy density of SS-Li($Ni_{0.5}Mn_{0.5}$)O_2. Initial tests on the capacity retention with full charge/discharge cycling are promising, with a fade of 0.6% per cycle for IE-Li($Ni_{0.5}Mn_{0.5}$)O_2 versus 0.8% per cycle for SS-Li($Ni_{0.5}Mn_{0.5}$)O_2 (*17*).

In conclusion, we have used ab initio computational modeling to infer that the combined use of low-valent transition-metal cations and low strain in the activated state are key strategies for increasing the rate capability of layered cathode materials, and we have successfully synthesized Li($Ni_{0.5}Mn_{0.5}$)O_2 with very little intralayer disordering to optimize those factors. In agreement with our theoretical predictions, this material retains its capacity at high rates. Substitution of Co for Ni and Mn can also be used to reduce the Li/Ni exchange and improve rate performance (*23*, *24*), although the use of Co increases the cost and reduces the safety of the material (*25*). Although Li($Ni_{0.5}Mn_{0.5}$)O_2 displays an exciting combination of high rate and high capacity, several other factors, such as thermal stability, cycle life, and the extra cost from the ion-exchange process, will need to be further investigated before its application in commercial products can be considered. If the outcome of such development studies is positive, Li($Ni_{0.5}Mn_{0.5}$)O_2 would be a potential cathode material for high rate applications.

References and Notes

1. M. S. Whittingham, *Science* **192**, 1126 (1976).
2. A. Van der Ven, G. Ceder, *Electrochem. Solid-State Lett.* **3**, 301 (2000).
3. A. Van der Ven, G. Ceder, *J. Power Sources* **97-98**, 529 (2001).
4. T. Ohzuku, Y. Makimura, *Chem. Lett. (Jpn.)* **8**, 744 (2001).
5. Z. Lu, D. D. MacNeil, J. R. Dahn, *Electrochem. Solid-State Lett.* **4**, A191 (2001).
6. J. Reed, G. Ceder, *Electrochem. Solid-State Lett.* **5**, A145 (2002).
7. J. M. Paulsen, J. R. Dahn, *J. Electrochem. Soc.* **147**, 2478 (2000).
8. M. M. Thackeray, *Prog. Solid State Chem.* **25**, 1 (1997).
9. Y. Makimura, T. Ohzuku, *J. Power Sources* **119-121**, 156 (2003).
10. Z. Lu, L. Y. Beaulieu, R. A. Donaberger, C. L. Thomas, J. R. Dahn, *J. Electrochem. Soc.* **149**, A778 (2002).
11. C. Delmas *et al.*, *J. Power Sources* **68**, 120 (1997).
12. M. S. Whittingham, U.S. Pat. 4,007,055 (1975).
13. E. J. Wu, P. D. Tepesch, G. Ceder, *Philos. Mag. B* **77**, 1039 (1998).
14. A. R. Armstrong, P. G. Bruce, *Nature* **381**, 499 (1996).
15. C. Delmas, J. J. Braconnier, A. Maazaz, P. Hagenmuleer, *Rev. Chimie Minérale* **19**, 343 (1982).
16. K. Kang *et al.*, *Chem. Mater.* **15**, 4503 (2003).
17. Materials and methods are available as supporting material on *Science* Online.
18. Y. S. Meng *et al.*, *Chem. Mater.* **17**, 2386 (2005).
19. H. Kobayashi *et al.*, *J. Mater. Chem.* **13**, 590 (2003).
20. W. S. Yoon *et al.*, *Electrochem. Solid-State Lett.* **5**, A263 (2002).
21. C. P. Grey, W. S. Yoon, J. Reed, G. Ceder, *Electrochem. Solid-State Lett.* **7**, A290 (2004).
22. C. Delmas *et al.*, *Int. J. Inorg. Mater.* **1**, 11 (1999).
23. Z. Lu, D. D. MacNeil, J. R. Dahn, *Electrochem. Solid-State Lett.* **4**, A200 (2001).
24. T. Ohzuku, Y. Makimura, *Chem. Lett. (Jpn.)* **7**, 642 (2001).
25. J. Jiang, K. W. Eberman, L. J. Krause, J. R. Dahn, *J. Electrochem. Soc.* **152**, A1879 (2005).

26. The authors would like to thank Y. Shao-Horn for valuable discussion. This work was supported by the Materials Research Science and Engineering Centers program of the National Science Foundation under award DMR 02-13282 and by the Assistant Secretary for Energy Efficiency and Renewable Energy, Office of FreedomCAR and Vehicle Technologies of the U.S. Department of Energy under contract DE-AC03-76SF00098, subcontracts 6517748 and 6517749, with the Lawrence Berkeley National Laboratory.

Supporting Online Material

www.sciencemag.org/cgi/content/full/311/5763/977/DC1
Materials and Methods
Figs. S1 to S4
References

2 November 2005; accepted 20 January 2006
10.1126/science.1122152

Plasma Acceleration Above Martian Magnetic Anomalies

R. Lundin,[1] D. Winningham,[2] S. Barabash,[1] R. Frahm,[2] M. Holmström,[1] J.-A. Sauvaud,[3] A. Fedorov,[3] K. Asamura,[4] A. J. Coates,[5] Y. Soobiah,[5] K. C. Hsieh,[6] M. Grande,[7] H. Koskinen,[8,9] E. Kallio,[8] J. Kozyra,[10] J. Woch,[11] M. Fraenz,[11] D. Brain,[12] J. Luhmann,[12] S. McKenna-Lawler,[13] R. S. Orsini,[14] P. Brandt,[15] P. Wurz[16]

Auroras are caused by accelerated charged particles precipitating along magnetic field lines into a planetary atmosphere, the auroral brightness being roughly proportional to the precipitating particle energy flux. The Analyzer of Space Plasma and Energetic Atoms experiment on the Mars Express spacecraft has made a detailed study of acceleration processes on the nightside of Mars. We observed accelerated electrons and ions in the deep nightside high-altitude region of Mars that map geographically to interface/cleft regions associated with martian crustal magnetization regions. By integrating electron and ion acceleration energy down to the upper atmosphere, we saw energy fluxes in the range of 1 to 50 milliwatts per square meter per second. These conditions are similar to those producing bright discrete auroras above Earth. Discrete auroras at Mars are therefore expected to be associated with plasma acceleration in diverging magnetic flux tubes above crustal magnetization regions, the auroras being distributed geographically in a complex pattern by the many multipole magnetic field lines extending into space.

Earth's polar aurora and related phenomena, such as magnetic and ionospheric disturbances, have been studied for well over half a century. The first proof that the aurora is caused by energetic electrons precipitating into Earth's topside atmosphere came from high-altitude sounding-rocket measurements (*1*). Electrons accelerated downward by magnetic field–aligned electric fields cause intense bright auroral arcs, often referred to as discrete auroras. Intense fluxes of nearly monoenergetic electrons (*2*) were the first evidence for magnetic field–aligned electric fields. Subsequent observations of accelerated electrons were made from polar orbiting satellites. The electrons' peak energy displayed a characteristic "inverted-V" signature in an energy-time spectrogram (*3*), which became the particle attribute of a discrete aurora. An additional proof of concept was observations of electrons and ions accelerated in opposite directions (*4*, *5*).

Inverted-V–like ion features near Mars, first reported by the Phobos-2 spacecraft (*6*), were associated with the temporal and spatial variability of the energy and momentum transfer between martian plasma and the solar wind (*7*, *8*). This was because auroras, specifically discrete auroras, are associated with magnetized planets, and no strong intrinsic magnetic fields were evident from Phobos-2 data, thus ruling out any analogy with the terrestrial aurora.

The Mars Global Surveyor (MGS) findings of crustal magnetic anomalies at Mars (*9*) considerably changed the picture. We now expect to find diverging magnetic field "cusps" above Mars (*10*) and closed magnetic loops (*11*), with local magnetic conditions similar to those found above Earth's polar region, albeit weaker and topologically different. A set of magnetic multipoles at specific longitudes and latitudes of Mars may characterize the crustal magnetization. Indeed, the first observation of auroral emission at Mars (*12*) was made above a strong crustal magnetization at 177°E and 52°S. The emissions in the 150- to 300-nm bands (CO and O) were most likely excited by high fluxes of charged particles.

Our study identified regions with downward-accelerated electrons and upward-accelerated ionospheric ions near local midnight. We studied how the acceleration regions map to magnetic cusps and clefts bound by strong magnetizations at Mars. We compared the energy spectra of accelerated electrons in the nightside of Mars with those associated with terrestrial discrete auroras. Finally, we computed the energy flux of precipitating electrons and estimated, from a

Electrodes with High Power and High Capacity for Rechargeable Lithium Batteries[1]

Kisuk Kang,[1] Ying Shirley Meng,[1] Julien Bre´ger,[2] Clare P. Grey,[2] Gerbrand Ceder[1]*

1. Center for Materials Science and Engineering and Department of Materials Science and Engineering, Massachusetts Institute of Technology, 77 Massachusetts Avenue,

2. Department of Chemistry, State University of New York, Stony Brook, NY 11794–3400, USA.

E-mail gceder@mit.edu

ABSTRACT: **This work utilized ion-exchange synthesis method to reduce the defects of the structure that improved the power density (charge/discharge rate) and cycle life a lot which increased the possibility of applying this material in the industry. With combining ab initio computational model and evidence from TEM images, the author successfully explained the high performance of the lithium nickel manganese oxide. With the modification of the structure of Lithium nickel manganese oxide, this material is promising especially in vehicle industry.**

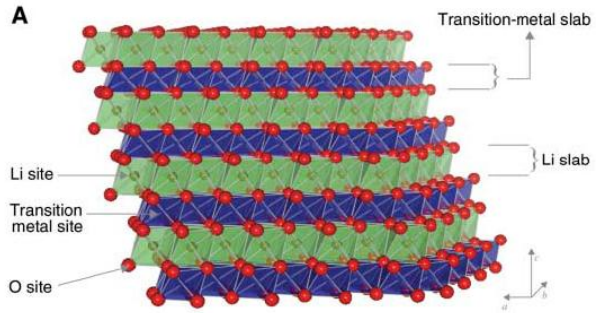

Figure 1. The structure of $LiNi_{0.5}Mn_{0.5}O_2$, both the lithium and transition metal located at the center of octahedral and oxygen will locate at the corner forming 2D layer structure.

Nowadays all the scientists spend enormous effort tried to solve the energy problem that we had in this generation. We used fuel as a source to generate power for decades and just recently we realized that the importance of global warming which we should reduce producing carbon dioxide as less as possible. Unfortunately, most of the vehicles still using combustion engine right now and that will produce huge amount of carbon dioxide. This compelled us to find an alternate way to provide power for vehicles. Electricity is a good candidate; however, the efficiency is low economical-wise. Lithium rechargeable battery appears in 1970s by M.S. Whittingham[1] and it's been used in laptop, cell phone and other portable tool for a long time, the market and technology became more and more mature. However, the power that lithium battery can provide to vehicles still relative low and slow. There are two critical requirements to be a suitable power for vehicle; first the power density should be high and second the life cycle should be acceptable. The layered-type $LiCoO_2$ has been used in cell phone and lap for a long time, in the small electronic devices LiCoO2 is a perfect cathode material and the market is very mature right now. However with $LiCoO_2$, the capacity is low and the power density is not enough to use in the car. Due to the requirements we mentioned above, as long as we can improve the power density and life cycle, the lithium battery will create another huge market in car industry like hybrid electric vehicles.

The traditional solid state syntheses have a lot of advantages including fewer steps and easily enlarge the scale to factory scale. Of course there are some drawbacks. If the compound itself is not thermal stable but is kinetic controlled, we may have difficult time to produce the pure phase. The other one is that there may be a lot of defects inside the structure.(The atoms might exchange position) In this article the author first synthesize the $Na\text{-}Ni_{0.5}Mn_{0.5}O_2$ by conventional solid state synthesis that just load the raw materials in the crucible and heat it up to the high temperature and use the product as a precursor. Subsequently by ion exchange, extract the Na ion and replace with Li.

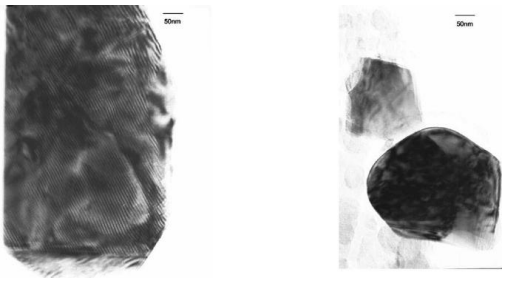

Figure 2.TEM image of $LiNi_{0.5}Mn_{0.5}O_2$: Left is synthesized from Ion-exchange ($IE\text{-}LiNi_{0.5}Mn_{0.5}O_2$), right is from Solid-state ($SS\text{-}LiNi_{0.5}Mn_{0.5}O_2$)

From the TEM image (Figure2) the left one is synthesized via ion-exchange ($IE\text{-}LiNi_{0.5}Mn_{0.5}O_2$), the layers between each other is well organized and barely see disorder inside the structure. The right one is $SS\text{-}LiNi_{0.5}Mn_{0.5}O_2$ that author synthesized from conventional high temperature synthesis. Although the particle is smaller than $IE\text{-}LiNi_{0.5}Mn_{0.5}O_2$ but the structure is less organized

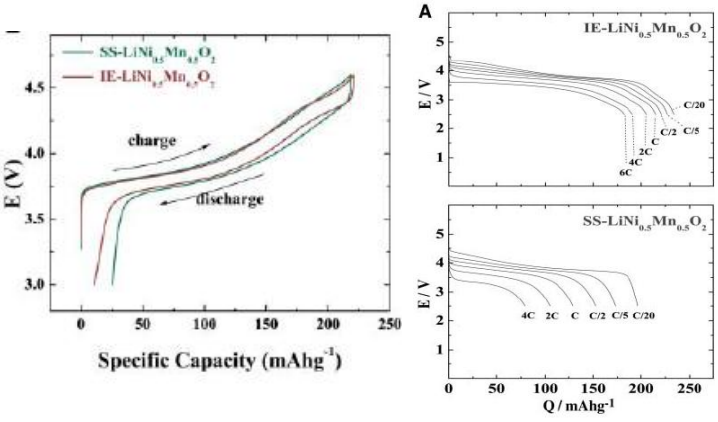

Figure 3(a). First cycle charge/discharge curves of $LiNi_{0.5}Mn_{0.5}O_2$ at C/20 rate **(b)** discharge curve at various C rates.

than it. The author mentioned in SS-$LiNi_{0.5}Mn_{0.5}O_2$ they always observed Li and Ni atoms exchange sites that will increase the activation barrier of lithium diffusion. The reason why there is less Li-Ni exchange site in IE-$LiNi_{0.5}Mn_{0.5}O_2$ is that according to the Shannon radii, the radius of Na^{+}(1.18) and Ni^{2+}(0.69) are quite different therefore using Na to synthesize $NaNi_{0.5}Mn_{0.5}O_2$ the exchange of Na and Ni is not likely happen. We can synthesize the framework first and replace the Na with Li; this will solve the site-exchange problem. If Ni is in Li site, the length of lithium slab will decrease and this will increase the lithium-oxygen bonding (Li-O) which higher the activation barrier. In Figure 4, base on the computational calculation if there is 8.3% Li-Ni exchange the barrier energy will increase 100mev which is pretty remarkable. According to SSNMR data in Figure 5, the peak at 670 and 1450 are lithium in lithium slab and transition slap respectively. It's quite obvious that the Li-Ni exchange in IE-$LiNi_{0.5}Mn_{0.5}O_2$ is really low which means the strategy (ion exchange) the author use is working.

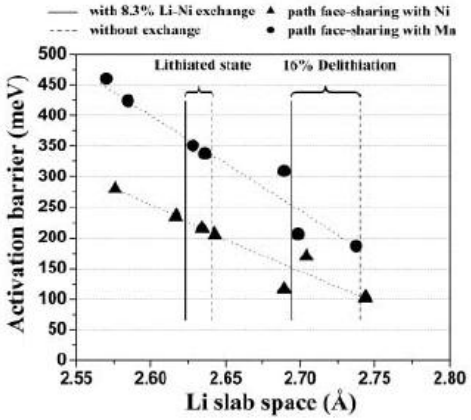

Figure 4.Calculate activation barrier as a function of Li slab space

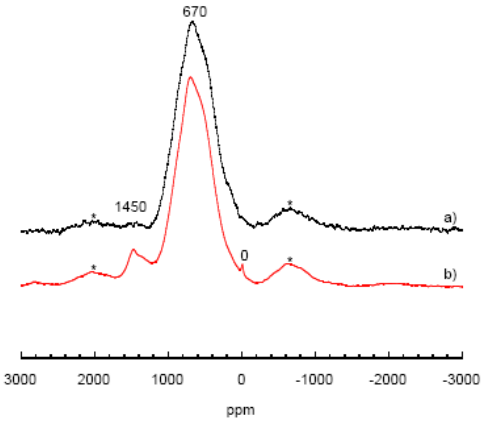

Figure 5. Solid-State NMR spectrum of IE-$N_{i0.5}Mn_{0.5}O_2$ and SS- IE-$N_{i0.5}Mn_{0.5}O_2$, the peak at 670ppm is Li at Li-slab and peak at 1450ppm is Li at Transition metal slab

In the first charge/discharge curves (Figure 4a), the difference is quite small. However, after cycles several times (Figure 5a) if there are defects inside the structure when lithium traveling inside, lithium will be trapped by the defects that will lower the capacity.

The cycle life will be better for IE-$LiNi_{0.5}Mn_{0.5}O_2$ than SS-$LiNi_{0.5}Mn_{0.5}O_2$ as well; the cycle life of lithium battery has something to do with thermal stability of structure. When the battery is working especially in high charge/discharge rate (Figure 3b) that will generate heat and inducing phase transition easily. Therefore, if the structure is well ordered that will improve the thermal stability and has longer life time. However one point I would like to address here, is the nano effect. If we can minimize the particle size, which means shorten the lithium diffusion distance and we can increase the power density. On the other hand, nano-particle usually has higher energy than bulk material which will lower the cycle life. The performance of nano material maybe excellent at begin but it will drop very fast either due to the aggregation or phase transition. The best case scenario is we can synthesize a nano-particle with no defect and is thermal stable.(Usually that won't happen in reality).

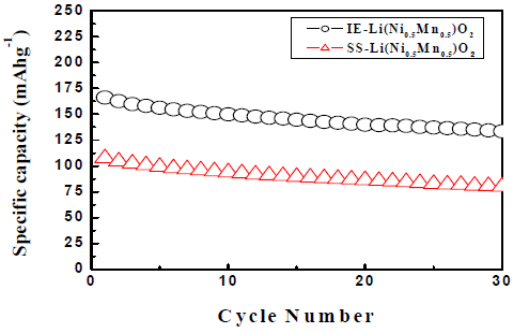

Figure 6. Cycle numbers test at 1C rate

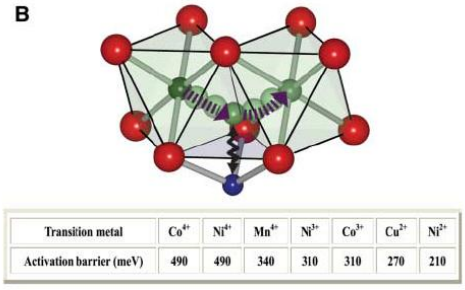

Transition metal	Co^{4+}	Ni^{4+}	Mn^{4+}	Ni^{3+}	Co^{3+}	Cu^{2+}	Ni^{2+}
Activation barrier (meV)	490	490	340	310	310	270	210

Figure 7.ab initio computational model for activation barrier of different transition metals

The other important issue is that how easily of lithium can move inside the structure and this one relate to the activation barrier. Lithium is coordinated octahedrally by oxygen and due to previous work[2,3] , the path way of lithium hopping inside the structure like Figure 5. Lithium ion will pass through the tetrahedral site, therefore the transition metals below that tetrahedral site will influence a lot and the activation barrier became rate determine step of lithium diffusion. The lower activation barrier energy the faster of lithium diffusion which means it can provide high power density. From the table the transition metals Ni^{2+} and Mn^{4+} give relative low energy barrier, this explains why the performance of $LiNi_{0.5}Mn_{0.5}O_2$ is better than others. In the article author mentions that the function of $LiCoO_2$

and $LiNi_{0.5}Mn_{0.5}O_2$ are fundamentally different. In $LiCoO_2$, Co has three positive charges when the lithium been extracted from the structure the cobalt will be oxidized to positive 4 and Co will be at high oxidation state, we can image the structure will be very unstable. On the other hand, $LiNi_{0.5}Mn_{0.5}O_2$ is bifunctional, the Ni^{2+} will lose two electrons act as double redox center[4-6] and Mn^{4+} will provide the stability for host structure.[7] That explains the reason why the performance of $LiNi_{0.5}Mn_{0.5}O_2$ is better than $LiCoO_2$.

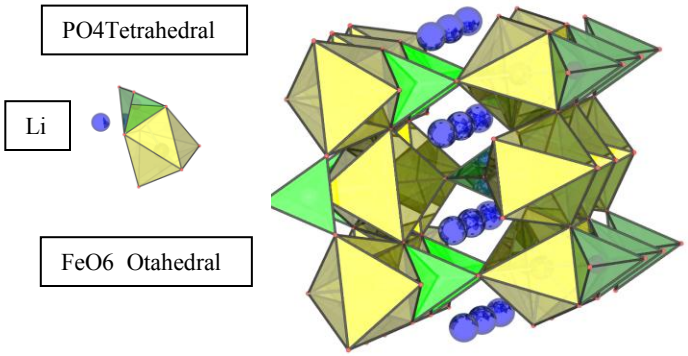

Figure 8. The structure of LiFePO4, Li will hop trough 1D channel.

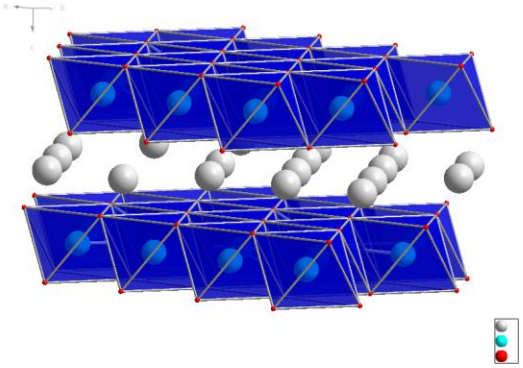

Figure 9. The structure of $LiCoO_2$, Li will hop trough 2D layered space.

There are still other promising cathode materials which like $LiFePO_4$ (Figure 8) proposed by john goodenough in1996.[8] The structure is 3D and very firm. The experimental capacity is very close to theoretical value and the life time is the longest among any all cathode materials used in lithium secondary battery right now. Nevertheless, it is very environmental-friendly and safe. The only disadvantage of LiFePO4 is low conductivity. With coating carbon on the surface we can improve the conductivity a lot. But still the power density is low compare to IE-$LiNi_{0.5}Mn_{0.5}O_2$. (IE-$LiNi_{0.5}Mn_{0.5}O_2$ is layer structure and LiFePO4 is 3D structure which lithium will have more freedom in layer structure)

The following are requirements that a good cathode material for vehicle should have:

1. high power density(lithium diffusion rate)
2. high capacity(how many Li can be extracted from structure)
3. thermal and electronic structure stability(during the redox reaction, the transition metal will change the electron state and something like Jahn-tell distortion will happen and induce the phase transition[9.10])
4. low price

In short, the author use ab initio computational model to verify the transition cation is a key that influence lithium hopping. And author successfully synthesizes low defects of $LiNi_{0.5}Mn_{0.5}O_2$ via ion-exchange process which can provide high power density. $LiNi_{0.5}Mn_{0.5}O_2$ will be potential candidate for lithium battery, however, the author also point out the extra cost of ion-exchange and cycle life need to be investigated further before commercialize it.

References

(1). M. S. Whittingham, *Science* **1976**, 192, 1126.
(2). A. Van der Ven, G. Ceder, Electrochem. *Solid-State Lett*. **2000**, 3, 301
(3). A. Van der Ven, G. Ceder, *J. Power Sources* **2001**, 97-98, 529
(4). T. Ohzuku, Y. Makimura, *Chem. Lett.* **2001,** 8, 744
(5). Z. Lu, D. D. MacNeil, J. R. Dahn, *Electrochem. Solid-State Lett.***2001**, 4, A191
(6). J. Reed, G. Ceder, Electrochem. *Solid-State Lett.* **2002**, 5, A145
(7). M. M. Thackeray, Prog. *Solid State Chem.* **1997**, 25, 1
(8) A.K. Padhi, K.S. Nanjundaswamy and J.B. Goodenough, *J. Electrochem.* **1997**, Soc., 144, 1188-1194.
(9) R.J. Gummow, A.de. Kock, M.M. Thackeray, Solid State Ionics 1994, 69, 59.
(10)M.M. Thackeray, Prog. *Solid State Chem.***1997**, 25, 1.

High catalytic activity of $Au/CeO_x/TiO_2(110)$ controlled by the nature of the mixed-metal oxide at the nanometer level

Joon B. Park[a], Jesus Graciani[a], Jaime Evans[b], Dario Stacchiola[a], Shuguo Ma[a], Ping Liu[a], Akira Nambu[a], Javier Fernández Sanz[c], Jan Hrbek[a], and José A. Rodriguez[a,1]

[a]Chemistry Department, Brookhaven National Laboratory, Upton, NY 11973; [b]Facultad de Ciencias, Universidad Central de Venezuela, Caracas, 1020-A, Venezuela; and [c]Departamento de Química Física, Universidad de Sevilla, E-41012-Seville, Spain

Edited by Gabor A. Somorjai, University of California, Berkeley, CA, and approved January 30, 2009 (received for review December 11, 2008)

Mixed-metal oxides play a very important role in many areas of chemistry, physics, materials science, and geochemistry. Recently, there has been a strong interest in understanding phenomena associated with the deposition of oxide nanoparticles on the surface of a second (host) oxide. Here, scanning tunneling microscopy, photoemission, and density-functional calculations are used to study the behavior of ceria nanoparticles deposited on a $TiO_2(110)$ surface. The titania substrate imposes nontypical coordination modes on the ceria nanoparticles. In the $CeO_x/TiO_2(110)$ systems, the Ce cations adopt an structural geometry and an oxidation state (+3) that are quite different from those seen in bulk ceria or for ceria nanoparticles deposited on metal substrates. The increase in the stability of the Ce^{3+} oxidation state leads to an enhancement in the chemical and catalytic activity of the ceria nanoparticles. The codeposition of ceria and gold nanoparticles on a $TiO_2(110)$ substrate generates catalysts with an extremely high activity for the production of hydrogen through the water–gas shift reaction ($H_2O + CO \rightarrow H_2 + CO_2$) or for the oxidation of carbon monoxide ($2CO + O_2 \rightarrow 2CO_2$). The enhanced stability of the Ce^{3+} state is an example of structural promotion in catalysis described here on the atomic level. The exploration of mixed-metal oxides at the nanometer level may open avenues for optimizing catalysts through stabilization of unconventional surface structures with special chemical activity.

heterogeneous catalysis | imaging | structural properties | surface reactivity

Mixed-metal oxides play a very important role in many areas of chemistry, physics, materials science, and geochemistry (1–6). In technological applications, they are used in the fabrication of microelectronic circuits, piezoelectric devices, and sensors and as catalysts. Over the years, there has been a strong interest in understanding the behavior of mixed-metal oxides at a fundamental level (1–3). What happens when nanoparticles (NPs) of a given metal oxide are deposited on the surface of a second (host) oxide (3, 7)? In principle, the combination of 2 metals in an oxide matrix can produce materials with novel structural and/or electronic properties. At a structural level, a dopant can introduce stress into the lattice of an oxide host, inducing in this way the formation of defects. On the other hand, the lattice of the oxide host can impose on the dopant element nontypical coordination modes. Finally, metal ↔ metal or metal ↔ oxygen ↔ metal interactions in mixed-metal oxides can give electronic states not seen in single-metal oxides.

In this article, we use photoemission, scanning tunneling microscopy (STM), and calculations based on density-functional theory (DFT) to study the behavior of ceria NPs in contact with $TiO_2(110)$. Ceria and titania are among the most widely used oxides in catalysis (1, 4–6, 8–12). These oxides are important components in catalysts used for the production of clean hydrogen through the water–gas shift reaction ($H_2O + CO \rightarrow H_2 + CO_2$) and for the oxidation of carbon monoxide ($2CO + O_2 \rightarrow 2CO_2$). Ceria and titania adopt different crystal lattices in their most stable bulk phases, fluorite and rutile, respectively (2, 13). Within the fluorite structure each Ce atom is bonded to 8 O atoms, whereas 6 O atoms surround the Ti atoms in the rutile structure. One of the most interesting properties of ceria is its ability to undergo a conversion between "+4" and "+3" formal oxidation states (13). The surface chemistry and catalytic properties of CeO_2 depend on the formation of Ce^{3+} ions (13), and different approaches are followed to maximize their concentration (4, 5, 8). In the $CeO_x/TiO_2(110)$ systems, the titania substrate imposes on the ceria NPs nontypical coordination modes with a subsequent change in the relative stability of the Ce^{3+}/Ce^{4+} oxidation states that leads to a significant enhancement in chemical activity. Furthermore, the deposition of gold NPs on $CeO_x/TiO_2(110)$ produces surfaces with an extremely high catalytic activity for the water–gas shift reaction and the oxidation of CO. This is quite remarkable because neither $Au/TiO_2(110)$ nor $Au/CeO_2(111)$ come close to matching the catalytic activity of $Au/CeO_x/TiO_2(110)$.

Experimental and Theoretical Methods

Microscopy, Photoemission, and Catalytic Tests. The microscopy studies were carried out in an Omicron variable temperature STM system that is directly attached to a main ultrahigh vacuum (UHV) chamber equipped with optics for low-energy electron diffraction, instrumentation for Auger electron spectroscopy and surface cleaning facilities (9, 14). Chemically etched W tips were used for imaging the surfaces. The $TiO_2(110)$ crystal was cleaned by several cycles of Ne^+ sputtering (1 keV, 40 min) and annealing (950 K, 5 min), and XPS/AES studies confirmed that there were no surface contaminants after this treatment (15).

Furthermore, the high-resolution STM images of the surface exhibited bright Ti rows separated by 6.5 Å, as typically observed for $TiO_2(110)$-(1x1) (16). Photoemission studies were performed at beamline U7A of the National Synchrotron Light Source (NSLS) at Brookhaven National Laboratory (9) by using a photon energy of 625 eV to collect the O 1s and Ti 2p regions, and 325 eV to collect the Ce 4d, Au 4f, and valence regions. In a separate UHV chamber, we acquired XPS spectra (Ce 3d, Ti 2p, O 1s, and Au 4f regions) and UPS spectra (valence region) using Mg Kα and He-I radiation, respectively. Ce and Au were deposited on $TiO_2(110)$ by using metal evaporators (9, 14, 17). The flux of the Au doser was calibrated by depositing Au onto a Mo(100) crystal and measuring the thermal desorption spectra of the admetal (17). The area of the titania surface covered by ceria

Author contributions: J.B.P., J.G., J.E., D.S., S.M., P.L., A.N., J.F.S., J.H., and J.A.R. designed research; J.B.P., J.G., J.E., D.S., S.M., A.N., and J.A.R. performed research; J.B.P., J.G., J.E., D.S., S.M., P.L., A.N., J.F.S., J.H., and J.A.R. analyzed data; and J.A.R. wrote the paper.

The authors declare no conflict of interest.

This article is a PNAS Direct Submission.

[1]To whom correspondence should be addressed. E-mail: rodrigez@bnl.gov.

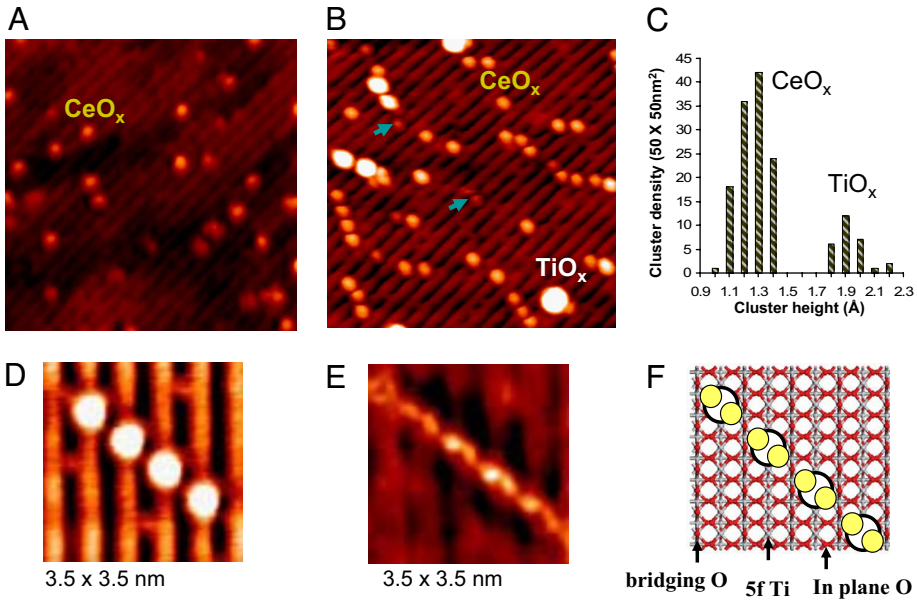

Fig. 1. STM results illustrating morphological changes of CeO_x on the TiO_2(110) surface. (*A*) STM image (15 × 15 nm) taken after depositing Ce atoms at 298 K in UHV (V_t = 1.3 V and I_t = 0.05 nA). (*B*) STM image (15 × 15 nm) acquired after depositing Ce atoms at 600 K and subsequent annealing at 900 K in O_2 (P_{O2} ≈1 × 10^{-7} Torr) (V_t = 1.2 V and I_t = 0.07 nA). (*C*) Height distribution for the spots seen in *B*. (*D* and *E*) Zoomed-in STM images (3.5 × 3.5 nm) of a diagonal array of CeO_x taken at different imaging condition of 1.2 V, 0.06 nA and 0.4 V, 0.06 nA, respectively. (*F*) Model showing possible orientations for the bright protrusions of CeO_x in *D* and *E*. The dimers of ceria are shown as a combination of white and yellow spheres.

and gold was estimated by using STM images or a combination of ion-scattering spectroscopy (ISS) and photoemission (9, 17).

The catalytic studies were carried out in a system that combines a batch reactor and a UHV chamber (9, 17). The sample could be transferred between the reactor and UHV chamber without exposure to air. Typically, it was transferred to the batch reactor at ≈298 K, and then the reactant gases were introduced (water–gas shift: 20 Torr of CO and 10 Torr of H_2O; CO oxidation: 4 torr of CO and 2 Torr of O_2). The catalytic activity for the water–gas shift was measured at 625 K (9, 17), with a temperature of 300 K for the oxidation of CO (10). Product yields were analyzed by gas chromatography or mass spectroscopy (9, 17). The amount of molecules produced was normalized by the active area exposed by the sample. In our reactor, a steady-state regime for the water–gas shift or the oxidation of CO was reached after 2–3 min of reaction time.

DFT Calculations. Periodic DFT + U calculations were performed by using the VASP code (18) using a (4 × 2) 6-layer thick supercell to model the TiO_2(110) surface (19). The adlayer and first 4 layers of the titania slab were allowed to relax during the DFT geometry optimizations. We used the Perdew–Wang 91 GGA functional for exchange-correlation, the projector-augmented wave approach, and plane-waves with a cutoff energy set at 400 eV. We treated the Ti (3s, 3p, 3d, 4s), Ce (4f, 5s, 5p, 5d, 6s), and O (2s,2p) electrons as valence states, whereas the remaining electrons were kept frozen as core states (19). The calculations were performed at the Γ point of the Brillouin zone (18). To reproduce the valence spectra of Ce/TiO_2(110), see below, we used U_{eff} parameters with a value of 4.5 eV for Ce and Ti. This value is close to those used in previous studies for bulk ceria or titania (20). The introduction of the U_{eff} parameters in the DFT calculations was found to be essential to correctly reproduce the position of the occupied Ce 4f and Ti 3d levels in the valence region, even though the trends found in the energetics for the coadsorption of Ce and O on TiO_2(110) were almost the same with or without the U_{eff} parameters.

Growth of Ceria on TiO_2(110)

In Fig. 1, we show STM images acquired after depositing cerium on TiO_2(110) under different conditions. Fig. 1*A* corresponds to an image obtained after dosing Ce atoms under ultrahigh vacuum (UHV) at a sample temperature of 298 K. The bright spots have an average height of 1.4 ± 0.2 Å over the flat terrace and correspond to clusters of cerium oxide. The corresponding XPS and UPS spectra indicated that cerium was in an oxidation state of +3, and, consequently, its deposition led to the partial reduction of titanium cations with the appearance of Ti^{3+}. Fig. 2 *Left* shows a typical UPS spectrum for this type of Ce/TiO_2(110) surface. The features ≈1 eV can be assigned to Ti^{3+} centers (1, 16), whereas those at 2–3.5 eV correspond to Ce^{3+} centers (21). The existence of Ce^{3+} is corroborated by the Ce 3d XPS data in Fig. 2 *Right*. The Ce 3d XPS spectrum for the as-prepared Ce/TiO_2(110) surface has the distinctive line shape of Ce^{3+} species (21, 22). Using DFT calculations, we investigated the bonding of Ce atoms to the TiO_2(110) surface. The Ce atoms prefer the bonding configuration shown at the bottom of Fig. 2, interacting simultaneously with bridging and in-plane O atoms of the titania substrate. Upon adsorption, Ce formally releases 3 electrons to the oxide host, which move from the 6s and 5d levels in Ce to the lower-energy 3d levels in Ti, reducing 3 Ti^{4+} cations to Ti^{3+}. The fourth valence electron from Ce is in a 4f level of lower energy than the 3d from Ti and therefore is not transferred, leaving the oxidation state of Ce as 3+. The adsorption of oxygen on the Ce/TiO_2(110) surfaces led to the disappearance of Ti^{3+} sites in the XPS/UPS spectra and in the DFT-calculated density of states. The stability of the Ce^{3+} cations was verified by their resistance to oxidation under UHV conditions. We had to expose the Ce/TiO_2(110) surfaces to an O_2 pressure of 1 Torr in the batch reactor to obtain the typical Ce 3d XPS spectrum of Ce^{4+} cations (21, 22), see Fig. 2 *Right*.

To avoid the reduction of the titania substrate, Ce atoms were deposited at 600 K and annealed to 900 K under O_2 (≈1 × 10^{-7} Torr) for 5 min. This led to the image shown in Fig. 1*B*. In this image, the features nonrelated to the ideal TiO_2(110) surface can be separated according to their height, as seen in Fig. 1*C*. Most of the spots (≈80%) have a height of 1.3 ± 0.2 Å. These spots

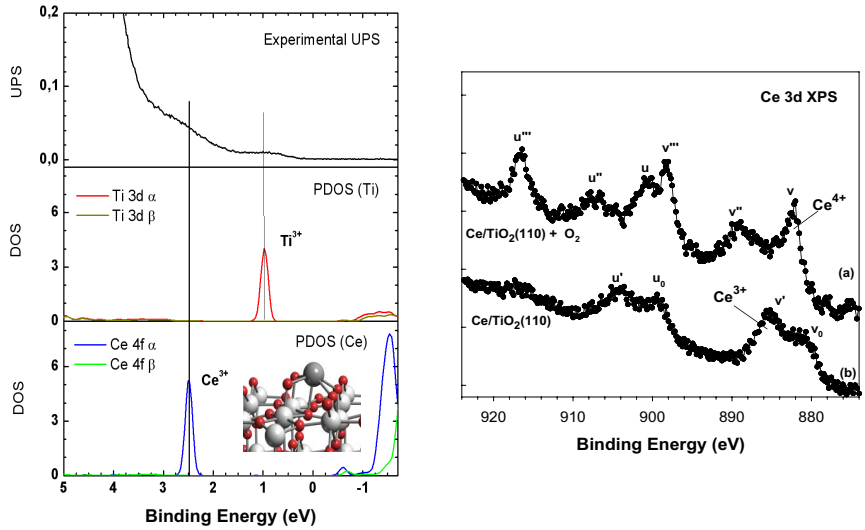

Fig. 2. Electronic properties of CeO_x/TiO_2 (110). (*Left*) (*Top*) Shown is a UPS spectrum acquired after depositing Ce atoms on TiO_2(110) at 298 K. The features marked by vertical lines are not seen on clean stoichiometric TiO_2(110). (*Middle* and *Bottom*) Displayed are DFT calculated density-of-states (DOS) for a Ce/TiO_2(110) surface, including occupied (positive binding energy) and unoccupied states (negative binding energy, states not observable in UPS). The drawing in the *Inset* shows the bonding configuration of the Ce atoms. Color code for spheres is gray, cerium; red, oxygen; white, titanium. (*Right*) Ce 3d XPS spectra taken after depositing Ce on TiO_2(110) at 298 K (lower), with subsequent exposure to 1 Torr of O_2 (upper). The change in the line shape denotes a $Ce^{3+} \rightarrow Ce^{4+}$ transformation (21, 22). The ''u'' and ''v'' peaks refer to various final states that are caused by transitions from valence band electrons into Ce 4f states (22).

can be attributed to CeO_x, after comparing with the image in Fig. 1*A* for Ce/TiO_2(110). A minority of the spots (≈20%) in Fig. 1*B* have a height of 1.9 ± 0.3 Å. These features were not seen for Ce/TiO_2(110) and probably correspond to (1 × 2) reconstructions of TiO_2(110) induced by O_2 chemisorption (11, 16). They are a consequence of the migration of interstitial Ti atoms from the bulk to the surface of the titania crystal (11, 16). We found them also in blank experiments for O_2/TiO_2(110). In Fig. 1*B*, the spots due to CeO_x are arranged forming units that are oriented ≈48°, 66°, or 90° with respect to the Ti rows of the oxide substrate. These units were not seen in blank experiments for Ce/TiO_2(110) or O_2/TiO_2(110) and are characteristic of the $O_2/CeO_x/TiO_2$(110) systems. Close-up images of a ≈44° aligned unit are shown in Fig. 1 *D* and *E*. In Fig. 1*D*, the bright ceria spots are centered on 5f Ti rows and all have a height close to 1.35 Å and a diameter of 6.8 Å. Their size and position suggests that each spot may contain 2 Ce atoms located in between the O bridging and 5f Ti rows. This is confirmed by scanning the same feature with lower imaging bias (0.4 V instead of 1.2 V), where the electron tunneling occurs at different density of states in CeO_x/TiO_2(110) systems (Fig. 1*E*). From the STM data, one can construct a structural model consisting of an array of dimers of ceria as displayed in Fig. 1*F*. According to our measurements of core and valence photoemission, the oxidation state of the Ce atoms inside the dimers is essentially +3. Thus, in the CeO_x/TiO_2(110) systems, the Ce cations adopt a structural geometry and an oxidation state that are quite different from those seen in bulk ceria (2, 13) or for NPs of ceria deposited on metal substrates (7, 9).

Using DFT, we investigated the process of adsorption–oxidation for Ce deposited on TiO_2(110). Fig. 3 shows the calculated energy pathway for such a process. The adsorption energy of atomic Ce is very high ($\Delta E = -7.23$ eV). On its most stable adsorption site, Ce interacts with 2 bridging and 1 in-plane O atoms (Fig. 3, step1). The fact that 3 electrons move from high to lower energy levels, $Ce(5d^16s^2) \rightarrow Ti(3d^1)$, explains in part the high adsorption energy of Ce. The adsorption process of atomic Ce could be described as

$$Ce + 3Ti^{4+}(TiO_2) \rightarrow Ce^{3+} + 3Ti^{3+}(TiO_2) \qquad [1]$$

The dissociation of O_2 near the adsorbed Ce is a highly exothermic process ($\Delta E = -6.66$ eV). The final structure is a unit of CeO_2 over TiO_2(110), where the O atoms are adsorbed on top of in-plane Ti atoms and strongly interact with the Ce atom (Fig. 3, step 2). The oxidation state of the Ce in this configuration is 4+

$$Ce^{3+} + 3Ti^{3+}(TiO_2) + O_2 \rightarrow CeO_2(Ce^{4+})/TiO_2 \qquad [2]$$

Such CeO_2 monomers could be assigned to the smallest spots observed in STM at very low coverages of ceria. For the surface in Fig. 1*B*, possible CeO_2 monomers are denoted by arrows and, as predicted by the DFT calculations, they are not located at the center of the Ti rows. The CeO_2 monomers are excellent sites for

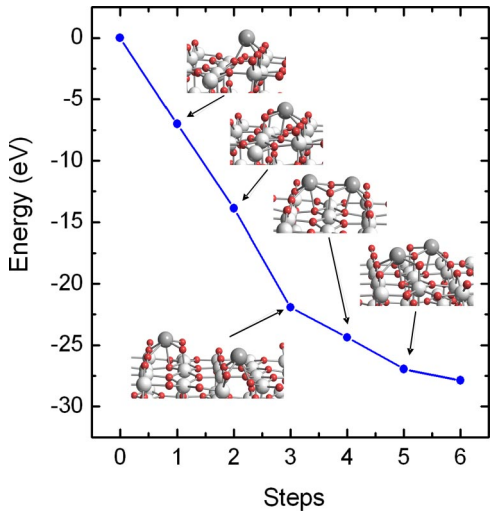

Fig. 3. DFT calculated energy pathway for the adsorption and oxidation of Ce on TiO_2(110). The following steps were examined: (1) adsorption of Ce; (2) O_2 adsorption-dissociation and formation of the first monomer (CeO_2); (3) adsorption of a second cerium atom; (4) formation of the first Ce_2O_2 dimer; (5) adsorption of ½O_2 and formation of the Ce_2O_3 dimer; and (6) adsorption of ½O_2 and formation of 2 CeO_2 monomers.

the adsorption of a second Ce atom to form dimers (Fig. 3, step 4). The increment in the adsorption energy with respect to the adsorption on a clean surface is due to the fact that 1 of the 3 electrons released by the incoming Ce does not go to the high-energy 3d levels of Ti but rather to the 4f of Ce^{4+} from the CeO_2 monomer, which is reduced to Ce^{3+}

$$CeO_2(Ce^{4+})/TiO_2 + Ce + 2Ti^{4+}(TiO_2) \rightarrow Ce_2O_2(Ce^{3+}) \text{ on } TiO_2 + 2Ti^{3+}(TiO_2) \quad [3]$$

The addition of oxygen to the Ce_2O_2 unit generates Ce_2O_3.

$$Ce_2O_2(Ce^{3+})/TiO_2 + 2Ti^{3+}(TiO_2) + \frac{1}{2}O_2 \rightarrow Ce_2O_3(Ce^{3+}) \quad [4]$$

on TiO_2, and the ceria dimer adopts a configuration (Fig. 3, step 5) where shared oxygen leads to a diagonal arrangement in agreement with the results of STM (Fig. 1 *E* and *F*). In the presence of oxygen, the complete oxidation of Ce has to be considered, going from a Ce_2O_3 dimer to 2 CeO_2 monomers (Fig. 3, step 6). Differently from the previous step, here, there are not high-energy Ti 3d electrons but 2 electrons in low-energy Ce 4f states. The process is exothermic but only by −0.92 eV, 3 times less than the energy released in the previous step. This means that as long as Ti^{3+} species exist, O_2 will prefer to adsorb and dissociate on them because the stabilization energy for the system is much higher. Therefore, even though the oxidation process of dimers is favorable, the other site is preferred for the adsorption and dissociation of O_2. This illustrates the complex interplay that one can have when dealing with the electronic and chemical properties of a mixed-metal oxide.

For applications in catalysis, the relative stability of the Ce^{3+}/Ce^{4+} oxidation states of ceria is a very important issue (1, 4–6, 13, 23, 24). We calculated the energy released by the reactions

$$Ce_2O_3 + \frac{1}{2}O_2 \rightarrow 2CeO_2 \quad [5]$$

$$2CeO_2 + CO \rightarrow Ce_2O_3 + CO_2 \quad [6]$$

for both bulk ceria and Ce_2O_3 dimers deposited on TiO_2(110). The ΔE for the oxidation process, (the reaction shown in **5**), was −2.56 eV in the case of bulk Ce_2O_3 and −0.92 eV for the Ce_2O_3 dimers bonded to titania. The reduction of CeO_2/TiO_2(110) by CO, (the reaction shown in **6**), was a very exothermic process with a ΔE of −2.35 eV. In contrast, the ΔE for the corresponding reaction of bulk CeO_2 was −0.71 eV. These trends were confirmed by comparing reduction/oxidation experiments on CeO_2 (111) and CeO_x/TiO_2(110). For example, a CeO_2(111) surface did not undergo reduction under an atmosphere of 20 Torr of CO at 400 K (17), but a CeO_2/TiO_2(110) surface (formed by exposing CeO_x/TiO_2(110) to 1 Torr of O_2 at 298 K) was completely transformed into Ce_2O_3/TiO_2(110). The high stability of the Ce^{3+} cations in CeO_x/TiO_2(110) is a consequence of their nontypical coordination mode and the effect of Ce (4f)–O (2p)–Ti (3d) bonding interactions.

Catalytic Activity of $Au/CeO_x/TiO_2$(110)

The WGS reaction is a critical catalytic process for the production of clean hydrogen in the chemical industry (4, 5). There is a continuous search for catalysts with a better WGS activity (4–6, 9). As shown below, the deposition of gold NPs on CeO_x/TiO_2(110) yielded surfaces with an extremely high catalytic activity for the WGS. Fig. 4 displays STM images acquired from the same surface area before (Fig. 4*A*) and after (Fig. 4*B*) depositing gold on CeO_x/TiO_2(110) at 298 K with subsequent annealing to 600 K (Fig. 4*C*). The CeO_x/TiO_2(110) was preannealed under O_2 (≈1 × 10^{-7} Torr) at 900 K and had a morphology similar to that seen in Fig. 1*B*. The deposition of Au at room temperature, ≈0.2 monolayer, produced 3-dimensional metal particles anchored to steps of the titania surface, "a" sites, to the (1 × 2) reconstructions of TiO_2(110), "b" sites, and to the CeO_x dimers, "c" sites. Annealing to 600 K produced large particles of Au that were simultaneously located on b and c sites. Au NPs with a diameter as large as 5.9 nm and a height of 1.3 nm were seen, but smaller metal particles were also present on the CeO_x/TiO_2(110) surface. On this surface, the dispersion of the Au NPs was substantially larger than seen on a pure TiO_2(110) surface where Au mainly binds to the steps (10, 15).

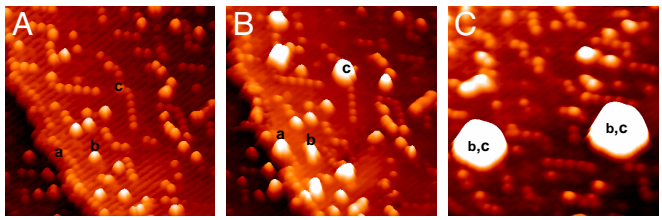

Fig. 4. Morphology of $Au/CeO_x/TiO_2$ (110). (*A*) STM image of a CeO_x/TiO_2(110) surface. Ce was deposited at 600 K under an atmosphere of O_2 (≈1 × 10^{-7} Torr) and then the sample was annealed at 900 K in O_2. (*B*) STM image for a $Au/CeO_x/TiO_2$(110) surface. The gold was deposited on the same area shown in *A* at 298 K. Approximately 6% of the surface was covered with Au. (*C*) STM image obtained after annealing the system in *B* to 600 K. All of the STM images correspond to an area of 20 × 20 nm and imaging conditions of V_t = 1.5 V and I_t = 0.03 nA.

Neither CeO_x/TiO_2(110) nor Au(111) were able to catalyze the WGS. However, $Au/CeO_x/TiO_2$(110) surfaces are outstanding catalysts for the WGS as shown in Fig. 5. We performed test experiments in which Au/TiO_2(110) surfaces were prepared following the same steps used for the synthesis of $Au/CeO_x/TiO_2$(110) but without the deposition of cerium. The Au/TiO_2(110) systems were good WGS catalysts, see Fig. 5 *Upper*, but they did not come close to match the activity of $Au/CeO_x/TiO_2$(110). The same is valid when comparing with the WGS activities of Au/CeO_2(111) (17), CeO_x/Au(111) (9), Cu/ZnO(0001) (17), and copper single crystals (17, 25). Cu/ZnO is the most common WGS catalyst used in the industry (5, 17, 25), and copper is the best pure-metal catalyst (25, 26). For the $Au/CeO_x/TiO_2$(110) catalyst in Fig. 5, one could assume that the concentration of active sites is proportional to the number of ceria regions in contact with gold NPs. Because only 12% of the titania support was covered by ceria, as measured by ion scattering spectroscopy (ISS), the $Au/CeO_x/TiO_2$(110) catalyst must be at least 300 times more active than a Cu (100) surface on a per-active-site basis.*

Postreaction characterization of the $Au/CeO_x/TiO_2$(110) surfaces with XPS showed the presence of metallic Au and Ce^{3+} cations. An identical result was found in in situ measurements of X-ray absorption spectroscopy for $Au/CeO_x/TiO_2$ powders under

*It is usually assumed that all atoms of a flat Cu(100) surface, 1.53 × 10^{15} atoms cm^{-2}, are active in the WGS reaction (25). The structural model in Fig. 1*F* was used to calculate the area occupied by a Ce_2O_3 dimer on the TiO_2(110) surface. Using this and the ceria coverage determined from ISS measurements (≈12% of the titania surface was covered), we find that the concentration of Ce in the $Au/CeO_x/TiO_2$(110) catalyst of Fig. 5 was in the order of 0.03 × 10^{15} atoms cm^{-2}. This is an upper limit to the actual concentration of the active sites, because not all of the Ce atoms had a Au particle nearby (see Fig. 4 *B* and *C*). After subtracting the WGS activity of Au/TiO_2(110) from that of $Au/CeO_x/TiO_2$(110), one finds that the Au/ceria sites are at least 300 times more active than the atoms in a Cu(100) surface.

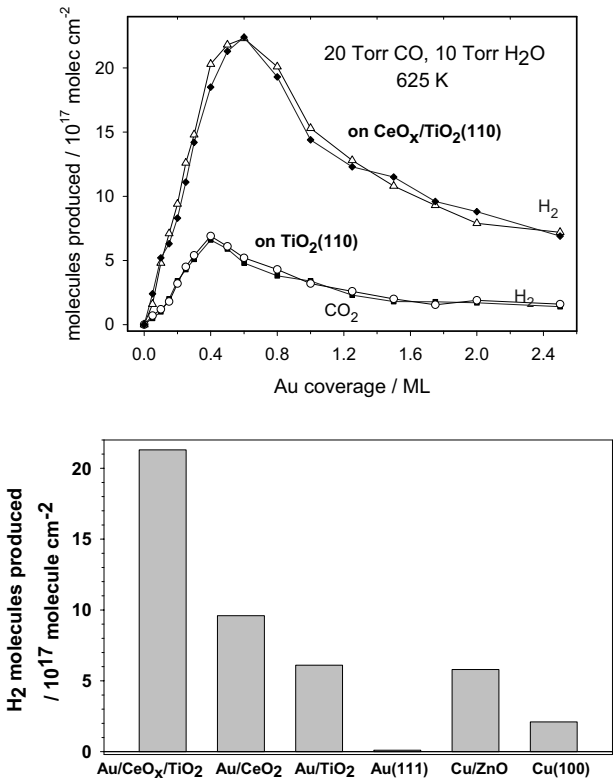

Fig. 5. Water-gas shift catalysis. (*Upper*) Water–gas shift activity of Au/TiO_2(110) and Au/CeO_x/TiO_2(110) as a function of Au coverage. The area of TiO_2(110) covered by CeO_x was measured with ISS, before depositing gold, and found to be ≈12% of the clean substrate. The reported values for the production of H_2 (blue curve) and CO_2 (black curve) were obtained after exposing the catalysts to 20 Torr of CO and 10 Torr of H_2O at 625 K for 5 min. The number of H_2 and CO_2 molecules produced is normalized by the sample surface area. (*Lower*) Comparison of the water–gas shift activity of Cu(100), Au(111), and 0.5 mL of Au supported on TiO_2(110), CeO_2(111) or CeO_x/TiO_2(110). The data for Cu(100), Cu/ZnO(0001) and Au/CeO_2(111) were taken from ref. 17.

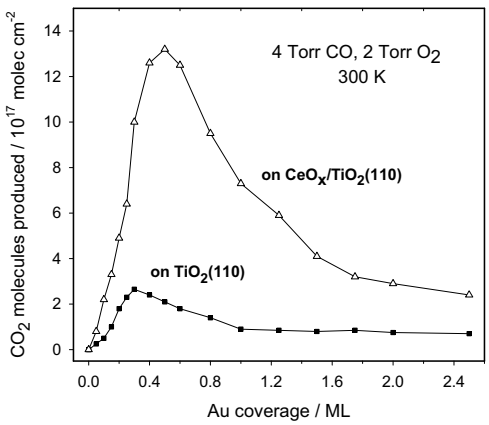

Fig. 6. CO oxidation activity of Au/TiO_2(110) and Au/CeO_x/TiO_2(110) as a function of Au coverage. The area of TiO_2(110) covered by CeO_x was measured with ISS, before depositing gold, and found to be ≈16% of the clean substrate. The reported values for the production of CO_2 were obtained after exposing the catalysts to 4 Torr of CO and 2 Torr of O_2 at 300 K for 5 min. The number of CO_2 molecules produced is normalized by the sample surface area.

WGS reaction conditions. The high catalytic activity of Au/CeO_x/TiO_2(110) can be attributed to the special chemical properties of the supported Ce_2O_3 dimers and cooperative effects at ceria–gold interfaces. Usually, the rate-determining step in the WGS reaction is the dissociation of water (9, 17, 26). Isolated NPs of gold cannot dissociate this molecule (27, 28). We found that the Ce^{3+} sites present in CeO_x/TiO_2(110) easily dissociate water, but, upon exposure to CO, highly stable HCO_x species were formed on the oxide surface and there was no production of H_2 or CO_2 gas. In Au/CeO_x/TiO_2(110), one has a bifunctional catalyst: The adsorption and dissociation of water takes place on the oxide, CO adsorbs on gold NP sites, and all subsequent reaction steps occur at oxide–metal interfaces. Au NPs do catalyze the reaction of OH with CO to yield a HOCO intermediate and then H_2 and CO_2 (27). Previous studies for the WGS on Au–CeO_2 catalysts point to a direct participation of the oxide in the reaction process (4, 5, 9). Our results illustrate the tremendous impact that an optimization of the chemical properties of nanoceria can have on the activity of a WGS catalyst.

Nowadays, the oxidation of CO on Au/TiO_2 catalysts is receiving a lot of attention (1, 10, 29, 30). Fig. 6 displays the CO oxidation activity of Au/TiO_2(110) and Au/CeO_x/TiO_2(110) as a function of Au coverage. In the case of Au/TiO_2(110) a maximum in the production of CO_2 is seen at a Au coverage of ≈0.3 mL. Previous studies have shown that there is a marked size effect on the catalytic activity, with Au clusters in the range of 3–3.5 nm exhibiting the maximum reactivity (10, 29). Our STM studies for Au/TiO_2(110) and Au/CeO_x/TiO_2(110) also show a strong variation in catalytic activity with Au particle size. In all cases, Au/CeO_x/TiO_2(110) is a much better catalyst for the oxidation of CO than Au/TiO_2(110). If the maximum catalytic activities seen in Fig. 6 are normalized by the number of Au atoms present on the oxide supports (10, 29), we estimate turnover frequencies (TOFs) for CO oxidation of 2.1 molecules per site^{-1} s^{-1} for Au/TiO_2(110) and 6.2 molecules per site^{-1} s^{-1} for Au/CeO_x/TiO_2(110). These should be taken as lower limits for the TOFs because we probably overestimated the number of exposed Au active sites. Here, we are following previous studies (10, 29) that estimate the TOFs assuming total dispersion of Au on the oxide substrate. In any case, the TOF of Au/CeO_x/TiO_2(110) is already larger than the TOF found, under similar conditions of pressure and temperature, for the oxidation of CO on a highly active Au ultrathin film supported on a reduced TiO_x substrate: ≈4 molecules per site^{-1} s^{-1} (30).

The rate-limiting step for the oxidation of CO on Au/oxide surfaces is the activation and dissociation of the O_2 molecule (31–33). The oxide probably helps in the stabilization of an OC·O_2 intermediate and the breaking of the O–O bond. The structure of the titania supported ceria nanoparticles should facilitate their direct interaction with an OC·O_2 intermediate. Postreaction surface analysis with XPS showed the presence of a significant amount of Ce^{3+} in the Au/CeO_x/TiO_2(110) catalysts. This and a relatively high dispersion of Au (Fig. 4*B*) could be responsible for the superior activity of Au/CeO_x/TiO_2(110) during the oxidation of CO at room temperature.

Summary and Conclusions

Scanning tunneling microscopy, photoemission, and density-functional calculations were used to study the behavior of ceria nanoparticles deposited on a TiO_2(110) surface. The titania substrate imposes nontypical coordination modes on the ceria nanoparticles. In the CeO_x/TiO_2(110) systems, the Ce cations adopt an structural geometry and an oxidation state (+3) that are quite different from those seen in bulk ceria or for ceria nanoparticles deposited on metal substrates. The increase in the stability of the Ce^{3+} oxidation state leads to an enhancement in the chemical and catalytic activity of the ceria nanoparticles. The codeposition of ceria and gold nanoparticles on a TiO_2(110) substrate generates catalysts with an extremely high activity for the production of hydrogen through the water–gas shift reaction ($H_2O + CO \rightarrow H_2 + CO_2$) or for the oxidation of carbon monoxide ($2CO + O_2 \rightarrow$

$2CO_2$). Our results illustrate the high impact that an optimization of the chemical properties of nanoceria can have on the activity of a WGS or CO oxidation catalyst. This approach should be valid in general for catalysts that contain ceria as part of a mixed-metal oxide (4–7), opening new directions for tuning catalytic activity by coupling appropriate pairs of oxides. The key issue is to take advantage of the complex interactions that occur in a mixed-metal oxide at the nanometer level.

ACKNOWLEDGMENTS. We thank M. Pérez for thought-provoking discussions about the mechanism for the WGS reaction on $Au/CeO_x/TiO_2(110)$. The work performed at Brookhaven National Laboratory was supported by the U.S. Department of Energy, Office of Basic Energy Sciences under contract DE-AC02-98CH10886. J.E. is grateful to the Instituto de Tecnología Venezolana para el Petróleo for partial support of the work carried out at the Universidad Central de Venezuela. The work done at Seville was funded by Ministry of Science and Innovation Grant MAT2008-04918 and Barcelona Supercomputing Center—Centro Nacional de Supercomputación (Spain).

1. Zhou B, Hermans S, Somorjai GA, eds (2004) *Nanotechnology in Catalysis* (Kluwer–Plenum, New York).
2. Rao CNR, Raveau B (1998) *Transition Metal Oxides: Structure, Properties and Synthesis of Ceramic Oxides* (Wiley, New York), 2nd Ed.
3. Knauth P, Schoonman J, eds (2002) *Nanocrystalline Metals and Oxides: Selected Properties and Applications* (Springer, Berlin).
4. Fu Q, Saltsburg H, Flytzani-Stephanopoulos M (2003) Active nonmetallic Au and Pt species on ceria-based water–gas shift catalysts. *Science* 301:935–938.
5. Burch R (2006) Gold catalysts for pure hydrogen production in the water–gas shift reaction: Activity, structure and reaction mechanism. *Phys Chem Chem Phys* 8:5483–5500.
6. Gonzalez ID, Navarro RM, Alvarez-Galvan MC, Rosa F, Fierro JLG (2008) Performance enhancement in the water–gas shift reaction of platinum deposited over a cerium-modified TiO_2 support. *Catal Commun* 9:1759–1765.
7. Fernández-García M, Martinez-Arias A, Hanson JC, Rodriguez JA (2004) Nanostructured oxides in chemistry: Characterization and properties. *Chem Rev* 104:4063–4104.
8. Esch F, et al. (2005) Electron localization determines defect formation on ceria substrates. *Science* 309:752–755.
9. Rodriguez JA, et al. (2007) Activity of CeO_x and TiO_x nanoparticles grown on Au(111) in the water–gas shift reaction. *Science* 318:1757–1760.
10. Valden M, Lai X, Goodman DW (1998) Onset of catalytic activity of gold clusters on titania with the appearance of nonmetallic properties. *Science* 281:1647–1650.
11. Wendt S, et al. (2008) The role of interstitial sites in the Ti3d defect state in the band gap of titania. *Science* 320:1755–1759.
12. Diwald O, Thompson TL, Goralski EG, Walck SD, Yates JT (2004) The effect of nitrogen ion implantation on the photoactivity of TiO_2 rutile single crystals. *J Phys Chem B* 108:52–57.
13. Trovarelli A (1996) Catalytic properties of ceria and CeO_2-containing materials. *Catal Rev Sci Eng* 38:439–520.
14. Ma S, Rodriguez JA, Hrbek J (2008) STM study of the growth of cerium oxide nanoparticles on Au(111). *Surf Sci* 602:3272–3279.
15. Park JB, Conner SF, Chen DA (2008) Bimetallic Pt-Au clusters on $TiO_2(110)$: Growth, surface composition, and metal-support interactions. *J Phys Chem C* 112:5490–5500.
16. Diebold U (2003) The surface science of titanium dioxide. *Surf Sci Rep* 48:53–229.
17. Rodriguez JA, et al. (2007) Water gas shift reaction on Cu and Au nanoparticles supported on $CeO_2(111)$ and $ZnO(000\bar{1})$: Intrinsic activity and importance of support interactions. *Angew Chem Int Ed* 46:1329–1332.
18. Kresse G, Furthmuller J (1996) Efficiency of ab-initio total energy calculations for metals and semiconductors using a plane-wave basis set. *Comput Mater Sci* 6:15–50.
19. Graciani J, Alvarez LJ, Rodriguez JA, Sanz JF (2008) N doping of rutile $TiO_2(110)$ surface: A theoretical DFT study. *J Phys Chem C* 112:2624–2631.
20. Fabris S, de Gironcoli S, Baroni S, Vicario G, Balducci G (2005) Taming multiple valency with density functionals: A case study of defective ceria. *Phys Rev B* 71:041101.
21. Liu G, Rodriguez JA, Hrbek J, Dvorak J, Peden CHF (2001) Electronic and chemical properties of $Ce_{0.8}Zr_{0.2}O_2(111)$ surfaces: Photoemission, XANES, density-functional, and NO_2 adsorption studies. *J Phys Chem B* 105(32):7762–7770.
22. Pfau A, Schierbaum KD (1994) The electronic-structure of stoichiometric and reduced CeO_2 surfaces—An XPS, UPS and HREELS study. *Surf Sci* 321:71–80.
23. Wang X, et al. (2008) Ceria-based catalysts for the production of H_2 through the water–gas-shift reaction: Time-resolved XRD and XAFS studies. *Top Catal* 49:81–88.
24. Jacobs G, et al. (2004) Water–gas shift: Comparative screening of metal promoters for metal/ceria systems and role of the metal. *Appl Catal A* 258:203–214.
25. Nakamura J, Campbell JM, Campbell CT (1990) Kinetics and mechanism of the water–gas shift reaction catalyzed by the clean and Cs-promoted Cu(110) surface—A comparison with Cu(111). *J Chem Soc Faraday Trans* 86:2725–2734.
26. Gokhale AA, Dumesic JA, Mavrikakis M (2008) On the mechanism of low-temperature water gas shift reaction on copper. *J Am Chem Soc* 130:1402–1414.
27. Liu P, Rodriguez JA (2007) Water–gas-shift reaction on metal nanoparticles and surfaces. *J Chem Phys* 126:164705.
28. Ojifinni RA, et al. (2008) Water-enhanced low-temperature CO oxidation and isotope effects on atomic oxygen-covered Au(111). *J Am Chem Soc* 130:6801–6812.
29. Bamwenda GR, Tsubota S, Nakamura T, Haruta M (1997) The influence of the preparation methods on the catalytic activity of platinum and gold supported on TiO_2 for CO oxidation. *Catal Lett* 44:83–87.
30. Chen MS, Goodman DW (2004) The structure of catalytically active gold on titania. *Science* 306:252–255.
31. Hernandez NC, Sanz JF, Rodriguez JA (2006) Unravelling the origin of the high-catalytic activity of supported Au: A density-functional theory-based interpretation. *J Am Chem Soc* 128:15600–15601.
32. Molina LM, Hammer B (2003) Active role of oxide support during CO oxidation at Au/MgO. *Phys Rev Lett* 90:206102.
33. Remediakis IN, Lopez N, Norskov JK (2005) CO oxidation on rutile-supported Au nanoparticles. *Angew Chem Int Ed* 44:1824–1826.

Review: High Catalytic Activity of $Au/CeO_x/TiO_2(110)$ Controlled by the Nature of Mixed-Metal Oxide at the Nanometer Level

Devan Turner

1 December 2010

ABSTRACT In this paper, Park et al. propose and characterize a new heterogeneous catalyst that consists of a metal supported by a mixed-metal oxide. The effectiveness of the catalyst has been measured by comparing it against other well known catalysts in the water-gas shift reaction as well as in the oxidation of carbon monoxide.

Introduction

The water-gas shift reaction is of great importance in the chemical community. In this reaction, water vapor and carbon monoxide interact to produce hydrogen gas and carbon dioxide. This is used in industry for the production of high-purity hydrogen, methanol production, and in fuel-cell powered vehicles. Methanol can be produced in a reaction between hydrogen gas and carbon dioxide, both of which are products of the water-gas shift (WGS) reaction[3]. The WGS reaction is also of import in fuel-cell technology due to the requirements of the system. In fuel-cells, there is a small amount, usually less than 10%, of carbon monoxide present. Carbon monoxide strongly interacts with transition metals; therefore it reacts with the platinum anode and severely decreases the lifetime of the fuel-cell. A strong WGS catalyst can effectively keep CO within acceptable levels and extend the lifetime of the fuel cell[1].

The WGS reaction is usually catalyzed by an oxide supported metal, which is the typical build of many heterogeneous catalysts, such as Cu/ZnO. There has been a great deal of debate about the role of the oxide support in these types of catalysts. It is thought to be a structural promoter[5]. In other words, the support creates a structure conducive to catalysis; there are active-sites created by the lattice network of the metal-oxide that consist of vacancies or defects and it is these defects that anchor the metal to the substrate[5,6,7,8]. This is best exemplified in the work of Yoon et al. The catalytic activity of gold octamers was determined on both defect poor and defect rich MgO. When analyzed with mass spectrometry, a higher concentration of CO_2 was produced in the species that contained more defects[8]. The support also participates in partial charge transfer with the metal support in these active sites[6,8]. Beyond its structural usefulness, the oxide support interacts with the reactants and aids the reaction at the metal-support interface where the oxide is available for oxidation and reduction or oxygen storage. Among the many types of metal oxides used as support, CeO_2 is one of the best[5,7].

A great deal of research has also gone into investigating the catalytic properties of different metals. Late transition metals, such as platinum, often show high catalytic activity when supported by metal oxides. Copper was also found to be a highly active metal[7]. In its bulk form, gold does not catalyze this reaction; however, in nano-sized clusters, its catalytic properties increase greatly. Recently, it has been found that nanosized gold particles supported by metal oxides are exceptionally effective catalysts for both the WGS reaction as well as CO oxidation[5,6,7,8]. This is because gold better adheres to the oxide support and is also enhanced by partial electron transfer from the oxide support. Its catalytic activity is dependent on the size of the gold nanoparticles as well as gold coverage of the oxide support[2]. The increased catalytic activity is also due to the fact that the gold clusters create electronic resonances with the $2\pi^*$ electronic levels of O_2[8].

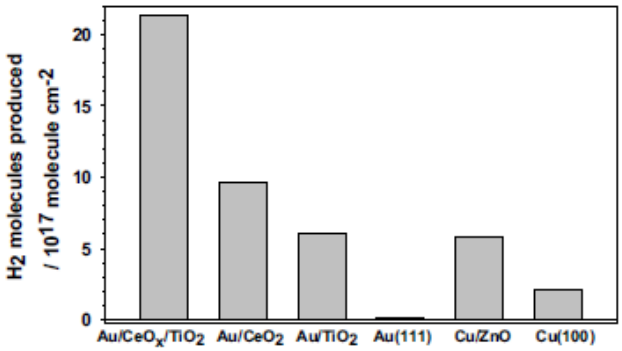

Figure 1 Comparison of the catalytic activity of Au/CeOx/TiO2 versus other oxide supported gold catalysts, Cu/ZnO, and gold and copper metal. The activity is determined by the amount of hyrdrogen gas produced by the reaction

Catalytic Activity of $Au/CeO_x/TiO_2(110)$

Building on the findings that metal-oxides doped with gold have high catalytic acitivty as well as other findings that catalysts using ceria as an oxide support are among the best catalysts, Park et al have synthesized a new heterogeneous catalyst using both of these components. Specifically in this article, the authors have found that a TiO_2 (titania) surface, doped with both CeO_2 (ceria) and gold nanoparticles will have catalytic activity that is much higher than the current WGS catalyst, Cu/ZnO as well as both titania or ceria supported gold nanoparticles. In order to produce $Au/CeO_x/TiO_2$, titania was first doped with ceria and the resulting species was then impregnanted with gold nanoparticles. In the optimization of ceria growth on titania, it was found that ceria dimers form when supported on titania; these dimers can spontaneously break back down into

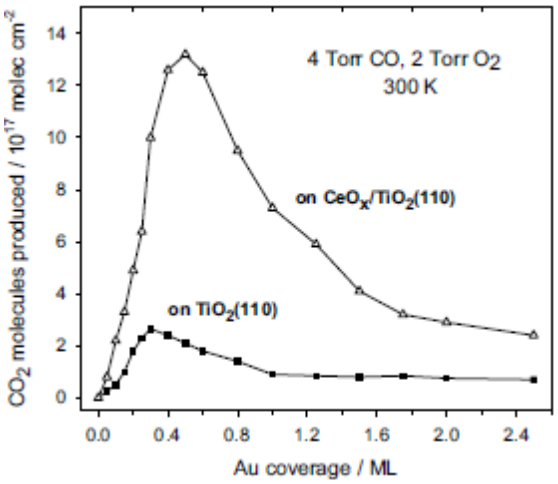

Figure 2 CO_2 production as a function of Au coverage on the mixed metal oxide and titania

monomers, but this is unlikely given that the dimers are highly stable species[2].

In a round of comparison studies, it was discovered that $Au/CeO_x/TiO_2$ was a better catalyst than Au/TiO_2 and Au/CeO_2 as well as the current WGS catalyst, Cu/ZnO. ***Figure 1*** shows how the catalytic activity of several well known heterogeneous catalysts compares to that of $Au/CeO_x/TiO_2$. It was found that $Au/CeO_x/TiO_2$ was a significantly better catalyst than any transition metal supported on a metal oxide surface. This is due the ability of $Au/CeO_x/TiO_2$ to act as a two-fold catalyst. In this species, ceria forms dimers in the form of Ce_2O_3 when supported on titania. ***Figure 3*** shows an STM image of titania supported ceria. The bright sports correspond to the ceria dimers. These dimers add to the stability of the Ce^{+3} cation, which dissociates water. The stability of the Ce^{+3} ion has already proven to be essential to the catalytic activity of any ceria supported metal catalyst. In ceria supported gold, before being reduced by CO molecules in the WGS reaction, there are Ce^{+4} ions present. Because Ce^{+3} are larger than Ce^{+4} reduction with CO puts strain on the lattice framework of ceria and the entire structure expands. This creates oxygen vacancies in the structure; water fills these vacancies and is dissociated by Ce^{+3}. This was shown in the work of Wang et al with gold doped ceria as well as copper doped ceria[7]. By comparing the doped ceria with a species in which Ce is known to be trivalent, they were able to show that Ce^{+3} cations were produced during the WGS reaction. The mechanism of action in this situation is similar to the mechanism involving $Au/CeO_x/TiO_2$. While the presence of oxygen vacancies in the lattice structure is still essential, it is the titania support rather than carbon monoxide that gives rise to the Ce^{+3} cation. In this mechanism, ceria does not oxidize CO. Ceria cations are formed as a result of electron transfer with titania and oxygen during the doping process. Water enters these active sites, or vacancies in the CeO_x structure, and is dissociated by the Ce^{+3} ions. Carbon monoxide associates with the gold nanoparticles, which act as a catalyst for the reaction between OH and CO, and the oxide-metal surface acts as a medium for the reaction between dissociated water and CO. The catalyst produced in this paper has a considerable advantage. Other oxide supported metal catalysts of

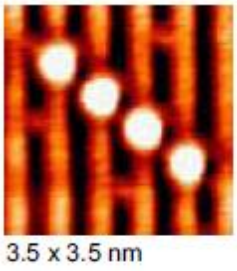

Figure 3 An STM image of titania supported ceria. The diagonal ceria array is plainly visible as bright spots.

comparable composition do not have the advantage of producing these stable dimers which play a large role in the reaction.

Beyond the WGS reaction, it was also found that $Au/CeO_x/TiO_2$ can also catalyze the oxidation of carbon monoxide. The catalytic acitivty of $Au/CeO_x/TiO_2$ was examined in this reaction and compared to the catalytic $Au/CeO_x/TiO_2$. In both cases, the amount of carbon dioxide was measured as a function of gold coverage on the oxide support. In this experiment it was found that the two species have different, but similar, optimal gold coverage. More importantly, it showed that at the maxima, the catalytic activity of $Au/CeO_x/TiO_2$ is nearly five times as high as that of an identically prepared catalyst that was not doped with ceria. ***Figure 2*** shows these results. This experiment also verifies that ceria plays a direct and essential role in the catalysis of this reaction and, in conjunction with the experiment in ***figure 1,*** that the increased stability of the Ce^{+3} cation leads to increased catalytic activity.

Conclusion

The work done in this paper is concerns electron-transfer as well as reduction-oxidation chemistry which are topics covered in this course. Electron transfer between Ce and Ti is responsible for the creation of dimers containing Ce^{+3} cations. This is discussed to work done in class because of its discussion of electron-transfer. Partial electron transfer also occurs between gold nanoparticles and the oxide support and reduction of Ce^{+4} to Ce^{+3} occurs in the production of Ce_2O_3 dimers.

In a more broad sense, the research done in this paper is connected to the work done in this course in through the methods used to identify and characterize the surfaces. Scanning tunneling microscopy (STM) was used. This is an analytical method that is used to image surfaces based on their electronic properties. A conducting needle is brought near the surface and the voltage difference between the surface and the needle allows the flow of electrons[4]. This can be connected to XANES spectroscopy in that they both contribute to the determination of charge. In STM charge density is denoted by the contrast on the picture[4] which is depicted in ***figure 3***; the bright spots correspond to ceria dimers which have more electron density than their titania support. In XANES the energy readout denotes the formal charges of atoms. The authors also used XPS spectroscopy to determine the chemical composition of the titania surface and to be sure that there were no surface contaminants. XPS was also used to confirm the presence of Ce^{+3} cations.

The findings of this paper can be used as a stepping stone for more research into optimizing mixed-metal oxide catalysis. Currently, heterogeneous catalysts tend to consist of metals

supported by one metal-oxide[1-3,5-8]. However, with these new findings, mixed-metal oxides as a support can be explored as a novel route to increasing the stability of certain ions or coordination modes that enhance the catalytic activity of the species. Also, catalysts similar to $Au/CeO_x/TiO_2$ can be created in order to increase the efficiency of fuel cells. Besides using this catalyst for the WGS reaction, its effectiveness in other reactions should also be examined. As a result of research into this area, reactions done on a large scale, mainly in industry, can be done with much less waste and with higher yields. Even more importantly, hydrogen gas, which is a major product of the WGS reaction, is a clean source of energy; therefore by optimizing catalysts of this type, production of an alternative energy source can be increased and the severity of the energy crisis can be reduced.

REFERENCES

1. Schumacher, N.; et al. "Trends in low-temperature water-gas shift reactivity on transition metals." Journal of Catalysis. 2005, 229, 265-275.
2. Park, J.; et al."High catalytic activity of Au/CeOx/TiO2(110) controlled by the nature of mixed-metal oxide at the nanometer level." Proceedings of the National Academy of Sciences. 2009, 108, 4975-4980.
3. Rasmussen, P.B.; et al. "Methanol synthesis on Cu(100) from binary gas mixture of CO2 and H2." Catalysis Letters. 1994, 26, 373-381.
4. Skoog, D.A.; Holler, F.J.; Crouch, S.R. Principles of Instrumental Analysis. 6th ed. 2007.
5. Molina, L.M.; Hammer, B. "Active role of oxide support during CO oxidation at Au/MgO". Phys Rev Lett. 2003, 90, 206102.
6. Sanchez, A. et al. "When Gold is Not Noble: Nanoscale Gold Catalysts" J. Phys. Chem. A. 1999, 103, 9573-9578.
7. Wang X, et al. "Ceria-based catalysts for the production of H2 through the water–gas-shift reaction: Time-resolved XRD and XAFS studies." Top Catal. 2008, 49,81–88.
8. Yoon, Bokwon; et al. "Charging Effects on Bonding and Catalyzed Oxidation of CO on Au_8 Clusters on MgO." Science. 2005, 307, 403-407.